UCGE Reports
Number 20360

Department of Geomatics Engineering

Refined Freeman-Durden for Harvest Detection using PolSAR data

(URL: http://www.geomatics.ucalgary.ca/graduatetheses)

by

Sina Taghvakish

Date

September 2012

UNIVERSITY OF CALGARY

Refined Freeman-Durden for Harvest Detection using PolSAR data

by

Sina Taghvakish

A THESIS
SUBMITTED TO THE FACULTY OF GRADUATE STUDIES
IN PARTIAL FULFILLMENT OF THE REQUIREMENTS FOR THE
DEGREE OF DOCTOR OF PHILOSOPHY

DEPARTMENT OF GEOMATICS ENGINEERING

CALGARY, ALBERTA

September, 2012

Abstract

To keep up with an ever increasing human population, providing food is one of the main challenges of the current century. Harvest detection, as an input for decision making, is an important task for food management. Traditional harvest detection methods that rely on field observations need intensive labor, time and money. Therefore, since their introduction in early 60s, optical remote sensing enhanced the process dramatically. But having weaknesses such as cloud cover and temporal resolution, alternative methods were always welcomed. Synthetic Aperture Radar (SAR) on the other hand, with its ability to penetrate cloud cover with the addition of full polarimetric observations could be a good source of data for exploration in agricultural studies. SAR has been used successfully for harvest detection in rice paddy fields. However, harvest detection for other crops without a smooth underlying water surface is much more difficult. The objective of this project is to find a fully-automated algorithm to perform harvest detection using PolSAR image data for soybean and corn.

The proposed method is a fusion of Freeman-Durden and H/A/αdecompositions. The Freeman-Durden algorithm is a decomposition based on three-component physical scattering model. On the other hand, the H/A/α parameters are mathematical parameters used to define a three-dimensional space that may be subdivided with scattering mechanism interpretations. The Freeman-Durden model has a symmetric formulation for two of its three scattering mechanisms. On the other hand the surface scattering component used by Freeman-Durden model is only applicable to Bragg surface scattering fields which are not the dominant case in agricultural fields. H/A/α can contribute to both of these issues. Based on the RADARSAT-2 images incidence angle, our field based refined Freeman-Durden model and a proposed roughness measure aims to discriminate harvested from senesced crops. We achieved 99.08 percent overall accuracy for cropped corn and 78.76 percent overall accuracy for soybean detection in a two step decision tree. The final conclusion was that C-band SAR

was more than adequate for corn discrimination but soybean needs additional source of data.

Acknowledgments

First of all, I would like to take this opportunity to express my deep gratitude to my current supervisor, Dr. Michael Collins, and my previous supervisor, Dr. Alexander Braun for supporting, guiding and mentoring me throughout my PhD research at the U of C. I also wish to acknowledge the Agriculture and Agri-Food Canada, and Canadian Space Agency. They provided me valuable RADARSAT-2 images, field observation data, and field boundaries.

I would also like to thank Dr. Yasser Maghsoudi and Habib Mazaheri, my fellow group members and Majeed Pooyandeh for their intellectual supports and feedbacks regarding this thesis. And also I would like to thank Dr. Holger Steffen for his advice about handling large datasets. Also my special thanks go to my ex-colleague Dr. Martin Orlob for pushing me to use Linux and LaTex as it has changed my life. I would also want to express my gratitude to Dr. Eric Pottier and Dr. Stephen Durden for shedding light on some of the concepts used in this research. And also a special thanks to all the authors mentioned in the bibliography page. Without you, I could not have taken this small step.

Finally, I would like to thank my parents for their uncompromising support of my studies, for their courage, and for standing behind me from far away. Mother and father, Pari and Gholam-Hossein you have been and always will be a source of inspiration for me. And last but not the least my sister, Mona whose presence and unflinching determination to help me was heartwarming.

Dedication

To my parents, my sister,

and a friend who changed my life.

Table of Contents

List of Tables

List of Figures and Illustrations

List of Symbols, Abbreviations and Nomenclature

Symbol	Definition
$\bar{A}$	A is an averaged value
$\underline{\mathrm{A}}$	A is a complex parameter
A^*	A conjugate
A^T	A transpose
$\vec{A}$	A is a vector
$\langle\rangle$	Temporal or spatial average
α	Freeman-Durden's alpha, co-polarized double bounce scattering ratio
α angle	H/A/α's directional cosine angle of the biggest eigenvector
A	Anisotropy
β	Freeman-Durden's beta, co-polarized surface scattering ratio
C	Covariance matrix
C	Band frequency for a radar with 4-8 cm wavelength
dB	deci-Bel
δ	Phase element
$\underline{\vec{\mathrm{E}}}$	Complex electric field vector
ϵ_r	Relative dielectric constant(permittivity)
Γ	Gamma function
H	Entropy
H/α	Entropy/α angle
H/A/α	Entropy/Anisotropy/α angle
H_{rough}	H//$mathring\alpha$ based roughness index

Hz	Hertz
κ	Kappa classification evaluation coefficient
k	Wave number
K	Band frequency for a radar with 1.1-1.7 cm wavelength
K_a	Band frequency for a radar with 0.8-1.1 cm wavelength
K_u	Band frequency for a radar with 1.7-2.5 cm wavelength
λ	Wavelength
l	Correlation length
L	Band frequency for a radar with 15-30 cm wavelength
ω	Angular frequency
$\underline{\Omega}$	Omega target vector
P	Span
π	3.141516
ψ	Orientation angle
Ψ_L	Lexicographic matrix
r	A ratio of absolute value of alpha over beta
R	Fresnel reflection coefficient
s	RMS (Root Mean Square) height
S	Scattering or Sinclair matrix
S	Band frequency for a radar with 8-15 cm wavelength
S_{ij}	Complex scattering coefficient or amplitude
σ	Radar cross section
σ^0	Normalized Radar cross section
τ	Angle of ellipticity

T	Coherency matrix
θ	Incidence angle
Var	Variance
X	Band frequency for a radar with 2.5-4 cm wavelength

Abbreviation	Definition
ALOS	Advanced Land Observation Satellite
ASAR	Advanced Synthetic Aperture Radar
CITARS	Crop Identification Technology Assessment for Remote Sensing
EM	Electro Magnetic
EM-PLR	Expectation Maximization with Probabilistic Label Relaxation
ERS	European Remote Sensing satellites
ERTS	Earth resource technology satellite
FQ	Fine Quad polarization beam type
GCP	Ground Control Point
GLAM	GLobal Agricultural Monitoring
H	Horizontal polarization
HH	Horizontally polarized transmitted and received
HV	Horizontally polarized transmitted and vertically polarized received
IEM	Integral Equation Model

JERS	Japan Earth Remote Sensing Satellite
LACIE	Large Area Crop Inventory Experiment
LAI	Leaf Area Index
OFD	Original Freeman Durden decomposition
NAD	North American Datum
NASA	National Aeronautics and Space Administration
NDVI	Normalized Differential Vegetation Index
NIR	Near Infra-Red
PALSAR	Phased Array type L-band Synthetic Aperture Radar
pdf	Probability density function
PH	Pedestal Height
PolSAR	Polarimetric Synthetic Aperture Radar
RADAR	RAdio Detection And Ranging
RADARSAT	RADAR SATellite
RFD	Refined Freeman Durden decomposition
RMSE	Root Mean Square Error
SAR	Synthetic Aperture Radar
SEASAT	SEA Satellite
SIR	Shuttle Imaging Radar
SLC	Single Look Complex product
SPM	Small Perturbation Model
SPOT	Systme Pour lObservation de la Terre
Tr	Trace of matrix
U of C	University of Calgary
US	United States of America
USDA	United States Department of Agriculture

USGS	United States Geological Survey
UTM	Universal Transverse Mercator
V	Vertical polarization
VH	Vertically polarized transmitted and horizontally polarized received
VPI	Vegetation Productivity Indicator
VV	Vertically polarized transmitted and received

Epigraph

You are really not going to like it, observed Deep Thought.

Tell us!

All right, said Deep Thought, The Answer to the Great Question ...

Yes ... !

Of Life, the Universe and Everything ... said Deep Thought.

Yes ... !

Is ...

Yes ... !!! ... ?

Forty-two. Said Deep Thought, with infinite majesty and calm.

Douglas Adams, The Hitchhiker's Guide to the Galaxy

Chapter 1

Introduction

1.1 Harvest Detection

The Earth's population officially reached seven billion people at the end of October 2011, and by 2050 this number is expected to be nine billion[12]. It appears that we are using most of our resources in terms of water, human labor, technology, and agricultural farmlands and yet we have one billion people undernourished[12]. But the future may not look as grim as it is always predicted, and new innovations along with new resources are yet to be discovered. But meanwhile using the available resources wisely is certainly the first step toward a brighter future and there comes the importance of agricultural studies.

Agricultural resources, an important input for agricultural studies are becoming more global than national, and a good understanding and estimate of these resources is inevitable. For example in 2009 Russia faced both drought and wildfire causing a considerable reduction in their wheat production. Like a butterfly effect, this ripple caused a surge in global wheat demands and consequently the price for wheat hit the rooftop [31]. Accurate and timely information on the type of the crop grown and their acreage, and the crop growth conditions are essential parameters for crop production estimations. These estimations are needed for guiding the decision makers in formulating optimal strategies for planning, distribution, marketing, transportation and storage of the essential agricultural product [54].

Therefore in any agricultural resource related studies, the knowledge about the type of the crop grown is a necessity. Like any other species on the planet Earth, each one of the agricultural crops have their own characteristics and therefore they should be treated differently. Thus we believe that it is time for us to properly introduce our two main guests in this research from these species. In the North American continent corn and soybeans are

the main food ingredients for human beings in the past decade[26]. Corn is a cold-intolerant crop, and its cultivation time in the temperate zones is usually in the spring. Having been first cultivated by indigenous peoples in the highlands of Mexico, it was later cropped all around the world. In Canada it is mainly cultivated in Manitoba, Ontario, and Quebec. Corn has a wide variety of uses from breakfast cereals to whiskey and from fuel to fabrics. The terminology for different parts of the corn plant is presented in figure 1.1.

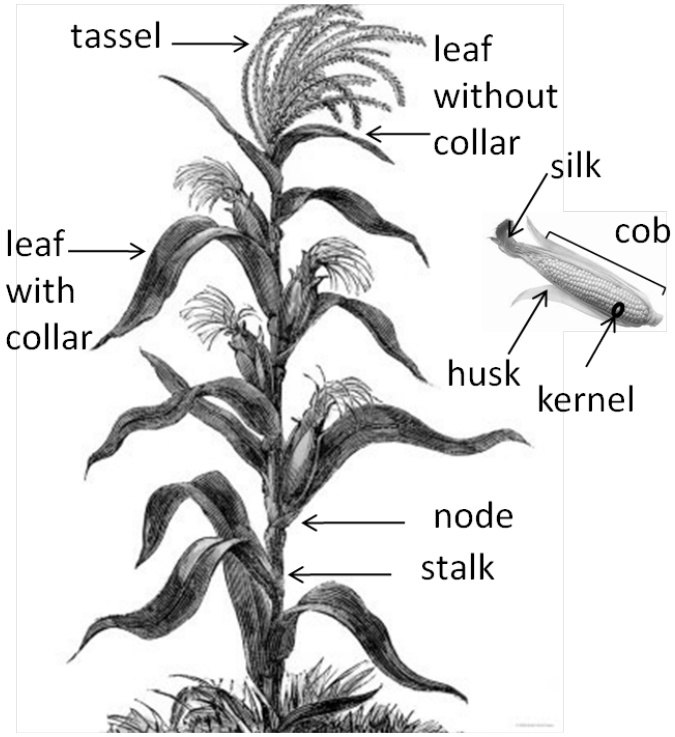

Figure 1.1: Corn plant's terminology adapted from allposters[1] and wpclipart[77]

Crop stage identification system used by Ritchie et al. divides corn plant development into vegetative (V) and reproductive (R) stages (figure 1.2). The (V) stages are designated numerically as V1, V2, V3, etc. through V(n), where n represents the number of leaves with visible collars for corn. The first and last (V) stages are designated as VE (emergence) and VT (tasseling). The reproductive stages are simply designated numerically [64].

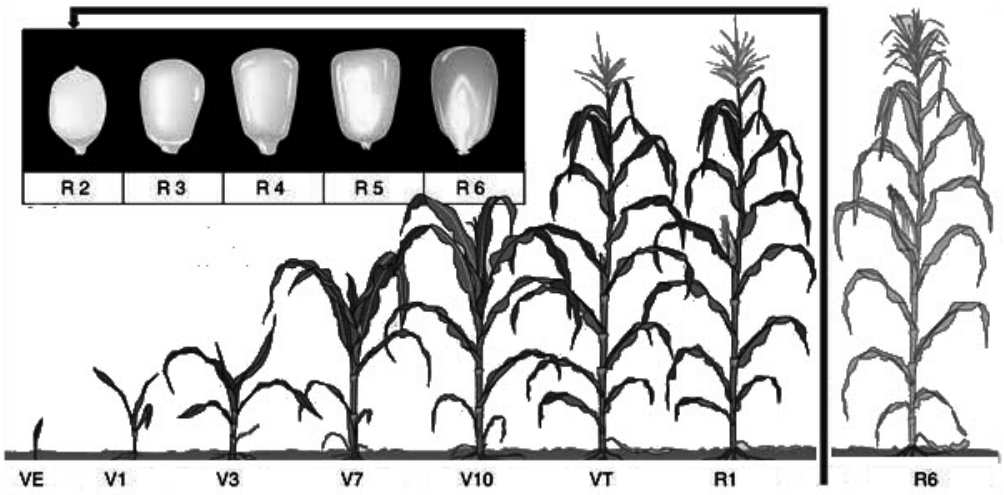

Vegetative stage		Reproductive stage		
Stage	**Description**	**Stage**	**Description**	**Height(cm)**
VE	Emergence	R1	Silking - silks visible outside the husks	250
V1	One leaf with collar visible	R2	Blister - kernels are white and resemble a blister in shape	250
V2	Two leaves with collars visible	R3	Milk - kernels are yellow on the outside with a milky inner fluid	250
V(n)	(n) leaves with collars visible	R4	Dough - milky inner fluid thickens to a pasty consistency	250
VT	Last branch of tassel is completely visible	R5	Dent - nearly all kernels are denting	250
		R6	Physiological maturity - the black abscission layer has formed	250

Figure 1.2: Corn growth stages adapted from Ritchie[64]

In the case of our second guest, soybeans, cultivation started from northeastern China and has been used in various types of human food form (e.g., soy milk, Tofu, soy sauce, and oil), or as animal feed (soybeans meal and roasted soybeans), as well as industrial products (e.g., printing ink, bio-diesel, and plastics). Soybeans arrived in Canada in the

mid 1800s, but it was after the Second World War that Statistics Canada began to collect data on the significance of soybeans with 4,400 hectares reported in 1941. Soybeans harvest reached 62,967 hectares by 1951 but they were mostly cultivated in southern Ontario, the region with the longest and warmest growing season in Canada. In the mid-1970s, intensive breeding on this incredibly versatile crop took place to cultivate across Canada. The 1.2 million hectares of soybeans reported on the Census of Agriculture in 2006 showed eightfold increase in comparison to census of 1976 [19]. And this increasing interest on soybeans cultivation in Canada is growing rapidly. The terminology for different parts of the soybeans plant is presented in figure 1.3.

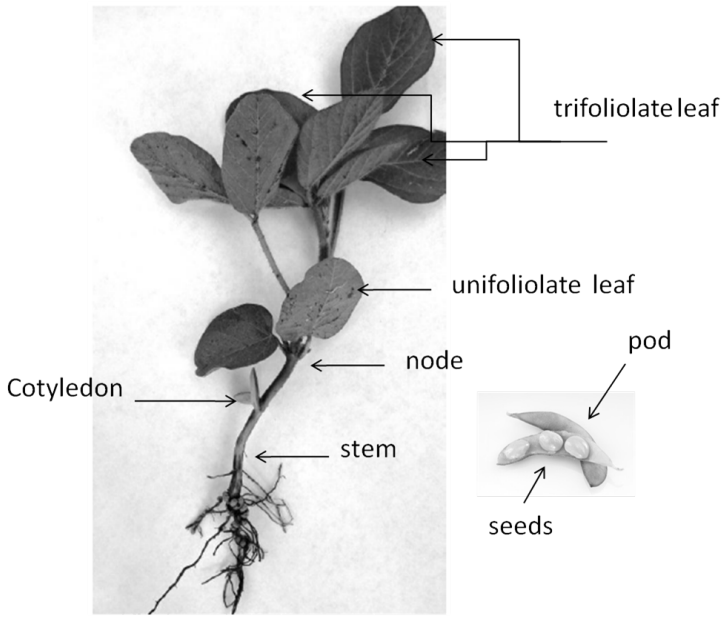

Figure 1.3: Soybean plant's terminology, adapted from Kandel[35] and Harris[29]

Crop stage identification system used by Ritchie et al. [65] divides soybean's plant development into vegetative (V) and reproductive (R) stages (Figure 1.4). The (V) stages are designated numerically as V1, V2, V3, etc. through V(n) where n represents the number for the last node stage of a specific variety of soybean. The first and second (V) stages are designated as VE (emergence) and VC (Cotyledon). The reproductive stages are simply designated numerically.

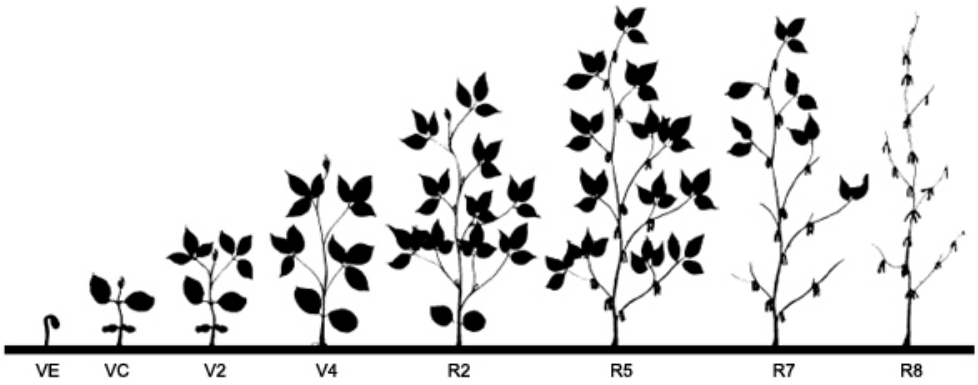

Vegetative stage		Reproductive stage		
Stage	**Description**	**Stage**	**Description**	**Height(cm)**
VE	Emergence	R1	Open flower at any node on the main stem	38 to 45
VC	Cotyledon	R2	Full bloom with opening flower at one of the two uppermost nodes on the main stem with a fully developed leaf and half the length of the full plant	43 to 58
V1	Although it is in its second node, unifoliolate and first trifoliolate leaves are fully developed	R3	Beginning of pod with 5 mm long at one of the four uppermost nodes on the main stem with a fully developed leaf	58 to 81
V2	Unifoliolate and first two trifoliolate leaves are fully developed with three nodes	R4	Full pod with 2 cm long at one of the four uppermost nodes on the main stem with a fully developed leaf	71 to 99
V3	Unifoliolate and first three trifoliolate leaves are fully developed	R5	Beginning of 3 mm long seed in the pod at one of the four uppermost nodes on the main stem with a fully developed leaf	76 to 109
V(n)	Unifoliolate and (n) trifoliolate leaves are fully developed	R6	Full seed with pod containing a green seed that fills the pod cavity at one of the four uppermost nodes on the main stem with a fully developed leaf	79 to 120
		R7	Beginning of maturity with one normal pod on the main stem that has reached its mature pod color	
		R8	95% of the pods have reached their mature pod color	

Figure 1.4: Soybean growth stages adapted from Ritchie[65]

Being the conclusion to a tremendous amount of labor and investment in agricultural fields, harvest is the act of gathering in the crops[30]. On a large spatial scale, the dynamic mapping of harvest allows optimized cutter deployment, transport operations, efficiency of factories, and eventually permits a better estimation of the effective yield[4]. And the amount of the yield is a significant factor for tax estimation, insurance, and more importantly food management[61]. Also erosion modeling[72] and managing of storage facilities for harvested crops depend on harvest detection information. Therefore harvest estimation is an invaluable source of information for policy makers.

Every type of crop has a certain time period for harvesting. Harvest timing is the balances between likely weather conditions and the degree of crop maturity. Yield and quality of the crop could be easily affected by weather conditions such as frost, rain, warmth or cold. Although early harvest date may avoid damaging conditions, but leads to a poor yield. On the other hand delayed harvest may result in a better harvest, but increases the risk of weather problems. It can be said that the timing of the harvest often amounts to a significant gamble [54].

For the case of corn, the maximum dry weight of all kernels on the ear is reached approximately 55 to 65 days after silking. When corn reaches its physiological maturity, a black or brown layer is formed where the kernel attaches to the cob. At this stage the leaf and husk tissue has already lost its green color but the stalk of the plant may remain green. Although there is much variation among hybrids and environmental conditions, the corn's kernel moisture content ranges from 30 to 35% when it is mature. This coincides with R6 (black layer formation) in figure 1.2. Depending on the usage, the moisture level of corn is different. For example if the goal is to store the grain, it requires 13% to 15% moisture level for shelled corn. Since drying the crop is expensive, harvesting at R6 or shortly after would be costly. Therefore as long as field losses would not become a problem, it may well be advantageous to let the crop partially dry in the field after R6. As mentioned before, the

rate of field drying after R6 depends on the hybrid and the environment [64].

As for soybean, the table attached to figure 1.4 shows that the full seed of soybeans appear at stage R6. At the last Reproduction stage (R8) as shown in figure 1.4 the plant is completely defoliated. Ideal moisture for harvesting the soybeans plant is 13%. But only 5 to 10 days after R8, with presence of drying weather conditions, soybeans can reach to less than 15% moisture level. It should also be noted that moisture below 13% results in increased pre-harvest shatter loss, increased number of split beans, and loss of weight to sell. Soy varies in growth and habit. The height of the plant varies from below 20 cm up to 2 meters. In modern cultivations it takes 80 to 120 days from sowing to harvesting to get to nominal 1 m height for soybeans (Figure 1.4).

Therefore there are no single predefined harvesting time existing for corn and soybeans fields and it is only the farmer's decision that counts. Historically the only practical way for harvest detection and estimation was field observations. An example of traditional harvest estimation was large scale sample survey method[54]. It involved selecting random villages for sampling procedure, and estimating the acreage of the crop before the harvest, provided by comprehensive field measurements in these villages. The final yields were being compiled through crop cutting experiment, carried out on a number of randomly selected fields in the sample village in a district. The estimate was available only after the harvest of crops [54]. The conventional field based methods such as large scale sample survey, extrapolate some parameters to adjust for the point wise nature of the data collection. There are too many models to be used for this extrapolation, for example Murthy [53] reports nine categories for the crop growth models: namely statistical, mechanistic, deterministic, stochastic, dynamic, static, simulation, descriptive, and explanatory models. Being the most common, statistical models look for the most influential factors throughout years of crop yield observations. Then the relation between the crop yield and those effective factors is established by an empirical equation and the coefficient of each factor are estimated. Most of the time, these factors are

environmental. Maximum temperature, sunshine hours, minimum temperature, and relative humidity in the morning are some examples of these parameters.

Although field based harvest estimation methods were statistically accurate, they were mostly point-wise. With time consuming observations, they most likely fail to provide timely information, not to say they may not be conclusive. And since the advent of remote sensing these practices are becoming gradually obsolete. Remote sensing refers to the observation of the Earth surface with use of the electromagnetic waves from platforms far away such as satellites. With proper composition of visible wavelengths (0.4 μm to 0.7 μm) some sensors can provide scenes comparable to what an enhanced human eye would perceive. The sensor systems with such ability are called optical remote sensing systems, although some of them include wider electromagnetic spectrum range(0.3 μm to 15 μm) than mere visible wavelengths. The Earth resource technology satellite 1 (ERTS-1) that later was renamed to be Landsat-1 was launched on July 23, 1972. It was the first satellite intended solely to study and monitor our planet's land masses. The then-director of the USGS(U.S. Geological Survey), Dr. V. E. McKelvey, has a famous quote: "The ERTS spacecraft represents the first step in merging space and remote-sensing technologies into a system for inventorying and managing the Earth's resources." Therefore this satellite was a changing point in the history of agriculture and remote sensing.

Since then optical remote sensing techniques have been used in pre-harvest and post-harvest crop inventories. Early solutions like Crop Identification Technology Assessment for Remote Sensing (CITARS), and Large Area Crop Inventory Experiment (LACIE) all used Landsat series data[54]. CITARS(1973) was the first major program to use Landsat-1 satellite [1] data to evaluate existing quantitative measures for identification of specific crops. This project was aimed at distinguishing corn from soybeans in the growing season. The CITARS results affected the design of then new-coming LACIE program. LACIE (1974-1976) being the first global remote sensing observation of crop production forecasting was

[1]Land Satellite originally named 'Earth Resources Technology Satellite-1 (ERTS-1)

focused on wheat. GLAM (GLobal Agricultural Monitoring) by the U.S. Department of Agriculture (USDA) and the National Aeronautics and Space Administration (NASA) is a follow up to those early assessments. This project assimilates NASA's Moderate Resolution Imaging Spectro-radiometer (MODIS) data and its products into an already existing decision support system for agricultural applications.

Raw remote sensing images was not always used to be a stand-alone solution for agricultural problems. It was also used to simply introduce some spectral indices to the models that already have been used as conventional and traditional approaches. Normalized Difference Vegetation Index ($NDVI$)[66] is probably the most well-known index that remote sensing has ever been contributed to vegetation related analysis. It works simply because healthy vegetation reflects very well in the near infrared (0.7 μm to 1.5 μm) part of the electromagnetic spectrum in comparison to the visible portion. This physical phenomenon is the main signature of vegetations in optical remote sensing.

Remote sensing could also be used to estimate real physical parameters, Leaf Area Index (LAI) is an example of a physically based agricultural parameter that optical remote sensing could provide. This physical parameter is one of the oldest scientific observations about agriculture and it is available worldwide since 1932 [70]. Remote sensing can also help physical modeling by updating a variable such as LAI or calibrating the model variables. Therefore physical models such as biomass [2] estimation are other widely used applications of remote sensing data. The same crop growth models that have been used in traditional methods could be modified to use optical remote sensing data.

There are also methods defined to classify the optical remote sensing's feature space. One such method is tasseled cap[14] which is developed to monitor agricultural crops in mid-west United States. It is a scene specific multi-spectral transformation based on the assumption that a 3-D sub-space of brightness, greenness and wetness could be defined. These three axes define two planes and a transition zone. Tasseled cap describes the spectral-temporal

[2]Mass of living biological organisms in a given area at a given time

development of agricultural crops in a graphical context. These few examples show that optical remote sensing is certainly a useful source of information for agricultural studies, but there is an English proverb: "Every path has its puddle".

One of the main weaknesses of optical remote sensing is its inability to acquire data in presence of cloud cover. The optical sensors use smaller wavelengths (0.3 μm to 15 μm) than cloud droplet particle sizes(10 μm to 100 μm). Due to *non-selective* scattering[3] phenomenon the visible and near infrared wavelengths would scatter equally and cause clouds to be white (saturated) in the visible bands. In the thermal infrared wavelengths (5 μm to 1000 μm) on the other hand, the emission from the surface is the main source of data. In this case the low temperature of the clouds lead to a smaller amount of emission in comparison to their neighborhood. The wavelength in thermal infrared become almost equal to cloud droplet particle sizes and therefore *Mie resonance* scattering[4] would accompany non-selective scattering in blocking the emission coming from the Earth surface beneath most of the cloud types. If we go a bit further in the electromagnetic spectrum, in the microwave (1 cm to 15 cm) portion clouds are generally invisible. The reason comes from a phenomenon called *Rayleigh* scattering [5]. Since cloud particles are considerably smaller than the incident wave's wavelength, the wavelength dependency of Rayleigh scattering becomes ignorable and the incidence wave passes through the clouds like they do not exist in the first place.

On the other hand most of the optical remote sensing sensors are passive, meaning they use the sun as the main source of incident radiation. Therefore they do not have the ability to acquire images at night. These two drawbacks of the optical remote sensing, being impregnable cloud cover and lack of day/night observations, affect the temporal resolution of these sensors. The temporal resolution is not the same concept as revisit cycle. The temporal resolution is a time difference between two successful image acquisitions of the same

[3]When the particles are much larger than the incident wave (wavelength independent)

[4]When the particles causing the scattering are larger than the wavelengths of incident wave in contact with them (wavelength dependent).

[5]When the particles causing the scattering are smaller in size than the wavelengths of incident wave in contact with them (wavelength dependent)

target. Therefore if the target pixel is cloudy, the temporal resolution necessitates another observation date. Therefore scientists have sought after alternatives to reduce/remove this uncertainty about the temporal resolution.

1.2 Motivation and Innovations

The main objectives of this research are

1. To find fully-automated algorithm to perform harvest detection for corn and soybeans, that is not affected by cloud cover or darkness.

Harvest detection plays a key role in food management as one of the main challenges of current century. Traditional harvest detection methods that rely on field observations are laborious and inefficiently time consuming. Moreover, they can't satisfy the current needs of the growing human population. As an alternative method, optical remote sensing enhances the process dramatically, though it has its own drawbacks such as cloud cover and temporal resolution issues.

Microwave frequencies on the other hand, could easily penetrate cloud cover since the wavelengths are considerably larger than cloud droplets. *RADAR* technology which stands for *RA*dio *D*etection *A*nd *R*anging uses microwave portion of the electromagnetic spectrum. Therefore the radar sensors used for remote sensing purposes could penetrate cloud covers. Also active microwave sensors could provide information about the ground even in night time which further increases their temporal resolution.

This research aims at applying radar remote sensing as a different approach for harvest detection. Synthetic Aperture Radar (SAR) has enough spatial resolution for harvest detection applications. While it has the same characteristics in generating global and spatial information as the optical remote sensing, SAR is also able to penetrate the cloud cover which gives it an edge in comparison to the optical remote sensing. Also harvest detection

using SAR data is a step toward more complex applications of SAR in agricultural disciplines (e.g., cultivation problem detection). Therefore the other objective of this research is

2. To develop a standalone algorithm to use PolSAR image to detect the harvest.

The parameter that describes the orientation of some particular waves oscillations is called polarization. The measurement and interpretation of polarization is called polarimetry. In SAR, polarimetry is one of the important sensor configurations and is defined in detail in chapter 2. But PolSAR is the concept of using polarimetric backscattering behavior as an additional source of data from SAR imagery. PolSAR is still an experimental technique in most of the agricultural studies [25]. Mapping soil tillage and crop residue, soil moisture, crop type mapping, crop condition are some of the most studied cases [47]. Harvest detection is another application that has been also studied widely especially for rice paddies[9][10][33][42][46]. But harvest detection is not as trivial when it gets to other types of agricultural practices as there is no smooth water surface absorbing or reflecting the radar wave from the bottom surface. The data available to this project includes only corn and soybeans fields, therefore this research would not be able to extrapolate to all of the agricultural crops. Another important aspect of our second goal is to use a single image and therefore methods such as change detection are not considered. Also the low temporal variation of our data as could be seen in later chapters was another factor for deciding not to perform change detection. This was also the main reason for not performing any time series analysis over the fields for harvest detection.

In order to achieve the aforementioned two goals we developed and implemented a new field based algorithm based on two well-established polarimetric decompositions. Also we proposed an additional roughness measure to further describe and distinguish crops situations(e.g. cropped, harvested,etc.). A first step decision tree classification approach is then proposed with decision rules based on the incidence angle for cropped corn discrimination. While for very steep incidence angles the roughness measure was the only criterion for deci-

sion rules, for less steep and shallow incidence angles a threshold over one of the proposed algorithm's outputs was sufficient.

In a second step, we proposed another decision tree step to distinguish cropped soybeans from the remaining of the fields. The decision rule was again based on the proposed algorithm but the source data was unfiltered PolSAR image. Therefore in two steps cropped fields were extracted from the PolSAR scenes and the remaining fields were harvested fields.

1.3 Organization of the Thesis

Chapter 2 provides the necessary background for SAR in agriculture. It includes some PolSAR concepts, as well as literature review about the similar efforts done by the scientific community to perform agricultural studies. This literature review is mainly focused on our specific crops and PolSAR sensitivity to them.

Chapter 3 describes the proposed methodology in addition to the datasets used in this research. Elaborating on the methodological aspects of the two well-known methods, namely Cloude and Pottier's[13] entropy/anisotropy/α angle (the *mathring* is only for differentiating α symbol in Freeman Durden algorithm and H/A/α algorithm) and Freeman-Durden's[23] decomposition, we propose a way of connecting these two methods. And thus we introduce a new method based on the integration of those two existing methods.

Chapter 4 provides some implementation details for our newly proposed method along with the results of several well-established unsupervised classification algorithms, which we shall use as baseline classification methods. Implementation details include the necessary data preprocessing, along with processing block diagrams for original Freeman-Durden decomposition (OFD) and our refined Freeman-Durden (RFD) algorithms. The RFD algorithm was analyzed in term of its possible solutions and in respect to the OFD algorithm. We also included the results of our baseline unsupervised classifications in this chapter since we wanted to compare the results of some of the well-established classification methods.

Chapter 5 includes results and discussion for corn. We discuss how we can distinguish cropped corn fields and why our method has indeed improved our ability to do so for corn fields. Then in chapter 6 we provide some insights to soybeans and our best guess for cropped soybeans discrimination from rest of the fields. Finally in Chapter 7 the conclusion and future works to improve the method and practice are proposed.

Chapter 2

PolSAR and Harvest Detection

The full coverage of all physical and mathematical concepts related to SAR is out of the scope of this document, thus section 2.1 of chapter 2 depicts some mathematical tools and parameters that is necessary for the remaining of this thesis. And we refer the reader to the references such as [6] and [45] for more in depth understanding about the SAR. We conclude chapter 2 with a literature review on SAR application for harvest detection.

2.1 Necessary SAR Concepts

Some radar and especially polarimetric concepts are necessary to understand section 2.2 and chapter 3. To have a better overview of the underlying scientific concepts, we broke them down to eight main subsections being imaging concepts, wave propagation, incoherence polarimetry, coherence polarimetry, vector polarimetry, scattering mechanisms, unsupervised PolSAR classifications, and classification evaluation.

Imaging concepts defines some satellite related parameters that defines the geometry of the SAR imaging system. Wave propagation on the other hand includes the basic concepts relating the electromagnetic field vector and the polarization concepts. Since any wave can be defined by phase and amplitude, incoherence polarimetry is mainly concerned with amplitude related parameters while coherence polarimetry is the phase related concepts. Another way to look at the same wave is to assume its vector properties and that is included in vector polarimetry section. Interaction with the target changes some characteristics of the wave; therefore another way to look at the same phenomenon is to observe the physical scattering mechanisms that influence the radar signal.

The previous concepts are all physically based definitions. Therefore there exist an-

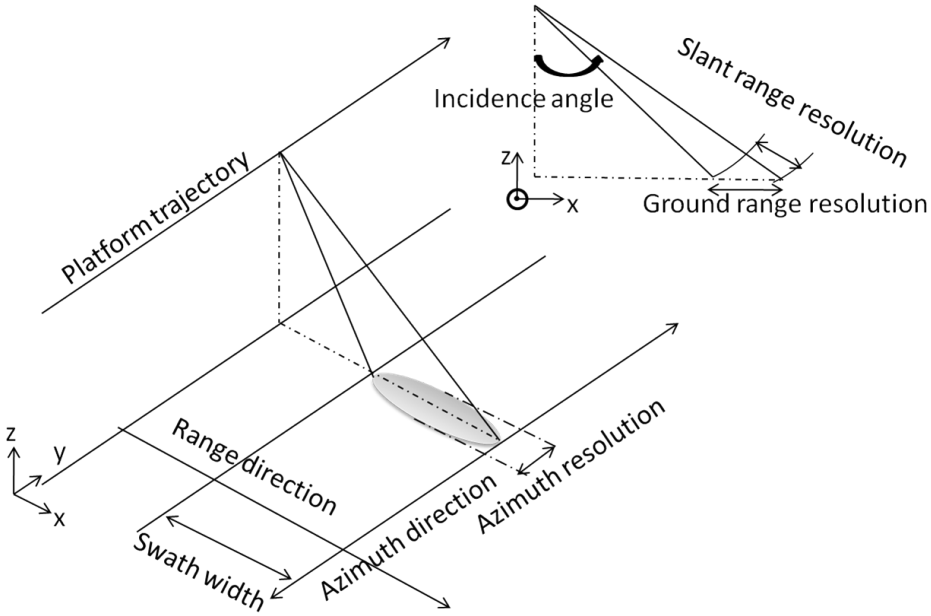

Figure 2.1: Radar imaging definitions

other method of observation based on empirical methods. Classification concepts and their evaluations for SAR are from this genre.

2.1.1 Imaging Concepts

In depth definitions and concepts of radar imaging system need a comprehensive tutorial. Therefore we only briefly introduce these parameters and present figure 2.1 as a visual aid in what these definitions would look like. *Incidence angle* is the angle formed by the incident ray on a surface and a perpendicular to the surface at the point of incidence. Small incidence angles are called steep while large ones are called shallow incidence angles.

Azimuth direction is parallel to the flight trajectory of the SAR platform, and *range direction* is perpendicular to azimuth direction while it is tangent to the surface of the ground. Since range and azimuth has different processing methods for SAR imagery, therefore azimuth and range spatial resolutions are different. Both ground and slant range resolutions are presented in 2.1. The *slant range* could be defined as the distance between the leading

and trailing edges of the radar pulse. And the *ground range* is the projection of the slant range on the ground. *Azimuth resolution* on the other hand, is determined after aperture synthesis across the beam in the azimuth direction. These concepts are definitions for *resolution cell* size because they are the footprints of the radar instantaneous field of view on the ground. However, *pixel* on the other hand is the picture element and is the single measurement presented as single element generating the final image.

One other important geometrical parameter in remote sensing is the swath width. The *swath width* in SAR is the distance on the ground between near range and far range beams.

Wave related parameters are very influential on what could be extracted from SAR data. For example the salt and pepper noise called *speckle* is an inherent characteristic of SAR images due to the rapid phase changes in neighboring resolution cells. Now that the geometry related parameters are partly defined, the wave propagation parameters should follow. One of the most influential concept in wave propagation in SAR imagery is polarimetry.

2.1.2 Wave Propagation Concepts

Radar polarimetry is concerned with the control of the polarimetric properties along with extraction of target properties from the behavior of the wave scattered or reflected from the target [6]. The *polarization* is conventionally defined to describe temporal behavior and orientation of the three dimensional complex electric field vector $\underline{\vec{E}}$ along with direction of propagation of the Electro-Magnetic (EM) wave in time. This motion could be described by components on the three axes x, y, and z. The z axis conventionally is in the direction of propagation, while the x and y axes lie in a plane perpendicular to the direction of propagation with (x, y, z) forming a right hand orthogonal set. Figure 2.2 shows a general depiction of analytical signal form of the wave vector changing with time and propagating in z direction. In general the real part of the electric field vector as it is seen in figure 2.2 spans an ellipse in xy plane. The electric field vector at any time instance, t, and z coordinate can be formulated as follows:

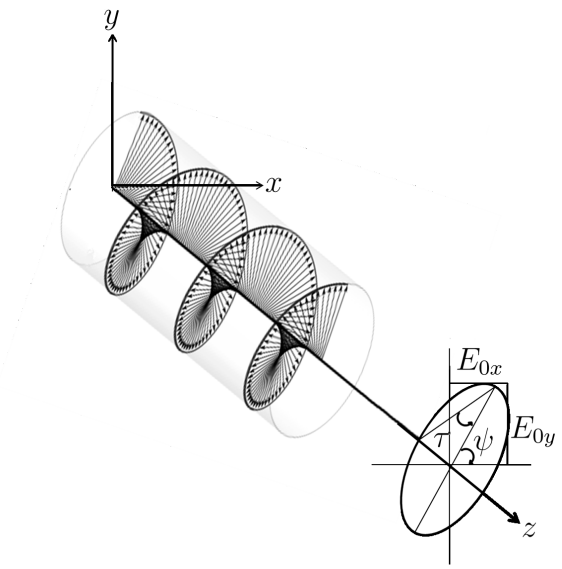

Figure 2.2: Electric Force propagation of EM.

$$\vec{E}\,(z,t) = \begin{bmatrix} E_{0x}\cos\left(\omega t - kz + \delta_x\right) \\ E_{0y}\cos\left(\omega t - kz + \delta_y\right) \\ 0 \end{bmatrix} \tag{2.1}$$

where E_{0x} and E_{0y} are the x and y *amplitudes* of the real part of the electric field, k is the wavenumber, ω is the angular frequency, and δ_x and δ_y are the *phase* elements for the sine waves in x and y direction. Therefore amplitude of this wave is $\sqrt{E_{0x}^2 + E_{0y}^2}$. In figure 2.2 the $\psi(0^\circ \leqslant \psi \leqslant 180^\circ)$ is the *orientation angle* which is the angle of the semi-major axis with respect to x axis and it could be calculated from equation 2.2

$$\tan\left(2\psi\right) = 2\frac{E_{0x}E_{0y}}{E_{0x}^2 - E_{0y}^2}\cos\delta \tag{2.2}$$

where $\delta = \delta_y - \delta_x$ is the phase difference between the x and y components of the electric field. The rest of the parameters are the same as equation 2.1. The *angle of ellipticity* $\tau(0^\circ \leqslant \tau \leqslant 45^\circ)$ is defined by equation 2.3.

$$\left|\sin 2\tau\right| = 2\frac{E_{0x}E_{0y}}{E_{0x}^2 + E_{0y}^2}\left|\sin\delta\right| \tag{2.3}$$

where all the parameters are already defined for equation 2.1.

As it can be seen from figure 2.2, τ is a measure of the ovality of the ellipse. So when in equation 2.1 both x and y components of electric field are in phase, according to equation 2.3 the magnitude of τ is equal to either zero or π. This type of polarization is called linear ($\tau = 0$) polarization because the ellipse becomes a line. If the x axis would be the same as the tangent of the geoid, for ψ of magnitude 0° or 180° the linear polarization by convention is called *Horizontal* (H) polarization. In contrast, if ψ is equal to 90° the linear polarization is called *Vertical* (V) polarization. Another especial case is when E_{0x} is equal to E_{0y} and τ is $\pm\pi/2$. In this case the ellipse becomes a circle and the wave is circularly polarized. By these conventions if the handedness of the circle or ellipse is the same as that of the coordinate system the polarization is *Right* (R) otherwise it is *Left* (L) hand polarization. As it will be shown in table 2.1, due to the target characteristics these especial cases for polarizations provide indispensable information for this research.

2.1.3 Incoherence Polarimetric Concepts

Radar cross section, σ is the most familiar incoherence parameter. Its dimensionality is $[m^2]$ and could be calculated from [6]:

$$\sigma = 4\pi r^2 \frac{\left|\vec{E_S}\right|^2}{\left|\vec{E_I}\right|^2} \tag{2.4}$$

where $\left|\vec{E_I}\right|^2$ and $\left|\vec{E_S}\right|^2$ are respectively the incidence and backscattered wave's power densities and r is the distance between the target and the receiving antenna. In case of agricultural fields the target is mostly a '*distributed target*' and it means that not all the targets are fixed or stationary. Even a simple breeze during the observation period can vibrate the leaves and change the backscattering center and direction, and thus their polarization. Another situation is when the target's size is smaller than the resolution cell; these two cases could be solved by averaging. There is two type of averaging most commonly used in SAR; one is the time averaging; and the other is spatial averaging. Averaging is normally denoted by the sign $\langle\rangle$ and could be formulated as [6]

$$\langle f(t)\rangle = \lim_{T\to\infty} \frac{1}{2T} \int_{-T}^{T} f(t)\, dt \tag{2.5}$$

where f is the averaged function, T could be either time or space, and the limit is not necessarily bound to infinity. When distributed scatterers are to be observed, normalized radar cross section σ° (average radar cross section per unit area) should be used instead of σ.

$$\sigma^0 = \frac{\langle\sigma\rangle}{A_0} \tag{2.6}$$

where A_0 is the averaging area and therefore σ° becomes dimensionless parameter. σ^0 is also called *scattering* or *backscattering coefficient*. The antenna could be tuned in a way to maximize a certain polarization for receiving and transmitting. For example if it is tuned to send horizontal and receive vertical polarization the returned backscatter cross section is demonstrated by σ_{HV}, and so on (σ_{HH}, σ_{VV}, and σ_{HV}). The same logic also applies to σ_{RL} (Right hand polarized transmitted and left hand polarized received), σ_{LR}, σ_{RR}, and σ_{LL}.

There exists different methods to extract information from σ^0, one of the widely used methods is the use of *signature plots*[6]. The three main axes of these plots are ellipticity angle, orientation angle, and normalized radar cross section. In these plots numerous parameters such as number of maxima and minima and their location on the signature plot provide information about the scattering phenomenon[6] [45].

2.1.4 Vector Polarimetric Concepts

The equations mentioned in the previous section are only associated with the polarization trough the power (scaler). Therefore the vector nature of the EM wave is not going to be explicitly observed by those parameters. The scattering at target must be defined as a function of EM field itself. A far field representation of such a relation could be written as equation 2.7,

$$\underline{E}_S = \frac{e^{-jkr}}{r} S \underline{E}_I = \frac{e^{-jkr}}{\sqrt{4\pi}r} \begin{bmatrix} S_{11} & S_{12} \\ S_{21} & S_{22} \end{bmatrix} \underline{E}_I \tag{2.7}$$

where $\underline{E}_S$ is the complex electric field matrix (e.g., $\underline{E_S} = \begin{bmatrix} \underline{E_x} \\ \underline{E_y} \end{bmatrix}_S$), the subscripts $_S$ and $_I$ respectively stands for scattered and incidence, S matrix is named as *scattering* or *Sinclair matrix* [45, 6], and the S_{ij} are the so called *complex scattering coefficients* or complex scattering amplitudes. The term $\frac{e^{-jkr}}{\sqrt{4\pi}r}$ takes into account the propagation effects both in amplitude and phase [45]. Using especial transformations, it is possible to change the coordinate system of scattering matrix to H and V coordinate system [45]. The polarimetric *covariance matrix* then can be defined in its most general form [45],

$$C_4 = \begin{bmatrix} \langle |S_{HH}|^2 \rangle & \langle S_{HH} S_{HV}^* \rangle & \langle S_{HH} S_{VH}^* \rangle & \langle S_{HH} S_{VV}^* \rangle \\ \langle S_{HV} S_{HH}^* \rangle & \langle |S_{HV}|^2 \rangle & \langle S_{HV} S_{VH}^* \rangle & \langle S_{HV} S_{VV}^* \rangle \\ \langle S_{VH} S_{HH}^* \rangle & \langle S_{VH} S_{HV}^* \rangle & \langle |S_{VH}|^2 \rangle & \langle S_{VH} S_{VV}^* \rangle \\ \langle S_{VV} S_{HH}^* \rangle & \langle S_{VV} S_{HV}^* \rangle & \langle S_{VV} S_{VH}^* \rangle & \langle |S_{VV}|^2 \rangle \end{bmatrix} \tag{2.8}$$

In radar applications, *reciprocity theory* states that receiving and transmitting properties of a radar antenna is the same. Therefore in *mono-static* case where the receiver and the transmitter antennas are the same, $S_{HV} = S_{VH}$ and consequently four dimensional covariance matrix 2.8 becomes three dimensional such as,

$$C_3 = \begin{bmatrix} \langle |S_{HH}|^2 \rangle & \sqrt{2} \langle S_{HH} S_{HV}^* \rangle & \langle S_{HH} S_{VV}^* \rangle \\ \sqrt{2} \langle S_{HV} S_{HH}^* \rangle & 2 \langle |S_{HV}|^2 \rangle & \sqrt{2} \langle S_{HV} S_{VV}^* \rangle \\ \langle S_{VV} S_{HH}^* \rangle & \sqrt{2} \langle S_{VV} S_{HV}^* \rangle & \langle |S_{VV}|^2 \rangle \end{bmatrix} \tag{2.9}$$

Another presentation of the second order statistics for scattering process is through *coherency matrix* T which is only a transformation of the C matrix. The transformation matrix

is D_4 and it is defined by equation 2.10

$$D_4 = \frac{1}{\sqrt{2}} \begin{bmatrix} 1 & 0 & 0 & 1 \\ 1 & 0 & 0 & -1 \\ 0 & 1 & 1 & 0 \\ 0 & j & -j & 0 \end{bmatrix} \tag{2.10}$$

where j is the imaginary unit. The transformation equations would be

$$\begin{aligned} T_4 &= D_4 C_4 D_4^{-1} \\ T_3 &= D_3 C_3 D_3^{-1} \end{aligned} \tag{2.11}$$

where T_4 and T_3 are three and four dimensional coherency matrix with D_4, and D_3 being the transformation matrices defined by equations 2.10 and 2.12.

$$D_3 = \frac{1}{2} \begin{bmatrix} 1 & 1 & 0 \\ 0 & 0 & \sqrt{2} \\ 1 & -1 & 0 \end{bmatrix} \tag{2.12}$$

The difference between the formulations for covariance and coherency arises from their spin matrix basis[45]. For example a Lexicographic matrix set as defined below are basis for covariance matrix definitions,

$$\{\Psi_L\} = \left\{ 2 \begin{bmatrix} 1 & 0 \\ 0 & 0 \end{bmatrix} \quad 2\sqrt{2} \begin{bmatrix} 0 & 1 \\ 0 & 0 \end{bmatrix} \quad 2 \begin{bmatrix} 0 & 0 \\ 0 & 1 \end{bmatrix} \right\}$$

and the resulted "3-D Lexicographic target vector" or "*3-D Ω target vector*" becomes

$$\underline{\Omega} = \begin{bmatrix} S_{HH} & \sqrt{2} S_{HV} & S_{VV} \end{bmatrix}^T \tag{2.13}$$

The insertion of factors 2, $\sqrt{2}$, or $2\sqrt{2}$ are to keep the total power invariant. *Span* (or total power) is defined as the power received by a fully polarimetric system and all the aforementioned covariance and coherency matrices are transformation invariant. Therefore trace of C_3 and T_3 are all the same and is equal to total span.

$$Span = |\underline{\Omega}|^2 = |S_{HH}|^2 + 2\,|S_{HV}|^2 + |S_{VV}|^2$$

2.1.5 Coherence Polarimetric Concepts

Coherence parameters are the parameters related to phase. One such parameter is Co-*polarized phase difference* (PPD) and it could be formulated like equation 2.14

$$PPD = \varphi_{HH-VV} = \left\langle \tan^{-1}\left(\frac{\Im(S_{HH})}{\Re(S_{HH})}\right) - \tan^{-1}\left(\frac{\Im(S_{VV})}{\Re(S_{VV})}\right) \right\rangle \tag{2.14}$$

where, $\Re$ and $\Im$ denotes the real and imaginary part of a complex number, $\langle\rangle$ denotes an average described by equation 2.5. In general *co-polar* refers to those situations in which the incident and scattered waves with same polarization states are considered (e.g., HH and VV) while *cross-polar* refers to the orthogonal polarization states (e.g., HV and VH). Therefore equation 2.14 is called "co-polarized" phase difference.

Change in the degree of polarization of partially polarized wave is called *depolarization*. If the polarization of the polarized component of the wave also changes, the wave is called *re-polarized*. Due to the abrupt or gradual change of refraction index (change in permittivity, magnetic permeability, or conductivity) state of polarization of a wave could change and wave will re-polarize [6]. These changes are important because they give information about the target and the medium that radar wave passes through and they are the reason that we are able to extract information from polarization configurations such as HH. On the other hand the motion of the vector tip in figure 2.2 can be considered as the sum of motion along an ellipse and a perturbation around that path. Such a wave is said to be *partially polarized*. The reason lies in the fact that there could be a random component in the polarization that cannot be described by the framework that is already set. The magnitude of this *un-polarized part* is normally observed by pedestal height.

Durden et al. showed that measuring the *pedestal height* is equivalent to measuring the ratio of the minimum eigenvalue to the maximum eigenvalue of the covariance matrix [45].

$$PH = \frac{min\left(\lambda_1, \lambda_2, \lambda_3, \lambda_4\right)}{max\left(\lambda_1, \lambda_2, \lambda_3, \lambda_4\right)} \tag{2.15}$$

2.1.6 Scattering Mechanisms

Scattering mechanism is a way to describe how polarizations interact with the target. A natural target always shows a complex scattering response due to the complexities in its reflectivity properties and geometrical structure[45]. Therefore some elementary targets could be defined to describe the canonical scattering mechanisms in order to provide bases for describing more complex structures. Some of these elementary scatterers that have been named in this research are *dipole*, *dihedral*, *helix*, and *prolate spheroid* scatterers. These types are depicted in figure 2.3 and for further information about their properties we refer the reader to literature such as [67], [45] and [6].

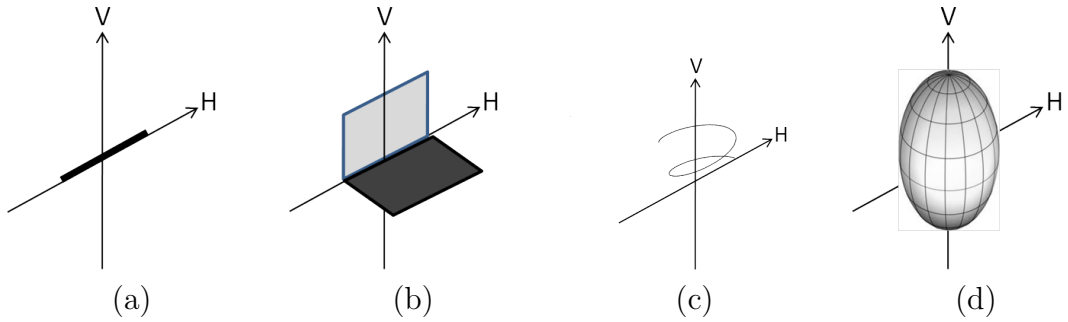

Figure 2.3: The shape of basic scatterers, (a) dipole, (b) dihedral, (c) helix, and (d) prolate spheroid.

More complex scattering mechanisms has also been defined and used for SAR imagery. These mechanisms are widely studied in the concept of *decompositions* (also in some literature called *radiative transfer models*) and they basically try to decompose the scattering matrix to physically or mathematically defined scatterers. *Freeman-Durden* algorithm[23] that will be used in this thesis is from the model based class of decompositions and it describes the scattering matrix as three main scattering mechanisms namely surface, volume (or multiple), and double-bounce scattering. While *volume scattering* describes the multiple scattering from canopy like scatterers, *surface scattering* describes the backscattering from moderately rough surface beneath the canopy. As for *double-bounce scattering*, some backscattered waves from the surface beneath the canopy bounce forward to hit the verti-

cally standing part of the vegetation (e.g., trunk, stem, etc.) and then scattered toward the sensor.

An ideal smooth surface has zero backscatter. In the Bragg scattering region where the variation of surface height is small relative to the wavelength, roughness can be seen as a perturbation of the smooth surface[52]. This model for backscattering coefficients are called Small Perturbation (SPM) or Bragg scattering Model, which is derived directly from Maxwells equations [24]. In this model, each one of the Fourier spectral components of the surface corresponds to an idealized sinusoidal surface. And the spectral component of the surface that has the same incidence angle and radar wavelength is used to describe the surface. It should be noted that Freeman-Durden utilizes Bragg scattering model for describing surface scattering and as for double-bounce scattering it uses dihedral scatterers with different properties for the orthogonal facets. The volume scattering in Freeman-Durden is presented in the form of a cloud of randomly oriented dipoles.

Also Cloude and Pottier's entropy, anisotropy and α angle is an eigenvector based decomposition that has also been used in this study. Although some definitions are presented in the following paragraphs but the equations and more in depth descriptions are provided in chapter 3. The α angle have been used to describe surface, double-bounce and volume scattering. And it is the directional cosine angle of the biggest eigenvector extracted from the mono-static coherency matrix. *Entropy* on the other hand presents a measure of the uncertainty associated with a random variable. In this sense if entropy increases the ability to extract information decreases. In case of mono-static radar where only three possible eigenvalues could be extracted from the T_3 matrix, $H = 0$ (equation 3.1) dictates $\lambda_1 = span$ and $\lambda_2 = \lambda_3 = 0$. Therefore only one single dominant scattering phenomenon exists for zero entropy. Another extreme case is $H = 1$ where three equal eigenvalues are inevitable, thus the polarization information becomes zero and the target scattering is no more than a random noise process[45]. Distributed targets could be defined between these two extremes.

Scattering mechanism	Scattering sources	Polarization features
Surface	Bare soil Herbaceous crops at low frequency	$\sigma^\circ_{HV} \ll \sigma^\circ_{HH} \leqq \sigma^\circ_{VV}$ $\sigma^\circ_{RL} \gg \sigma^\circ_{RR}$ $PPD \sim 0^\circ$ Small Pedestal Height
Double bounce	Crop stalks (L, C-band)	$\sigma^\circ_{HV} \ll \sigma^\circ_{VV} \leqq \sigma^\circ_{HH}$ $\sigma^\circ_{RL} \geqq \sigma^\circ_{RR}$ $PPD \to 180^\circ$ Large Pedestal Height
Volume/cylinders	Crop stems	$\sigma^\circ_{HV} <\sim \sigma^\circ_{VV}, \sigma^\circ_{HH}$ $\sigma^\circ_{RL} \sim \sigma^\circ_{RR}$ $\sigma^\circ_{RL}, \sigma^\circ_{RR} > \sigma^\circ_{VV}, \sigma^\circ_{HH}$
Volume/disks	Leaves	$\sigma^\circ_{HV} <\sim \sigma^\circ_{VV}, \sigma^\circ_{HH}$ $\sigma^\circ_{RL} > \sigma^\circ_{RR}$

Table 2.1: Radar Mechanisms, adapted from Baroneti et al. [5]

Last but not the least is the *anisotropy* parameter that measures the relative importance of the two sub dominant scattering mechanisms.

Surface, volume and double-bounce are abstract physical concepts and table 2.1 shows the main characteristics of these mechanisms in relation to some of the already defined polarimetric parameters. For more details about the relations mentioned above please refer to [45] and [6].

2.1.7 Unsupervised PolSAR Classifications

PolSAR imagery can be treated as any other remote sensing imagery and thus they can be classified both with supervised and unsupervised methods. If the classification is based on the external help of the user then it is called supervised classification but if there is no intervention from the user in classification then it is called unsupervised classification although at the end of the process the user must interpret the classes, based on knowledge of the land use or ground observation data. Since one of the main objectives of this research is to maintain an automatic process, we reduced the human influence. Therefore we solely focused on unsupervised approaches and in this section we provide a brief description of the

used unsupervised classifiers.

A SAR classifier needs to compensate for speckle effect. Speckle reduces the performance of some of the most common classifiers because it drastically affects the statistics of the data. Therefore some especial algorithms have been developed solely for SAR applications. One such algorithm is H/α segmentation [13]. We provide some in-depth descriptions of this algorithm since it will be used in our methodology. The concept of H/α segmentation is provided in figure 3.1 and the detail of each of the resulting eight class is in section 3.1.

Statistical models have also been used to describe the speckle effect in SAR. It is a theory that the measured covariance matrices C of the SAR imagery follows the complex Wishart distribution[45]. For a homogeneous region ω_i with Gaussian backscattering, characterized by a polarimetric covariance matrix $\sum_i = E\left(C|C \in \omega_i\right)$, the Wishart probability density function (PDF) is as follows [62]

$$P\left(C|\sum_i\right) = \frac{n^{qn}\left|C\right|^{n-q}\exp\left[-nTr\left(\sum_i^{-1}C\right)\right]}{\left|\sum_i\right|^n \pi^{q\left(\frac{q-1}{2}\right)}\prod_{j=1}^{q}\Gamma\left(n-j+1\right)} \tag{2.16}$$

where q denoting the dimensionality of C (e.g., 4) with n degrees of freedom, $Tr(...)$ the trace of a matrix, $|...|$ the determinant operator and Γ is the Gamma function.

General K-means Wishart is one example of unsupervised classifiers that uses the Wishart PDF. It has the K-means classification steps along with Wishart PDF used as a distance function. At first an arbitrary set of initial class centers is assumed and the pixels are assigned to their most likely classes by using Wishart distance. A set of updated class centers is derived from all pixels in each class, and a new class assignment is carried out. This iterative process is repeated until class membership converges. Since general K-means Wishart classification has been applied successfully to the PolSAR data [44][62] we also implemented this algorithm.

Another method that combines the two previous classifications is H/A/α unsupervised K-means Wishart classifier. The detail of this classification is described in details by Ferro

Famil et al. [21]. In any radar image the pixels would be thrown into the H/α sub-space and each of the eight possible zones would give the initial class centers for that image. Thus for each polarization channel an eight class K-means Wishart classification are performed but instead of arbitrary initial class centers, H/α driven class centers are used. Then all the classes for all the channels are combined. For example in case of dual polarization, 8×8 classes would be produced. A pixel belonging to class X_i in the first image and to X_j in the second one is assigned to a combined class . Then this set of 64 classes would be used as initial classes for another K-means Wishart classification. After the classification terminated a reduction process based on a separability measure would be applied to provide more efficient classification.

A more efficient classification for SAR imagery, Expectation Maximization (EM) classification was introduced by Richards et al.[63]. The Expectation Maximization algorithm starts with an initial guess of a non-optimal set of class centers. Once initial class centers are known, the a-posteriori probabilities of a pixel belonging to each class will be estimated in the so-called expectation step. Using the values obtained for a-posteriori probabilities, an updated set of class centers can be calculated in the subsequent maximization step. This cycle will be repeated until some criteria will be met. This algorithm is significantly different from unsupervised classification in the classical k-means sense, where each pixel is assigned to only one, namely the most likely class [62].

On the other hand Expectation Maximization with Probabilistic Label Relaxation is a method introduced by Reigber et al. [62] to use neighborhood function and label relaxation with Wishart PDF. They believe that when homogeneous area base results in comparison to point-wise classification are desired, as it is usually the case in agricultural or forested areas, EM-PLR is going to produce higher quality results than conventional approaches based only on the analysis of the covariance matrices. These classifications are in no way conclusive list of available classifications, but they only selected to show a rough idea of how these

unsupervised classifications behave for our problem without taking any special measures.

2.1.8 Some Classification Evaluation Concepts

If n_{ij} is the number of pixels belonging to reference class j that were classified as class i and k is the total number of classes, then we can define the overall accuracy of a classification as:

$$Accuracy = \frac{1}{n}\sum_{i=1}^{k} n_{ii} \tag{2.17}$$

Overall accuracy is a cumulative measure of correctly classified pixels. Since it is a global measure, it does not provide any insight to the evaluation of each class. In order to compensate for this issue user and producer's accuracies have been used.

$$Producer\ accuracy\ for\ class\ j\ = \frac{n_{jj}}{\sum_{i=1}^{k} n_{ij}} \tag{2.18}$$

The producer's accuracy is the fraction of reference data that is correctly classified. And it is the number that the analyst wants to make as large as possible while user's accuracy,

$$User\ accuracy\ for\ class\ i\ = \frac{n_{ii}}{\sum_{j=1}^{k} n_{ij}} \tag{2.19}$$

as defined above is the fraction of pixels classified as class i that actually belong to the reference class i. It resembles a percentage of the class i in the final classification results that are likely to be class i according to the reference data. It is ideal to also have a global measure that somehow counts for user and producer accuracies. The κ coefficient presents the difference between actual agreement and the agreement expected by chance and is defined by

$$\kappa = \frac{P_0 - P_C}{1 - P_C} \tag{2.20}$$

, where P_0 is overall agreement and P_C is the chance agreement as described by

$$P_0 = \sum_{i=1}^{k} P_{ii} = \tfrac{1}{n}\sum_{i=1}^{k} n_{ii}$$
$$P_C = \sum_{i=1}^{k}\left(\sum_{j=1}^{k} P_{ij}\sum_{j=1}^{k} P_{ji}\right) = \tfrac{1}{n^2}\sum_{i=1}^{k}\left(\sum_{j=1}^{k} n_{ij}\sum_{j=1}^{k} n_{ji}\right)$$

Band Names	Frequency in GHz	Wavelength in cm
L	1 to 2	15 to 30
S	2 to 4	8 to 15
C	4 to 8	4 to 8
X	8 to 12	2.5 to 4
K_u	12 to 18	1.7 to 2.5
K	18 to 26.5	1.1 to 1.7
K_a	26.5 to 40	0.8 to 1.1

Table 2.2: Microwave frequencies used in radar according to Radio Society of Great Britain

This will compensate overall accuracy for chance agreement. While $\kappa = 0$ makes the classifier no better than a random assigner of pixels, as it increases toward 1 the accuracy of classification also increases.

2.2 SAR Literature Review

Since SAR image is generated from the backscattering wave from the interaction between the incident polarimetric wave and the target itself, different sensor parameters regarding this interaction could provide different information. The wavelength and frequency of the incident wave permit objects with certain sizes to interact differently with the target and the Rayleigh, Mie resonance, and non-selective scattering mentioned in chapter 1 describe these physical interactions. Table 2.2 presents different microwave bands used in radar remote sensing. A 5 *cm* diameter sphere standing on the surface of a completely smooth and vast surface, is invisible in L-band while produces very small attenuation (gradual loss in intensity) in S-band due to the Rayleigh scattering. The same sphere will produce considerable backscatter in C-band due to Mie resonance scattering, while in X, K_u, K, and K_a non selective scattering dictates that every different part of the sphere (based on the wavelength size and local incidence angle) would produce different backscattering values.

Multi polarization is another concept used in SAR to provide various range of information about the target. Conventionally SAR sensors are classified as single-, dual-, multiple-, and

full(or quad)-polarimetric based on the number of the polarimetric channels they could provide. The first active SAR satellite SEASAT[1], launched in 1978 was an L-Band single HH polarization. SEASAT opened the door for next missions such as SIR-A and SIR-B[2] by NASA in 1981 and 1984. SIR-A was again an L-Band single HH polarization radar, but SIR-B was the first one to have multiple incidence angles. Incidence angles are very important in SAR interaction with the target since they change the effective area of radar cross section. Although the importance of multiple incidence angles was observed for the SAR data but for some years single incidence angles were the main trend for the SAR sensor designs. For example the follow up to SIR missions, European ERS-1, and ERS-2[3] in 1992 and 1995, and JERS-1[4] in 1992 by Japan were all fixed incidence angle systems. While ERS-1 and ERS-2 were single VV polarization C-band SAR, JERS-1 was a single HH polarization L-band SAR. Almaz-1, a single HH polarization S band SAR with multiple incidence angles were USSR SAR sensor launched in 1991. SIR-C/X-SAR in 1994 was another shuttle mission that evolved SAR once again to a new level. This American/German joint project had multiple frequency C- and L-band radar, and separate only VV polarized X-Band SAR system. The C and L-band system was a multiple incidence angle, fully polarimetric radar.

Then the first real commercial radar satellite RADARSAT-1[5] was launched in 1995. Canadian RADARSAT-1 was a single HH polarization C-band SAR with multiple incidence angles and beam types. Multiple beam types became another important source of information from SAR imagery as the beam type defines the interaction area between the incidence wave and the target. SAR remote sensing has been developed largely since those days and it has been used widely in vegetation related studies.

The backscatter signal from vegetated surfaces are affected by many factors from target, including plant biomass, structure (leaf size, stem density, LAI, etc.), soil moisture, surface

[1]SEA Satellite
[2]Shuttle Imaging Radar
[3]European Remote Sensing satellites
[4]Japan Earth Remote Sensing Satellite
[5]RADAR Satellite

roughness, as well as their interactions with sensor configurations (e.g., frequency, polarization, and incidence angle) [33, 50]. The basic Maxwell's equations that define the behavior of the electromagnetic wave results in a relation between the changes in refraction index (e.g., change in dielectric constant) of the target and the consequent changes in $\vec{E_S}$ due to propagation effects. The detail of this phenomenon is extensively analyzed in literature such as [67] and [45]. Therefore water content (an influential parameter on electric constant) of the soil and vegetation could severely change the backscattering values from the ground. On the other hand target shape and roughness could change the interaction details between the incidence wave and the target. Therefore dielectric constant and shape properties are main target parameters that affect the backscattered signal. These complex behaviors arise from the physical optics governing most of the SAR interactions. In *physical optics* the wave nature of the light has been taken into consideration in comparison to the *geometrical optics* where light propagation is described in terms of rays. Geometrical optics that governs the optical remote sensing is an excellent approximation when the wavelength is very small compared with the size of structures with which the light interacts. But it cannot describe the SAR applications where wavelengths are comparable to the target size. Therefore it is not hard to deduce that SAR is a very complex source of data in comparison to optical imagery. But section 1.1 provides enough reasoning as to why SAR imagery has been used for agricultural purposes. One such reason is the existence of the clouds.

In tropics and subtropics, cloud free days could reach as low as 60 days per year (e.g., Hanoi, North Vietnam). The crops which grow in these regions are widely observed by radar remote sensing. One such crop is sugarcane; Baghdadi et al. [3] assessed the potential of different SAR sensors for monitoring of sugarcane. They have used TerraSAR-X (X band, HH), ASAR/Envisat[6](C band, VV, HH, VV/HH, HV/HH, or HV/VV) and PALSAR/ALOS[7] (L band, fully polarimetric) for mapping of harvested sugarcane crop. In

[6]Advanced Synthetic Aperture Radar

[7]Phased Array type L-band Synthetic Aperture Radar/Advanced Land Observation Satellite

mapping of the harvested fields they have found out that higher incidence angles and longer wave lengths are more sensitive to sugarcane crop height.

Another example of tropic crops observed extensively with SAR is rice [10, 33, 42, 46, 73]. Le Toan et al.[42] used ERS-1 data to map rice in cites in Indonesia and Japan, and developed a rice field mapping method. They have transformed the SAR image into plant height image and plant biomass image. The model based on the physical description of rice produced by Le Toan et al. had a very good agreement with experimental data. Based on daily in-situ measurements of multi-frequency backscattering coefficients (K_a, K_u, X, C, and L) Inoue et al.[33] find out that LAI of rice paddies was best correlated with the C-band's HH and VV polarizations. While their biomass was best correlated with the L-band's HH and HV polarizations. They also observed, higher frequency bands (K_a, K_u, and X) has lower correlations with LAI and biomass. On the other hand the weight of heads (indicator of the harvesting stage) correlated better with the K_a and K_u bands backscattering coefficients rather than X, C or L band.

Tan et al.[73] used RADARSAT-1 data, extensive ground measurements, and simulated training data from theoretical model to classify rice crops in different dates. On the other hand Chen et al.[10] has established an empirical relationship between backscattering coefficient and ground measurements of height and biomass of rice. They have seen a potential in operational rice mapping for China based on ENVISAT ASAR data. On the other hand Lopez-Sanchez et al. [46] have observed the potential of TerraSAR-X for rice monitoring applications in Spain, they have shown that high resolution TerraSAR-X imagery can be used for detection of areas with cultivation problem. Also dual-polarimetric H/α decomposition with X-band co-polar data would be useful for rice plant growth stage separation. Lopez-Sanchez et al. presented a physical interpretation of the backscattering, PPD, and H/α of radar in different times and polarizations [46].

Rice is a perfect crop to be observed by SAR since the background is water and does not

have the roughness of the surface beneath the crop, but this is not the case for so many of other crops such as corn, barley, soybeans, wheat, etc.. In case of these crops the planting configuration is one of the most important factors affecting the SAR data. In case of corn, the traditional configuration is as wide as 96 cm row spacing [37]. Pedersen et al. found out that row spacing of less than 76 cm are not beneficial although they are becoming more common [60]. A standardized height of corn stem is 2.5 meters. The conventional distance between two seeds in a single row is between 10 cm to 20 cm. The stems are erect, conventionally with many nodes, casting off flag-leaves at every node. Corn stems superficially resemble bamboo canes and the inter-nodes can reach 20-30 cm. The lower leaves being like broad flags, 50-100 cm long and 5-10 cm wide. Therefore mature corn field is 2.5 meter tall dense vegetation in most of the microwave frequencies.

Soybeans row spacing varies from 19 cm up to 76 cm [7] [59]. In the case of twin-row it has 19-57-19 cm configuration [36]. The distance between two seed in one row is around 5 cm. Soy varies in growth and habit, but the nominal height of 1 m is assumed. For example C-band radar could not sense the 5 mm to 11 mm diameter seed, and the only main structure that could be sensed by C-band is the pods with 3 cm to 8 cm heights.

Paris[57] compared the separability of corn and soybeans in different incidence angles and three different channels of C, L, and Ku bands. He concluded that in incidence angles below 25 degrees the effect of row direction of crops is significant while in the rest of the incidence angles, no matter what polarization used: incidence angle did not have any effect on the outcome. In his study he used human driven decision making on the differentiation of corn and soybean. He noticed that C band is the best channel at separating corn and soybeans while trees were also classified as corn. He also mentioned the superiority of the depolarization ratio for soybeans detection. Also the wet conditions reduced the separability ability of SAR data for his purpose.

Wu et al.[78] made a research on which portions of soybean, corn, and wheat canopies

are responsible for the backscatter in X band. Their observations are very interesting but it would be hard to extrapolate the results for other channels such as C band SAR data. The soybeans plant in X band has most of its backscattering from upper 30% portion including leaves and stems of the canopy while for corn; it is solely from the leaves. On the other hand Chiu et al.[11] used a season long C, L and X-band ground based SAR measurements over young and aged soybeans crop. For the near harvest dry soybeans plant they observed that backscattering coefficient is sensitive to soil moisture and scattering attenuation from soybeans itself are reduced. They also believe that this observation is very much like the behavior of the bare soil.

Dobson et al. [18] performed a single image based classification for a 30° incidence angle SIR-B data in L-band. This study resulted in to three classes: 1) corn, 2) corn stubble and Plowed bare soil, and 3) disked bare soil, soybeans, soybeans stubble, alfalfa, and clover. They were not able to distinguish soybeans from its stubble or even a disked bare soil. Kouskoulas and Ulaby[39] used a pixel based classification on a multi-temporal dataset. They have accomplished 93% classification accuracy in classifying short vegetations such as corn, soybeans, alfalfa and wheat. Polarimetric data also has been segmented using non-polarimetric segmentation tools by Hoekman and Vissers [32]. They empirically assumed simpler PDF functions rather than Wishart for homogeneous SAR data, and they were able to classify agricultural fields including corn fields very accurately. Mathematical polarimetric parameters also have been widely used for agricultural applications. Some examples of these parameters are co-polarized phase deference (PPD) [49], co-polarization signature plots [49], pedestal height [3][49], circular polarized backscatter [3][49], and Linear Polarized Backscatter [3][49].

Le Toan et al. [41] believe that empirical model cannot convey the complex situation of vegetation backscattering and theoretical models should be preferred. The random medium model used by Le Toan et al, is based on two different correlation length in vertical and

horizontal directions with spherical correlation function. The final results of their modeling was compared to a ground C-band radar backscattering coefficient observations over soybeans fields. They also used other ground measurements such as volumetric water content of canopy.

De Roo et al. [17] modeled the scattering mechanisms of the agricultural canopies as a cloud of water vapor over the rough ground. They used the empirical Oh model[55] for the rough ground backscattering. They believe that since L-band is sensitive to both soil moisture and biomass while C-band response is largely dependent on biomass, together they can be used for inversion of the soil moisture. Although they were only observing in a fixed (45°) incidence angle, they had successfully modeled the radar backscattering in terms of angle of incidence, vegetation water mass, vegetation height, and volumetric soil moisture. They have also used some 'free' parameters to describe the strength of various scattering and extinction mechanisms. These free parameters were used to tune their model to provide the best fit to the measured backscatter. The final results were some empirical equations to relate σ_{HV} over σ_{VV} ratio to estimate the soil moisture of the soil beneath the soybeans canopy and eventually the vegetation water mass.

De Roo et al. [16] used the MIMICS model developed by Michigan University with some modifications to estimate the soil moisture of the soil beneath the soybeans canopy. They assumed that unlike corn, soybeans lacks the interactions associated with stems and therefore they removed the stem related parts from the MIMICS model. Also some assumptions were made on the ratio of sand and clay inside the soil, and they believed that the row direction was not an important factor for an ensemble averaged soybeans field. Once again vegetation water mass was observed as ground measurement necessary for the estimations. They have used various measured or assumed to be known input parameters to solve their model therefore although they reached a very good regression coefficient of $R^2 = 0.89$ but these degrees of freedom rather effects the repeatability of their method.

Using C band data with field measurements such as soil moisture and canopy water content, Wigneron et al.[76] introduced a simple model to measure water contents of the soybeans canopy. They believe that there are either semi-empirical or physical approaches to retrieve surface variables from radar data; the former could not be accountable for specific structure characteristics of various vegetation types while the latter would be insufficient for direct inversion processes in terms of the absolute accuracy. Thus they believe that recalibration of one or several parameters are a necessity. They calibrated parameters based on discrete radiative transfer model. Because of the diffuse nature of the soybeans canopy, where the vegetation elements are not dominant; the first order approximation of the radiative transfer equations was sufficient. They have used Integral Equation Model (IEM) based on a Gaussian surface correlation function for surface scattering. The integral equation model is based on analytical solutions of the integral equations for tangential surface fields[52]. It is a fairly complex model with too many degrees of freedom such as the relative magnetic permeability (usually equal to unity for soils), and the single-parameter Fourier transform of the surface correlation coefficient. The IEM used by Wigneron et al. also needed surface roughness height and correlation length which were also obtained from field measurements. The result was an equation to relate the direct vegetation backscattering to optical depth (tau), where tau is assumed to be related to the amount of water in the canopy. The calibration time was for growth season of the soybeans field and they extrapolated the results of the calibration to fruit development and crop senescence stages. However both calibration and validation of their model was based on same data set, therefore as they also pointed out, robustness of their model was unclear.

Kim et al.[38] had L-, C- , and X-band radar sensors with fixed incidence angle (40°) to estimate Radar Vegetation index and subsequently Vegetation Water Content. They concluded that only L-Band radar was more successful for soybeans and rice's VWC estimation than C- or X-band radar.

Kwon et al.[40] estimates the direct backscatter from a vegetation canopy to reach the soil moisture. Kwon uses observed soil moisture content and leaf moisture content measurements to perform a regression on some unknowns related to estimation of vegetation backscatter. In conclusion soil moisture of the soybeans fields were successfully measured using X band data. It also proves that the direct backscatter has been successfully removed from the vegetation by X band SAR.

Modeling has been widely used for crops such as corn and soybean, but where so many of the models use various set of input measurements and assumptions, they add one too many degrees of freedom to the solution. This affects the applicability of such models to an extended number of agricultural fields' scenario. But as always there are exceptions such as Freeman-Durden algorithm available. Although Freeman-Durden model was originally designed for forestry applications, but it has also been used for agricultural studies[34]. Freeman-Durden[23] is a physical model decomposing every scattering to three physically defined scattering mechanisms, namely surface, double-bounce and volume scattering. These decomposed mechanisms could be used to describe certain phenomenon in the agricultural fields.

Different scattering mechanisms such as multiple, volume, and surface scattering are likely to happen in large biomass crop canopies like corn. Scattered from the stalks, the incident wave will be attenuated by the canopy and then reflected from the ground. The upward reflection from the ground is likely to result in higher HH backscatter relative to VV. Surface scattering will attenuate the dominant double-bounce scattering coming from corn canopy. Frequency and incidence angle most likely influence the mixture of scattering mechanisms from these targets [49]. In a research conducted by de Matthaeis et al. [15] they came across an observation that volume scattering from the leaves will weaken the double-bounce scattering expected from the corn canopy at C-Band. The larger the incidence angles, the higher are the effects of volume scattering attenuations. Therefore the effects of single

and the double-bounce scattering is reduced [49]. RL is most likely to have lower values than RR or LL because of the effects of other mechanisms rather than surface scattering.

Since Freeman-Durden is a standalone model with no other input than SAR observations, it has become a focus for so many other models. In the follow-up to the 1998 Freeman-Durden algorithm, Freeman[22] introduced a novel two component scattering model decomposition in 2007. In contrast to the old model, two component scattering decomposition had equal number of equations and unknowns and no further assumptions for double-bounce and surface scattering were necessary. On the other hand model had an additional degree of freedom for volume scattering where instead of dipoles, prolate spheroids was used. This model was tailored to the tropical forest applications where either double-bounce term or surface scattering from ground can be set to zero. Hence this model has its drawback as mentioned frequently by Freeman himself in his paper that the model is ill-conditioned for farmlands where the possibility of both surface and double scattering exists. He also mentioned that when volume scattering is dominant in comparison to surface and double-bounce scattering, the returned backscatter will be overwhelmed by estimation errors since signal to noise ratio becomes very small. Also for bare soil Small Perturbation Model could fail in estimating the volume scattering portion.

The four components Yamaguchi et al.[80] is another very similar scattering model to Freeman-Durden. In this model reflection symmetry [8] that was necessary to Freeman-Durden model is not the case and a helix scattering component has been added to the three scattering mechanisms of Freeman-Durden decomposition. This helix scattering term is important in complex urban area scattering and disappears for a natural distributed scatterer such as agricultural fields. But Yamaguchi noticed the existence of negative power (span) values in the Freeman-Durden algorithm. Yajima et al.[79] further explored these negative roots and proposed a modified four component decomposition to remove them.

Sato et al.[69] took a further step for the four-component Yamaguchi model with ex-

[8]The correlation between co- and cross-polarized channels is assumed to be zero

tended volume scattering model. It has been found that the Yamaguchi model has problems of overestimation in the volume scattering. This is especially the case in negative power occurrence and in urban areas and it is caused by a large cross-polarization component.

An et al. [2] observed that the original Freeman-Durden would eventually encounter some negative power values due to the inconsistency of the physical model. In order to reduce the number of these negative spans (powers) An et al. proposed de-orientation process to remove the remaining influence of randomly distributed target orientation angle from Freeman-Durden algorithm. Therefore they also modified the volume scattering to have solely random scattering instead of Freeman-Durden's randomly oriented dipoles. For even further removal of all the negative spans they put some restrictions on power estimations of the original Freeman-Durden. They also believed that volume scattering in Freeman-Durden algorithm most of the time is overestimated and thus small double-bounce or surface scattering may not be properly observed.

Chapter 3

Methodology and Materials

3.1 Entropy, Anisotropy and α

Cloude [6] introduced polarimetric entropy H and polarimetric anisotropy A' to be defined as

$$H = \sum_{i=1}^{3} -P_i \log_3 (P_i); \quad P_i = \frac{\lambda_i}{\sum_{r=1}^{3} \lambda_r}; \quad A = \frac{\lambda_2 + \lambda_3}{\lambda_2 - \lambda_3} \tag{3.1}$$

where $\lambda_i, i = 1, 2, and\ 3$ are representing the three eigenvalues of the polarimetric coherency matrix, T (equation 2.11 with $\lambda_1 > \lambda_2$ or λ_3. Later on Cloude and Pottier [13] completed this set by introducing another parameter, polarimetric eigenvector α defined as

$$\alpha = \sum_{i=1}^{3} \frac{\lambda_i}{\sum_{r=1}^{3} \lambda_r} \cos^{-1}\left(e_i^1\right) \tag{3.2}$$

where e_i^1 is the first element of the i^{th} eigenvector and the rest of the parameters are the ones introduced in equation 3.1. Cloude and Pottier [45] defined H/α plane which allows the quantitative analysis of PolSAR imagery as shown in Figure 3.1. In this two dimensional H/α sub-space all possible random and any deterministic scattering mechanism can be represented. In theory α can be subdivided into surface, volume, and double-bounce scattering. But when considering the effects of chaos (low, mid, and high entropy) different zones of α may be defined through the use of different orders of the scattering theories. A very short description of the nine subdivided zones of the H/α sub-space is provided here:

Zone I: High entropy multiple scattering

In a high entropy environment we can still distinguish some double-bounce scattering. This is the case in forestry and from vegetation which has a well developed branch and crown structure[13];

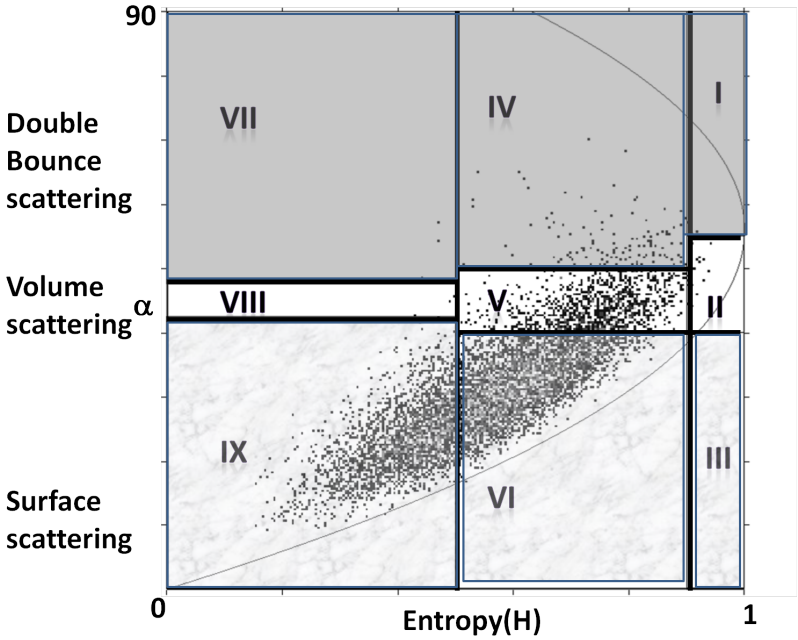

Figure 3.1: H/α feature space calculated for the field number 350100710 at 15^{th} of the September 2009. A description of the roman enumerated zones is presented in the section 3.1.

Zone II: High entropy vegetation scattering

Single scattering arises from a cloud of anisotropic needle-like particles or multiple scattering from a cloud of low loss symmetric particles. The feasible region of H/α sub-space is increasingly shrinking[13];

Zone III: High entropy surface scatter

This scenario is not feasible because surface scattering cannot be distinguished. This region was included by Cloude and Pottier[13] to emphasize the idea that our ability to use polarimetric data is limited by increasing entropy;

Zone IV: Medium entropy multiple scattering

This region accounts for dihedral scattering inside moderate entropy environment. Double-bounce followed by propagation through a canopy[13];

Zone V: Medium entropy vegetation scattering

Scattering from vegetated surfaces with anisotropic scatterers with moderate correlation of scatterer orientations[13];

Zone VI: Medium entropy surface scatter

Random surface scattering due to a higher roughness and existence of disks or leaves. This zone represents any increase in entropy in surface scattering due to the changes in roughness (see section 5.1) and the effects of propagation through canopy[13];

Zone VII: Low entropy multiple scattering

For low entropy double or even bounce scattering events like metallic dihedral events[13];

Zone VIII: Low entropy dipole scattering

Strongly correlated mechanisms with a large imbalance between S_{HH} and S_{VV} amplitude[13];

Zone IX: Low entropy surface scatter

Low frequency surface scattering (in physical optics) like Bragg surface scattering and high frequency surface scattering like geometrical optics[13]. This could be a very important part of surface scattering for agricultural fields since the surface can be smooth enough for the Bragg surface scattering to be dominant. The limitations of polarimetry dictates that the events that should have lied in the (impossible) Zone III would migrate toward this zone and thus some very rough surfaces (geometrical optics) would also represented by this zone.

In our data, we observed that the zones IX, VI, and V were most dominant cases for harvested fields as well as soybeans and bare fields while corn fields are dominated by zones VII, VI, V, and IV. The classification results from this approach as will be seen from

section 4.6 were not satisfactory. The reasons may lie in H/A/α's two main drawbacks[45]; first, the resolution of H/A/α decomposition is always reduced because of the rigidly defined zone boundaries; and the second, this method does not take amplitude information into consideration. But since this method covers all the possible scenarios for scattering models, especially surface scattering, we will use this algorithm as a part of our process. We incorporated this method into two important parameter of our algorithm which we will describe in sections 3.2, and 3.4.

3.2 Surface Roughness from H/A/α

Surface roughness is a highly influential parameter in backscattering modeling and early attempts to model rough surfaces go back to 1877 when Lord Rayleigh defined the Rayleigh criterion to determine the degree of roughness in a surface. Another well-known development in the backscattering theory is the small perturbation model [71][68] which is very important due to its fundamental role in the Freeman-Durden algorithm. In her PHD thesis, Hajnsek [27] tried to answer the question that: "how accurate and under what conditions can roughness be estimated from fully polarimetric SAR data?", in other words, when we can say that roughness is too high that the polarimetry data becomes no more than some random values.

Statistical description of surface roughness is done by parameters such as RMS height, s, which describes the vertical surface roughness. RMS height is defined as the standard deviation of the surface height variation in centimeter.

$$RMS_{height} = s = \sqrt{\frac{\sum_{i=1}^{n} (z_i - \bar{z})^2}{n-1}} \tag{3.3}$$

where z_i is the height of any single scatterer in the scattering patch and n is the number of those scatterers.

Another important parameter in roughness analysis is correlation length,l, which depends on the surface correlation function. The surface correlation describes the statistical inde-

pendence of two points on a surface therefore it increases with the correlation between two neighboring points. Thus for a smooth surface $l = \infty$.

Based on the single scale roughness theory, s and l are independent from each other[27]. Therefore l can be large or small for a high or low s. Experimental data acquired over natural surfaces indicates, that most bare soil surfaces are characterized by large spatial variations, thus it makes it difficult to determine consistent roughness parameters for modeling and inversion purposes[13]. Correlation length and RMS height have been studied extensively in remote sensing[27], in this section we will introduce a new index. This index has some potential for roughness analysis as will be shown in section 5.1.

Both low frequency theories like Physical Optics (e.g., Bragg scatter), and high frequency theories like Geometrical Optics have theoretical zero entropy. In between these two extremes, entropy increases due to the physics of secondary wave propagation and scattering mechanisms. Therefore any increase in roughness or decrease in correlation length of a surface will increase its entropy[13].

As we already discussed in section 3.1 an increase in the entropy really does limit the ability to use polarimetric behavior to classify the targets[13], in a way that zone III (High entropy surface scatter) of the H/α sub-space is theoretically and practically empty. Medium entropy surface scatter are in zone VI of the H/α sub-space where the entropy increases due to changes in surface roughness and canopy propagation effects[13]. And in the H/α sub-space, Bragg surface scattering has zero entropy, $H = 0$, and α angle is independent of surface roughness and directly related to the angle of incidence, dielectric constant of the surface[13], and scattering mechanism. This means that the Bragg scattering phenomenon used by the original Freeman-Durden (OFD) model should be confined to zone IX of the H/α sub-space (figure 3.1). Let's assume that Zone IX only contains the low entropy surface scattering where the surface is smooth (ignoring the geometrical optics instances). Therefore we used zones IX and VI as an indicator of the surface roughness of low to medium entropy

surface scattering

$$H_{rough} = \begin{cases} \dfrac{n_{VI} - n_{IX}}{n_{VI} + n_{IX}} & n_{VI}+n_{IX}>0 \; low \; to \; Medium \; entropy \\ 0 & n_{VI}+n_{IX}=0 \; high \; entropy \end{cases} \tag{3.4}$$

where n_J represents the number of pixels lying in the J zone. Hence, H_{rough} is a normalized index varying between -1 and 1 , and represents roughness of a set of pixels. Smooth fields will have more pixels in zone IX and thus H_{rough} will be closer to -1 while rougher surfaces will have increased H_{rough} values. In the very rough geometrical optic cases H_{rough} will be pushed toward positive one value. Although this exception makes it difficult to decide whether we have a physical optics smooth or geometrical optic rough but on the other hand this is an inherent characteristics of PolSAR data and therefore we believe that it is the weakness of the observation rather than the index. The details of analysis for this index is provided in section 5.1.

3.3 Freeman-Durden Decomposition

Freeman-Durden is a decomposition based on three independent scattering mechanisms. And it is important because it does not utilize any ground measurements [6]. The three mechanisms are a canopy scatter from a cloud of randomly oriented dipoles, even or double-bounce scatter from a pair of orthogonal surfaces with different dielectric constants and Bragg scatter form a moderately rough surface [23] [45]. In the following sections these scattering mechanisms (figure 3.2) will be explained in more details.

3.3.1 Volume Scattering

The model for the volume scattering consists of the contribution from a cloud of randomly oriented cylinder-like scatterers. In order to simulate such scatterers let us assume an elementary dipole expressed in the orthogonal linear xy plane such that it is horizontally oriented[45]. Equation 3.5 describes the scattering matrix of such a scatterer.

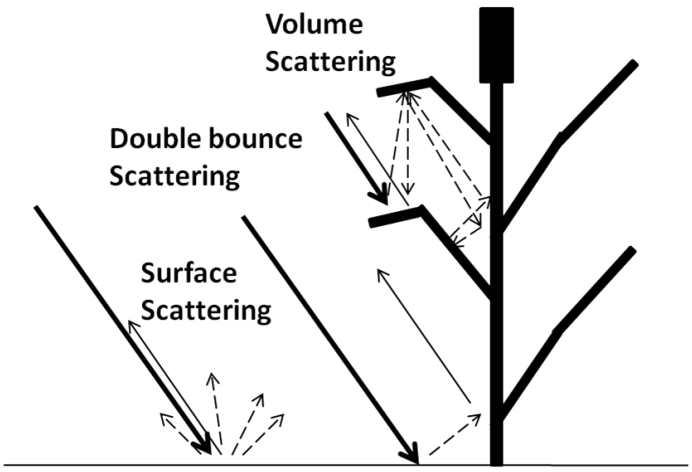

Figure 3.2: Three main scattering mechanisms

$$\begin{bmatrix} a & 0 \\ 0 & b \end{bmatrix}_{a \gg b} \tag{3.5}$$

where a and b are the complex scattering coefficients in the particle characteristics coordinate system. And the $a \gg b$ is due to the assumption that the dipole is horizontally aligned. Rotated with the angle τ around the radar line of sight (see figure 3.3), the scattering matrix of the rotated dipole is

$$\begin{aligned} S_\tau = \begin{bmatrix} S_{HH} & S_{HV} \\ S_{VH} & S_{VV} \end{bmatrix} &= \begin{bmatrix} \cos\tau & \sin\tau \\ -\sin\tau & \cos\tau \end{bmatrix} \begin{bmatrix} a & 0 \\ 0 & b \end{bmatrix} \begin{bmatrix} \cos\tau & -\sin\tau \\ \sin\tau & \cos\tau \end{bmatrix} \\ &= \begin{bmatrix} a\cos^2\tau + b\sin^2\tau & (b-a)\sin\tau\cos\tau \\ (b-a)\sin\tau\cos\tau & a\sin^2\tau + b\cos^2\tau \end{bmatrix} \end{aligned} \tag{3.6}$$

Since radar transmit and receive coordinate systems are identical, the resulting scattering matrix should be symmetric and therefore $S_{HV} = S_{VH}$. Scatterers can be randomly oriented about the radar look direction with the PDF of $p(\tau)$, where τ is the rotation angle from the vertical axis. Thus the expected value of our functions $f(\tau)$ are

$$\langle f \rangle = \int_0^{2\pi} f(\tau)\, p(\tau) d\tau \tag{3.7}$$

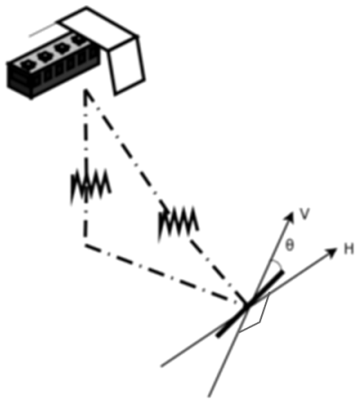

Figure 3.3: Dipole oriented at an angle τ in respect to the radar line of sight

Using 3.7 to compensate for the backscattered wave from all of the orientations and comparing it with the backscattered covariance matrix $C_{3_{vol}}$ (the second-order statistics of the scattering matrix), we can write the following equations:

$$\begin{aligned}\langle S_{HH}S_{HH}^{*}\rangle = \left\langle S_{\tau_{11}}S_{\tau_{11}}^{*}\right\rangle &= \int_{0}^{2\pi}\left(a\cos^{2}\tau + b\sin^{2}\tau\right)\left(a\cos^{2}\tau + b\sin^{2}\tau\right)^{*}p\left(\tau\right)d\tau \\ &= \int_{0}^{2\pi}\left(\left|a\right|^{2}\cos^{4}\tau + \left|b\right|^{2}\sin^{4}\tau + 2\Re\left(ab^{*}\right)\sin^{2}\tau\cos^{2}\tau\right)p\left(\tau\right)d\tau \\ = \left|a\right|^{2}\int_{0}^{2\pi}\cos^{4}\tau p\left(\tau\right)d\tau + \left|b\right|^{2}\int_{0}^{2\pi}\sin^{4}\tau p\left(\tau\right)d\tau &+ 2\Re\left(ab^{*}\right)\int_{0}^{2\pi}\sin^{2}\tau\cos^{2}\tau p\left(\tau\right)d\tau\end{aligned}$$

and,

$$\begin{aligned}\langle S_{HH}S_{HV}^{*}\rangle = \left\langle S_{\tau_{11}}S_{\tau_{12}}^{*}\right\rangle &= \int_{0}^{2\pi}\left(a\cos^{2}\tau + b\sin^{2}\tau\right)\left(b-a\right)^{*}\sin\tau\cos\tau p\left(\tau\right)d\tau = \\ &\left(b-a\right)^{*}\int_{0}^{2\pi}\left(a\cos^{3}\tau\sin\tau + b\sin^{3}\tau\cos\tau\right)p\left(\tau\right)d\tau = \\ &\left(b-a\right)^{*}\left(a\int_{0}^{2\pi}\cos^{3}\tau\sin\tau p\left(\tau\right)d\tau + b\int_{0}^{2\pi}\sin^{3}\tau\cos\tau p\left(\tau\right)d\tau\right)\end{aligned}$$

and,

$$\begin{aligned}\langle S_{HV}S_{HV}^{*}\rangle = \left\langle S_{\tau_{12}}S_{\tau_{12}}^{*}\right\rangle &= \int_{0}^{2\pi}\left(\left(b-a\right)\sin\tau\cos\tau\right)\left(\left(b-a\right)^{*}\sin\tau\cos\tau\right)p\left(\tau\right)d\tau = \\ &\left|b-a\right|^{2}\int_{0}^{2\pi}\left(\sin^{2}\tau\cos^{2}\tau\right)p\left(\tau\right)d\tau\end{aligned}$$

and,

$$\langle S_{HH}S_{VV}^{*}\rangle = \left\langle S_{\tau_{11}}S_{\tau_{22}}^{*}\right\rangle = \int_{0}^{2\pi}\left(a\cos^{2}\tau + b\sin^{2}\tau\right)\left(a\sin^{2}\tau + b\cos^{2}\tau\right)^{*}p\left(\tau\right)d\tau =$$
$$\int_{0}^{2\pi}\left(\left|a\right|^{2}\cos^{2}\tau\sin^{2}\tau + ab^{*}\cos^{4}\tau + ba^{*}\sin^{4}\tau + \left|b\right|^{2}\cos^{2}\tau\sin^{2}\tau\right)p\left(\tau\right)d\tau =$$
$$\left(\left|a\right|^{2} + \left|b\right|^{2}\right)\int_{0}^{2\pi}\sin^{2}\tau\cos^{2}\tau p\left(\tau\right)d\tau + ab^{*}\int_{0}^{2\pi}\cos^{4}\tau p\left(\tau\right)d\tau + a^{*}b\int_{0}^{2\pi}\sin^{4}\tau p\left(\tau\right)d\tau$$

and,

$$\langle S_{VV}S_{VV}^{*}\rangle = \left\langle S_{\tau_{22}}S_{\tau_{22}}^{*}\right\rangle = \int_{0}^{2\pi}\left(a\sin^{2}\tau + b\cos^{2}\tau\right)\left(a\sin^{2}\tau + b\cos^{2}\tau\right)^{*}p\left(\tau\right)d\tau =$$
$$\int_{0}^{2\pi}\left(\left|a\right|^{2}\sin^{4}\tau + \left|b\right|^{2}\cos^{4}\tau + 2\Re\left(ab^{*}\right)\sin^{2}\tau\cos^{2}\tau\right)p\left(\tau\right)d\tau =$$
$$\left|a\right|^{2}\int_{0}^{2\pi}\sin^{4}\tau p\left(\tau\right)d\tau + \left|b\right|^{2}\int_{0}^{2\pi}\cos^{4}\tau p\left(\tau\right)d\tau + 2\Re\left(ab^{*}\right)\int_{0}^{2\pi}\sin^{2}\tau\cos^{2}\tau p\left(\tau\right)d\tau$$

and,

$$\langle S_{HV}S_{VV}^{*}\rangle = \left\langle S_{\tau_{12}}S_{\tau_{22}}^{*}\right\rangle = \int_{0}^{2\pi}\left(\left(b-a\right)\sin\tau\cos\tau\right)\left(a\sin^{2}\tau + b\cos^{2}\tau\right)^{*}p\left(\tau\right)d\tau =$$
$$\left(b-a\right)\int_{0}^{2\pi}\left(a^{*}\sin^{3}\tau\cos\tau + b^{*}\cos^{3}\tau\sin\tau\right)^{*}p\left(\tau\right)d\tau =$$
$$\left(b-a\right)\left(a^{*}\int_{0}^{2\pi}\sin^{3}\tau\cos\tau p\left(\tau\right)d\tau + b^{*}\int_{0}^{2\pi}\cos^{3}\tau\sin\tau p\left(\tau\right)d\tau\right)$$

,

therefore the following equations will produce all the elements of the covariance matrix that represent the volume covariance matrix of all the dipoles existing in each observation cell.

$$\begin{aligned}
\langle S_{HH}S_{HH}^{*}\rangle &= \left|a\right|^{2}I_{1} + \left|b\right|^{2}I_{2} + 2\Re\left(ab^{*}\right)I_{4}\\
\langle S_{HH}S_{HV}^{*}\rangle &= \left(b-a\right)^{*}(aI_{5} + bI_{6})\\
\langle S_{HV}S_{HV}^{*}\rangle &= \left|b-a\right|^{2}I_{4}\\
\langle S_{HH}S_{VV}^{*}\rangle &= \left(\left|a\right|^{2} + \left|b\right|^{2}\right)I_{4} + ab^{*}I_{1} + a^{*}bI_{2}\\
\langle S_{VV}S_{VV}^{*}\rangle &= \left|a\right|^{2}I_{2} + \left|b\right|^{2}I_{1} + 2\Re\left(ab^{*}\right)I_{4}\\
\langle S_{HV}S_{VV}^{*}\rangle &= \left(b-a\right)(a^{*}I_{6} + b^{*}I_{5})
\end{aligned} \tag{3.8}$$

where

$$\begin{aligned} I_1 &= \textstyle\int_0^{2\pi} \cos^4\tau p(\tau)d\tau & I_2 &= \textstyle\int_0^{2\pi} \sin^4\tau p(\tau)d\tau \\ I_3 &= \textstyle\int_0^{2\pi} \sin^2\tau\cos^2\tau p(\tau)d\tau & I_4 &= \textstyle\int_0^{2\pi} \cos^3\tau\sin\tau p(\tau)d\tau \\ & & I_5 &= \textstyle\int_0^{2\pi} \sin^3\tau\cos\tau p(\tau)d\tau \end{aligned} \tag{3.9}$$

assuming uniform distribution for the probability density function ($p(\tau) = 1$) of the orientation angle we can calculate the following integrals as:

$$I_1 = \int_0^{2\pi} \cos^4\tau p(\tau)d\tau = \left.\frac{\cos^3\tau\sin\tau}{4}\right|_0^{2\pi} + \frac{3}{4}\int_0^{2\pi}\cos^2\tau d\tau =$$

$$0 + \frac{3}{4}\left(\frac{1}{2}\left(\tau + \frac{\sin 2\tau}{2}\right)\Big|_0^{2\pi}\right) = \frac{3\pi}{4}$$

$$I_2 = \int_0^{2\pi} \sin^4\tau p(\tau)d\tau = -\left.\frac{\sin^3\tau\cos\tau}{4}\right|_0^{2\pi} + \frac{3}{4}\int_0^{2\pi}\sin^2\tau d\tau =$$

$$0 + \frac{3}{4}\left(\frac{1}{2}\left(\tau - \frac{\sin 2\tau}{2}\right)\Big|_0^{2\pi}\right) = \frac{3\pi}{4}$$

$$I_3 = \int_0^{2\pi} \sin^2\tau\cos^2\tau p(\tau)d\tau = \int_0^{2\pi}\frac{1}{4}\sin^2 2\tau d\tau = \frac{1}{4}\int_0^{2\pi}\left(\frac{1-\cos 4\tau}{2}\right)d\tau =$$

$$\frac{1}{4}\left(\frac{1}{2}\tau - \frac{1}{4}\sin 4\tau\Big|_0^{2\pi}\right) = \frac{\pi}{4}$$

$$I_4 = \int_0^{2\pi} \cos^3\tau\sin\tau p(\tau)d\tau = \left.\frac{1}{4}\cos^4\tau\right|_0^{2\pi} = 0$$

$$I_5 = \int_0^{2\pi} \sin^3\tau\cos\tau p(\tau)d\tau = \left.\frac{1}{4}\sin^4\theta\right|_0^{2\pi} = 0$$

it follows that,

$$I_1 = I_2 = \tfrac{3\pi}{4}, \quad I_3 = \tfrac{\pi}{4}, \quad I_4 = I_5 = 0 \tag{3.10}$$

If the cloud of randomly oriented, cylinder-like scatterers are assumed to be not only horizontal but also thin, then $a \to 1$ and $b \to 0$. By substituting these values in equation set of 3.8 and ignoring the $\frac{3\pi}{4}$ factor, the volume averaged covariance matrix $\langle C_{3_{vol}}\rangle_\tau$ is thus

given by

$$\langle C_{3_{vol}} \rangle_\tau = \frac{f_v}{3} \begin{bmatrix} 3 & 0 & 1 \\ 0 & 1 & 0 \\ 1 & 0 & 3 \end{bmatrix}$$

where f_v is the contribution of the volume scattering to the total $|S_{VV}|^2$ component. This matrix is calculated physically based on the target vector $\underline{\Omega} = \begin{bmatrix} S_{HH} & S_{HV} & S_{VV} \end{bmatrix}^T$, and $C(2,2) = \langle |S_{HV}|^2 \rangle = \frac{f_v}{3}$. But the new target vector $\underline{\Omega} = \begin{bmatrix} S_{HH} & \sqrt{2}S_{HV} & S_{VV} \end{bmatrix}^T$ (equation 2.13) used in the rest of this thesis implies that $C(2,2)$ should be $2\langle |S_{HV}|^2 \rangle$. Thus conversion of $C4$ to $C3$ dictates that the second element in diagonal of $C3$ matrix to be

$$C(2,2) = \langle |S_{HV}|^2 \rangle = 2\frac{f_V}{3} \tag{3.11}$$

and eventually the volume scattering component of covariance matrix is:

$$\langle C_{3_{vol}} \rangle_\tau = \frac{f_v}{3} \begin{bmatrix} 3 & 0 & 1 \\ 0 & 2 & 0 \\ 1 & 0 & 3 \end{bmatrix} \tag{3.12}$$

3.3.2 Surface Scattering

As for surface scattering, a first order Bragg surface scatterer model was chosen to represent a rough surface with negligible cross-polarized component. The scattering S matrix for a Bragg surface has the following form[45]

$$S = \begin{bmatrix} S_{HH} & S_{HV} \\ S_{VH} & S_{VV} \end{bmatrix} = \begin{bmatrix} R_H & 0 \\ 0 & R_V \end{bmatrix} \tag{3.13}$$

where the R_H and R_V are Fresnel or reflection coefficients for horizontally and vertically polarized waves (equation 3.28b). Using the same analogy as in the volume scattering case,

this scattering matrix yields a surface scattering covariance matrix $C_{3_{sur}}$ given by

$$C_{3_{sur}} = \begin{bmatrix} S_{HH}S_{HH}^* & \sqrt{2}S_{HH}S_{HV}^* & S_{HH}S_{VV}^* \\ \sqrt{2}S_{HH}S_{HV}^* & 2S_{HV}S_{HV}^* & \sqrt{2}S_{HV}S_{VV}^* \\ S_{VV}S_{HH}^* & \sqrt{2}S_{VV}S_{HV}^* & S_{VV}S_{VV}^* \end{bmatrix} = \begin{bmatrix} |R_H|^2 & 0 & R_H R_V^* \\ 0 & 0 & 0 \\ R_V R_H^* & 0 & |R_V|^2 \end{bmatrix} = f_s \begin{bmatrix} |\beta|^2 & 0 & \beta \\ 0 & 0 & 0 \\ \beta^* & 0 & 1 \end{bmatrix} \tag{3.14}$$

where f_s corresponds to the contribution of the single-bounce scattering to the total $|S_{VV}|$ component, with

$$f_s = |S_{VV}|^2 \quad and \quad \beta = \frac{R_H}{R_V} \tag{3.15}$$

Since β is related to surface scattering, there should be no phase difference between HH and VV return. Therefore theoretically Freeman and Durden assumed that β is a real value [23]. Although for practical reasons, some implementations of this algorithm (OFD) assumed that β is complex (please refer to Appendix A).

3.3.3 Double-Bounce Scattering

The model for the double-bounce scattering component was based on scattering from a dihedral corner reflector. In this case the two reflecting surfaces can be made of different dielectric materials such as is the case with ground and crop scenario depicted in figure 3.2. Let us assume that the vertical trunk surface has reflection coefficients R_{TH} and R_{TV} for horizontal and vertical polarizations, respectively. And also the horizontal ground surface has Fresnel reflection coefficients R_{GH} and R_{GV}. We incorporate the propagation factors $e^{2j\gamma_H}$ and $e^{2j\gamma_V}$ to generalize this model, where the complex coefficients γ_H and γ_V represent any propagation attenuation and phase change effects. The scattering S matrix for double-

bounce scattering is then[45]

$$S = \begin{bmatrix} S_{HH} & S_{HV} \\ S_{VH} & S_{VV} \end{bmatrix} = \begin{bmatrix} e^{2j\gamma_H} R_{TH} R_{GH} & 0 \\ 0 & e^{2j\gamma_V} R_{TV} R_{GV} \end{bmatrix} \tag{3.16}$$

The double-bounce scattering covariance matrix $C_{3_{db}}$ yielded from this scattering matrix is then given by

$$\begin{aligned} C_{3_{db}} &= \begin{bmatrix} S_{HH}S_{HH}^* & \sqrt{2}S_{HH}S_{HV}^* & S_{HH}S_{VV}^* \\ \sqrt{2}S_{HH}S_{HV}^* & 2S_{HV}S_{HV}^* & \sqrt{2}S_{HV}S_{VV}^* \\ S_{VV}S_{HH}^* & \sqrt{2}S_{VV}S_{HV}^* & S_{VV}S_{VV}^* \end{bmatrix} \\ &= \begin{bmatrix} e^{2j\gamma_H} R_{TH}R_{GH} e^{-2j\gamma_H} R_{TH}^* R_{GH}^* & 0 & e^{2j\gamma_H} R_{TH}R_{GH} e^{-2j\gamma_V} R_{TV}^* R_{GV}^* \\ 0 & 0 & 0 \\ e^{2j\gamma_V} R_{TV}R_{GV} e^{-2j\gamma_H} R_{TH}^* R_{GH}^* & 0 & e^{2j\gamma_H} R_{TV}R_{GV} e^{-2j\gamma_H} R_{TV}^* R_{GV}^* \end{bmatrix} \\ &= \begin{bmatrix} |R_{TH}R_{GH}|^2 & 0 & e^{2j(\gamma_H-\gamma_V)} R_{TH}R_{GH}R_{TV}^*R_{GV}^* \\ 0 & 0 & 0 \\ e^{2j(\gamma_V-\gamma_H)} R_{TV}R_{GV}R_{TH}^*R_{GH}^* & 0 & |R_{TV}R_{GV}|^2 \end{bmatrix} \\ &= f_d \begin{bmatrix} |\alpha|^2 & 0 & \alpha \\ 0 & 0 & 0 \\ \alpha^* & 0 & 1 \end{bmatrix} \end{aligned} \tag{3.17}$$

where f_d corresponds to the contribution of the double-bounce scattering to the $|S_{VV}|^2$ component, with

$$f_d = |R_{TV}R_{GV}|^2 \quad and \quad \alpha = e^{2j(\gamma_H-\gamma_V)} \tfrac{R_{TH}R_{GH}}{R_{TV}R_{GV}} \tag{3.18}$$

3.3.4 Superposition of the scattering models

Assuming that the volume, double-bounce, and surface scatter components are uncorrelated, the total second-order statistics are the sum of the above statistics for the individual

mechanisms. Thus, the model for the total backscatter is

$$\begin{aligned} C_3 &= C_{3_{sur}} + C_{3_{db}} + \langle C_{3_{vol}} \rangle_\tau \\ &= \begin{bmatrix} f_s\beta^2 + f_d\left(\Re(\alpha)^2 + \Im(\alpha)^2\right) + f_v & 0 & f_s\beta + f_d\alpha + \frac{f_v}{3} \\ 0 & \frac{2f_v}{3} & 0 \\ f_s\beta + f_d\alpha^* + \frac{f_v}{3} & 0 & f_s + f_d + f_v \end{bmatrix} \end{aligned} \tag{3.19}$$

We may use this covariance matrix to write seven equations.

$$\left\langle |S_{HH}|^2 \right\rangle = f_s\beta^2 + f_d\left(\Re(\alpha)^2 + \Im(\alpha)^2\right) + f_v \tag{3.20}$$

$$\left\langle |S_{VV}|^2 \right\rangle = f_s + f_d + f_v \tag{3.21}$$

$$\Re\left(\langle S_{HH}S_{VV}^* \rangle\right) = f_s\beta + f_d\Re(\alpha) + \frac{f_v}{3} \tag{3.22}$$

$$\Im\left(\langle S_{HH}S_{VV}^* \rangle\right) = f_d\Im\left(\alpha\right) \tag{3.23}$$

$$2\left\langle |S_{HV}|^2 \right\rangle = \frac{2f_v}{3} \tag{3.24}$$

$$\langle S_{HH}S_{HV}^* \rangle = 0 \tag{3.25}$$

$$\langle S_{HV}S_{VV}^* \rangle = 0 \tag{3.26}$$

Since all the scattering elements are our observations, covariance matrix can be easily calculated. Then we can estimate the magnitude of f_v from equation 3.24. And denote the simplified equation 3.22 by subtracting $\frac{f_v}{3}$ from $\Re\left(\langle S_{HH}S_{VV}^* \rangle\right)$ with "new" subscript. Also, equations 3.20 and 3.21 may be simplified by subtracting f_v from $\left\langle |S_{VV}|^2 \right\rangle$ and $\left\langle |S_{HH}|^2 \right\rangle$ and presented by "new" subscript. Therefore we have the following four equations.

$$\left\langle |S_{HH}|^2 \right\rangle_{new} = f_s\beta^2 + f_d\left(\Re(\alpha)^2 + \Im(\alpha)^2\right) \tag{3.27a}$$

$$\left\langle |S_{VV}|^2 \right\rangle_{new} = f_s + f_d \tag{3.27b}$$

$$\Re\left(\langle S_{HH}S_{VV}^* \rangle\right)_{new} = f_s\beta + f_d\Re(\alpha) \tag{3.27c}$$

$$\Im\left(\langle S_{HH}S_{VV}^* \rangle\right) = f_d\Im\left(\alpha\right) \tag{3.27d}$$

3.4 Rationale for $\frac{|\alpha|}{\beta}$ Ratio

As we discussed earlier, the volume scattering part of the Freeman-Durden algorithm is solved by equation 3.24 relating the already known $\langle |S_{HV}|^2 \rangle$ parameter from covariance matrix to the unknown f_v. The β parameter is the ratio of horizontal to vertical polarized reflection coefficient from surface scattering. While the α parameter as defined in the Freeman-Durden is the ratio of the horizontal to vertical polarized reflection coefficient of the ground multiplied by the same reflection ratio from the vegetation trunk, it also incorporates propagation factors to compensate for the losses and phase changes during double-bounce scattering phenomenon. It should be noted that Freeman-Durden's α is different from the directional cosine angle of the biggest eigenvector, α angle used in H/A/α decomposition.

In theory α angle may be subdivided to surface, volume, and double-bounce scattering. Figure 3.1 is an example of H/α sub-space, where each data point represents a pixel with the dominant scattering type according to its position in the H/α sub-space. As can be seen from figure 3.1 the boundaries for double-bounce and surface scattering is somewhat distinct due to the existence of volume scattering in the middle. Therefore the total number of pixels available in zones I, IV and VII can represent the double-bounce portion of reflection while the total number of pixels in zones IX, VI may represent the surface scattering portion of reflections received from a single field. These values are polarization as well as roughness[28] independent. These characteristics of H/α sub-space might be used as the 5^{th} equation to break the symmetry in the original Freeman-Durden equation sets. In the following sections we describe such a scenario and its implications.

3.4.1 Single Pixel Scenario

When a plane wave is incident upon a non-perfectly conducting infinite plane, the reflected wave depends upon the polarization of the incident wave. The Fresnel or reflection coefficients

for horizontally (R_H) and vertically (R_V) polarized waves [28] are given by

$$R_H = \frac{\cos\theta - \sqrt{\epsilon_r - \sin^2\theta}}{\cos\theta + \sqrt{\epsilon_r - \sin^2\theta}} \tag{3.28a}$$

$$R_V = \frac{(\epsilon_r - 1)\{\sin^2\theta - \epsilon_r(1 + \sin^2\theta)\}}{\left(\epsilon_r \cos\theta + \sqrt{\epsilon_r - \sin^2\theta}\right)^2} \tag{3.28b}$$

where, θ is the local incidence angle and ϵ_r is the relative permittivity of the surface. Relative permittivity is a generally complex dimensionless number. The imaginary part of ϵ_r corresponds to the phase shift of the outgoing wave in comparison to the incoming wave to the medium and leads to the attenuation of the electromagnetic wave. Since we assume that there is no phase shift in surface scattering for HH and VV, the relative permittivity for surface scattering is real. Note that R_H and R_V are also called Bragg scattering coefficients perpendicular and parallel to the incident plane. Both are functions of the relative permittivity ϵ_r and local incidence angle θ.

Therefore in a simple Bragg surface scattering case the co-polarized ratio, β can be defined as:

$$\beta = \frac{R_H}{R_V} = f\left(\theta, \epsilon_r\right) \tag{3.29}$$

Also $\epsilon_r \geq \sin^2\theta$ almost always is satisfied for natural surfaces other than ice since the maximum value for Sine function is 1. Since both θ and ϵ_r are real values, therefore R_H, R_V and consequently β are not complex values.

Using the same concept as surface scattering, the double-bounce scattering model can be defined as scattering from two plane surfaces with different dielectric properties. Scattering from two surfaces is, again, represented by reflection coefficients: R_{TH} and R_{TV} as trunk coefficients and R_{GH} and R_{GV} as ground coefficients. Ignoring any attenuation and phase changes between H and V due to propagation one will have the double-bounce co-polarized ratio, $|\alpha|$ as:

$$|\alpha| = \left| e^{2j(\gamma_H - \gamma_V)} \frac{R_{TH}R_{GH}}{R_{TV}R_{GV}} \frac{R_{TH}R_{GH}}{R_{TV}R_{GV}} \right| = \frac{R_{TH}R_{GH}}{R_{TV}R_{GV}} \frac{R_{TH}R_{GH}}{R_{TV}R_{GV}} \tag{3.30}$$

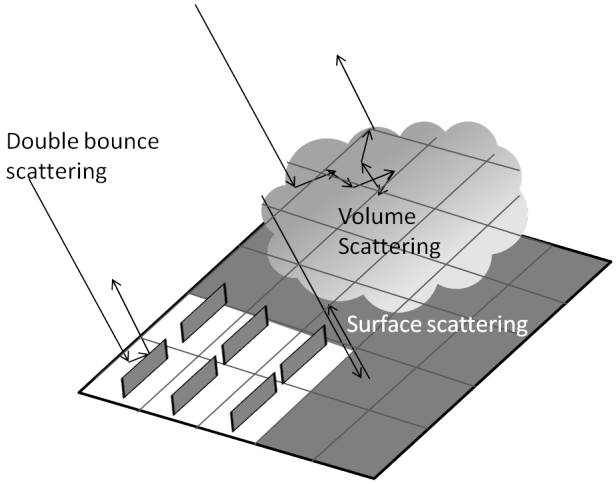

Figure 3.4: Scattering scenarios in a single field

In reality R_{TH}, R_{GH}, R_{TV}, and R_{GV} are all complex values due to the attenuation by the medium, but we can assume that all the phase shift effects has been modeled by an attenuation coefficient $e^{2j(\gamma_H - \gamma_V)}$. Therefore by taking an absolute value of α, all the reflection coefficients will be real values. And thus one of the most important results of equation 3.29 and 3.30 is that β and $|\alpha|$ depend only on the local incidence angle and permittivity.

3.4.2 Field-Based Scenario

Our refined Freeman-Durden (RFD) is a field-based algorithm. A simple example is an agricultural field imaged by a radar sensor, where the RFD algorithm produces a single set of values. Let us assume that this field contains n pixels and the only possible scattering scenarios are surface, double-bounce and volume scattering. Since in the Freeman-Durden algorithm the scattering processes are assumed to be independent, we can roughly assume that

$$n = n_s + n_{db} + n_v$$

where n_s, n_{db} and n_v are the number of surface, double-bounce and volume scattering occurrences in the field. Figure 3.4 is a representation of this field, and different scattering phenomena are divided into three separate regions of pixels. The model for β in a single

field is

$$\beta = \sum_{i=1}^{n} \frac{R_{i}H}{R_{i}V} = \underbrace{\sum_{i=1}^{n_s} \frac{R_{i}H}{R_{i}V}}_{Surface} + \underbrace{\sum_{i=1}^{n_{db}} \frac{R_{i}H}{R_{i}V}}_{Double\,bounce} + \underbrace{\sum_{i=1}^{n_v} \frac{R_{i}H}{R_{i}V}}_{Volume} \tag{3.31}$$

As we mentioned before, equation 3.31 only holds for special circumstances of Bragg surface scattering. Since Bragg scattering is only valid for a small surface scattering range (below 0.3 ks,k is the wave number and s is RMS height) it cannot be defined for volume scattering where the standard deviation of the RMS height is higher than Bragg scattering limits. On the other hand the double-bounce scattering is modeled by two separate surface scattering. Thus volume and double-bounce scattering are not representable by a simple Bragg surface scattering model. Our refined Freeman-Durden model assumes that only surface scattering pixels can contribute to β and therefore the summation for double-bounce and volume scattering are zero. Thus when the β parameter is going to be estimated, the field is reduced to only surface scattering pixels. A similar concept is applicable to double-bounce scattering $|\alpha|$ and we have,

$$|\alpha| = \underbrace{\sum_{i=1}^{n_{db}} \frac{R_{iTH}R_{iGH}}{R_{iTV}R_{iGV}}}_{Double\,bounce} \tag{3.32a}$$

$$\beta = \underbrace{\sum_{i=1}^{n_s} \frac{R_{i}H}{R_{i}V}}_{Surface} \tag{3.32b}$$

These $|\alpha|$ and β are also only function of permittivity and local incidence angle. If the field is relatively small we can assume that the local incidence angle is relatively constant. Also the change in permittivity is very gradual and can be approximated by a constant mean value for all the pixels in the field. This concept is generally called constant cross section[56] or cartoon model. In many cases, SAR images can be divided into regions of similar intensity. According to cartoon model we can postulate that the image consists of a cartoon of regions of approximately constant underlying cross section. Since homogeneity is one of the base assumptions for agricultural fields the cartoon postulate should be valid in each individual agricultural field. Therefore $\frac{R_{i}H}{R_{i}V}$ and $\frac{R_{iTH}R_{iGH}}{R_{iTV}R_{iGV}}$ are constant values for all the pixels in one

field. Thus we have,

$$\frac{|\alpha|}{\beta} = \frac{\sum_{i=1}^{n_{db}} \frac{R_{iTH}R_{iGH}}{R_{iTV}R_{iGV}}}{\sum_{i=1}^{n_s} \frac{R_{iH}}{R_{iV}}} = \frac{n_{db} \times \frac{R_{TH}R_{GH}}{R_{TV}R_{GV}}}{n_s \times \frac{R_H}{R_V}} = \frac{n_{db}}{n_s} \times c$$

For further simplification we assume that unit co-polarized ratio for surface and double-bounce scattering are equal and therefore $c = 1$. This means that the field ratio of $\frac{|\alpha|}{\beta}$ is proportional to the number of double-bounce to surface scattering pixels.

Each data point in the H/α sub-space (e.g., figure 3.1) represents a pixel with dominant scattering type according to its position. Thus the total number of pixels in zones IX, VI may represent the surface scattering n_s, while number of pixels available in zones I, IV and VII can represent the double-bounce n_{db}.

$$\frac{n_I + n_{IV} + n_{VII}}{n_{VI} + n_{IX}} = \frac{n_{db}}{n_s} \tag{3.33}$$

where $n_I, n_{IV}, n_{VI}, n_{VII}$, and n_{IX} are the number of pixels in zones I, IV, VI, VII, and IX of the H/α sub-space. Equation 3.34 expresses this characteristics of H/α sub-space as the 5^{th} equation to break the symmetry in the original Freeman-Durden equation sets.

$$\frac{|\alpha_i|}{\beta_i} = \sqrt{\frac{\Re(\alpha)^2 + \Im(\alpha)^2}{\beta^2}} = \frac{n_I + n_{IV} + n_{VII}}{n_{VI} + n_{IX}} \tag{3.34}$$

3.5 Refined Freeman-Durden

Let us come back to the four equations with five unknowns of 3.27a, 3.27b,3.27c, and 3.27d mentioned in section 3.3. To those we may add equation 3.34 from H/α sub-space to give a total of five equations. And let us take one other step and add a negative sign to the real and imaginary part of α in equations 3.27c and 3.27d. This is due to the $\pm\pi$ phase shift between the HH and VV components in double-bounce scattering. For simplification the right hand term of equation 3.34 will be simply called r (as it stands for ratio).

3.5.1 General Case

By substituting equation 3.34 in equation 3.27a we will have

$$\left\langle |S_{HH}|^2 \right\rangle_{new} = f_s\beta^2 + f_d\beta^2 r^2$$

By substituting f_s from equation 3.27b in the previous equation we can estimate f_d based on β by the help of equation 3.35.

$$f_d = \frac{\left\langle |S_{VV}|^2 \right\rangle_{new}}{(1-r^2)} - \frac{\left\langle |S_{HH}|^2 \right\rangle_{new}}{\beta^2(1-r^2)} \tag{3.35}$$

On the other hand by manipulating equations 3.27c, 3.27d, and 3.34 we have

$$\Re(\alpha)^2 + \Im(\alpha)^2 = \left(-\frac{\Re\left(\langle S_{HH}S_{VV}^*\rangle\right)_{new} - f_s\beta}{f_d}\right)^2 + \left(-\frac{\Im\left(\langle S_{HH}S_{VV}^*\rangle\right)}{f_d}\right)^2 = \beta^2 r^2$$

, now we can substitute f_d from 3.35 into previous equation

$$\left(\Re\left(\langle S_{HH}S_{VV}^*\rangle\right)_{new} - \beta\left\langle |S_{VV}|^2\right\rangle_{new} + \frac{\beta^2\left\langle |S_{VV}|^2\right\rangle_{new} - \left\langle |S_{HH}|^2\right\rangle_{new}}{\beta^2(1-r^2)}\right)^2 + \Im\left(\langle S_{HH}S_{VV}^*\rangle\right)^2 = \left(\frac{\beta^2\left\langle |S_{VV}|^2\right\rangle_{new} - \left\langle |S_{HH}|^2\right\rangle_{new}}{\beta^2(1-r^2)}\right)^2 \beta^2 r^2$$

finally, we have the following forth degree polynomial where β is the only unknown,

$$\begin{aligned}\beta^4\left\langle |S_{VV}|^2\right\rangle_{new}^2 r^2 - 2\beta^3\Re\left(\langle S_{HH}S_{VV}^*\rangle\right)_{new}\left\langle |S_{VV}|^2\right\rangle_{new} r^2 - \beta^2\Re\left(\langle S_{HH}S_{VV}^*\rangle\right)_{new}^2 \\ -\beta^2\Im\left(\langle S_{HH}S_{VV}^*\rangle\right)^2 + \beta^2\Re\left(\langle S_{HH}S_{VV}^*\rangle\right)_{new}^2 r^2 + \beta^2\Im\left(\langle S_{HH}S_{VV}^*\rangle\right)^2 r^2 \\ +2\beta\left\langle |S_{HH}|^2\right\rangle_{new}\Re\left(\langle S_{HH}S_{VV}^*\rangle\right)_{new} - \left\langle |S_{HH}|^2\right\rangle_{new}^2 = 0\end{aligned} \tag{3.36}$$

where S_{ij} are the elements of the covariance matrix (scattering values), H and V subscripts stand for the horizontal and the vertical polarizations. The "new" subscript stands for the modification due to the removal of $|S_{HV}|^2$ (in Freeman-Durden terms: f_v) multipliers. And the $\frac{|\alpha|}{\beta}$ is represented by r. The quadratic polynomial based on Abel's theory always has a discrete solution for its roots[20]. Therefore the detailed solution for β, based on equation 3.36 is provided in Appendix B.

Due to physical constraints, f_s and f_d may not have negative values since they are contributions of surface and double-bounce scattering to the always positive $\langle |S_{VV}|^2 \rangle$. Also, β based on the assumption made in surface scattering modeling (see section 3.4), is a real and positive value. We calculate f_d from equation 3.35. Then from equation 3.27d we estimate $\Im(\alpha)$. And from equation 3.27b we calculate f_s and from equation 3.27c we estimate $\Re(\alpha)$.

$$\Im(\alpha) = \frac{\Im(\langle S_{HH} S_{VV}^* \rangle)}{f_d} \tag{3.37a}$$

$$f_s = \langle |S_{VV}|^2 \rangle_{new} - f_d \tag{3.37b}$$

$$\Re(\alpha) = \frac{\Re(\langle S_{HH} S_{VV}^* \rangle)_{new} - \beta f_s}{f_d} \tag{3.37c}$$

Finally the contribution of each scattering mechanism to the span P (trace of matrix C_3 in equation 3.19) may be estimated

$$P = P_s + P_d + P_v \equiv \left(|S_{VV}|^2 + 2|S_{HV}|^2 + |S_{VV}|^2 \right) \tag{3.38}$$

with

$$\begin{aligned} P_s &= f_s \left(1 + |\beta|^2\right) \\ P_d &= f_s \left(1 + |\alpha|^2\right) \end{aligned} \tag{3.39}$$

and

$$P_v = 8\frac{f_v}{3} \tag{3.40}$$

Note that P is just four times the usual expression for total power[45].

3.5.2 No Double-Bounce Scattering

Equation 3.34 yields no results when the numerator, $n_I + n_{IV} + n_{VII}$ is equal to zero (i.e. $|\alpha_i| / \beta_i = 0$). This is the case when no double-bounce scattering is present, therefore $\alpha = 0$

and $f_d = 0$. Then the following formulation is the direct result of equations 3.27a through 3.27d.

$$f_v = 3\left\langle |S_{HV}|^2 \right\rangle \tag{3.41a}$$

$$f_s = \left\langle |S_{VV}|^2 \right\rangle - f_v \tag{3.41b}$$

$$\beta = \frac{(\Re\left(\langle S_{HH} S_{VV}^* \rangle\right) - f_v/3)}{f_s} \tag{3.41c}$$

Contributions to the power (P) can be again calculated from equations 3.39 and 3.40.

3.5.3 No Surface Scattering

Equation 3.34 is not defined when the denominator, $n_{VI} + n_{IX}$ is equal to zero (i.e. $|\alpha_i| / \beta_i = \infty$). This is the case when no surface scattering is present, therefore $\beta = 0$ and $f_s = 0$. Then the following formulation is the direct result of equations 3.27a through 3.27d.

$$f_v = 3\left\langle |S_{HV}|^2 \right\rangle \tag{3.42a}$$

$$f_d = \left\langle |S_{VV}|^2 \right\rangle - f_v \tag{3.42b}$$

$$\alpha = \frac{(\Re\left(\langle S_{HH} S_{VV}^* \rangle\right) - f_v/3)}{f_d} \tag{3.42c}$$

Likewise contributions to the power (span) can be again calculated from equations 3.39 and 3.40.

3.5.4 No Volume Scattering

In equation 3.34 when both numerator, $n_I + n_{IV} + n_{VII}$ and denominator, $n_{VI} + n_{IX}$ is equal (or close) to zero (i.e. $|\alpha_i| / \beta_i = \frac{0}{0}$) volume scattering is dominant, therefore all β, α,f_s and

f_d are zero. Thus only f_v will have a value,

$$f_v = 3\left\langle |S_{HV}|^2 \right\rangle \tag{3.43a}$$

$$\tag{3.43b}$$

Contributions to the power can be again calculated from equations 3.39 and 3.40. The summerized diagram of RFD computation details is presented in figure 3.5

3.6 Study Area

The study area is in Ontario, Canada. The average latitude and longitude of the fields are respectively 45° 22′ 23″ North and 74° 55′ 11″ West. While the closest village is Casselman (17 km), which is 66 km distance from Ottawa. The fields are along the Trans-Canada highway (417) and mostly on the northern side. The study area is in the Mixedwood plains ecozone of North America with 250 cm of snowfall[52] in winter that remains on the ground from December to March. It is within the South Nation River watershed[52]. Since the general climate of eastern Ontario is humid continental with large seasonal changes, the area has fairly warm, humid, and long summers. In terms of the annual precipitation, it amounts to 95 cm[52]. Figure 3.6 shows the relative location of our study area on the Canadian map.

3.7 Data Sets

3.7.1 Field Measurements

On seven different dates, some field observations was observed by Agriculture and Agri-Food Canada. In each agricultural field crop situation, crop type, and crop's direction was observed. The crop situation had three possibilities, 'Cropped/current year', 'No crop/harvested', 'Partially harvest'. On the other hand crop's type are soybean, corn and only one instance

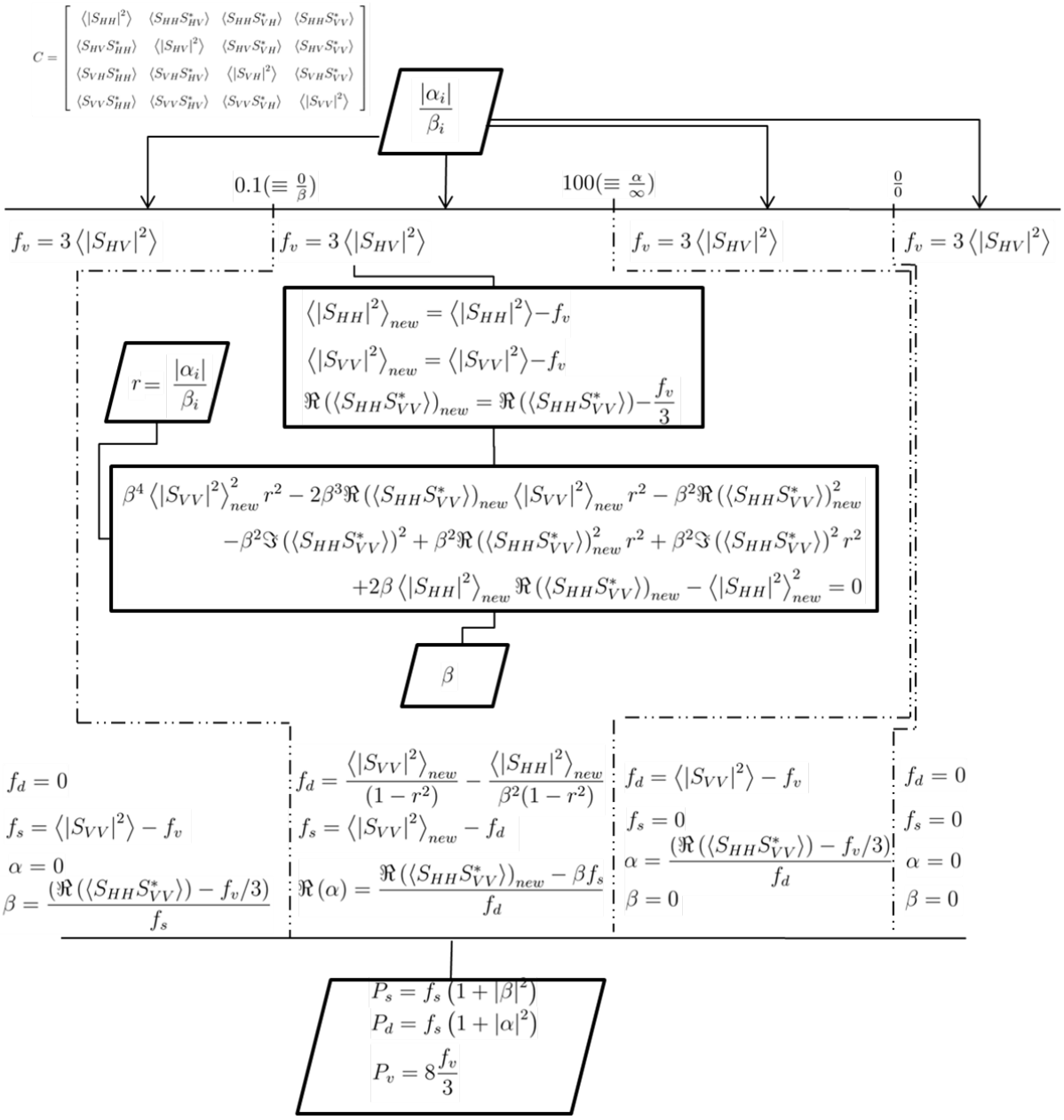

Figure 3.5: Refined Freeman-Durden flowchart

Figure 3.6: Casselman, Ontario on Canadian soil

of unharvested small grain. Also for some of the 'No crop/harvested' fields the crop type was not available. In the case of small grain field observations, they belong to a single field that majority of the time has observed as partially soybean. Table 3.1 shows that this field was only observed as small grains when the it was harvested. Therefore it did not matter whether or not it was a soybeans or a small grain field. In agricultural fields monitoring,

Table 3.1: Field data for field 350101211

Date	Crop/Harvest situation	
9/21/2009	Partially harvest	Soybeans
10/13/2009	No crop/harvested	Small grains
10/15/2009	Partially harvest	Soybeans
11/4/2009	Partially harvest	Soybeans
11/9/2009	Partially harvest	Soybeans
11/13/2009	No crop/harvested	Small grains

row directions play great role in the scattering from the fields[75]. The simplest example is the comparison between the scatterings from a field parallel to the azimuth directions versus a perpendicular one. In the exact same conditions, the former will have higher scattering values in comparison to the latter. Therefore in reality this effect is one of the most influential parameters in agricultural SAR applications. But in order to have a standalone algorithm for harvest detection that would use the least amount of field observations, we decided to merge different row directions altogether.

type of harvest (corn harvest for silage versus grain) - Tillage effects

In order to maintain the objectives of this thesis we did not take crop direction or soil type into consideration. Crop's direction was observed for all the cropped fields while only partially observed for the harvested fields, and the main types are 'Par. major axis' (parallel to major axis), 'Approx. E - W' (approximately in east-west direction), 'Other - per. to road' (other- perpendicular to road), and 'Other - par. to road' (other-parallel to road).

Figure 3.8 is a time line graphical description of the available ground observation data as well as RADARSAT-2 data. The six downward looking bars in the lower left hand side of figure 3.8 represents the dates of the ground observations. A total of 678 observations are

provided, out of which 113 entry belongs to each of the September 21^{th}, October 13^{th}, October 15^{th}, November 4^{th}, November 9^{th}, and November 12-13^{th} dates. The field observation in November 12 and 13^{th} are basically complimentary. Therefore we presented them as a single entity in this thesis. From these 113 fields, 50 fields are cropped with soybean, 55 fields with corn, 1 field with small grains/soybean, and 7 fields had no particular agricultural practice. Table 3.2 represents the summary on the Meta data for ground observation. As can be seen the transition between September 21^{th} to October 15^{th} through October 13^{th} is rather difficult to explain. Apparently some cultivation practices happened during this period which is very unlikely. Unfortunately this period introduced some inconsistencies in the results for some particular fields. In summary on October 13^{th}, three harvested corn and two partially harvested corn fields were probably still cropped corn and also four harvested soybeans were most likely still cropped soybeans. The detail of the noted problematic fields are mentioned in section 5.3 of chapter 5.

Table 3.2: Summary of the meta data for agricultural fields

	Cropped		Harvested		Partially harvested			
Date	corn	soybeans	corn	soybeans	corn	soybeans	Small grains	No crop
9/21/2009	54	48	0	1	0	3	0	7
10/13/2009	46	23	5	20	3	8	1	7
10/15/2009	51	25	3	16	0	11	0	7
11/4/2009	42	10	7	35	5	7	0	7
11/9/2009	30	8	14	36	11	7	0	7
11/13/2009	22	6	24	39	9	5	1	7

3.7.2 Agricultural Field Boundaries

A shape file containing field boundaries in zone 19 of Universal Transverse Mercator, UTM projection system are available. Although there is no height information provided in the data, the vertical datum of the data is North American Datum 1983(NAD83). The only two attributes of each field are an identification number and a soil surface type. The observed

soil surface types are very fine clay, clay, sand, loam, and organic fields. The total number of fields is 420 and figure 3.7 presents all the fields. Corn, Soybean and 'no crop' fields from the ground observation data are highlighted with different hues of gray in figure 3.7 and in total they are 113 fields. The remaining fields are presented by only bounding box (no inside color) where although boundaries are known but no ground observation is reported.

3.7.3 SAR Data

Eight images acquired in fine quad-polarized (FQ) mode by RADARSAT-2 on the Casselman test site are provided through Agriculture and Agri-Food Canada. Launched on 14 December 2007, RADARSAT-2 was commissioned on 25 April, 2008. RADARSAT-2's wave length is 5.55 cm and thus it is a C-band (5.405 GHz) SAR. It provides fully polarimetric (HH, HV, VH, and VV) radar imagery as well as multiple beam modes, resolutions and incidence angles. As for the orbital description, it has a polar sun synchronous orbit at an altitude of approximately 798 km. This orbit dictates a period of 101 minutes and allows for a 24 day ground repeat. But its real temporal resolution is higher than 24 hours due to the different incidence angles. Table 3.3 presents principal characteristics of the FQ beam RADARSAT-2 data. The FQ beam type shows that RADARSAT-2 image have fine resolution with quadratic polarizations (HH, VV, HV and VH). Practically FQ beam mode should obtain the highest spatial resolution in quad polarizations.

In figure 3.8, the eight RADARSAT-2 image acquisition dates from September 15^{th} till November 8^{th} are presented in the upper side by the means of upward looking bars and to the right hand side there is a legend available which shows some necessary information about each image such as beam type and their corresponding incidence angle. Some descriptions of FQ beam type is presented in 3.3 such as Nominal Range and Azimuth resolutions as well as nominal swath width and incidence angle. The pixel spacing in FQ mode is 4.7×5.1 m^2 ([Range $\times$ Azimuth]). The small arrow on top of each RADARSAT-2 acquisition date is to show whether it has been taken in an ascending ($\uparrow$) or descending ($\downarrow$) pass. All our FQ16

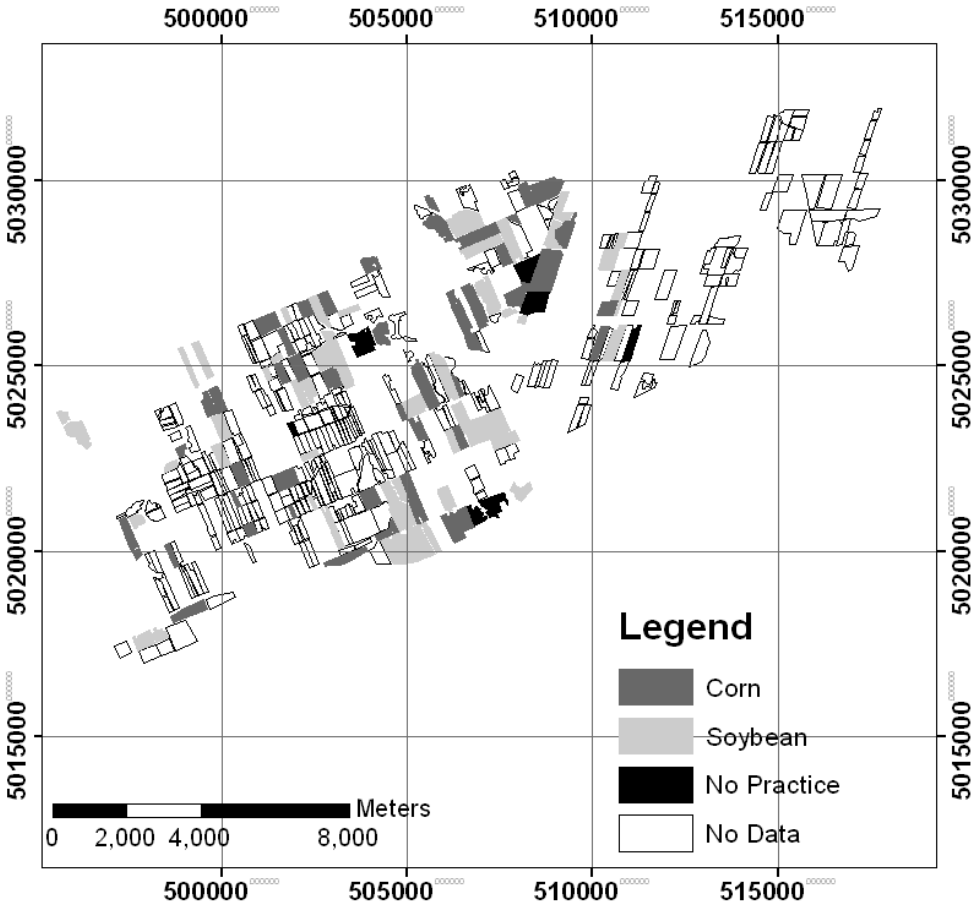

Figure 3.7: Field vectors in UTM coordinate system, crop types are also presented by different hues of gray.

Table 3.3: RADARSAT-2 FQ beam type specifications[51]

Band	C-band
Frequency	5.405 GHz
Polarization	HH, HV, VV, VH
Nominal Range resolution	16.5 m to 6.8 m
Minimum Azimuth resolution	8 m
Nominal swath width	25 km
Nominal incidence angle	18° to 49°
Altitude (average)	798 km
Inclination	98.6°
Period	100.7 minutes
Sun-synchronous	14 orbits per day
Repeat cycle	24 hours

images are descending pass images with acquisition times of 7:09 AM, 7:09 AM, and 6:09 AM for September 15^{th}, October 9^{th}, and November 2^{nd}. On the other hand all the other beam types are obtained in the evening, 6:42 PM for September 18^{th} and October 12^{th}, 6:54 PM for October 15^{th}, 5:42 PM for November 5^{th}, and 5:54 PM for November 8^{th}.

The radar data are available in single look complex (SLC) format, thus each resolution cell had complex pairs for each of the four polarimetric bands. Since there is no interpolation to the ground range for SLC data format, the data are in original slant range-azimuth coordinate system, and radar range sampling affects the range resolution[51]. Slant range-azimuth coordinate is a SAR imaging projection system and it is not connected to the ground and thus it may need geo-referencing.

Figure 3.8 shows that the only time SAR data and field observations coincide is on October 15^{th}. Therefore there are gaps between the observed SAR data and the field observations for any other dates. The fields can change during pre- or post-acquisition of SAR imagery in respect to the observed field information.

3.7.4 SPOT Data

A single panchromatic band Systme Pour lObservation de la Terre (SPOT) image was acquired from Geobase that had complete overlap with our field vectors and RADARSAT-2

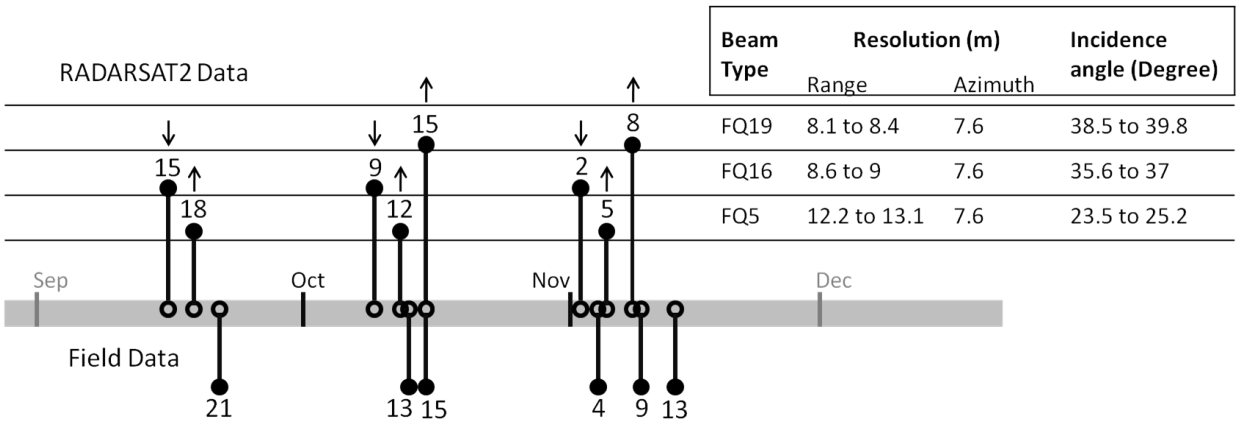

Beam Type	Resolution (m)		Incidence angle (Degree)
	Range	Azimuth	
FQ19	8.1 to 8.4	7.6	38.5 to 39.8
FQ16	8.6 to 9	7.6	35.6 to 37
FQ5	12.2 to 13.1	7.6	23.5 to 25.2

Figure 3.8: Time-line of the available datasets. The upper filled bars represents the days that RADARSAT-2 images are acquired. The numbers on top of each bar is the day that image was taken. The height of the upper bars correlates to the right hand side table which describes the detail of the images. The lower bars coincide with field observation dates, and they all have the same height.

scenes. Geobase (www.geobase.ca) is a portal for Canadian geo-spatial information operated by the Canadian Council on Geomatics. The data are part of national coverage of south of the 81^{st} parallel. The purpose was the full coverage with medium resolution ortho-imagery and starting from 2005 they have gathered SPOT-4 and SPOT-5 satellite images. SPOT is a French high resolution optical satellite. The downloaded Panchromatic SPOT image had 10 m spatial resolution. The projection system of the image, similar to our field vectors, is Zone 18 of UTM with NAD83 datum. The upper left pixel's geographic coordinate is 75° 33′ 26″ West and 45° 55′ 8.44″ North. The name of the file,

`S4_07505_4536_20070919_p10_1_utm18`

shows that the acquisition date was September 19^{th}, 2007 and the first two numbers separated by the underscore are row and path number of the image from SPOT 4 satellite. The sole purpose of this image is to calculate the transformation parameters between each slant range-azimuth and the UTM coordinate system. It covers roughly 60 km by 60 km area. The radiometric resolution is 8 bits. The data is in GeoTIFF format. Figure 3.9 presents the downloaded optical image where field vectors are highlighted on it.

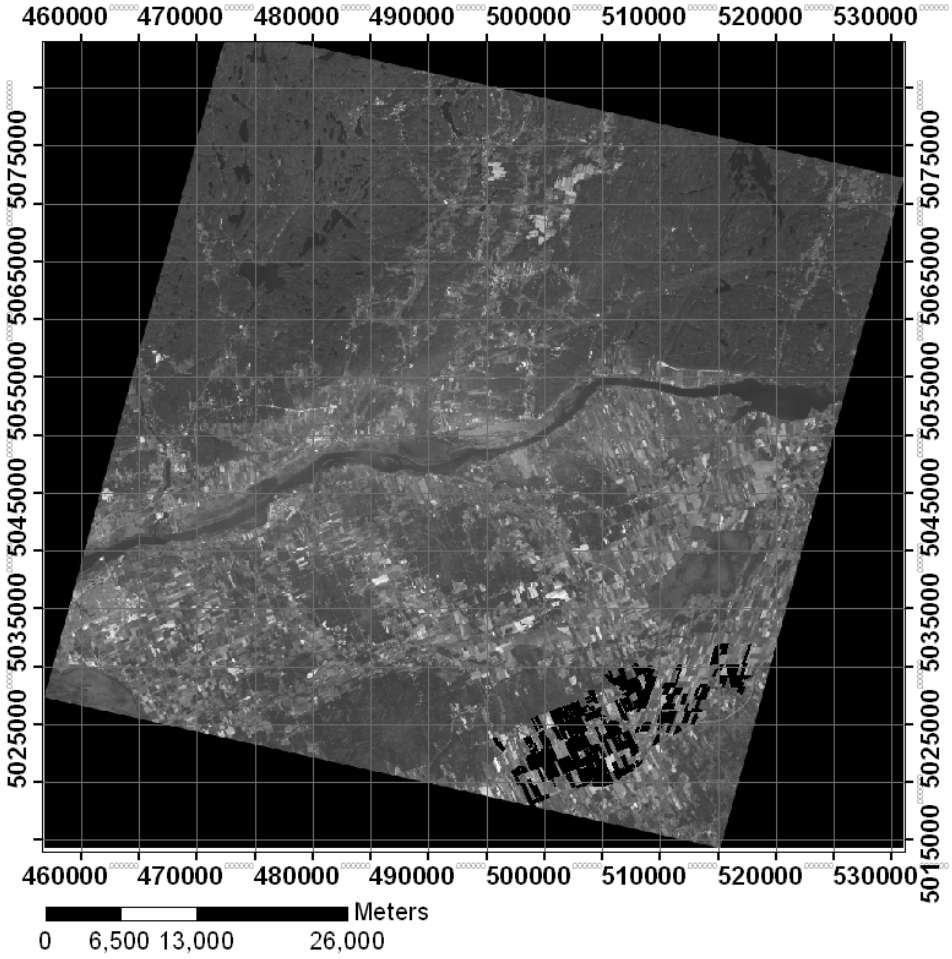

Figure 3.9: SPOT panchromatic band image where agricultural field vectors are highlighted in black color.

Chapter 4

Implementation

4.1 Data Preprocessing

In order to have a useful image for any remote sensing process two steps are necessary: geometric and radiometric corrections. A geometrically corrected image would enable the user to establish the relationship between each element of the image and the corresponding entity on another image, map or ground. Thus the resulted image is called registered or if it is the ground, geo-referenced. While radiometric corrections would maintain the relationship between the remote sensing measurement and some physical property of that entity on the ground. The methods used and amount of processing is application dependent. In our case, the geometric correction is described in section 4.1.2 and radiometric correction is described in section 4.1.1

4.1.1 Speckle Filtering

The coherent interference of waves from the elementary scatterers inside a single SAR measurement produces a salt and pepper effect on SAR images which is called speckle[45]. Speckle complicates the image interpretation and reduces the accuracy of image segmentation and classification [45]. Therefore the PolSAR images had to be filtered. Filtering improves the clustering ability but decreases the spatial resolution.

The simplest filter for speckle is the box car filter. This filter is a simple averaging for each element of the covariance matrix inside a certain window size. Since it will be performed uniformly for all elements of covariance matrix, it will preserve the polarimetric information. And since for each pixel, each element of covariance matrix is averaged independently, there is no cross talk between the polarimetric information. On the other hand this filter is a

very simple low pass filter and thus it has blurring effects and it does not preserve the edges or peaks inside the fields. In case of agricultural fields where homogeneity is expected and sharp changes in polarimetric behavior are not, even a simple boxcar filter should be enough. The window size in boxcar filter determines the amount of smoothing. In general small window sizes such as 3 by 3 or 5 by 5 may keep more high frequency information while larger window sizes tends to lose the high frequency and provide a higher degree of smoothening. We performed boxcar filter with 3 by 3, 5 by 5 and 11 by 11 to observe the effects of filtering. There are various filter types available but the application and data itself are the main factors that dictate the type and specification of the filter. Some sophisticated filters are specially designed for SAR applications. One such filter is the refined Lee filter that keeps some of the sharp polarimetric changes inside the SAR image while maintaining the same smoothing effects[45].

Lee refined his filter by adding an edge-aligned window, and its filter preserves the polarimetric properties and scattering characteristics (e.g., edge sharpness and point targets) while avoids the cross talk between polarization channels[45]. The first step in implementing the refined Lee filter is to select a proper edge-aligned window. Thus the direction of the edge in the span image (R:HH, G:VH+HV, B:VV) is used to select a non-square window. The second step is to compute the filtering weights. The refined Lee filter is an adaptation of the Lee filter[43], and thus it is a standard deviation based filter. The weight calculation is based on a local standard deviation statistics over span image for each pixel. If x would be the noise free value and y would be the original noisy value, we can define the weight, b as

$$b = \frac{Var(x)}{Var(y)}$$

where $Var(y)$ is the variance of the values inside a certain window size surrounding the main pixel. And $Var(x)$ could be calculated by

$$Var(x) = \frac{Var(y) - \bar{y}^2\sigma_v^2}{1 + \sigma_v^2}$$

where $\bar{y}$ is the mean of the values inside that window size and noise standard deviation, σ_v is a predefined value. The final step is to use the estimated weight and the selected window to replace the pixel value with a filtered covariance value. This could be done with

$$\hat{\bar{S_{ij}}} = \bar{S_{ij}} + b(S_{ij} - \bar{S_{ij}})$$

where S_{ij} is elements of the covariance matrix, i and j subscripts are polarization types, and $\bar{S_{ij}}$ is the local mean covariance estimated with edge directed window for each element.

Speckle filtering is a necessary step in most of SAR applications. In our case we used speckle filtering in three parts of analysis. The first part is in the conventional polarimetric section 4.6. Some of our preliminary classifications that were not mentioned in that section did not perform well with simple boxcar filter. Therefore we decided to use the refined Lee filter with 7 by 7 window size for speckle removal before classifications. One other use of the speckle filter was for OFD algorithm. Since Freeman-Durden algorithm needs to calculate the scattering parameters from covariance matrix and speckle could show itself as a dominant scattering error, it should be removed prior to OFD algorithm. In this case we tried all the boxcar and refined Lee filtered images with some variation of window sizes. Last but not the least is the H/α calculations in RFD algorithm where we again used boxcar and refined Lee filter with some variation of window sizes. In RFD algorithm the Freeman-Durden estimation part mainly shown in diagram 3.5 is a field-based estimation. Therefore for each element of the covariance matrix, an average over all the pixels inside the agricultural field is estimated. Due to this averaging, speckle removal has been done inherently. But for H/α part of RFD algorithm where each pixel inside the field would be used to generate the H/α plot, filtering is necessary. The main reason is that speckle is a purely random process and therefore statistically it has zero entropy. If not removed, speckle forces all the pixels inside the H/α domain to move toward zero entropy line. This could be observed in more details in section 6.3.

4.1.2 Registration

Since the goal of this research is to analyze some agricultural fields from SAR imagery, we need to relate the field polygons mentioned in section 3.7.2 to the RADARSAT-2 data mentioned in section 3.7.3. For us, maintaining the phase properties of each observed pixel were more important than its location. The reason is that for agricultural fields we assumed that they are homogeneous and the location of each pixel inside the field is rather irrelevant to the outcome of the classification, while phase information should have not been disturbed to have accurate polarimetric processes. On the other hand each field has a field ID number and it is possible to present the fields in geo-referenced projection system any time but for processing purpose it is not a necessary condition. Therefore we decided to take slant range-azimuth as our main projection system and convert any other source of data to this projection system.

SPOT image were downloaded to estimate the inverse projection parameters used to covert UTM coordinate system to slant range-azimuth projection system. The first step in such a process is to choose a proper set of ground control points (GCP's). In each image, we chose 10 ground control points and 4 check points for evaluation of the registration. For example table 4.1 contains the coordinates of the ten control points in both slant range-azimuth and UTM for October 15^{th}. UTM coordinate system is at least three orders of magnitude larger than slant range-azimuth image coordinate system, therefore we had to downscale the X and Y values by 1000.

Since the first order polynomials did not produce an acceptable error boundary, and the third to higher order would have been more accurate on GCP's while introducing distortions elsewhere, some second order polynomial with 8 parameters were chosen. For example second order polynomial in equation 4.1 is the result of least square estimation to convert X, Y coordinates from SPOT image to x, y set in October 15^{th} slant range-azimuth image. Table 4.1 also shows the estimated x, y errors along with the root mean square error (RMSE).

$$\begin{cases} x = -2301.47 + 1346.23 \times X - 212.96 \times Y - 5.55 \times X \times Y \\ y = -11522.22 + 356.41 \times X + 2073.52 \times Y + 0.99 \times X \times Y \end{cases} \tag{4.1}$$

Table 4.1: GCP coordinates in both UTM of SPOT image and slant range-azimuth of October 15^{th} RADARSAT-2 along with the estimated errors

UTM		slant range-azimuth		error		
X	Y	x	y	dx	dy	RMSE
3729250	6595500	1177.75	3507.5	-0.15	0.34	0.371618
3931250	5488750	1700.75	1281.25	-1.53	-0.05	1.530817
4780250	5168750	2897	921	0.99	-2.46	2.651735
4275500	6688750	1871.5	3900	0.28	0.84	0.885438
5073500	5659750	3164.5	2052.25	0.5	2.21	2.265855
4471000	5924000	2305.25	2381.75	-3.73	0.72	3.798855
4519000	6582000	2213	3766	-2.4	0.27	2.41514
3565200	5950200	1116.75	2105.25	3.51	-2.06	4.069853
4015400	5272000	1863.75	863.5	-0.24	2.04	2.054069
5078200	6439200	2985	3670	2.78	-1.86	3.344847

The four test points for October 15^{th} image are presented in table 4.2. Since radar imagery are fundamentally different from optical imagery, choosing control points on the radar imagery solely based on their similarity to optical imagery is a difficult process. On the other hand radar's famous distortion errors make it even more difficult to be sure about the precision of the selected points. Better results might be achieved with higher resolution optical images and higher number of control points. The 15 m spatial resolution of the SPOT image and roughly 8 m spatial resolution of quad fine beam types dictate that 2 pixels were the highest meaningful RMSE achievable for our registrations. But due to the difficulties mentioned above and lack of higher resolution imagery, we decided that RMSE smaller than 5 pixels should suffice. The proposed method in this thesis is field based therefore an averaging process has been taken for each field. On the other hand, fields are assumed to be homogeneous and therefore the pixels wrongfully included in each field are in minority in each field. Assuming an average 8 m spatial resolution, 5 pixels RMSE leads to error ellipses with 40 m diameter. On the other hand, the median size of our agricultural fields

is 4115 pixels and the 5 pixels RMSE can take up to 30 percent of such a field. Although homogeneity assumption and averaging reduce the effects of registration error but it could well be a possible source of error in the final outcomes.

Table 4.2: Test points coordinates in both UTM of SPOT image and slant range-azimuth of October 15^{th} RADARSAT-2 along with the estimated errors

UTM		slant range-azimuth		error		
X	Y	x	y	dx	dy	RMSE
3630800	6243800	1131.5	2739.75	0.58	-1.17	1.305871
3836800	5778200	1510.25	1845.5	0.07	-2.92	2.920839
5234600	6249600	3236	3333	2.97	-1.5	3.327296
4622400	5260800	2664	1058.5	-2.04	0.8	2.191255

The same registration process described for October 15^{th} image has been performed for the other images and the results are presented in Appendix C. The left hand side image in Figure 4.1 presents the original field vectors overlaid on the SPOT image, while the transformed field vectors in October 15^{th} are overlaid on corresponding RADARSAT-2 image. The grid coordinates in the left image are in UTM coordinate system while the grid numbers in the right hand side image of figure 4.1 are pixel numbers based on the top left origin image coordinate system. Some of the fields on the right hand side have not been presented on the RADARSAT-2 image since they were outside of the image boundaries. The change of scale is evident and it is different for x and y axis also there is a slight clockwise rotation along with the change of the origin.

4.1.3 Polygon Extraction

The result of these registrations are some second order polynomials used for transforming shape files of agricultural boundaries UTM coordinate systems to slant range-azimuth in different dates. The next step is to cut out those fields from the RADARSAT-2 imagery. Figure 4.2 is a small area selected from the RADARSAT-2 image presented in figure 4.1b. The depicted SAR image is the real part of the HH polarization results and has no speckle

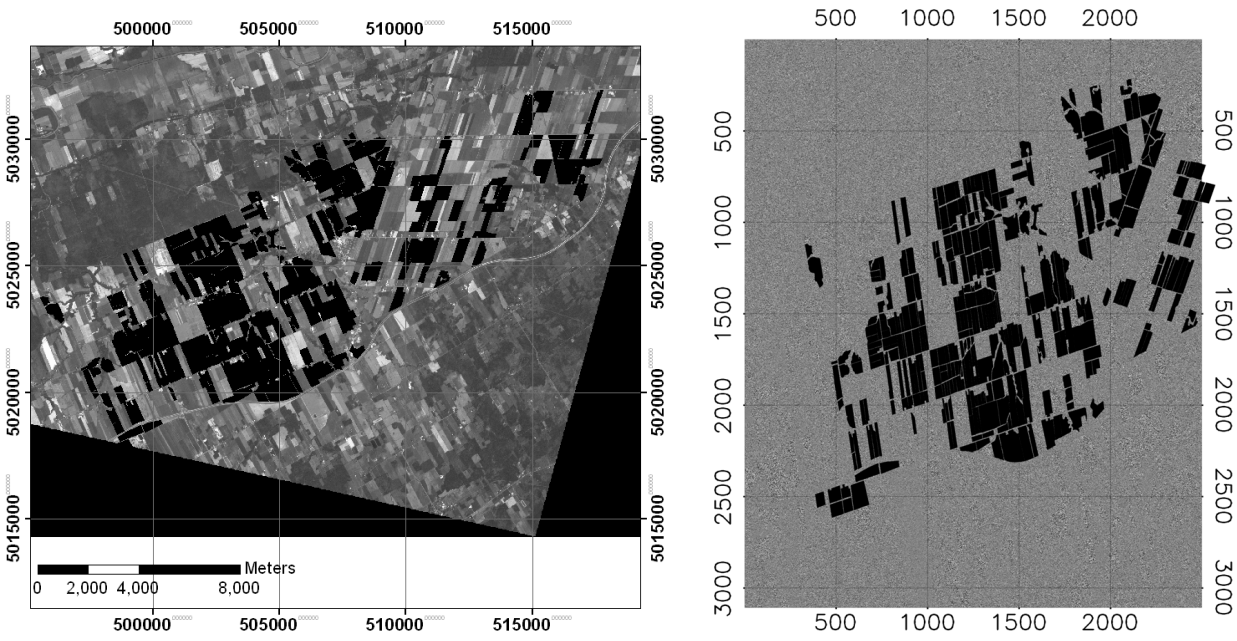

Figure 4.1: Left:Agricultural field boundaries overlaid on SPOT image, Right: registered field boundaries overlaid on October 15^{th}RADARSAT-2 image.

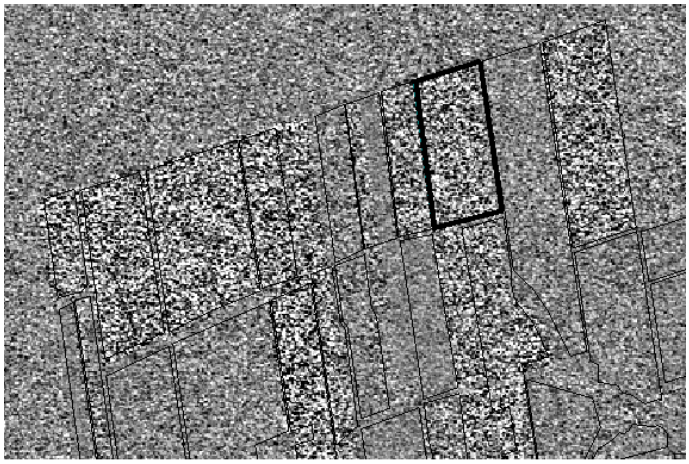

Figure 4.2: Registered field boundaries overlaid on October 15^{th}RADARSAT-2 image

filtering. Therefore the salt and pepper pattern of speckle is very evident and some of the agricultural fields, such as field number 350101253 which is highlighted in figure 4.1b, have distinct behavior in comparison to their surrounding area. Extraction process needs to be referenced to slant range-azimuth coordinate system. For example for field 350101253 we saved bounding box, a 103 by 55 by 16 coherency matrix, and a mask (named 'Inregion') for the polygon inside the coherency matrix. The bounding box contained the pixel location of the top-left and bottom-right points of the surrounding rectangle of the field polygon (e.g, $\begin{bmatrix} 2234 & 2397 \\ 2336 & 2451 \end{bmatrix}$ being $\begin{bmatrix} TopLeft_x & TopLeft_y \\ BottumRight_x & BottumRight_y \end{bmatrix}$). These three parameters are sufficient for referencing any results estimated for each field on any date. Therefore we extracted these triples for each field in each of the eight RADARSAT-2 images, saved them as the main properties of each field, and used them as the base of our field oriented RFD calculations.

4.2 Processing Block for OFD

Original Freeman-Durden algorithm should also be implemented to perform a meaningful comparison between the results of RFD and OFD. Unfortunately we could not find any code that perform the same procedure as it was described by Freeman and Durden [23] in their original paper, but open source scientific software such as PolSARPro©and RAT©has developed their own version of the Freeman-Durden code. This code was written by Eric Pottier and Laurent Ferro-Famil and since we could not find any written document describing the details of this implementation either, we had to provide a mathematical reasoning for the code. Therefore we tried to describe the Pottier and Ferro-Famil's solution in Appendix A and the Matlab©translation of the code is provided in Appendix D. The flowchart of OFD algorithm proposed by Pottier and Ferro-Famil is presented in figure 4.3 but for further details please read Appendix A. We use this method as original Freeman-Durden solution and henceforth we call it OFD.

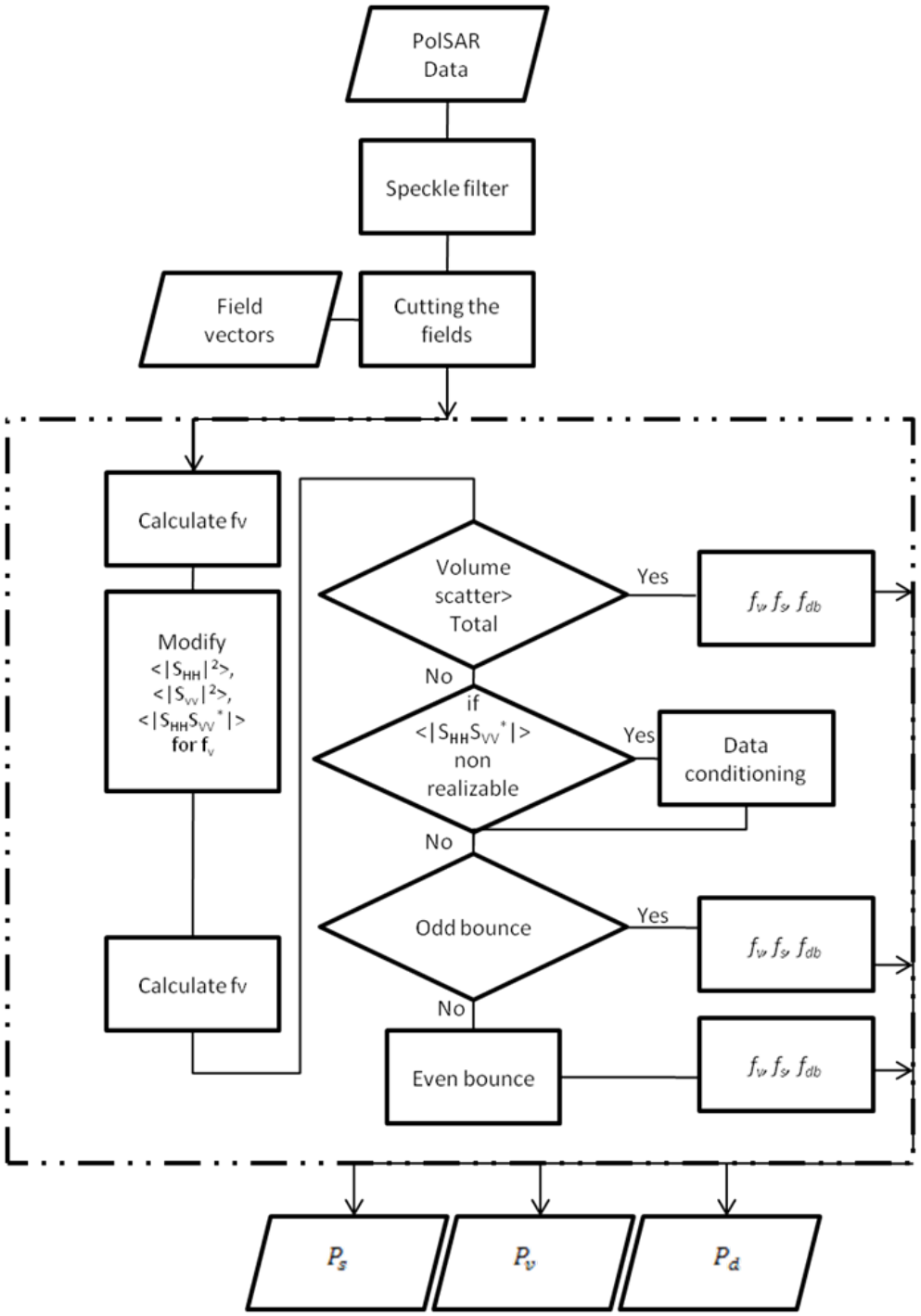

Figure 4.3: Freeman-Durden by Pottier and Ferro-Famil's solution flowchart

4.3 Processing Block for RFD

The schematic of the refined Freeman-Durden algorithm is provided in figure 4.4. Initially covariance matrix is calculated for each pixel based on equation 2.8. Then we filter the covariance matrix based on the methods described in section 4.1.1. Transformation of the covariance to coherency matrix based on relations described in section 2.1.4 was the next step. Then Covariance and Coherency matrix of the filtered Radar image will be cut for each field. This has two benefits being less computationally expensive while producing field oriented results. As it can be seen from figure 4.4 in each field the coherency matrix (T_4) for each pixel were used to calculate the corresponding H/A/α. Then Equation 3.34 were used to estimate a single $\frac{|\alpha_i|}{\beta_i}$ ratio value for each field.

Then a single averaged covariance matrix for each field will be produced and along with the H/A/α resulted ration it will be inputted to Freeman-Durden based formulation described in the block diagram in figure 3.5. Then the contribution of the volume, double-bounce, and surface scattering for Span will be estimated and used to describe each field's behavior. A code has been developed for the RFD algorithm and is included in Appendix E.

4.4 RFD Processing Routes

In this section we present the analysis made on the different root scenarios and their speculated solutions. The forth degree polynomial described in equation 3.36 with only β (co-polarized surface scattering reflection ratio of horizontal to vertical polarization) as unknown is the direct result of refined Freeman-Durden algorithm. Also especial cases of no double-bounce, no volume, and no surface scattering would also add to the complexity of the scenario.

The behavior of the processing route for the RFD algorithm is an important aspect of the RFD implementation. The details of the algorithm were described in the methodology chap-

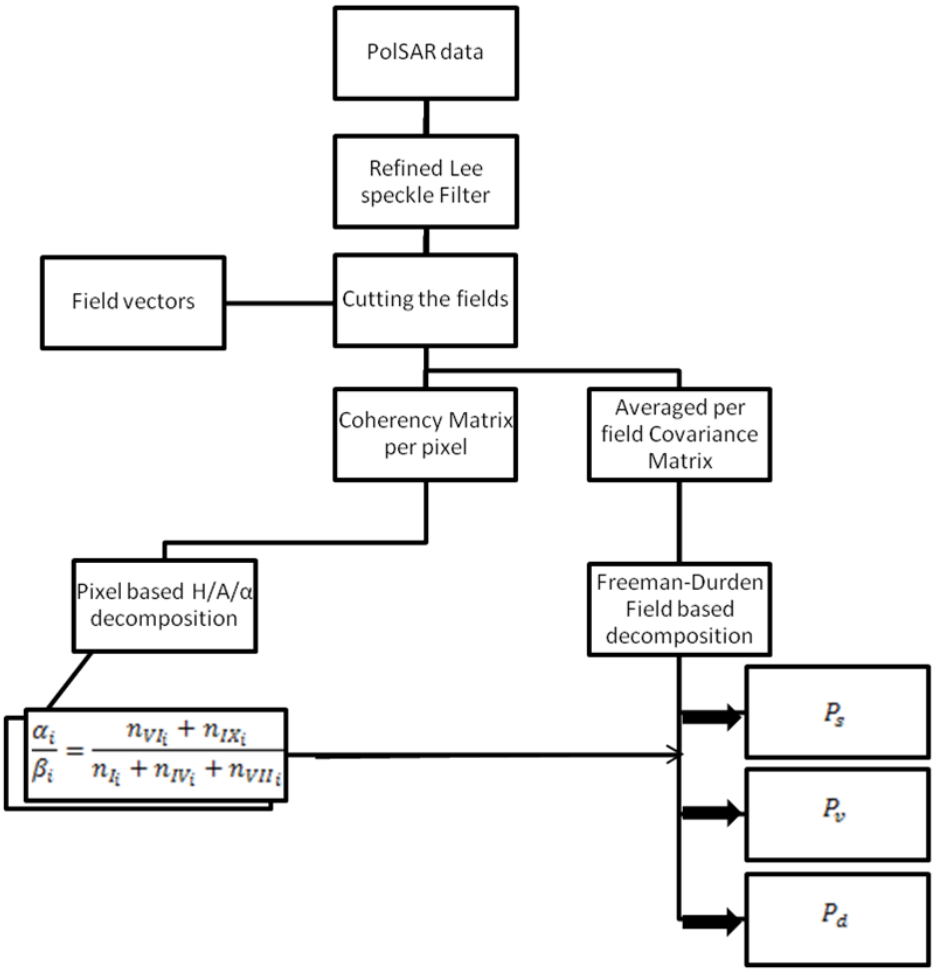

Figure 4.4: Freeman-Durden and H/A/α merging flowchart

ter (chapter 3) also figure 3.5 is informative regarding the possible routes. In RFD, processing routes can be classified to 18 classes as described by {a.1,a.2,...,a.5,b.1,b.2,...,b.6,c.1,c.2,...,c.7} in table 4.3. The a.i series (i=1,2,...,5) are for the cases that a single positive root is detected for β. In case of refined Lee filtered image used for RFD, the majority of the agricultural fields are in single positive root processing route. Some possible calculation paths generating a single positive root are described in section 3.5.2, section 3.5.3, and section 3.5.4. But quadratic equation 3.36 in section 3.5.1 could also produce a single root.

In general, the quadratic form can behave in three categories. First, a unique single positive root will be estimated along with three negative or imaginary roots. These roots are classified inclusively as a.i series in table 4.3. The a.1 class is when both double-bounce and surface scattering are positive (nonzero) and therefore it is the sole result of the single positive β root for the quadratic equation 3.36. An example of this case is presented in section 4.4.1. On the other hand, a.2 is when we have a single positive root but $f_d = 0$, this is especially the case for section 3.5.2. The a.3 class is when we have a single positive root for β but it results in a negative span values. Similar cases where a root was estimated but one of the spans becomes negative are available in all three categories, and the classes a.5, b.3, b.5, c.3, and c.5 share the same problem. We discuss the reasoning and a simplified solution for this negative span phenomenon in section 4.4.3. While a.4 class is generally the result of section 3.5.3, a.5 class is again another route that comes from the issue described in section 4.4.3.

Second series could be multiple real positive roots with the remaining roots being either negative or imaginary. These roots were the sole members of b.i (i=1,2,...,6) series in table 4.3 and we did not observe a single occurrence for these fields. Even the filter free images did not have any b.i member. Therefore this group is mathematically possible but physically they were not the case for our fields.

We call the third group, multiple good complex roots and we describe them in section

4.4.2. These roots are sole providers for c.i (i=1,2,...,7) series.

Table 4.3: Classification of RFD algorithm's routes for different dates. The values are based on the 11 by 11 window size refined Lee filtered images.

					Sep15th	Sep18th	Oct.9th	Oct. 12th	Oct.15th	Nov. 2nd	Nov. 5th	Nov. 8th
single positive real root			$f_d > 0$ AND $f_s > 0$	a.1	11	3	50	9	21	36	1	25
			$f_d = 0$	a.2	87	109	53	104	60	62	112	69
			$f_d < 0$	a.3	2	0	0	0	0	0	0	0
			$f_s = 0$	a.4	0	0	0	0	32	7	0	18
			$f_s < 0$	a.5	2	1	0	0	0	7	0	1
number of real positive roots > 1	was able to select one real positive root using H/α space		$f_d > 0$ AND $f_s > 0$	b.1	0	0	0	0	0	0	0	0
			$f_d = 0$	b.2	0	0	0	0	0	0	0	0
			$f_d < 0$	b.3	0	0	0	0	0	0	0	0
			$f_s = 0$	b.4	0	0	0	0	0	0	0	0
			$f_s < 0$	b.5	0	0	0	0	0	0	0	0
	was not able to select one real positive root using H/α space			b.6	0	0	0	0	0	0	0	0
number of real positive roots == 0	number of good complex roots = 1		$f_d > 0$ AND $f_s > 0$	c.1	3	0	8	0	0	0	0	0
			$f_d = 0$	c.2	0	0	0	0	0	0	0	0
			$f_d < 0$	c.3	0	0	0	0	0	0	0	0
			$f_s = 0$	c.4	0	0	0	0	0	0	0	0
			$f_s < 0$	c.5	3	0	0	0	0	0	0	0
	number of good complex roots > 1			c.6	5	0	2	0	0	1	0	0
	number of good complex roots = 0			c.7	0	0	0	0	0	0	0	0

4.4.1 Unique Roots

Since equation 3.36 is a forth degree polynomial, it should produce four roots for any sets of coefficients. Most of the time the roots has the form $(a, -c, b_1 + b_2 i, b_1 - b_2 i)$ were a and c are always positive real values while b_1 and b_2 could be either positive or negative real values. Since β is the co-polarized reflection coefficient ratio and defined to be a real positive value, only the real positive root (i.e., a) has been considered as the proper root for this equation. An example of this case is the following set with coherency matrix such as:

$$T_4 = \begin{bmatrix} 1.710 \times 10^8 & 1.471 \times 10^6 + 2.216 \times 10^6 i & ... \\ 1.471 \times 10^6 - 2.216 \times 10^6 i & 1.354 \times 10^7 & ... \\ 7.995 \times 10^5 - 1.770 \times 10^6 i & 1.262 \times 10^7 + 3.681 \times 10^5 i & ... \\ 8.489 \times 10^6 - 2.488 \times 10^7 i & 1.371 \times 10^6 - 8.542 \times 10^4 i & ... \end{bmatrix}$$
$$\begin{bmatrix} ... & 7.9952 \times 10^5 + 1.7704 \times 10^6 i & 8.4893 \times 10^6 + 2.4883 \times 10^7 i \\ ... & 1.2624 \times 10^7 - 3.6810 \times 10^5 i & 1.3707 \times 10^6 + 8.5417 \times 10^4 i \\ ... & 1.3640 \times 10^7 & 1.0227 \times 10^6 + 8.5266 \times 10^4 i \\ ... & 1.0227 \times 10^6 - 8.5266 \times 10^4 i & 1.0913 \times 10^8 \end{bmatrix}$$

Therefore one can calculate the known parameters as,

$$\left\langle |S_{VV}|^2 \right\rangle_{new} = 68512878.5411$$
$$\left\langle |S_{HH}|^2 \right\rangle_{new} = 130356253.6250$$
$$\Re\left(\langle S_{HH} S_{VV}^* \rangle\right)_{new} = -5048998.2148$$
$$\Im\left(\langle S_{HH} S_{VV}^* \rangle\right) = 24882733.9194$$
$$r = 0.4704$$

By substituting these values in equation 3.36, the forth degree polynomial can be rewritten.

$$\begin{aligned} 1038878078290641.9000\beta^4 - 153118469824116.8400\beta^3 \\ - 50984765946972.2000\beta^2 - 619150447301287.8400\beta^2 \\ + 5641967592543.5712\beta^2 + 137030216524517.4400\beta^2 \\ - 1316336983692309.3000\beta - 16992752859141719.0000 = 0 \end{aligned} \quad (4.2)$$

The roots for equation 4.2 are $(2.1093, -2.0309, -0.1129 + 1.9508i, -0.1129 - 1.9508i)$. And therefore 2.1093 being the only real positive root is the answer for β.

4.4.2 Multiple Complex Roots

But sometimes another scenario for the roots of equation 3.36 has been observed. In these cases they all have at least one (up to 4) root(s) with infinitesimally small imaginary part (e.g.,$(\times 10^{-40})$). We assume that in these cases complex roots with large imaginary parts are not answers due to the real number constraint on β,

An example of this case is for the following set

$$T_4 = \begin{bmatrix} 8.1588 \times 10^7 & 3.6099 \times 10^5 + 3.8727e \times 10^5 i & ... \\ 3.6099 \times 10^5 - 3.8727 \times 10^5 i & 8.7311 \times 10^6 & ... \\ -6.8954 \times 10^4 - 4.1630 \times 10^5 i & 7.8514 \times 10^6 + 1.8467 \times 10^5 i & ... \\ 3.7649 \times 10^7 + 2.7832 \times 10^6 i & 2.5038 \times 10^5 + 2.0941 \times 10^5 i & ... \end{bmatrix} \quad (4.3)$$

$$\begin{bmatrix} ... & -6.8954 \times 10^4 + 4.1630 \times 10^5 i & 3.7649 \times 10^7 - 2.7832 \times 10^6 i \\ ... & 7.8514 \times 10^6 - 1.8467 \times 10^5 i & 2.5038 \times 10^5 - 2.0941 \times 10^5 i \\ ... & 9.0986 \times 10^6 & -1.3192 \times 10^5 - 4.2386 \times 10^5 i \\ ... & -1.3192 \times 10^5 + 4.2386 \times 10^5 i & 6.7629 \times 10^7 \end{bmatrix}$$

So we calculate the known parameters as,

$$\begin{aligned}
&\left\langle |S_{VV}|^2 \right\rangle_{new} = 41436091.6223 \\
&\left\langle |S_{HH}|^2 \right\rangle_{new} = 55394433.4426 \\
&\Re\left(\langle S_{HH} S_{VV}^* \rangle\right)_{new} = 28917797.4542 \\
&\Im\left(\langle S_{HH} S_{VV}^* \rangle\right) = -2783221.5787 \\
&r = 0.0545
\end{aligned} \tag{4.4}$$

By substituting these values in equation 3.36 one can calculate

$$\begin{aligned}
&5102244585965.9737\beta^4 - 7121601952429.7375\beta^3 \\
&\quad - 1672478019215099.8000\beta^2 - 7746322356237.7475\beta^2 \\
&\quad + 2485044254265.6500\beta^2 + 23019679352.3089\beta^2 \\
&\quad + 3203770012776967.7000\beta - 3068543256426751.4000 = 0
\end{aligned} \tag{4.5}$$

And the roots for equation 4.5 are $(11.4242{+}2.2286{\times}10^{-39}i, 1.9549{+}4.1852{\times}10^{-38}i, 1.9347{-}4.2953\times10^{-38}i, -13.9181-1.1279\times10^{-39}i)$. In this case we assume that the small imaginary parts are zero and therefore the roots are $(11.42, 1.95, 1.93, -13.92)$.

β could not be negative and therefore the selection should be made on the three remaining positive roots. We call these positive real part complex roots with small imaginary parts *good complex roots*. Multiple good complex roots will introduce a difficulty as to which root is the real answer. This group of answers is positioned in c.6 class in table 4.3. Although the number of these cases was only 8 in all of the processed images, our algorithm cannot provide a single solution to those cases. Thus they are the weak point of this algorithm.

Multiple complex roots could also result in a single positive complex root with the rest of the roots having either negative real part with small imaginary part or just being simply complex values. These cases are also observed and classified as c.1, c.2, c.3, c.4, or c.5 based on the resulted span values. Very rare but also possible are the cases when no good

complex root were detected. These cases will be classified as c.7 class in table 4.3. Multiple roots could also simply occur because of the error propagation and computational errors. According to the complex conjugate root theorem if the coefficients of a polynomial are real, then the non-real roots appear in conjugate pairs. Therefore the example provided for multiple roots is most likely an estimation problem that needs to be fixed rather than a physical phenomenon but further analysis is necessary.

Reduction of RFD's Multiple Roots

In order to reduce the number of multiple roots an *H/α based criteria* has been defined. It basically counts the number of occurrences of the pixels in different H/α zones for each agricultural field. After summation over zones with the same scattering mechanism (e.g., $n_{IX} + n_{VI}$ for surface scattering), the mechanism with maximum number of occurrences is assumed to be dominant. Also for each multiple root, the RFD spans were calculated. A multiple roots that had the same maximum span mechanism as the H/α criteria mechanism would pass this test. This did not improve our results drastically in the 113 fields, thus we tested this idea on a wider range of fields.

In order to analyze the behavior of the roots and the effectiveness of the H/α criteria, table 4.4 were produced. The first two columns of this table are RADARSAT-2 scenes acquisition date and the beam type while total number of polygons has been provided in the third column. The total number of fields with two multiple roots are provided in 4th and 7th column for before and after applying the H/α's criteria. The same could be said for 5th and 8th column for three multiple roots. While four multiple roots as it could be seen in $6^{th}$and 9^{th} column were empty. The total number of fields for each date is generally larger than 113 fields. Table 4.4 shows clearly that H/α criteria reduced the number of multiple roots, but it did not completely removed them. There are still multiple roots for some fields that have same dominance based on H/α criteria and the resulted RFD spans.

The physical reason for the existence of multiple roots is unclear. A hypothesis is that

Table 4.4: Multiple Roots behavior with applying H/α criteria

Date	Beam Type	No. of fields	Before applying H/α criteria (Number of multiple roots)			After applying H/α criteria (Number of multiple roots)		
			II	III	IV	II	III	IV
2009_09_15	FQ16	113	0	5	0	0	5	0
2009_09_18	FQ5	383	1	2	0	0	2	0
2009_10_09	FQ16	404	1	19	0	2	17	0
2009_10_12	FQ5	381	0	0	0	0	0	0
2009_10_15	FQ19	367	0	0	0	0	0	0
2009_11_02	FQ16	405	3	17	0	9	10	0
2009_11_05	FQ5	383	0	2	0	2	0	0
2009_11_08	FQ19	367	7	1	0	0	1	0

multiple roots are due to homogeneity pre-condition of RFD. For simple illustration, let us assume that we have two different surface scattering levels in one field. Equations that solve β then face two different values for β and therefore they produce multiple values. But exceptions to this case were observed in chapter 5 where field (350101101) with probably two different scattering mechanisms did not produced any multiple roots.

4.4.3 Negative Spans

Negative powers are nothing new to Freeman-Durden algorithm[79][80][2]. Yajima et al. [79] believes that although the number of negative cases is generally low but they are mostly related to man-made structures. The main reason for these negative span cases are large values of $|S_{HV}|$ in the scattering matrices in comparison to $|S_{HH}|$ or $|S_{VV}|$. Yamaguchi [80] believes that the fundamental idea to avoid this situation is to use the $2\left\langle|S_{HV}|^2\right\rangle$: $\left\langle|S_{HH}|^2\right\rangle$ *or* $\left\langle|S_{VV}|^2\right\rangle$. He believes that experimentally co-pol radar channel power and cross-pol channel power are statistically of the magnitude ratio of 2 : 1. Yajima[79] on the other hand classifies the negative power cases to three categories of 1)$P_v < 0$, 2) $P_v + P_c >$ *total power*, and 3)$P_s < 0$ or $P_d < 0$. His algorithm is a follow up to Yamaguchi's[81] four

component decomposition where P_c is for the circular polarization power coming from helix like scatterers. He mentions that negative P_v is mainly from residential and man-made areas. And $P_v + P_c > total\ power$ happens when volume scattering is dominant and it is the case for forest, some crop fields, and oriented urban blocks. Last but not the least in his classification are the cases of $P_s < 0$ or $P_d < 0$. He believes that these cases are due to setting either $\alpha = 0$ or $\beta = 0$. In our case we could not have the first or second class since volume span is always positive in our algorithm and the helical scatterers (mostly representing man-made objects) should not be dominant features in agricultural fields. As for the third class Yajima performs the following power corrections: If $P_s < 0$, then $P_s = 0$ and $P_d = Total\ Power; P_v - P_c$ and if $P_d < 0$, then $P_d = 0$ and $P_s = Total\ Power; P_v - P_c$.

In all the 904 (113×8) calculation instances in table 4.3 only 15 fields had negative spans. In order to tackle this problem, we took Yajima's[79] approach. Since no helical component exist in our model, after assuming that the negative power would become zero we simply calculated the other power based on the rest of the equations. For case of negative f_s, the f_s was assumed to be zero. Thus equation 3.27c, ($\left\langle |S_{VV}|^2 \right\rangle_{new} = f_s + f_d$) provides us with an estimate of f_d. Also for case of negative f_d, the f_d was assumed to be zero. And therefore equation 3.27c once again provides us with an estimate of f_s.

4.5 RFD Processing Results in Comparison to OFD

RFD algorithm uses the same physical model as OFD algorithm, therefore it is important to investigate the independence of our proposed RFD algorithm. In this section we observe the differences and similarities of these two algorithms in terms of their span results and processing routes. Based on November 2^{nd} data, table 4.3 had both multiple roots and negative spans, therefore we choose this date to compare the results.

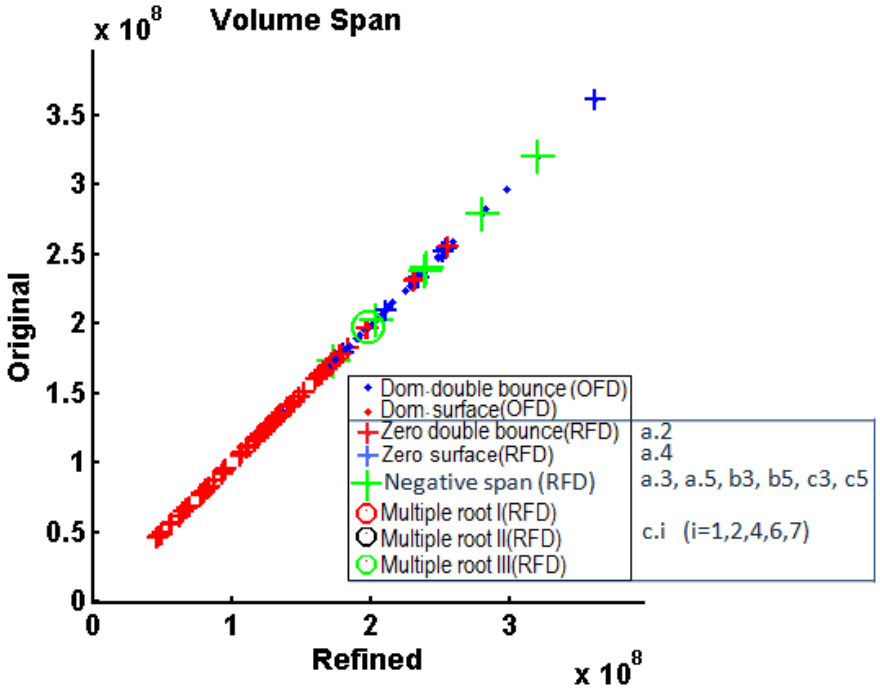

Figure 4.5: The volume scattering span of OFD versus RFD observed on November 2^{nd} by RADARSAT-2. The symbols are processing routes for both methods.

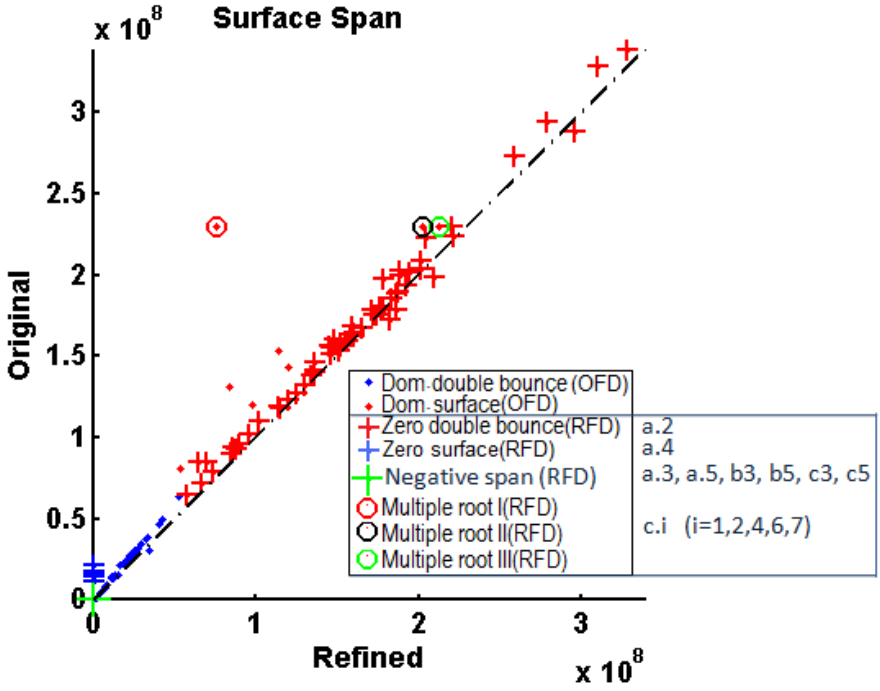

Figure 4.6: The surface scattering span of OFD versus RFD observed on November 2^{nd} by RADARSAT-2. The symbols are processing routes for both methods.

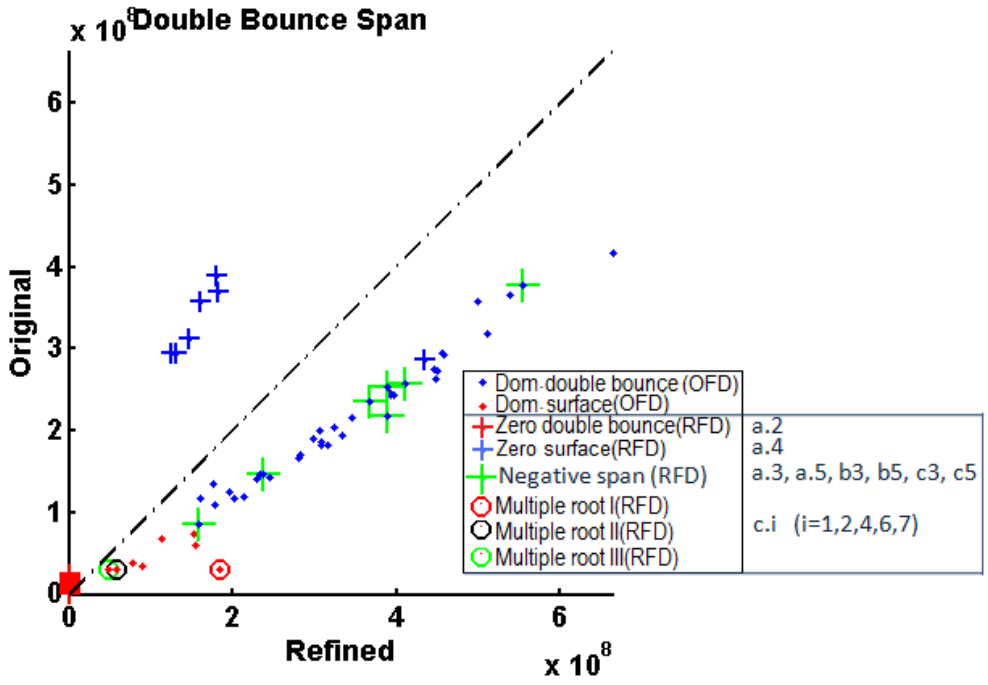

Figure 4.7: The double-bounce scattering span of OFD versus RFD observed on November 2^{nd} by RADARSAT-2. The symbols are processing routes for both methods.

Figure 4.5 shows that there is a one to one relationship between OFD and RFD's volume scattering. This was expected as both methods use the same input and equation for calculating volume scattering span, but figures 4.6 and 4.7 show that surface and double-bounce spans have different stories to tell for these two algorithms. Every point on these plots shows two information based on RFD (circum-symbol) and OFD (in-symbol) results. For example there are fields that have circum-symbols (e.g. green cross sign form the legend) from RFD with in-symbols of colored dots inside of them from OFD. Also there are fields that have only single dots.

Out of 113 fields, 36 fields had a.1 processing routes. These fields are presented by blue or red dots (with no circum-symbol). The color difference is because of the OFD processing routes rather than the RFD algorithm. Therefore the blue dots close to the $x = y$ line are polygons that have dominant even bounce (double-bounce scattering) by OFD's algorithm. The a.1 fields are generally following a center passing line in both surface and double-bounce scattering. But these lines do not necessarily coincides with $x = y$ line.

Sixty two red cross signs have a.2 (no double-bounce scattering) processing route. The red dots inside those red cross signs are evident of correct assignment for dominant surface scattering by OFD. Thus these fields are accumulated on the y-axis of figure 4.7. Relatively small double-bounce values, in this figure shows that in this especial date the double-bounce values estimated by original Freeman-Durden had also small double-bounces for these fields. But this is not the case for some other dates and therefore we believe that this is not a general trend. In terms of surface scattering, figure 4.6, a.2 fields are gathered along the equality line ($x = y$) and thus predicted very closely by both methods. Although angular deviation and sometimes clustering have also been observed for a.2 fields on surface scattering plots, but majority of the fields in different dates followed the aforementioned trend.

There were no instances of a.3 (negative double-bounce scattering) processing route on this data. If there was any, there would present themselves as green cross signs on the y-axis of double-bounce scattering scatter-plot (figure 4.7), and they could have been anywhere on surface scattering scatter-plot.

The seven blue cross signs are the fields that take a.4 (no surface scattering) processing route, and thus they have dominant double-bounce scattering. This also confirmed by the OFD algorithm trough the existence of blue dot signs inside each blue cross sign. 'Zero' surface scattering in RFD (route a.4) results in blue cross signs accumulated on the y axis of figure 4.6. This pattern was also a general trend.

Only seven fields had a.5 (negative P_s ,i.e, $P_s < 0$) processing routes. These fields are observable with green cross circum-signs in figures 4.5, 4.6, and 4.7. The volume scattering calculation is the same process for both method thus all the results are aligned on the $x = y$ line (equality line) which demands an equal value by both RFD and OFD algorithms. But since they have moved to zero in P_s (see section 4.4.3), they have aligned on the y axis of the figure 4.6. The interesting observation is that they had the same rotational behavior of the OFD's dominant double-bounce (even bounce) scattering on figure 4.7. This observation

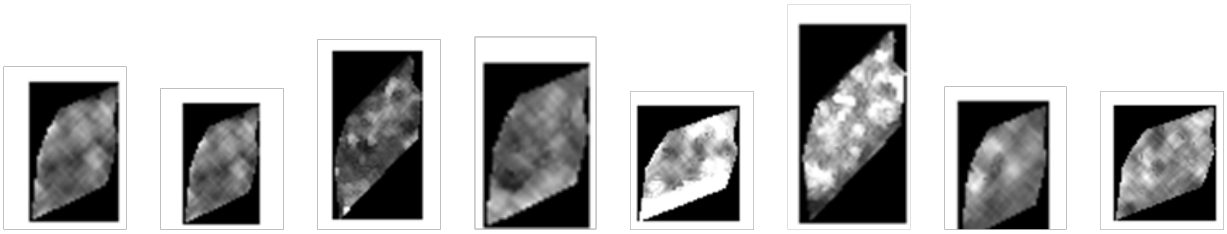

(a) (b) (c) (d) (e) (f) (g) (h)

Figure 4.8: The $|S_{HH}|^2$ image of field 350101259 in (a)09/15/2009, (b)09/18/2009, (c)10/09/2009, (d) 10/12/2009, (e) 10/15/2009,(f) 11/02/2009, (g) 11/05/2009, and (h) 11/08/2009

was also a general trend and it showed that transforming negative spans to zero probably did not introduce a large error to the calculation of the other span.

As we mentioned earlier there are no observation of b.i (i=1,2,...,6) series in any of our polygons, therefore no comments are provided for these possibilities in RFD algorithm. Circle circum-symbols represent c.i (i=1,2,...,7) series. The green circle observable in figure 4.5 represents the existence of a single multiple roots among the observed fields. This observation is more distinct where the three green, black, and red circles are evident in figure 4.6, and it shows that the aforementioned field had three multiple roots. The gradual movement of these roots toward the equality line is also observable and the red dot in their center is due to the dominance of surface scattering detected by OFD. The multiple roots field is field number 350101259 and it has been presented by figure 4.8 on the eight RADARSAT-2 image acquisitions. On figure 4.8(f), field 350101259 clearly has a wide range of HH backscattering coefficient and therefore the postulate that inhomogeneous fields may produce multiple roots holds true for this field.

In summary, volume scattering spans are the same for both RFD and OFD. As for double-bounce and surface scattering, these too methods produce similar values for some fields but in comparison they could both underestimate and overestimate in respect to each other. Therefore we believe that since our RFD method will produce different results in terms of surface and double-bounce scattering, it could generate substantially different results from

Class Abbreviation	Class description
CC	Cropped fields of Corn
CS	Cropped fields of Soybeans
HC	Harvested fields of Corn
HS	Harvested fields of Soybeans
PC	Partially harvested fields of
PS	Partially harvested fields of
NC	No Crop

Table 4.5: Class name abbreviations used for classifications

OFD.

4.6 Implemented Unsupervised Classifications

In order to understand the nature of the data and the behavior of different crops, some baseline unsupervised polarimetric classifications have been implemented. Some information regarding these algorithms is provided in section 2.1.7. The field data provided to this project shows that there are seven classes of interest. For the sake of simplicity an abbreviation of these classes is presented in Table 4.5.

The first step in SAR classification is preprocessing. Therefore speckle filtering described in 4.1.1 was performed on the SAR data and since all the classifications were performed in slant range-azimuth coordinate system therefore vector files were registered as it was described in section 4.1.2. The implemented unsupervised classifications are as follows:

- General K-means Wishart

  The classification was performed with 8 classes and maximum of 10 iterations.

- H/α segmentation

  Each region in H/α feature space produces a single class. Therefore eight classes is the result of this segmentation.

- H/A and α unsupervised K-means Wishart

  The classification was performed with 8 classes and maximum of 10 iterations.

- Expectation Maximization

  The classification was performed with 8 classes and maximum of 10 iterations.

- Expectation Maximization with Probabilistic Label Relaxation (EM-PLR)

  The classifications were performed with 8 classes, 20 iterations (K=20) for 10 times more probable labels (for more information please refer to [62])

  The classifications were also performed with 16 classes, 20 iteration (K=20) for 10 times more probable labels

After the results of an unsupervised classification was available a labeling procedure were performed so that each unsupervised class would acquire one of the seven labels from Table 4.5. Then the classes with the same name were merged together in order to calculate the confusion matrix. A description of such a process is described the Appendix F.

All the implemented classifications were pixel based. Then two different labeling processes were performed. The first one used all the statistical information of all the pixels in the same class and assigned a label to all of them. The result of this process was pixel based labeling. The other labeling process used all the statistics of all the pixels inside a certain field and attributed a label to that certain field. A detailed description of an example for this process is presented in Appendix F.

Table 4.6 lists all the performed classifications along with their total number of classes, accuracy, and κ coefficients. Although for each date we did not perform all the possible classifications but table 4.6 roughly shows that these conventional polarimetric classifications were not satisfactory. The highest accuracy achieved was 73% for field-based labeled EM-PLR

Table 4.6: Performed unsupervised classifications results

Classification type	Date	classes	Accuracy(%)	κ
Pixel based labeling				
EM-PLR(N=10,K=20)	9/18/2009	4	28.212	0.0883
EM-PLR(N=10,K=20)	10/9/2009	4	24.8844	0.0964
EM-PLR(N=10,K=20)	10/12/2009	6	37.3748	0.1916
EM-PLR(N=10,K=20)	10/15/2009	5	69.7937	0.549
EM-PLR(N=10,K=20)	11/2/2009	5	12.5458	0.0754
EM-PLR(N=10,K=20)	11/5/2009	5	16.816	0.1031
EM-PLR(N=10,K=20)	11/8/2009	6	52.2375	0.2991
Wishart General	10/15/2009	4	52.9002	0.3259
Wishart General	11/2/2009	6	24.2746	0.1534
Wishart General	11/5/2009	3	24.8589	0.1452
Wishart General	11/8/2009	6	28.4771	0.1722
Wishart HaA	10/15/2009	4	45.9554	0.1873
Wishart HaA	11/2/2009	6	26.1702	0.1585
Wishart HaA	11/5/2009	5	19.4787	0.116
Wishart HaA	11/8/2009	6	32.0383	0.2039
EM	10/15/2009	4	41.1056	0.1916
EM	11/5/2009	4	47.025	0.2867
EM	11/8/2009	3	53.5449	0.2835
HaA Segmentation	10/15/2009	5	38.7968	0.2517
HaA Segmentation	11/5/2009	4	24.8553	0.1453
HaA Segmentation	11/8/2009	6	42.0559	0.2881
Field-based labeling				
EM-PLR(N=10,K=20)	10/15/2009	3	73	0.46
EM-PLR(N=10,K=20)	11/5/2009	4	39.0202	0.2361
EM-PLR(N=10,K=20)	11/8/2009	3	67.9114	0.5304
Wishart General	11/8/2009	3	32.1964	0.168
Wishart HaA	11/2/2009	5	38.4221	0.2747
EM	11/8/2009	2	63.3107	0.2728

on October 15^{th} of 2009. Some of these higher accuracy classification results had produced too few classes (e.g., three classes out of seven possible classes for the aforementioned classification). The κ coefficient were generally low with highest achieved on field-based labeled EM-PLR on November 8^{th}. This shows that most of the classifications were on the side of random assignment. On the other hand no single classification is the best for our problem. For example while on October 15^{th} among the pixel based classifiers EM-PLR produced the best results, the same classification performed worst for the November 2^{nd}.

Table 4.7: The effect of field-based versus pixel based labeling over accuracy and κ coefficient

		Before			After field-based labelling		
Type	Date	Classes	Accuracy(%)	κ	Classes	Accuracy(%)	κ
EM-PLR	10/15/2009	5	69.79	0.55	3	73	0.46
Wishart HaA	11/02/2009	5	26.17	0.15	5	38.42	0.27
Wishart General	11/05/2009	5	16.82	0.1	4	39.02	0.23
EM_PLR	11/05/2009	6	52.24	0.3	3	67.91	0.53
EM	11/05/2009	3	24.86	0.15	3	32.2	0.17
EM_PLR	11/08/2009	4	47.03	0.29	2	63.31	0.27

As it can be seen from table 4.7, field-based labeling tends to decrease the number of classified classes but on the other hand increases the accuracy of the classifications. The reason might be that the field-based classifications were only labeled the pixel based classifications and in nature they are still pixel based. Therefore it might be necessary to perform the field-based classifications rather than the pixel based ones. This idea also is one of the backbones of introducing RFD algorithm as a field oriented method.

As a field-based labeled classification result, table 4.9 shows that H/α Wishart classier for November 2^{nd} classified only 22.57% of the cropped corn fields while it had been 100 percent accurate. And cropped soybeans has similar situation to cropped corn only more accurate. On the contrary, most of the harvested corns were classified as harvested corn (96.73% producer's accuracy) but low user's accuracy shows that other types of fields from different classes were also wrongfully classified as harvested corn fields. The low overall accuracy and κ suggest that this classification was not a success. This could be because of

higher number of classes as chances for error becomes higher.

Table 4.8: Final assessment results of unsupervised EM-PLR with 10 times more probable, K=20 of 10/15/2009 with the field data of the 10/15/2009.

Class	Prod. Acc. (Percent)	User Acc. (Percent)	Prod. Acc. (Pixels)	User Acc. (Pixels)
CC	70.57	100	175914/249289	175914/175914
NC	96.89	70.9	43803/45211	43803/61779
HC	39.8	8.4	4989/12535	4989/59424
Overall Accuracy =			(224706/307035) =	73.19%
Kappa Coefficient =				0.4608

Table 4.9: Final assessment results of H/A and α unsupervised K-means Wishart classification of 11/02/2009 with the field data of the 11/04/2009.

Class	Prod. Acc. (Percent)	User Acc. (Percent)	Prod. Acc. (Pixels)	User Acc. (Pixels)
PC	41.11	13.01	8761/21313	8761/67343
HC	96.73	18.86	25011/25857	25011/132637
CS	58.04	86.99	28936/49851	28936/33265
CC	22.57	100	40205/178108	40205/40205
NC	45.6	57.08	17770/38969	17770/31132
Overall Accuracy =			(120683/314098) =	38.42%
Kappa Coefficient =				0.2747

If cropped corn and cropped soybeans classes would be extracted, we could assume that the rest of fields are harvested. The usage of these field- based classifications with the method we described in Appendix F were not satisfactory for cropped corn or cropped soybeans classification because we do not have any control on the outcome of classification classes. For example the tables 4.12 and 4.11 did not have any cropped corn class. As for the cropped soybean, the number of unclassified cases increases to three tables of 4.8, 4.11, and 4.13. Therefore low performance and uncertainty about classifying the proper classes for unsupervised classifications leaded us to propose our RFD algorithm to perform the automatic classification of harvested (or cropped) fields.

Table 4.10: Final assessment results of unsupervised EM-PLR with 10 times more probable, K=20 of 11/05/2009 with the field data of the 11/04/2009.

Class	Prod. Acc. (Percent)	User Acc. (Percent)	Prod. Acc. (Pixels)	User Acc. (Pixels)
CC	69.94	99.24	15069/21545	15069/15184
CS	85.08	34.43	27991/32900	27991/81301
HC	9.88	23.33	1102/11150	1102/4724
HS	11.63	100	7882/67782	7882/7882
Overall Accuracy =			(52044/133377) =	39.02%
Kappa Coefficient =				0.2361

Table 4.11: Final assessment results of unsupervised EM classification of 11/05/2009 with the field data of the 11/04/2009.

Class	Prod. Acc. (Percent)	User Acc. (Percent)	Prod. Acc. (Pixels)	User Acc. (Pixels)
PC	87.68	61.95	13576/15483	13576/21916
HS	60.08	98.37	70160/116779	70160/71320
Overall Accuracy =			(83736/132262) =	63.31%
Kappa Coefficient =				0.2728

Table 4.12: Final assessment results of unsupervised general Wishart classification of 11/05/2009 with the field data of the 11/04/2009.

Class	Prod. Acc. (Percent)	User Acc. (Percent)	Prod. Acc. (Pixels)	User Acc. (Pixels)
HS	9.85	100	11504/116779	11504/11504
PC	95.18	20.44	14736/15483	14736/72078
CS	77.37	36.27	27991/36176	27991/77181
Overall Accuracy =			(54231/168438) =	32.20%
Kappa Coefficient =				0.168

Table 4.13: Final assessment results of unsupervised EM-PLR with 10 times more probable, K=20 of 11/08/2009 with the field data of the 11/12/2009.

Class	Prod. Acc. (Percent)	User Acc. (Percent)	Prod. Acc. (Pixels)	User Acc. (Pixels)
CC	47.06	89.76	22335/47458	22335/24884
NC	97.67	100	18508/18950	18508/18508
PC	85.72	46.6	20481/23892	20481/43949
Overall Accuracy =			(61324/90300) =	67.91%
Kappa Coefficient =				0.5304

Chapter 5

Result and Discussion for Corn

The development and implementation details of the RFD algorithm were discussed elaborately in previous chapters. The question is how well this algorithm could perform in a real case scenario such as corn fields. In order to relate the RFD results to the field observations we further introduce a roughness parameter, which not only enhance our ability to discern corn fields but also it provides us with a more in depth understanding of both RFD results and the undergoing field phenomenon. All the results in this chapter are based on a refined Lee 11×11 window size speckle filtered image that gone through the process depicted on figures 4.4 and 3.5.

5.1 Surface Roughness versus RFD Surface Scattering

The span values calculated in RFD algorithm were extremely large numbers and they did not portray the familiar range of negative to positive tens of dB associated with power. Therefore we defined the relative surface span based on equation 5.1,

$$R_{P_s} = 10 \times log \overset{norm}{P}_s = 10 \times log \frac{4 \times P_s}{(P_v + P_s + P_d)} \tag{5.1}$$

where the denominator normalizes the span values, so different fields are comparable no matter how many pixels they have. Also the 4 multiplier is due to the fact that estimated powers are four times the normal power values[23].

We plotted the surface span against our defined roughness parameter, H_{rough} (equation 3.4). In order to present the underlying idea of the figure 5.1(a) we added two lines (figure 5.1(b)) that highlights the general behavior of the fields. As roughness in the surface increases (from -1 to 0.7), the mathematical relationship between H_{rough}, described by equation 3.4,

and the relative surface span power is a relatively vertical line with negative slope. Therefore up to some degree, surface span is related logarithmically to the introduced roughness measure.

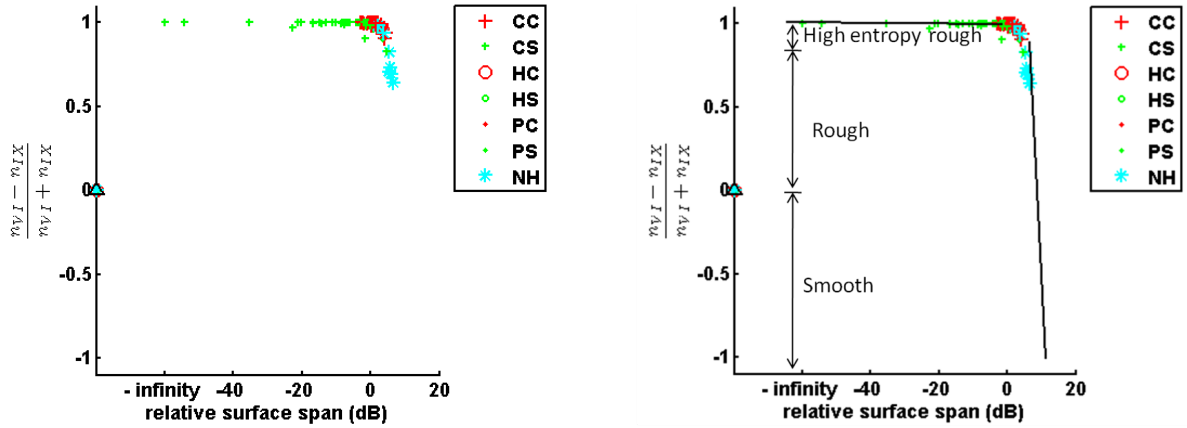

(a) (b)

Figure 5.1: The relative surface span of RFD versus H_{rough} of the fields observed on the September 15^{th} RADARSAT-2 image in (a), and (b) has the two added trend lines. The symbols represent different crop/harvest situation based on ground observations on September 21^{th}. CC, CS, HC, HS, PC, PS, and NH stands for Cropped Corn, Cropped Soybean, Harvested Corn, Harvested Soybean, Partially harvested Corn, Partially harvested Soybean, and No crop/Harvest situation.

From 0.7 to 0.9, H_{rough} has a transition curve with two relatively perpendicular ends. The second line describes the relation between H_{rough} and relative surface span in 0.9 to 1 (higher entropy rough surfaces) region of H_{rough}. In this region, the close to horizontal line that imitates our results shows a fast drop on surface span. This situation is somewhat expected. We believe that this is the same concept of going toward randomness that Cloude and Pottier [13] mentioned where increase in roughness will impede our ability to measure surface roughness. For further details please refer to zone III on H/A/α descriptions.

In figures 5.1, 5.2, and 5.3 while red symbols belongs to corn fields, the green ones are soybeans fields. Some blue signs are also observable that belongs to the fields that no cultivation practice was ongoing. The cross signs belong to cropped fields while the circle signs are harvested fields and dots belongs to partially harvested fields.

Relative surface span versus H_{rough} plots shows that soybeans follows the two above-

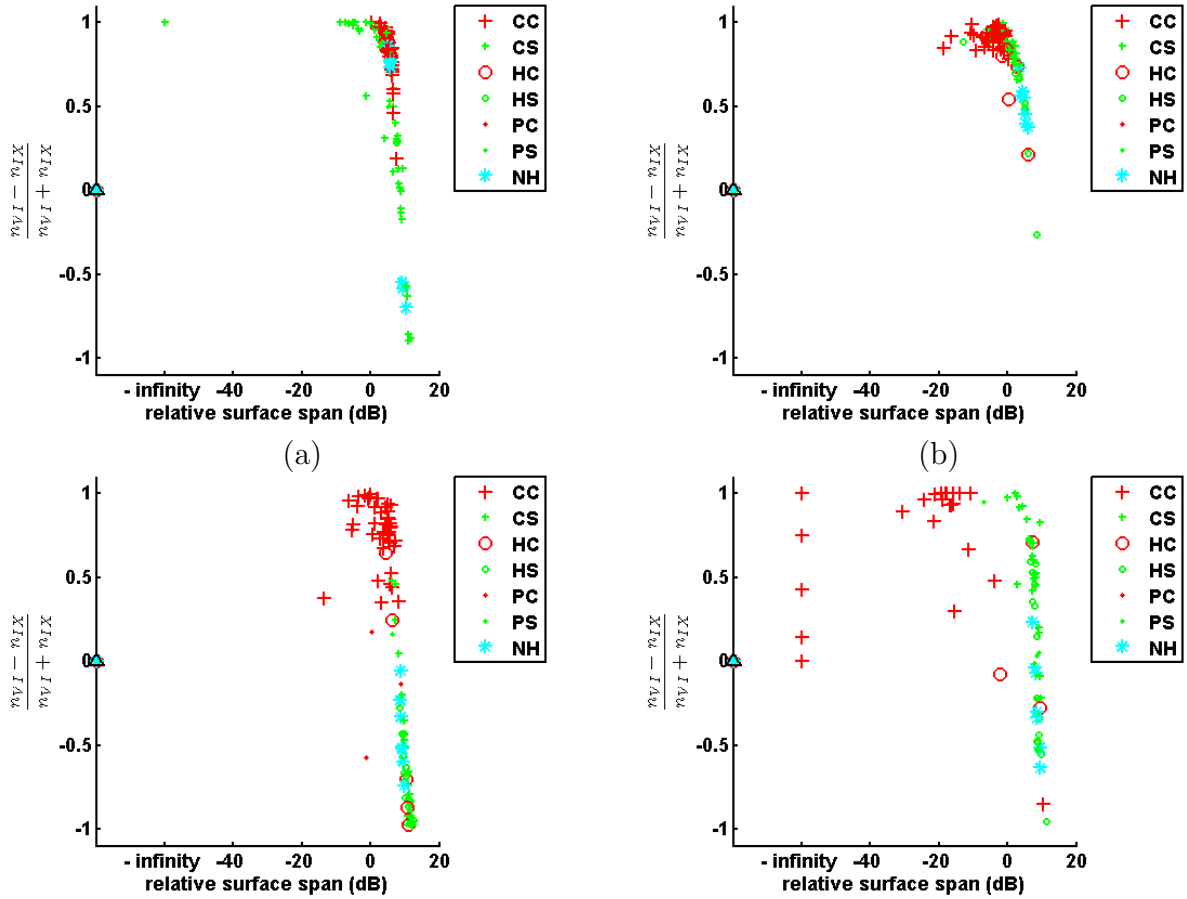

Figure 5.2: The relative surface span of RFD versus H_{rough} of the fields observed on (a) September 18^{th}, (b) October 9^{th}, (c) October 12^{th}, and (d) October 15^{th} RADARSAT-2 image. The symbols represent different crop/harvest situation based on (a) September 21^{th}, (b) and (c) October 13^{th}, and (d) October 15^{th} ground observations. CC, CS, HC, HS, PC, PS, and NH stands for Cropped Corn, Cropped Soybean, Harvested Corn, Harvested Soybean, Partially harvested Corn, Partially harvested Soybean, and No crop/Harvest situation

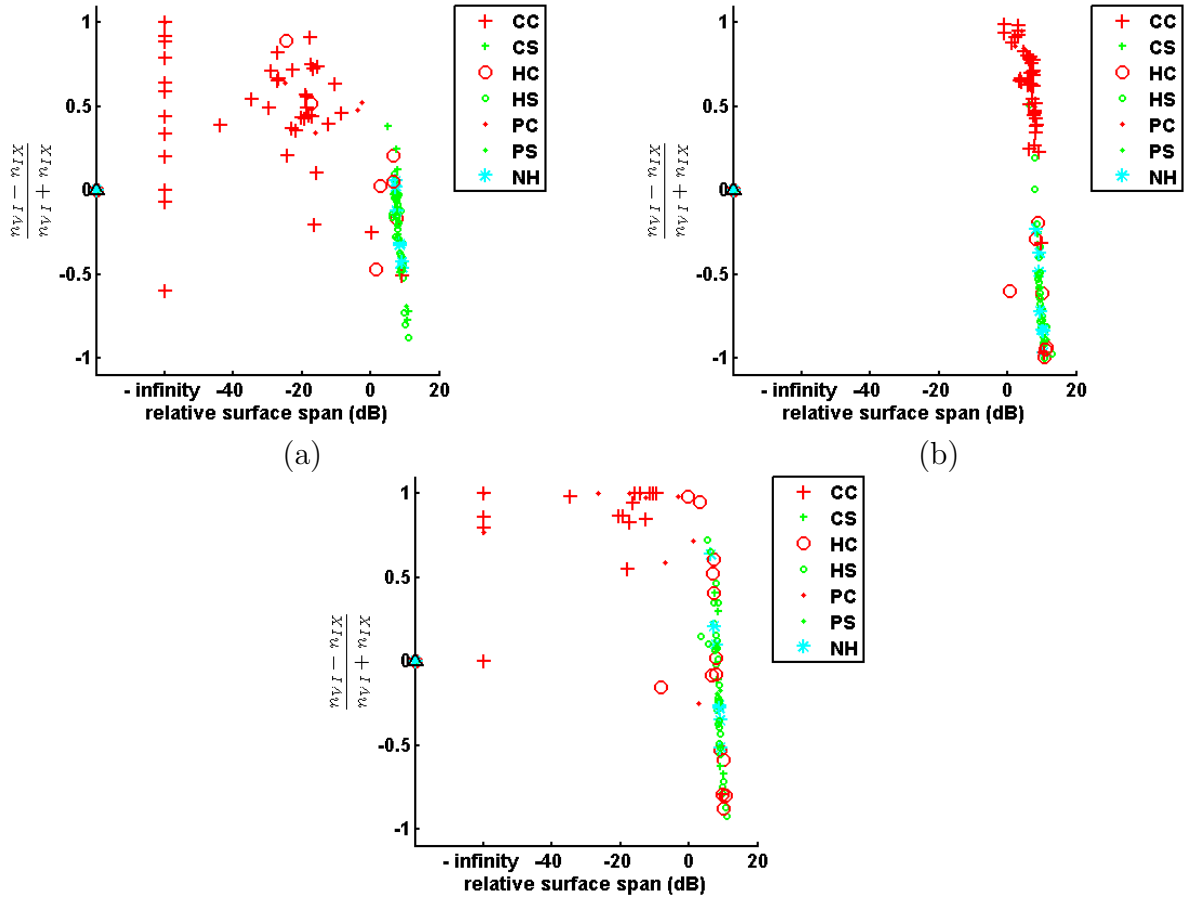

Figure 5.3: The relative surface span of RFD versus H_{rough} of the fields observed on (a) November 2^{nd}, (b) November 5^{th}, and (c) November 8^{th} RADARSAT-2 image. The symbols represent different crop/harvest situation based on (a) and (b) November 4^{th}, and (c) November 9^{th} ground observations. CC, CS, HC, HS, PC, PS, and NH stands for Cropped Corn, Cropped Soybean, Harvested Corn, Harvested Soybean, Partially harvested Corn, Partially harvested Soybean, and No crop/Harvest situation

mentioned trends, the soybeans fields (green symbols) have a gradual increase in their smoothness as they get closer to -1. Meanwhile figure 5.1(a) through 5.3(c) shows that soybean's surface scattering increases throughout the observed time period. And also there is no perceivable difference in smoothness between cropped and harvested soybeans fields in any of the plots. This lack of difference unfortunately has been also observed for different parameters in chapter 6.

Negative infinite relative surface spans that does not follow the aforementioned trends are first appear in figure 5.2(d). The negative infinity implies that these cropped corn fields have only a few pixels in surface scattering portion of H/α sub-space and therefore the calculated H_{rough} values are irrelevant. In comparison to soybeans fields, the cropped corn fields most of the time exhibit high entropy behavior, while harvested corn fields are significantly smoother. For example in figure 5.2(c) most of the harvested corn fields are on the vertical line trend while cropped corn fields are only partially on the horizontal line and mostly have $H_{rough} > 0.5$. The higher values of roughness makes the surface scattering span behave rather more chaotic and therefore instead of surface scattering, maybe double-bounce scattering can provide more insight to the cropped corn fields.

5.2 Corn Fields in H/α Sub-space

Surface scattering from standing corn fields have values toward rougher side of the H_{rough}. In figure 5.4(a) low entropy surface (Zone IX) scattering is empty while medium entropy surface scattering has the largest portion of pixels. Gradually, entropy of surface scattering from corn become higher and since zone III is physically impossible other regions such as volume scattering becomes more dominant in figures 5.4(b), 5.4(c), and 5.4(d). In figure 5.4(e) the corn starts to dry and therefore radar wave is able to penetrate the canopy and reach the ground. This will produce double-bounce scattering where the double-bounce scattering zones (over 50° α angle) are detectable in figures 5.4(e), 5.4(f), and 5.4(h).

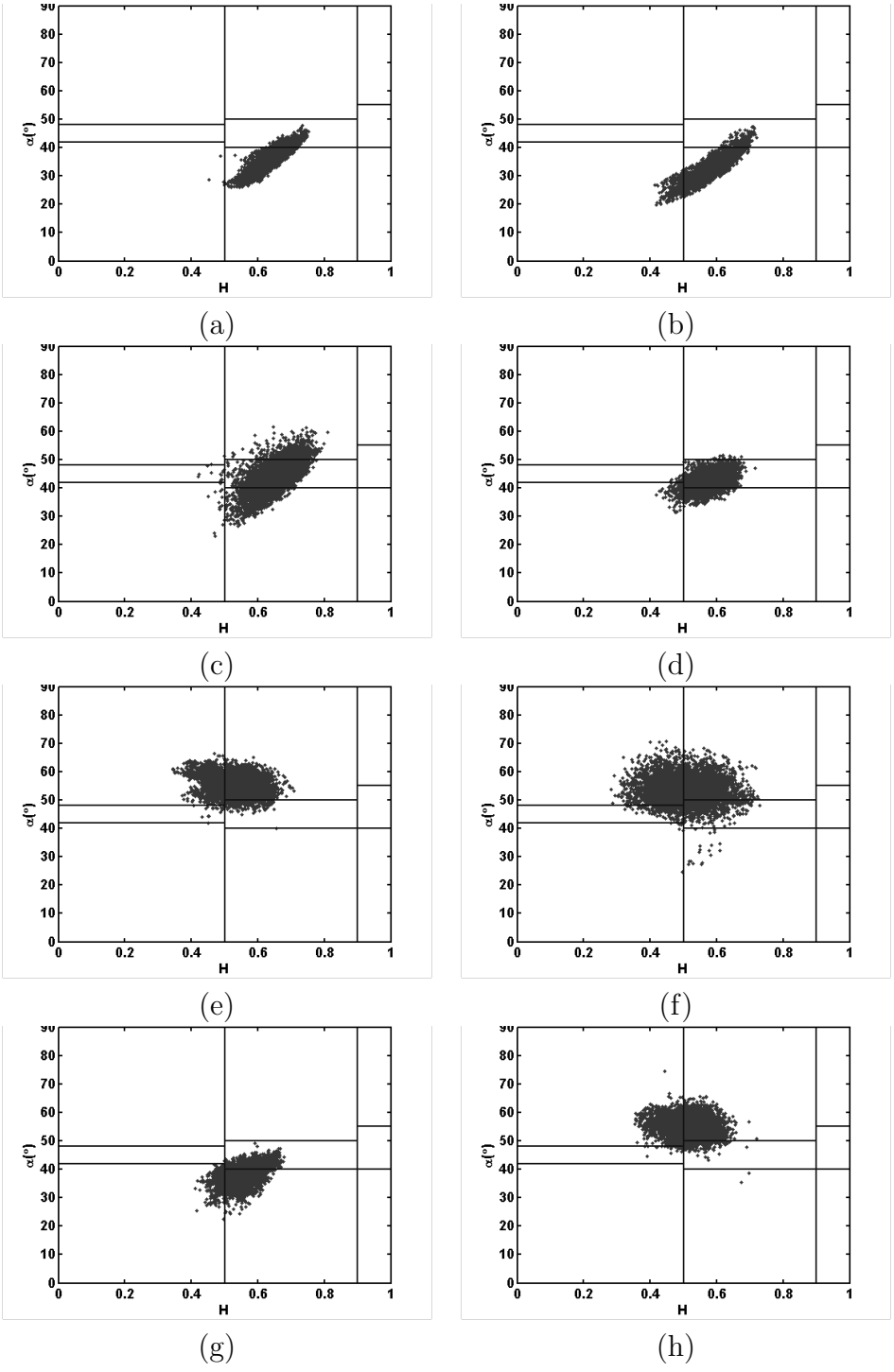

Figure 5.4: H/α sub-space behavior of a typical cropped corn in (a) 09/15/2009, (b) 09/18/2009, (c) 10/09/2009,(d) 10/12/2009, (e) 10/15/2009, (f) 11/02/2009, (g) 11/05/2009, and (h) 11/08/2009 RADARSAT-2 image.

It seems that November 5^{th}, October 12^{th}, and September 18^{th} defy the explanations regarding the double-bounce scattering in corn fields. We believe that the main reason for these dates not following the aforementioned patterns is the steep incidence angles. The steep incidence angle of FQ5 beam type figures make them inappropriate for double-bounce scattering observation but it enhances their ability to observe surface scattering. Therefore for these beam types we used H_{rough} for corn discrimination purposes. More information about the behavior of the other types of fields in H/α sub-space is provided in section 6.4.

5.3 Surface Roughness Vs. RFD Double-Bounce Scattering

As we have already established in the previous two sections, H_{rough} index is capable of highlighting cropped corn. On the other hand standing cropped corn is a very tall structure (up to 2m height) and thus when it is dry enough for the wave to penetrate through the dried leaves, considerable double-bounce scattering is expected. In order to distinguish cropped corn from rest of the fields, we plotted the relative double-bounce span described by equation 5.2 against H_{rough} index. This will exploit these two characteristics of cropped corn.

$$R_{P_d} = 10 \times log \overset{norm}{P}_d = 10 \times log \frac{4 \times P_d}{(P_v + P_s + P_d)} \tag{5.2}$$

In equation 5.2 the denominator normalizes the power values, so once again different fields are comparable no matter how many pixels they have, and the 4 multiplier is due to the fact that estimated powers are four times the normal power values[23]. Note that if P_d goes toward zero, R_{P_d} goes toward $-\infty$.

5.3.1 September 15^{th}

The results from September 15^{th} RADARSAT-2 image is considerably different from the rest of the images. The field observation prior to this date was not available and the closest ground observations were made on September 21^{th}. Based on these field measurements, there is no harvested corn field exists and therefore it is impossible to differentiate between cropped

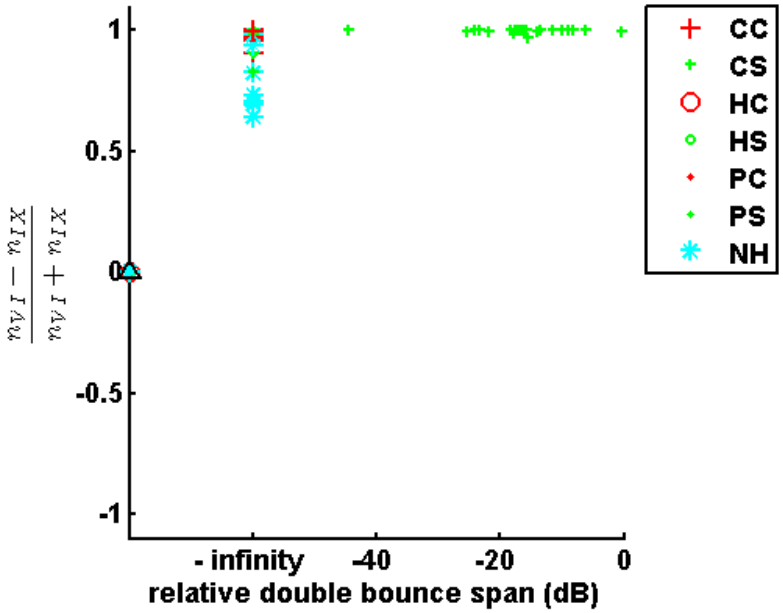

Figure 5.5: The relative double-bounce span of RFD versus H_{rough} of the fields observed on the September 15^{th} RADARSAT-2 image. The symbols represent different crop/harvest situation based on field observations on September 21^{th}. CC, CS, HC, HS, PC, PS, and NH stands for Cropped Corn, Cropped Soybean, Harvested Corn, Harvested Soybean, Partially harvested Corn, Partially harvested Soybean, and No crop/Harvest situation

and harvested corn fields. Similar to figure 5.4(a), all the cropped corn fields in figure 5.5 exhibit high entropy surface scattering behavior with medium entropy being dominant and no double-bounce what so ever. On this date the corn canopy should be in its full liveliness therefore volume scattering and medium entropy surface scattering is observable from the top of the canopy.

As for the soybeans fields, only one harvested field exists in the image. This field having zero double-bounce span and roughness around 0.9, has the same signature as of bare soil. Two cropped soybeans fields also had the bare soil signature, but rest of the cropped soybeans had very high entropy surface scattering with diverse double-bounce values. There are also three partially harvested fields in 21^{th}, but it is hard to decide whether or not they were partially harvested on the 15^{th}. Since only one harvested soybeans fields exist on September 15^{th} the discrimination between cropped and harvested soybeans is not possible. On the other hand next chapter is dedicated to soybeans fields therefore further details about these fields are mainly provided in the first three sections of the next chapter.

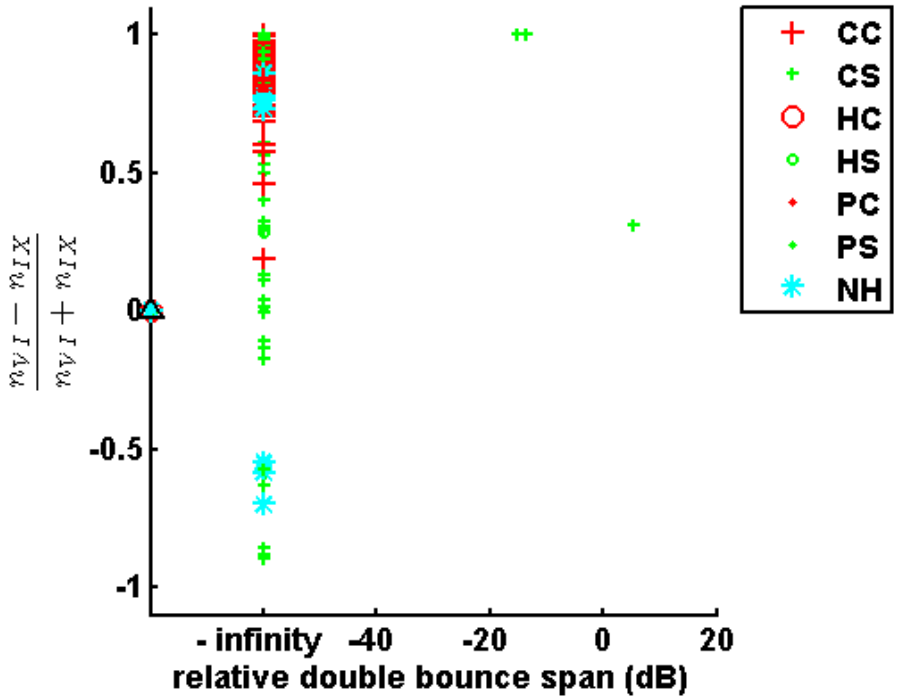

Figure 5.6: The relative double-bounce span of RFD versus H_{rough} of the fields observed on the September 18^{th} RADARSAT-2 image. The symbols represent different crop/harvest situation based on ground observations on September 21^{th}. CC, CS, HC, HS, PC, PS, and NH stands for Cropped Corn, Cropped Soybean, Harvested Corn, Harvested Soybean, Partially harvested Corn, Partially harvested Soybean, and No crop/Harvest situation

A double-bounce scattering needs to have either a considerable man made structure in the field or a wall of agricultural plants that stand stark in comparison to the fields next to them. It is highly unlikely that fields with no particular agricultural practice would produce any of the two situations. Based on our meta-data in the whole duration of observation there were seven fields that have "no crop" status all along. Therefore no crops fields (7 fields), had the same signature as the bare soil in having no double-bounce spans.

5.3.2 September 18^{th}

The September 18^{th} image had FQ5 beam type. The highly steep incident angle of this beam type reduces the amount of possible double-bounce scattering and enhances the sensitivity to surface scattering (figure 5.6). Since only one harvested field is available, it is not possible to perform any harvest detection. Cropped corns have rough (high entropy) surface scattering (

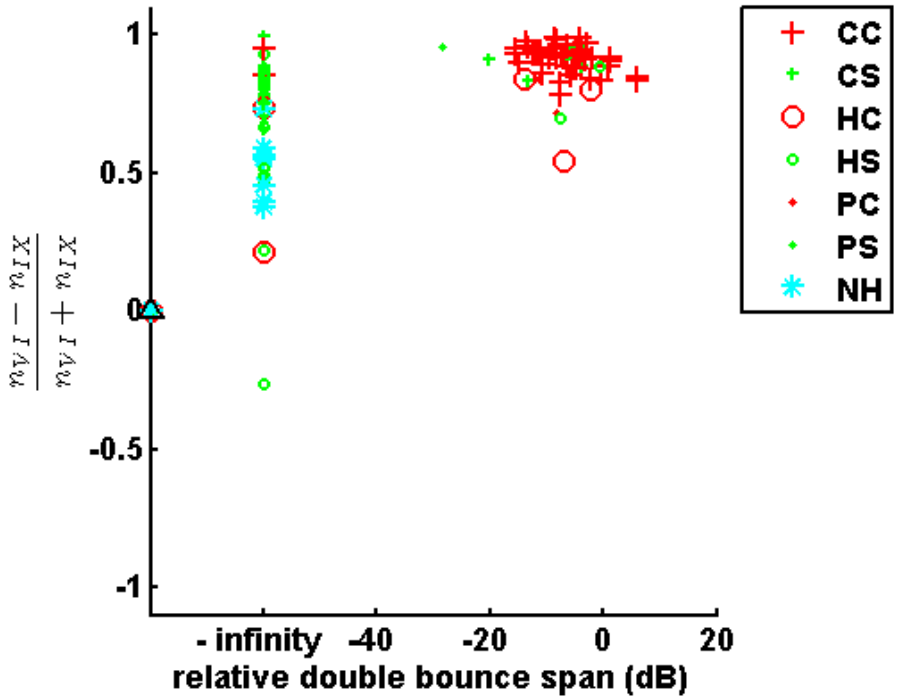

Figure 5.7: The relative double-bounce span of RFD versus H_{rough} of the fields observed on the October 9^{th} RADARSAT-2 image. The symbols represent different crop/harvest situation based on ground observations on October 13^{th}. CC, CS, HC, HS, PC, PS, and NH stands for Cropped Corn, Cropped Soybean, Harvested Corn, Harvested Soybean, Partially harvested Corn, Partially harvested Soybean, and No crop/Harvest situation

$0.18< H_{rough} <1$) with zero double-bounce while cropped soybeans fields have very different behaviors from very smooth ($H_{rough} = -1$) up to high entropy ($H_{rough} = 1$). Although some cropped soybeans fields still have double-bounce span values but as it is expected from the beam type, the majority of the fields have zero double-bounce spans. In this stage the leaves are almost dead and the water should be in the stalks but the steep incidence angle reduces the double bounce scattering dramatically 5.6.

The only harvested field is a soybeans with $H_{rough} = 0.28$ and zero double-bounce span. There are no partially harvested corn fields, and partially harvested soybeans are not distinguishable from cropped soybeans fields. As for the fields with no crop, roughness values are varied from $-0.7 < H_{rough} < 0.8$.

5.3.3 October 9^{th}

We had both pre and post date field observations for October 9^{th} RADARSAT-2 data, namely September 21^{st} and October 13^{th}. We chose October 13^{th} because of closer ground observation date for figure 5.7. In this date, all of the cropped corn fields have high roughness ($0.7 < H_{rough} < 1$) and double-bounce scattering has been observed for majority of them ($-16dB < R_{P_d} < 5dB$). There are only two fields that have zero double-bounce scattering namely 350101219 and 350101326. These two fields do not share any Meta data that can explain the situation. Maybe the corn crops in these two fields were in the late R5 or early R6 stages of corn crop stage identification system, and they had higher level of water in their leaves. Also as it is roughly perceivable in figure 6.9(b) in section 6.3, when 3 by 3 boxcar filter has been used these fields had double-bounce values (no corn field with $R_{P_d} = \infty$ exists). Whether it is the filtering effect or the crop stage effect due to the precipitation is unclear and it needs more detailed ground observation data.

We observed cropped soybeans fields in figure 5.7 to have high entropy ($0.6 < H_{rough} < 1$) with some fields with considerable double-bounce scattering spans. The progression of the images for different dates shows that the number of soybeans fields with double-bounce scattering is decreasing rapidly. In figure 5.5 majority of the soybeans fields had double-bounce scattering, and steep incident angle decreased this phenomenon in figure 5.6. But in figure 5.7 with the same incident angle as September 15^{th} (FQ16$\sim 36^{\circ}$) the number of soybeans fields with double-bounce scattering dwindled to the point that only one left toward the end of our data (figure 5.13).

There are only five harvested corn fields on figure 5.7, three of them 350100756, 350100151, and 350100467 have some double-bounce scattering while the rest have zero double-bounce. Two of these three fields had a peculiar Meta data according to tables 5.7 and 5.8 and probably were still cropped fields on the RADARSAT-2 acquisition date. In case of field 350100151, it is possible that it was partially harvested on 9^{th} while it is completely har-

vested on 13^{th}. It is noteworthy that all of the harvested corn fields lie on the rough side of surface scattering based on H/α sub-space.

Four harvested soybeans fields with peculiar ground observation are detected. These four fields are 350100465 with table 5.1, 350100835 with table 5.2, 350101486 with table 5.3, and 350102038 with table 5.4. Harvested soybeans fields had wide range of roughness with majority of them having zero double-bounce scattering (17 fields). Only three non-zero double-bounce span cases are observed for HS and none of them are one of the four problematic fields. It is not clear that whether the filtering effect or the crop stage effect is the reason for these three fields.

Table 5.1: Field data for field 350100465

Field Id number	Date	Crop/Harvest situation	
2009_350100465	9/21/2009	Cropped/currentyear	Soybeans
2009_350100465	10/13/2009	Nocrop/harvested	Soybeans
2009_350100465	10/15/2009	Cropped/currentyear	Soybeans
2009_350100465	11/4/2009	Cropped/currentyear	Soybeans
2009_350100465	11/9/2009	Cropped/currentyear	Soybeans
2009_350100465	11/13/2009	Nocrop/harvested	Soybeans

Table 5.2: Field data for field 350100835

Field Id number	Date	Crop/Harvest situation	
2009_350100835	9/21/2009	Cropped/currentyear	Soybeans
2009_350100835	10/13/2009	Nocrop/harvested	Soybeans
2009_350100835	10/15/2009	Cropped/currentyear	Soybeans
2009_350100835	11/4/2009	Nocrop/harvested	Soybeans
2009_350100835	11/9/2009	Nocrop/harvested	Soybeans
2009_350100835	11/13/2009	Nocrop/harvested	Soybeans

Table 5.3: Field data for field 350101486

Field Id number	Date	Crop/Harvest situation	
2009_350101486	9/21/2009	Cropped_currentyear	Soybeans
2009_350101486	10/13/2009	Nocrop_harvested	Soybeans
2009_350101486	10/15/2009	Cropped_currentyear	Soybeans
2009_350101486	11/4/2009	Cropped_currentyear	Soybeans
2009_350101486	11/9/2009	Cropped_currentyear	Soybeans
2009_350101486	11/13/2009	Nocrop_harvested	Soybeans

Table 5.4: Field data for field 350102038

Field Id number	Date	Crop/Harvest situation	
2009_350102038	9/21/2009	Cropped/currentyear	Soybeans
2009_350102038	10/13/2009	Nocrop/harvested	Soybeans
2009_350102038	10/15/2009	Cropped/currentyear	Soybeans
2009_350102038	11/4/2009	Nocrop/harvested	Soybeans
2009_350102038	11/9/2009	Nocrop/harvested	Soybeans
2009_350102038	11/13/2009	Nocrop/harvested	Soybeans

Partially harvested fields are too few (3 for corn and 8 for soybean) and the lack of more in depth meta data about these type of fields produce more uncertainty thus no analysis have been performed on them. The same problems with ground observation data are also observed for partially harvested corn fields 350101394 (table 5.5) and 350101490 (table 5.6), but no problem has been observed for partially harvested soybeans fields.

Table 5.5: Field data for field 350101394

Field Id number	Date	Crop/Harvest situation	
2009_350101394	9/21/2009	Cropped/currentyear	Corn
2009_350101394	10/13/2009	Partiallyharvest	Corn
2009_350101394	10/15/2009	Cropped/currentyear	Corn
2009_350101394	11/4/2009	Cropped/currentyear	Corn
2009_350101394	11/9/2009	Partiallyharvest	Corn
2009_350101394	11/13/2009	Partiallyharvest	Corn

Table 5.6: Field data for field 350101490

Field Id number	Date	Crop/Harvest situation	
2009_350101490	9/21/2009	Cropped/currentyear	Corn
2009_350101490	10/13/2009	Partiallyharvest	Corn
2009_350101490	10/15/2009	Cropped/currentyear	Corn
2009_350101490	11/4/2009	Cropped/currentyear	Corn
2009_350101490	11/9/2009	Partiallyharvest	Corn
2009_350101490	11/12/2009	Partiallyharvest	Corn

As for the fields with no cultivation practice (NH in figure 5.7), again no double-bounce is detectable and they tend to become smoother in comparison to figure 5.5. In terms of roughness, the general transition toward smoothness is starting from this date with maximum of $H_{rough} = 0.92$ and minimum of $H_{rough} = -0.267$.

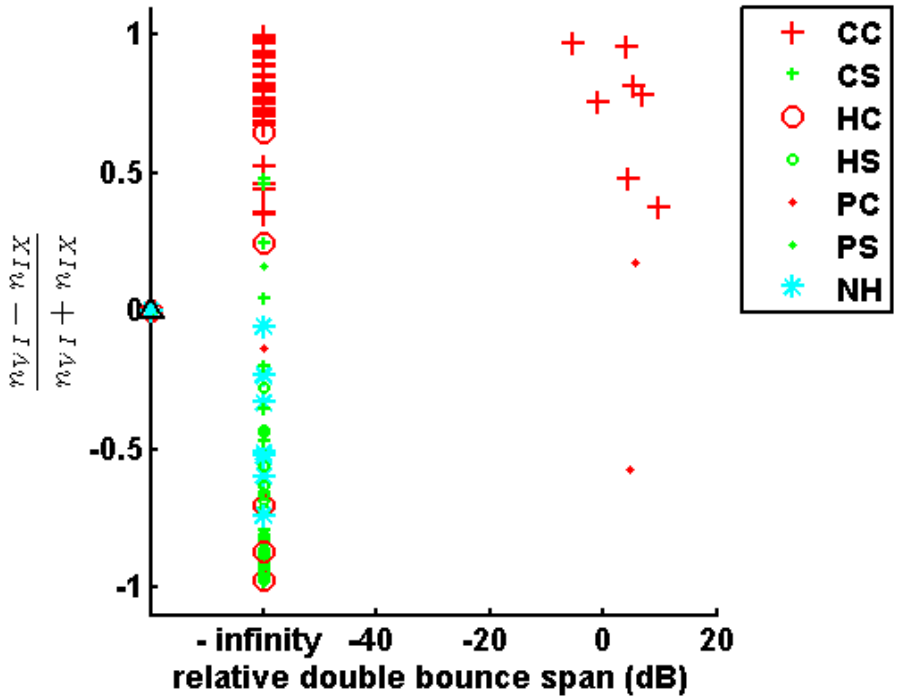

Figure 5.8: The relative double-bounce span of RFD versus H_{rough} of the fields observed on the October 12^{th} RADARSAT-2 image. The symbols represent different crop/harvest situation based on ground observations on October 13^{th}. CC, CS, HC, HS, PC, PS, and NH stands for Cropped Corn, Cropped Soybean, Harvested Corn, Harvested Soybean, Partially harvested Corn, Partially harvested Soybean, and No crop/Harvest situation

5.3.4 October 12^{th}

The October 12^{th} RADARSAT-2 scene is another FQ5 beam type image, this beam type hinders the ability to measure the double-bounce backscatter and significantly reduces the number of $P_d \neq 0$. This is evident in figure 5.8 where the number of cropped corn fields with $P_d \neq 0$ are decreased to seven fields while the rest of the cropped corn fields are moved to $P_d = 0$ line (relative span $= \infty$). The cropped corn fields once again exhibit high surface roughness values, $H_{rough} > 0.3$. On the other hand all of the cropped soybeans fields have zero double-bounce span and their roughness is reduced to the range of $-1 < H_{rough} < 0.5$ in comparison with previous dates. Therefore roughness measure can be used to distinguish cropped corn fields.

All of the harvested corn fields are extremely smooth in $\sim 24°$ incident angle. The two

exceptions in figure 5.8 belongs to already mentioned 350100756 and 350100467 fields. These two fields, as it can be observed from tables 5.7 and 5.8 have exceptional behavior. A normal corn field would need at least 55 to 65 days to be ready for some sort of harvest, assuming an accurate ground observation these two fields will be cropped and harvested in no more than a month period (from 13 th of October till 13 th of November).

Table 5.7: Field data for field 350100467

Field Id number	Date	Crop/Harvest situation	
2009_350100467	9/21/2009	Cropped/current year	Corn
2009_350100467	10/13/2009	No crop/harvested	Corn
2009_350100467	10/15/2009	Cropped/current year	Corn
2009_350100467	11/4/2009	Cropped/current year	Corn
2009_350100467	11/9/2009	No crop/harvested	Corn
2009_350100467	11/13/2009	No crop/harvested	Corn

Table 5.8: Field data for field 350100756

Field Id number	Date	Crop/Harvest situation	
2009_350100756	9/21/2009	Cropped/current year	Corn
2009_350100756	10/13/2009	No crop/harvested	Corn
2009_350100756	10/15/2009	Cropped/current year	Corn
2009_350100756	11/4/2009	Cropped/current year	Corn
2009_350100756	11/9/2009	Cropped/current year	Corn
2009_350100756	11/13/2009	No crop/harvested	Corn

The harvested soybeans fields are varied when it gets to roughness ($H_{rough} < 0.4$) and no double-bounce are observed in these fields. If an un-harvested part exists on a corn field, double-bounce scattering will be observed. But since there is a gap between RADARSAT-2 acquisition date and the ground observation date, once again it is hard to say partially harvested fields would belong to which category, harvested or cropped. As for the seven no cultivation practice fields, they are relatively smooth ($-0.1 < H_{rough} < -0.7$).

5.3.5 October 15^{th}

The October 15^{th} image had also ground observations on the same day and its FQ19 beam type (incident angle $\sim 39°$) makes it more prone to double-bounce scattering. Therefore all

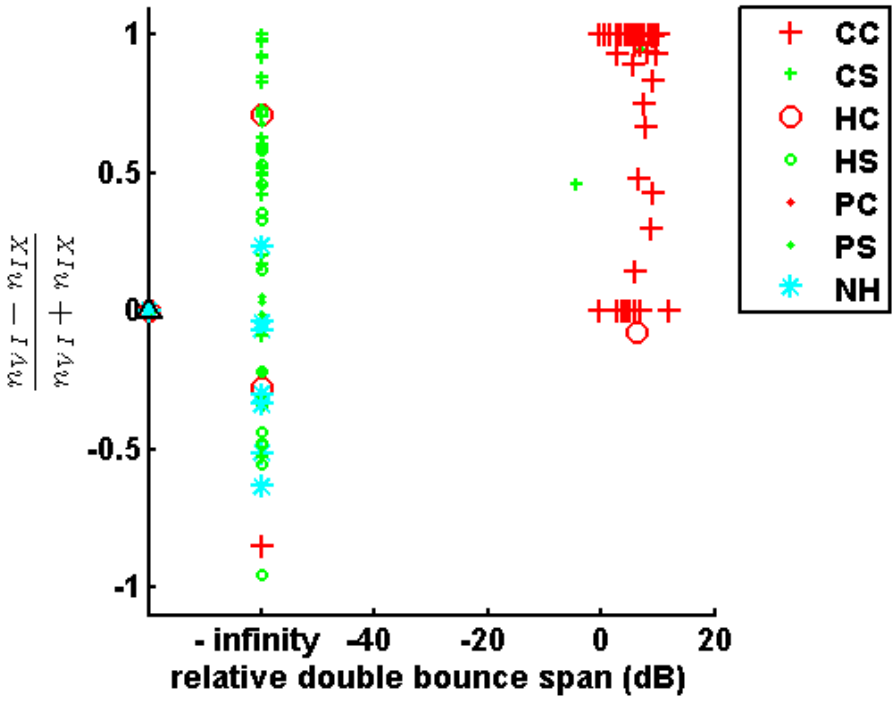

Figure 5.9: The relative double-bounce span of RFD versus H_{rough} of the fields observed on the October 15^{th} RADARSAT-2 image. The symbols represent different crop/harvest situation based on ground observations on October 15^{th}. CC, CS, HC, HS, PC, PS, and NH stands for Cropped Corn, Cropped Soybean, Harvested Corn, Harvested Soybean, Partially harvested Corn, Partially harvested Soybean, and No crop/Harvest situation

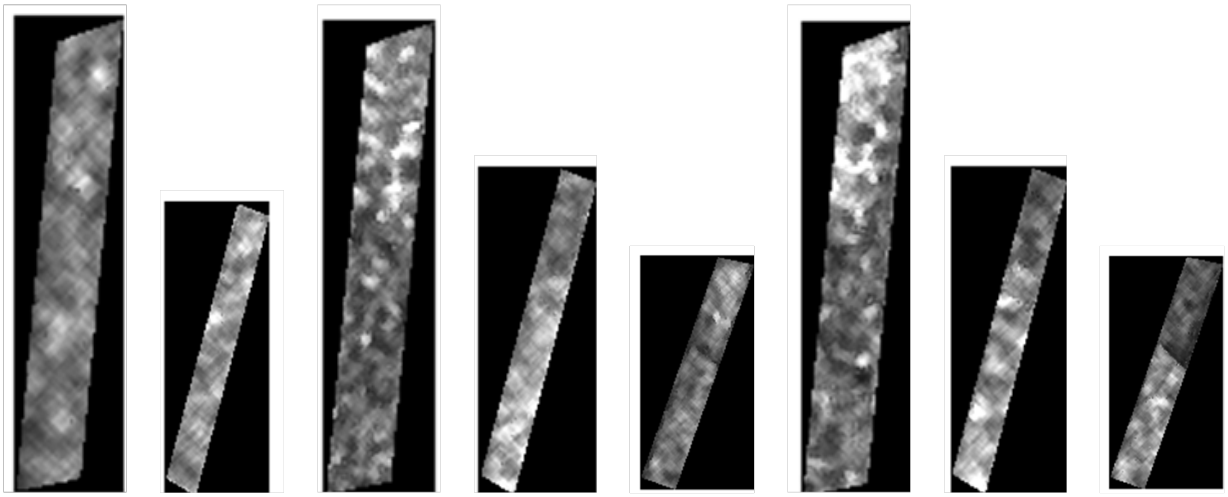

(a) (b) (c) (d) (e) (f) (g) (h)

Figure 5.10: The $|S_{HH}|^2$ image of field 350101101 in (a)09/15/2009, (b)09/18/2009, (c)10/09/2009, (d) 10/12/2009, (e) 10/15/2009,(f) 11/02/2009, (g) 11/05/2009, and (h) 11/08/2009

the cropped corn fields have double-bounce values. The only exception is the field 350101551 with zero double-bounce. Table 5.9 shows that this field had out of ordinary ground measurements. It seems that this field was really harvested on October 13^{th} and never cropped again or maybe cropped and harvested on November 13^{th} . The reason is that in all the remaining dates this field exhibit zero double-bounce, this can happen because of lack of corn crop on the field or the existence of corn in early vegetative stages. Most of the cropped corn fields have rough surface scattering $H_{rough} > 0.1$. In some cases the entropy is so high that only volume and double-bounce scattering is detectable and polarimetric surface roughness by definition becomes zero. The field in figure 5.4(e) is such a case. Cropped soybeans fields all have zero double-bounce with the exception of field 350101259 (please read the next subsection regarding this field). As for the surface roughness they have a verity from high entropy to partially smooth ($-0.6 < H_{rough}$).

There are only three harvested corn fields, two of which had $P_d = 0$. These two fields are harvested in a way that no standing stem is left on the ground for C-Band SAR to observe a double-bounce. The one exceptional field is field 350101101 and is depicted in figure 5.10.

This field will repeatedly exhibited non-zero double-bounce in the remaining of the RADARSAT-2 observations. Figure 5.10 shows that this field is clearly parted into two sections, and the boundary between the two regions produced a significant signal. This boundary roughly exists on October $9th$ images but the double-bounce signal appeared from October 15^{th} forward. The reason for this delay is that field 350101101 had probably two different cultivations, but only after a while the height difference between the two crops became stark enough to produce a double-bounce signal. The harvested corn fields are relatively diverse in their roughness behavior, probably due to their different practice of harvesting. As for the harvested soybeans fields, they all have zero double-bounce while their roughness are much similar to the cropped ones only that they seem to be smoother (H_{rough} <0.75). Partially harvested fields are only soybeans and we are not able to categorize them under harvested or cropped fields. No crop fields are once again show very smooth transition toward smoother parts ($-0.65 < H_{rough} < 0.23$).

5.3.6 November 2^{nd}

The FQ16 beam type RADARSAT-2 image form November 2^{nd} once again shows that $P_d \neq 0$ is a good indicator for fully grown cropped corn fields (figure 5.11). The only exception is field 350101551, a field with less than a one month period for cropping and harvesting (table 5.9) exhibits zero double-bounce scattering. We discussed this particular field on the previous date, October 15^{th} image analysis. As for roughness all range of smooth (4 fields), rough (35 fields) and high entropy (1 field) surface roughness are perceivable in figure 5.11. The cropped soybeans fields on the other hand have again zero double-bounce and varied roughness ($-0.8 < H_{rough} < 0.4$) except the same 350101259 field as in October 15^{th} that exhibited the same behavior on figure 5.9. Except on October 12^{th} on all of the RADARSAT-2 images up to November 2^{nd}, this field had non-zero double-bounce. This is not a typical characteristic of the soybeans field therefore after screening different channels on different dates; it appears that different areas have significantly different backscatters inside this field.

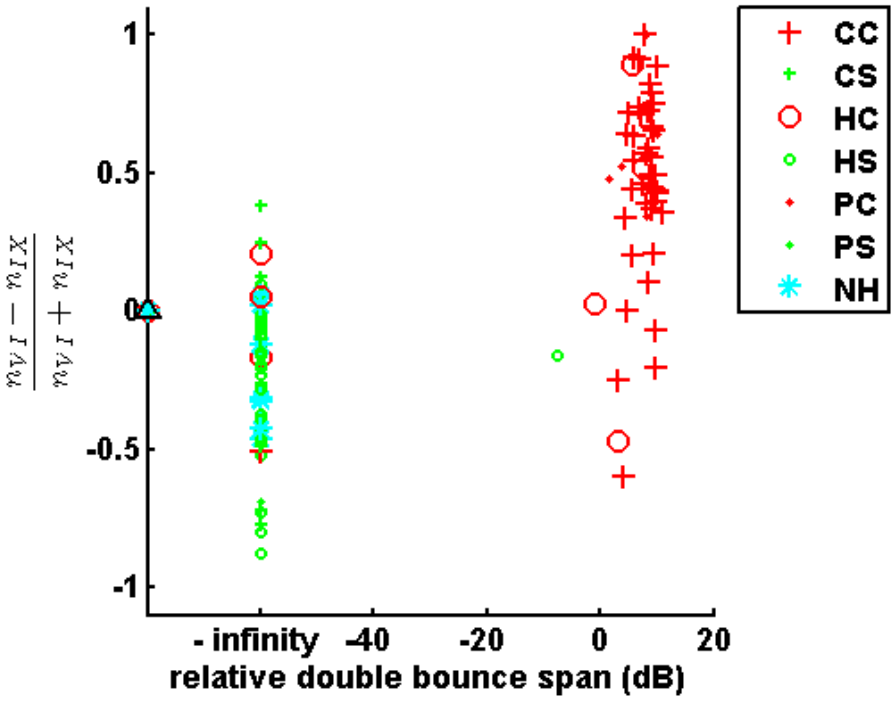

Figure 5.11: The relative double-bounce span of RFD versus H_{rough} of the fields observed on the November 2^{nd} RADARSAT-2 image. The symbols represent different crop/harvest situation based on ground observations on November 4^{th}. CC, CS, HC, HS, PC, PS, and NH stands for Cropped Corn, Cropped Soybean, Harvested Corn, Harvested Soybean, Partially harvested Corn, Partially harvested Soybean, and No crop/Harvest situation

These variations are observable on figure 4.8.

Table 5.9: Field data for field 350101551

Field Id number	Date	Crop/Harvest situation	
2009_350101551	9/21/2009	Cropped/current year	Corn
2009_350101551	10/13/2009	No crop/harvested	Corn
2009_350101551	10/15/2009	Cropped/current year	Corn
2009_350101551	11/4/2009	Cropped/current year	Corn
2009_350101551	11/9/2009	Cropped/current year	Corn
2009_350101551	11/13/2009	No crop/harvested	Corn

There are three harvested corn fields with $P_d \neq 0$. Fields 350101253, 350101595, and 350101088 are most likely partially cropped on November 2^{nd} while they are harvested by November 4^{th}. The reason is that firstly they used to be harvested on October 15^{th} and secondly they exhibit similar behavior to cropped corns ($P_d \neq 0$). The remaining harvested corn fields have zero double-bounce and $-0.2 < H_{rough} < 0.3$. Field 350101101 is the only harvested corn field that have $P_d \neq 0$ and it is fairly smooth too ($H_{rough} = -0.46$). On the other hand all the harvested soybeans fields (except 350101259) have zero double-bounce and moved toward smoother surface scattering (H_{rough} <0.1).

All the partially harvested corn fields have non-zero double-bounce span and they are fairly rough ($0.4 < H_{rough}$), therefore they are similar to cropped corn fields. But partially harvested soybeans fields could belong to either harvested or cropped soybeans categories. In figure 5.11, no crop fields are still moving toward smoother surface roughness($-0.4 < H_{rough} < 0.1$).

5.3.7 November 5^{th}

The November 5^{th} RADARSAT-2 scene is another steep angle FQ5 image, where double-bounce scattering will be reduced and roughness measure weighs more importance. This is evident even in all of the cropped corn fields while these fields will have high entropy with $0.2 < H_{rough}$. The only exception is field 350101394, another strange field as it is perceivable

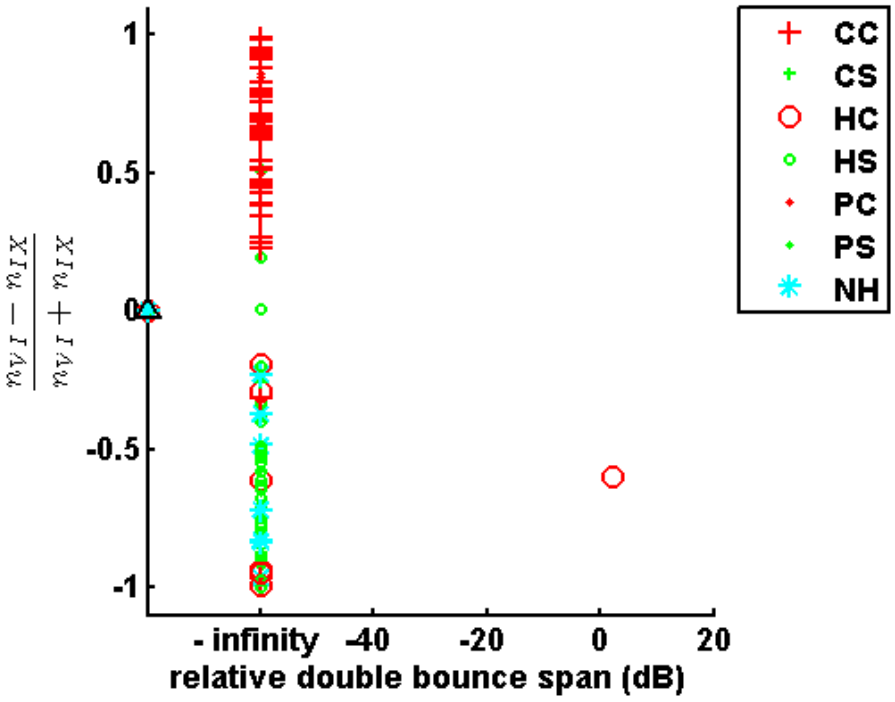

Figure 5.12: The relative double-bounce span of RFD versus H_{rough} of the fields observed on the November 5^{th} RADARSAT-2 image. The symbols represent different crop/harvest situation based on ground observations on November 4^{th}. CC, CS, HC, HS, PC, PS, and NH stands for Cropped Corn, Cropped Soybean, Harvested Corn, Harvested Soybean, Partially harvested Corn, Partially harvested Soybean, and No crop/Harvest situation

from table 5.5. This field was cropped and partially harvested and again cropped in a period of 20 days. Since H_{rough} is equal to -0.3146, maybe this field is only partially harvested all the time and had a fairly smooth part that overwhelmed the rest of the rough corn field. This phenomenon is confirmed by screening the field as two completely different regions are visible. On the other hand all the cropped soybeans are fairly smooth with $H_{rough} < -0.2$ while had zero double-bounce spans.

As it is also the case with November 2^{nd}, harvested corn field number 350101101 also shows similar roughness and double-bounce value in November 5^{th} ($H_{rough} = -0.5993$ and $R_{P_{sb}} = 2.287$). All the rest of the harvested soybeans fields have zero double-bounce while they are fairly smooth with $H_{rough} < -0.1$. Harvested soybeans fields on the other hand are varied in roughness from slightly rough (3 fields) to fairly smooth fields (32 fields). All the partially harvested corn fields perform similar to cropped corn fields but it is not possible to categorize the partially harvested soybeans fields. The seven fields that have no cropping are fairly smooth with$-0.9 < H_{rough} < -0.2$ and no double-bounce span.

5.3.8 November 8^{th}

All the cropped corn fields on November 8^{th} RADARSAT-2 image have non-zero double-bounce span and fairly rough (38 fields) to high entropy (3 fields) surface scattering ($0.5 < H_{rough}$). The only exception is field 350101551 in figure 5.13. This field has a very peculiar case as it had also an unexpected zero double-bounce on October 15^{th} and November 2^{nd}. The meta-data for field 350101551 is provided in table 5.9. It has also zero double-bounce in November 8^{th} with a very smooth surface scattering. As for cropped soybeans fields, they all have zero double-bounce and are varied in roughness from $H_{rough} = 0.4$ to $H_{rough} = -0.8$.

Two of the harvested corn fields namely 350100416 and 350100834 are likely to be still cropped or partially cropped on 8^{th} because they were cropped fields on 4^{th} while they are harvested on 9^{th}. These fields have the same behavior as the cropped corn fields. The remaining harvested corn fields all have zero double-bounce scattering with the exception of

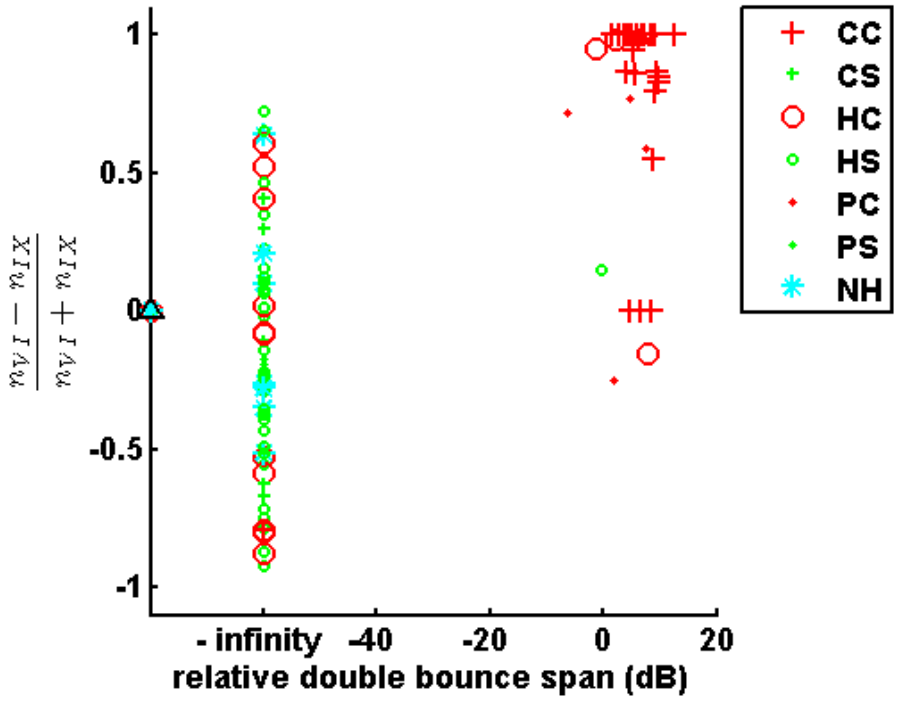

Figure 5.13: The relative double-bounce span of RFD versus H_{rough} of the fields observed on the November 8^{th} RADARSAT-2 image. The symbols represent different crop/harvest situation based on ground observations on November 9^{th}. CC, CS, HC, HS, PC, PS, and NH stands for Cropped Corn, Cropped Soybean, Harvested Corn, Harvested Soybean, Partially harvested Corn, Partially harvested Soybean, and No crop/Harvest situation

.

field 350101101 that has non-zero double-bounce span. This field has already been discussed in November 15^{th} image. Surface roughness of harvested corn fields varies between high entropy till very smooth ($-0.9 < H_{rough} < 0.7$). Harvested soybeans fields are also very diverse in roughness, $-1 < H_{rough} < 0.8$ and all except field 350101131 have zero double-bounce. Screening of this field showed that there are patches of different intensity visible in the field but it is hard to say that they are man-made or natural. In any case this field is hard to explain.

All the partial corn fields still have standing corn on them so they have double-bounce values and majority of them are still fairly rough except field 350101394. This field has the same behavior as in previous date (figure 5.12). As for partial soybeans, once again it is not possible to categorize it under harvested or cropped situations. The seven no crop

fields are showing exceptionally diverse behavior from very rough, $H_{rough} < 0.7$ to fairly smooth $-0.6 < H_{rough}$ while they have no double-bounce scattering. Maybe some unwanted vegetation is the cause.

5.4 First Step of Decision Tree

We established the ability of the RFD's relative double-bounce span and H/α's H_{rough} parameter for corn discrimination in section 5.3. Our corn discrimination algorithm in reality is a one step decision tree. Therefore only two output class namely, "Cropped Corn" (CC) and "Not a Cropped Corn" (NCC) exists at this stage.

Our Decision tree classification algorithm is as follows:

I: For incidence angles smaller than 25° (FQ5 beam type), an $H_{rough} > 0.3$ is a cropped corn field.

II: For incidence angles larger than 25° (FQ16 and FQ19 beam types), a non-zero double-bounce is a cropped corn field.

Since accuracy assessment is an integral part of every scientific observation, the accuracy evaluation is necessary. This section provides some statistics about the accuracy assessment of the mentioned decision trees. The confusion matrices are included in Appendix G. Since our algorithm is based on some physical and statistical definitions and not the field data itself, training and testing data do not convey any meaning therefore all the ground points have been used as testing data.

Based on our ground measurement data observed on September 21^{th}, the first two observation dates, September 15^{th} and 18^{th} had no harvested corn fields. Since no harvesting activity is in progress on these dates they should have been excluded from the results, but they prove an important point therefore they are included. That point is that our algorithm is defined only for the harvesting season and will not provide proper information when the

agricultural fields are young.

September 15^{th} has FQ16 beam type, therefore $P_d \neq 0$ or equivalently $R_{P_s} \gg -\infty$ should detect the cropped corn fields. The overall accuracy of this classification is 31.85% and the κ coefficient is -0.39. The negative κ implies that our classification is extremely wrong and classification failed. September $18th$ classification on the other hand had a better accuracy of 65.49% with a κ coefficient of 0.33. The low user accuracy for cropped corn class shows that the classified fields are not necessarily cropped corns and the resulted low κ value implies the lack of consistency. As already mentioned these weak results are expected as our scheme is for harvesting season. Therefore the selection of proper dates is important.

Table 5.10: Final assessment results of September 15^{th} decision tree for corn.

Class	Prod. Acc. (Percent)	User Acc. (Percent)	Prod. Acc. (Pixels)	User Acc. (Pixels)
CC	0	0	0/54	0/23
NCC	61.01695	40	36/59	36/90
Overall Accuracy =			(36/113) =	31.86%
Kappa Coefficient =				-0.39

Table 5.11: Final assessment results of September 18^{th} decision tree for corn.

Class	Prod. Acc. (Percent)	User Acc. (Percent)	Prod. Acc. (Pixels)	User Acc. (Pixels)
CC	98.14815	58.24176	53/54	53/91
NCC	35.59322	95.45455	21/59	21/22
Overall Accuracy =			(74/113) =	65.49%
Kappa Coefficient =				0.33

October 9^{th} (table 5.12) is a FQ16 beam type and resulted in a substantially consistent classification with a rise of 20% in accuracy from the previous dates. It followed by October 12^{th} (table 5.13) and October 15^{th} (table 5.14) almost perfect classifications. The accuracies reached above 95% with a κ factors of above 0.9. The beam type did not affect the result of our classification as these two dates had two different rules for classification. From this point forward the accuracies start to decrease to 90% for November 2^{nd} (table 5.15) and

November 5^{th} (5.16) with κ factor showing substantial consistency for the results. The final date's classification results from table 5.17 is 85.84 % with again substantial consistency in chance agreement of 0.68. There are no changes in the results due to the incidence angle and all of these six classifications are very accurate.

Table 5.12: Final assessment results of October 9^{th} decision tree for corn.

Class	Prod. Acc. (Percent)	User Acc. (Percent)	Prod. Acc. (Pixels)	User Acc. (Pixels)
CC	93.47826	72.88136	43/46	43/59
NCC	76.1194	94.44444	51/67	51/54
Overall Accuracy =			(94/113) =	83.19%
Kappa Coefficient =				0.66

Table 5.13: Final assessment results of October 12^{th} decision tree for corn.

Class	Prod. Acc. (Percent)	User Acc. (Percent)	Prod. Acc. (Pixels)	User Acc. (Pixels)
CC	100	93.87755	46/46	46/49
NCC	95.52239	100	64/67	64/64
Overall Accuracy =			(110/113) =	97.35%
Kappa Coefficient =				0.95

Table 5.14: Final assessment results of October 15^{th} decision tree for corn.

Class	Prod. Acc. (Percent)	User Acc. (Percent)	Prod. Acc. (Pixels)	User Acc. (Pixels)
CC	98.03922	94.33962	50/51	50/53
NCC	95.16129	98.33333	59/62	59/60
Overall Accuracy =			(109/113) =	96.46%
Kappa Coefficient =				0.93

RFD algorithm and the introduced roughness measure are both field-based methods. They simply sense the standing corn crops on the field. Therefore there is no difference between a partially harvested corn field and a fully cropped corn field. If we merge partially cropped corn and cropped corn fields as one class, the accuracies would improve drastically.

Table 5.15: Final assessment results of November 2^{nd} decision tree for corn.

Class	Prod. Acc. (Percent)	User Acc. (Percent)	Prod. Acc. (Pixels)	User Acc. (Pixels)
CC	97.61905	80.39216	41/42	41/51
NCC	85.91549	98.3871	61/71	61/62
Overall Accuracy =			(102/113) =	90.27%
Kappa Coefficient =				0.80

Table 5.16: Final assessment results of November 5^{th} decision tree for corn.

Class	Prod. Acc. (Percent)	User Acc. (Percent)	Prod. Acc. (Pixels)	User Acc. (Pixels)
CC	88.09524	86.04651	37/42	37/43
NCC	91.5493	92.85714	65/71	65/70
Overall Accuracy =			(102/113) =	90.27%
Kappa Coefficient =				0.79

Table 5.17: Final assessment results of November 8^{th} decision tree for corn.

Class	Prod. Acc. (Percent)	User Acc. (Percent)	Prod. Acc. (Pixels)	User Acc. (Pixels)
CC	96.66667	65.90909	29/30	29/44
NCC	81.92771	98.55072	68/83	68/69
Overall Accuracy =			(67/113) =	85.84
Kappa Coefficient =				0.68

Table 5.18 presents these results. Previously only two images reached above 95% accuracy but with this correction, five images have above 95% accuracy and the rest are unchanged.

It appears that important field properties such as row direction, type of harvest, and tillage effects did not affect our ability to distinguish cropped corn from the rest of the fields. Due to the time constraints the detailed analysis of these parameters was not performed.

Table 5.18: The result of cropped corn decision tree with mixing CC and PC classes

Date	Accuracy	κ
09/15/2009	31.86%	-0.39955
09/18/2009	65.49%	0.327894
10/09/2009	83.19%	0.66646
10/12/2009	97.35%	0.94556
10/15/2009	96.46%	0.928774
11/02/2009	94.69%	0.892038
11/05/2009	99.08%	0.979381
11/08/2009	95.58%	0.905786

5.5 RFD versus Other Methods

The simple comparison between the classification assessment results in section 5.4 and section 4.6, shows that the selected PolSAR unsupervised classifications had never reached even close to the RFD based classification for corn. Although those classifiers have been able to classify some other classes such as harvested soybean, they did not have consistency in finding same classes. Therefore we believe that RFD classification performed better for corn fields in respect to the implemented unsupervised classifications. Since no results for the original Freeman-Durden based classification is presented in section 4.6 it is necessary to compare this two methods in terms of classification capability.

It has been demonstrated (in section 4.5) that RFD has sometimes significantly different outcome in comparison to OFD. Figure 5.14 shows the relative double-bounce span in each field on x-axes and the estimated H_{rough} on the y-axes for both (a) RFD and (b) OFD algorithms. These estimations are based on the October 9^{th} RADARSAT-2 scene and October

13^{th} ground observations. The -400 dB for the OFD actually represents close to $-\infty$ relative double-bounce spans (zero double-bounce scattering). Figure 5.14(a) is the same as figure 5.7, the only difference is that in the x-axis negative infinity has been moved farther to be comparable to OFD results.

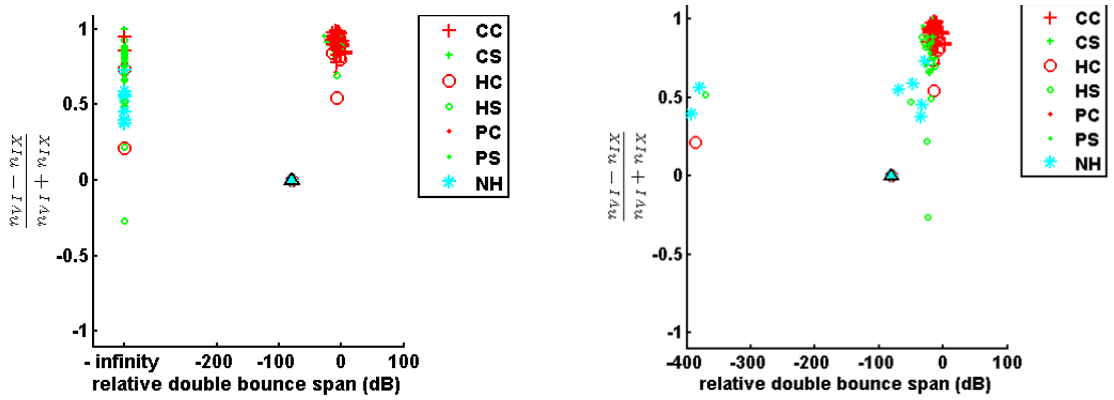

(a) (b)

Figure 5.14: Comparison between the results of (a) RFD (b) OFD

In RFD, figure 5.14(a), the cluster of cropped corns are very much distinct while for OFD, figure 5.14(b), the cluster that had corn fields are mixed with other classes. The double-bounce span of RFD has been zeroed based on the $\frac{|\alpha|}{\beta}$ ratio from H/α sub-space. As in OFD, the fates of the fields are decided based on the van Zyl[74] criteria. The van Zyl[74][23][45] criteria states that surface scattering is dominant when $\Re\left(\langle S_{HH}S_{VV}^{*}\rangle\right)_{new} \geq 0$, otherwise double-bounce scattering is dominant. OFD has been formulated in a way that even if there is a dominant scattering mechanism, other mechanisms would rarely become zero. Therefore there is no difference between partially dominant and completely dominant cases in OFD. This resulted in having different classes mixed up in one cluster and therefore hard to classify. One would argue that even in figure 5.14(b) we can define a boundary to discriminate corn, but the selection of the proper thresholds and uncertainty about them working for other dates proves that RFD significantly performed better in picking the corn fields. Ans due to the observed variation in the thresholds on OFD results we were unable to devise a classification scheme for OFD algorithm whether for corn or soybeans.

Also our roughness parameter performed extremely well for FQ5 beam types. In these steep angle scenes, double-bounce observation will weaken. This is the same for both RFD and OFD algorithms. Therefore once again an H/α driven parameter, helped to classify the corn fields. Even though only October $9th$ comparison is provided but this pattern was also observable on the other dates and all of the remaining seven RADARSAT-2 scenes had comparable ambiguity in OFD and comparable differentiation in RFD results.

Chapter 6

Result and Discussion for Soybeans

After devising a decision tree to find the senesced corn, now in this chapter we investigate C-Band RADARSAT-2 SAR data for discrimination of senesced soybean. We start our analysis with general concept of roughness in SAR and then observe different polarimetric parameters for soybean. Then the filtering effect is observed for the proposed RFD algorithm along with its effects on H/α sub-space. And the second step rule for harvest detection decision tree is introduced and evaluated.

6.1 PolSAR Sensitivity to Crops

Roughness is a target parameter that should be estimated prior to any analysis in order to predict radar behavior. The modified Rayleigh criterion considers a surface, smooth when

$$\triangle h < \frac{\lambda}{25 \times \cos\theta} \tag{6.1}$$

and rough when [58]

$$\triangle h > \frac{\lambda}{4.4 \times \cos\theta} \tag{6.2}$$

where h is the RMS height, λ is the wavelength, and θ is the incidence angle. For FQ 5, 16, and 19 (Figure 3.8) beam types the nominal incidence angles are 23.5° to 39.8° . On the other hand RADARSAT-2 C-band has a 5.5 cm wavelength. Therefore according to equation 6.1 the modified Rayleigh smoothness criterion is 0.24 cm to 0.29 cm, and based on equation 6.2 the roughness criterion is 1.36 cm up to 1.63 cm. These calculations and the geometrical structure defined in section 2.2 implies that senesced corn is rough enough for RADARSAT-2 but the same cannot be said about senesced soybeans.

For senesced soybeans crop, the 5 mm to 11 mm diameter seed (less than radar smooth)

will not be sensed by RADARSAT-2. Since the leaves fall before the seeds are mature, it should be expected that surface scattering is the most dominant mechanism. The only main structure that can be sensed by RADARSAT-2 C-band is the pods with 3 cm to 8 cm lengths. Assuming that the pods and stems stand vertical, there are some vertically aligned structures causing small amount of attenuation. They would most likely cancel out surface scattering effect and unlike corn there would not be a significant difference between HH backscatter and VV backscatter. As for circular polarizations, RR scattering would also be similar to LL scattering but RL is going to have higher values due to the dominance of surface scattering (please refer to Table 2.1).

On the other hand, it appears that the whole soybeans plant is cut down when soybeans are harvested. And that small amount of attenuation due to the stems can be further reduced. This may be the only difference between the senesced soybeans and the harvested soybeans fields. And since this signal might be too weak, filtering would considerably affect the sensing ability. We further analyze this hypothesis in the next section.

6.2 Polarimetric Parameters and Soybeans

There is wide range of polarimetric parameters defined for observations on SAR data. One such parameter is the simple σ° defined for different polarizations such as HH. The y axes of figure 6.1 are the average HH cross section coefficients per field. Each dot represents a soybeans field and the vertical lines differentiate between cropped, harvested, and partially harvested soybeans fields. The starting date begins with October 9^{th} chosen based on our ground truth information regarding the start of the harvest season for soybean. It should be noted that the fields are classified to three groups of cropped, harvested and partially harvested solely based on the ground truth data.

Figure 6.1 shows that there is no significant difference between cropped and harvested soybeans for σ°_{HH}. Similar plots are generated for HV, VV, RR, and RL polarizations.

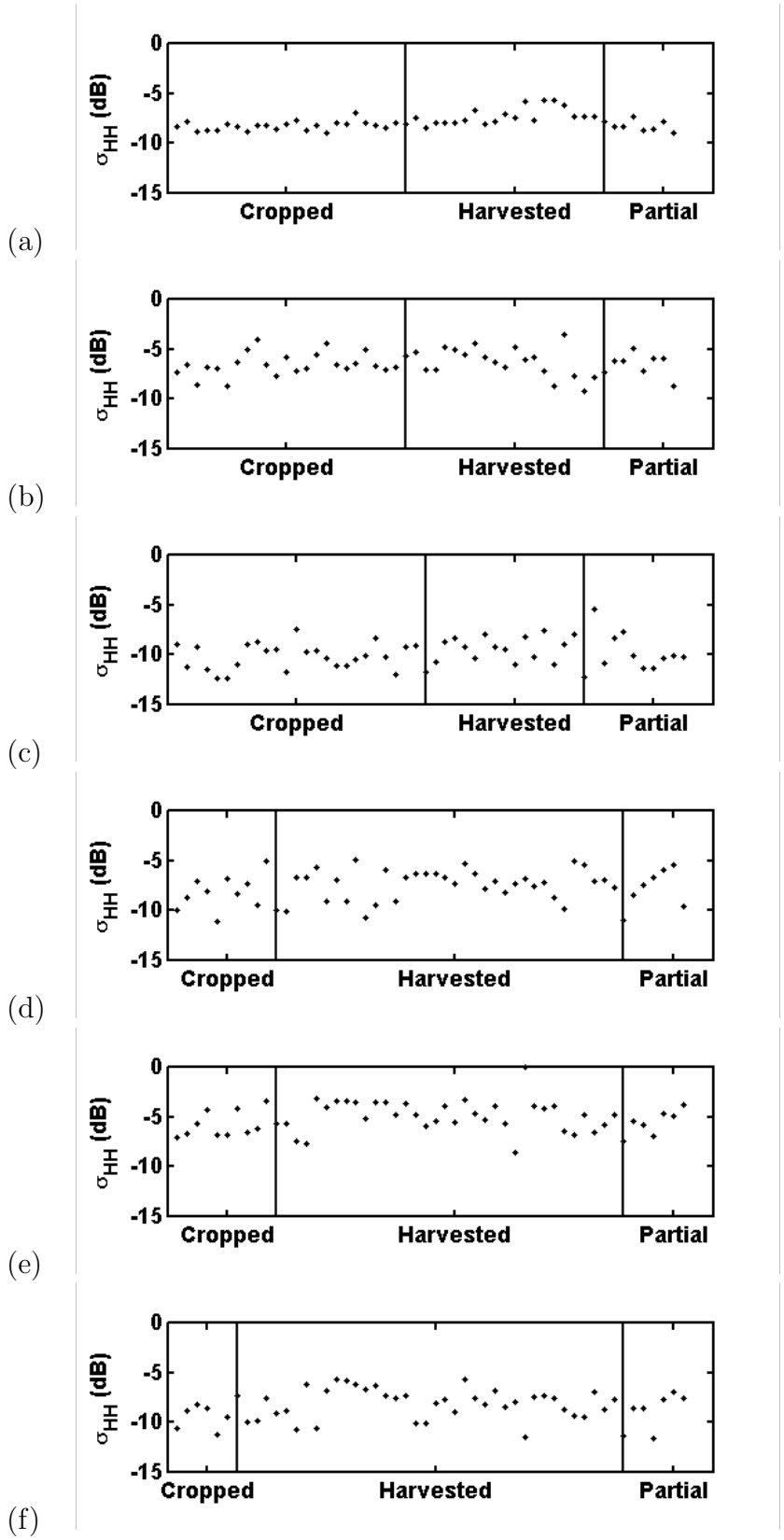

Figure 6.1: σ°_{HH} plots of the cropped, harvested and partially harvested soybeans in (a) 10/09/2009, (b) 10/12/2009, (c) 10/15/2009,(d) 11/02/2009, (e) 11/05/2009, and (f) 11/08/2009

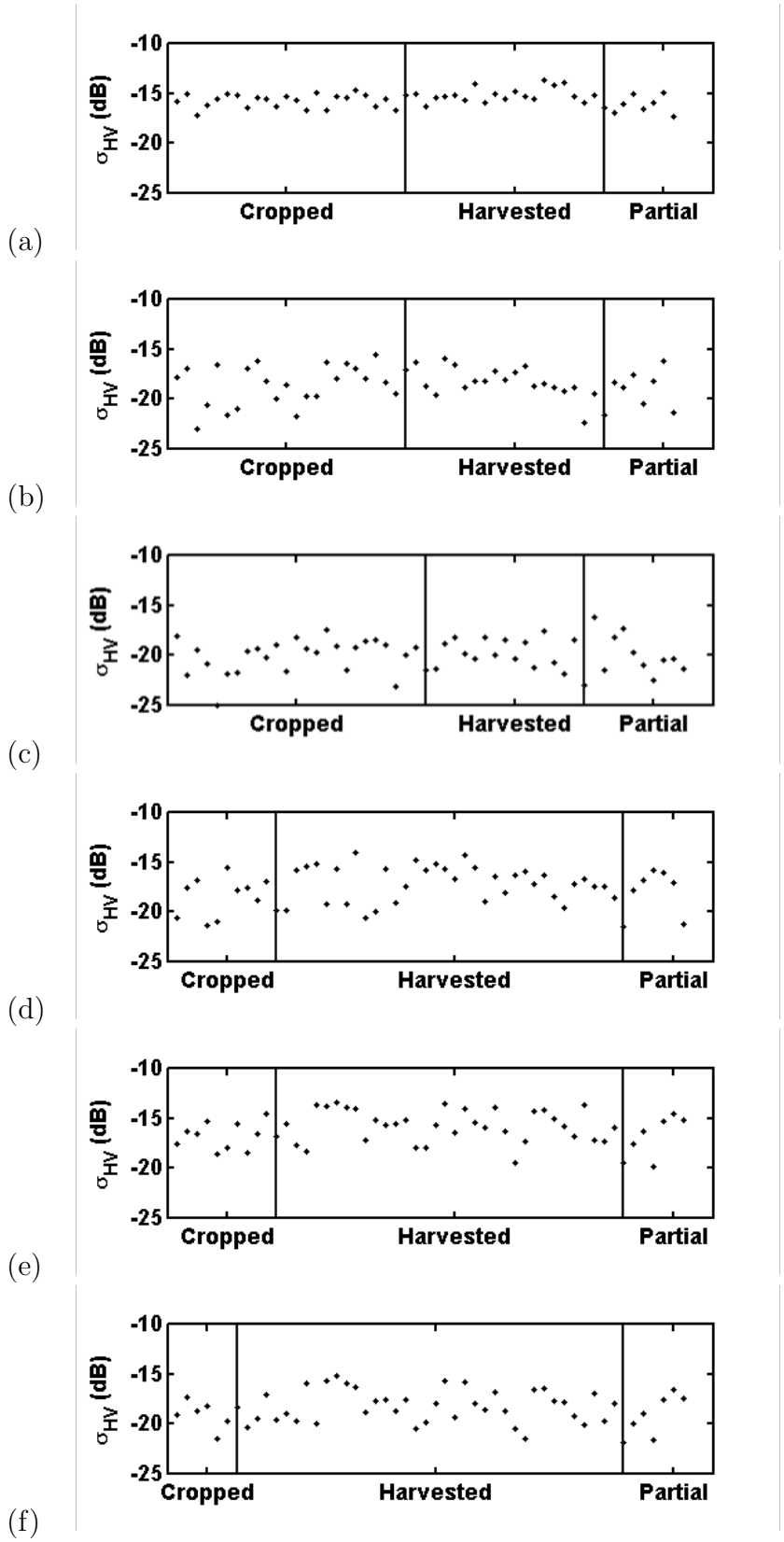

Figure 6.2: σ°_{HV} plots of the cropped, harvested and partially harvested soybeans in (a) 10/09/2009, (b) 10/12/2009, (c) 10/15/2009,(d) 11/02/2009, (e) 11/05/2009, and (f) 11/08/2009

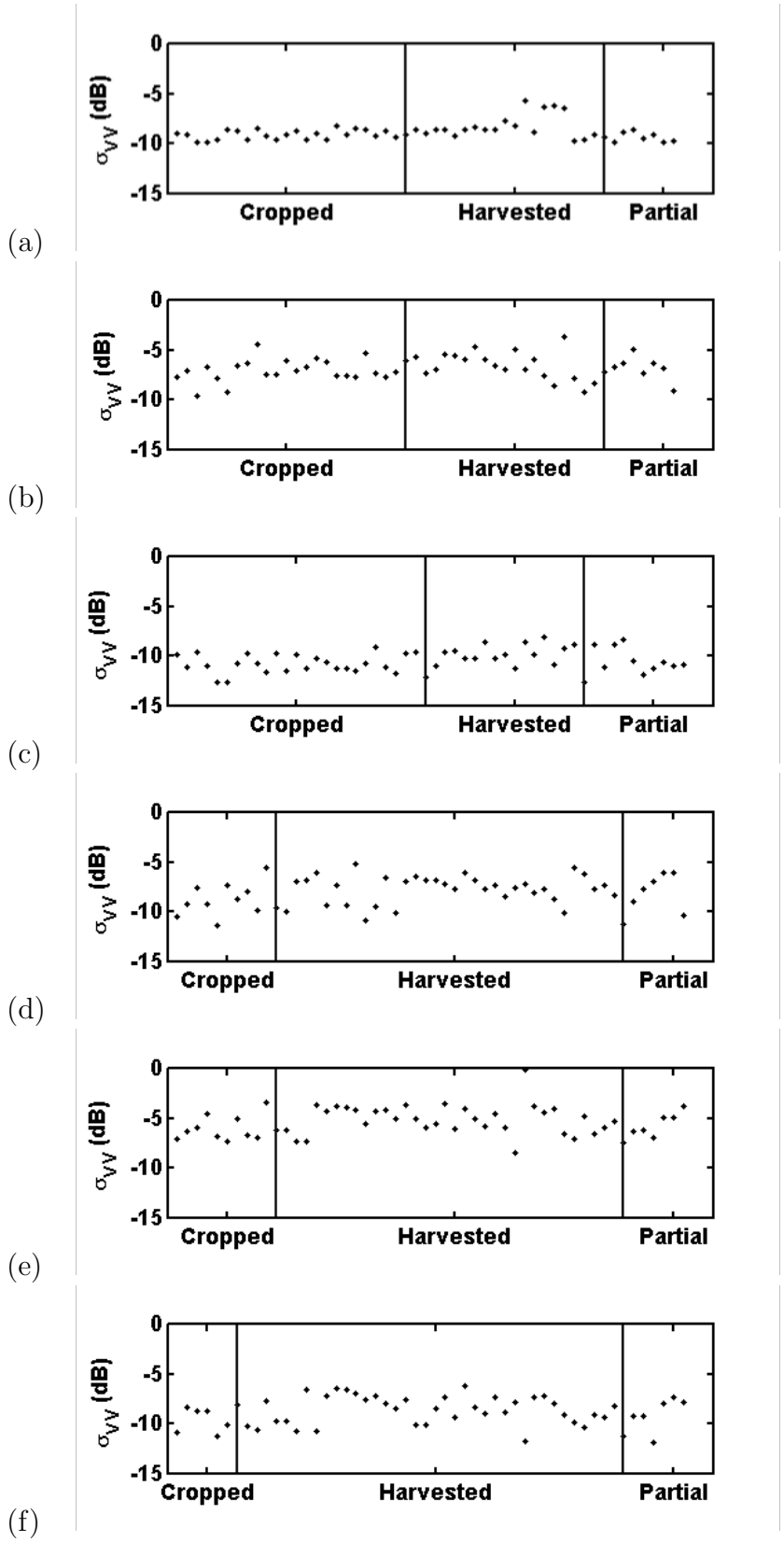

Figure 6.3: σ°_{VV} plots of the cropped, harvested and partially harvested soybeans in (a) 10/09/2009, (b) 10/12/2009, (c) 10/15/2009,(d) 11/02/2009, (e) 11/05/2009, and (f) 11/08/2009

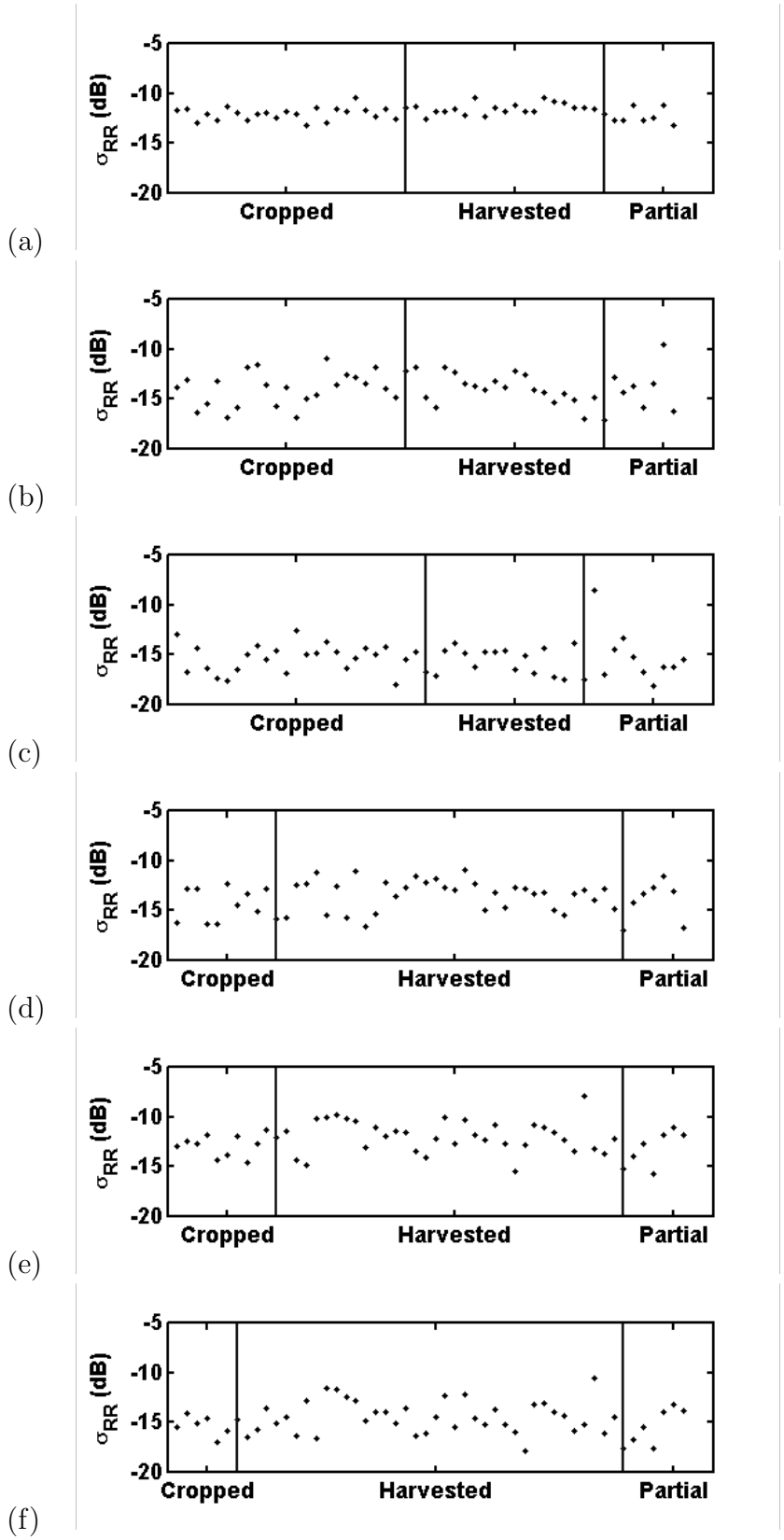

Figure 6.4: σ°_{RR} plots of the cropped, harvested and partially harvested soybeans in (a) 10/09/2009, (b) 10/12/2009, (c) 10/15/2009,(d) 11/02/2009, (e) 11/05/2009, and (f) 11/08/2009

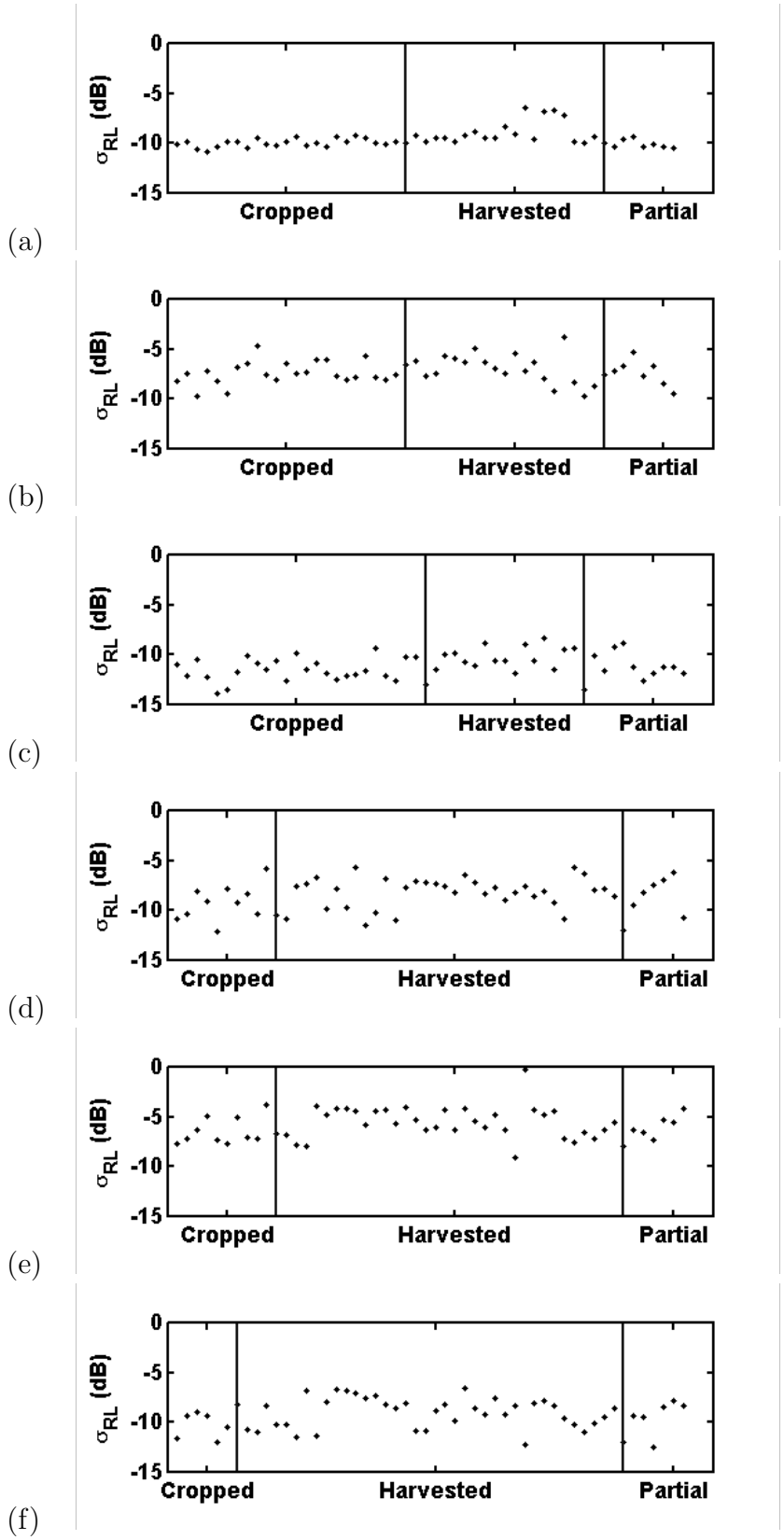

Figure 6.5: σ°_{RL} plots of the cropped, harvested and partially harvested soybeans in (a) 10/09/2009, (b) 10/12/2009, (c) 10/15/2009,(d) 11/02/2009, (e) 11/05/2009, and (f) 11/08/2009

Without exception in all of the plots, values observed for cropped soybeans have similar counterparts in the harvested soybeans fields. We did not include the results of ratio based equations such as co-polarized, cross-polarized, etc. but they also did not produce any meaningful results. For example in October 9^{th}, figure 6.5(a) has an ascending pattern for σ_{HH}. But even this weak pattern does not exist for October 15^{th} (figure 6.5(c)). Therefore since no stark descending or ascending pattern is observable in any of the sub plots of our five plots, no ratio based equation could also be defined solely based on these parameters for soybeans crop discrimination. Also based on our observations, polarimetric parameters such as depolarization ratio[57] were not successful for our soybeans fields.

Figure 6.6 depicts the co-polarimetric phase difference (PPD). The zero value for the phase shift between HH and VV shows that surface scattering is the dominant mechanism for all the fields whether they are cropped or harvested. Also $\sigma^{\circ}_{HV} \ll \sigma^{\circ}_{HH} = \sigma^{\circ}_{VV}$, $\sigma^{\circ}_{RL} \gg \sigma^{\circ}_{RR}$, and $PPD \sim 0^{\circ}$ are observed from figures 6.1, 6.2, 6.3, 6.4, and 6.5. Based on our observation presented in this section, soybeans fields do not show characteristics necessary for either of double-bounce or volume scattering. Close to zero PPD values shows that no double-bounce scattering is observable. Also having σ°_{RL} considerably bigger than σ°_{RR} by itself shows that volume scattering from leaves or stems are not observable. Therefore based on the descriptions provided in table 2.1 almost all the fields have surface scattering as their main mechanism and they have behaved very similar to bare soil. Of course there are exceptions, and those fields were described in chapter 5 but these exceptions are too few to change the general trend.

6.3 The Filtering Effect on RFD Results

Volume scattering in agricultural fields largely depends on the biomass of the crops. Since senesced soybeans is completely defoliated when it is ready to harvest, and the stems are sparsely spaced because of the row spacing, volume scattering from soybeans fields and bare

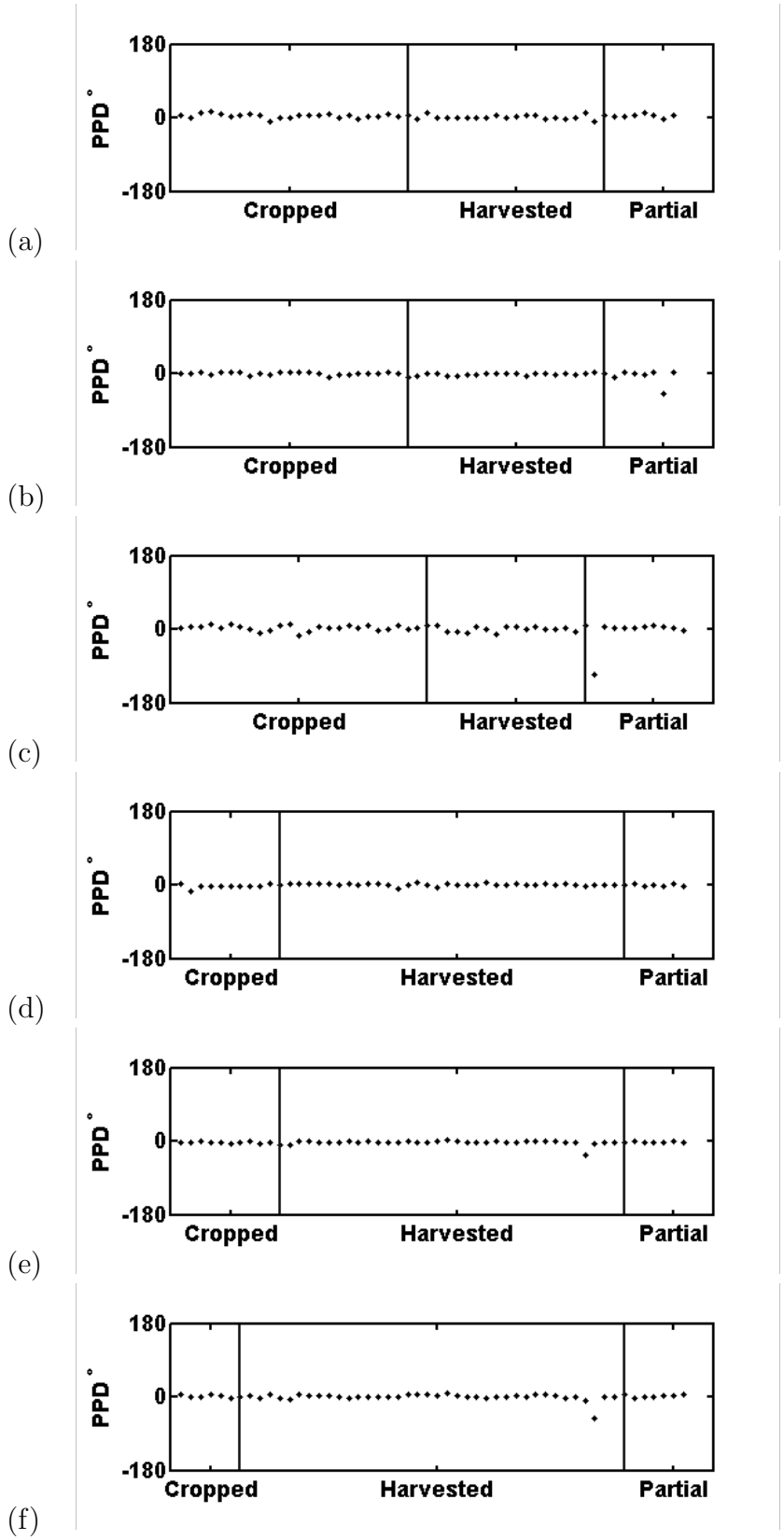

Figure 6.6: PPD plots of the cropped, harvested and partially harvested soybeans in (a) 10/09/2009, (b) 10/12/2009, (c) 10/15/2009,(d) 11/02/2009, (e) 11/05/2009, and (f) 11/08/2009

soil is not likely to be large enough for a C-band sensor to detect. Therefore we focus our observation on the double-bounce and surface scattering behavior of the fields in our RFD algorithm results. Figures 6.7 to 6.14 presents the behavior of filtering effect for these two spans in our data. Each figure is subdivided into four sub figures. And each sub-figure represents a result of boxcar filtering with a certain window size. In each sub-figure, relative surface span (y axes) is plotted against the relative double-bounce span (x axes) in dB units. On the other hand, based on equation 5.1 and equation 5.2, negative infinity for relative spans is only the case for zero spans. Therefore the zero span cases described in section 4.4.3 are positioned on the axes of each sub-figure. The total number of fields in each sub-figure is 113 fields. The corn fields are presented by cross (+) signs, while the soybeans fields are presented by small circle($\circ$) signs the seven not cultivated fields are presented by star ($*$) sign. These symbols were assigned to the fields based on the ground observations mentioned in section 3.7.1. The general trend in each figure is that only small amount of fields have zero surface or double-bounce spans (Negative infinity in case of relative spans) when no filtering has been applied to the image. The number of these zero spans will gradually increase with the increase of the window size. This increase is the main reason that we believe filtering will hinder our ability to sense the soybeans crop for C-Band RADARSAT-2 data. It appears that the very weak attenuation signal due to the stems and pods of the soybeans crop would disappear with the increase in window size of filtering.

Since SAR sensors mainly detect target structure and water volume content, the crop stages depicted by figures 1.2 and 1.4 show that time can be an important factor on how crops behave in SAR imagery. This is especially observable in our filtering plots. In our first two observation dates, September 15^{th} and 18^{th} plots, figures 6.7 and 6.8 shows that soybeans fields are very much alive and the stems are lively enough to have considerable double-bounce even after 11 by 11 boxcar filter. This observation is also in complete agreement with our ground observations where in table 3.2 September 21^{th} has the smallest possible amount

of harvested fields for soybeans crops. Most of the soybeans fields have probably been in one of the early to medium levels of the reproductive (R2 till R5) stages. The defoliation should have not started or is in a very early stage and stems are full of water, therefore double-bounce scattering has a significant role in the received power.

As for corn fields in the September 15^{th} and 18^{th}, the corn canopy is probably so dense that most of the scattering is in the form of surface scattering from the top layer of corn canopy. Wu et al. [78] in their elaborate observation of the effects of corn and soybeans plants morphology on the SAR response believe that for a lively corn most of the scattering are from the leaves. Therefore the radar wave cannot reach the ground to double-bounce back from the corn stems and thus the corn fields have no double-bounce portion in September 15^{th} and 18^{th} RADARSAT-2 images. This is also in agreement with the corn structure as we expect. The corn canopy as it is portrayed in section 2.2 with tall stems far enough for the radar wave to reach the ground, and large number of leaves that are long enough to cover the row spacing distance and dense enough to imitate a surface is a canopy that generates a layer that can have surface scattering from its top layer.

The number of soybeans fields with double-bounce span observed in 11 by 11 boxcar filtered 18^{th} of September plot, figure 6.8 are reduced in comparison to September 15^{th} plot. This trend may represent the gradual aging of the soy canopy and it seems to be completed in October 9^{th} plot. The 11 by 11 filtered sub-plot, figure 6.9(d) has no trace of soybeans fields with double-bounce scattering. And all the fields with double-bounce values are corn fields. Table 3.2 suggest that some harvesting should have started and therefore some of the corn fields should have passed the R6 reproductive stage. In those fields, corn start to dry out and leaves are no longer the main source of backscattering therefore corn stems would start to dominate the backscattered wave. Henceforth corn fields with double-bounce will appear even in 11 by 11 filtered plot. This behavior of corn fields is part of what we used in previous chapter to discriminate between cropped and harvested corn fields.

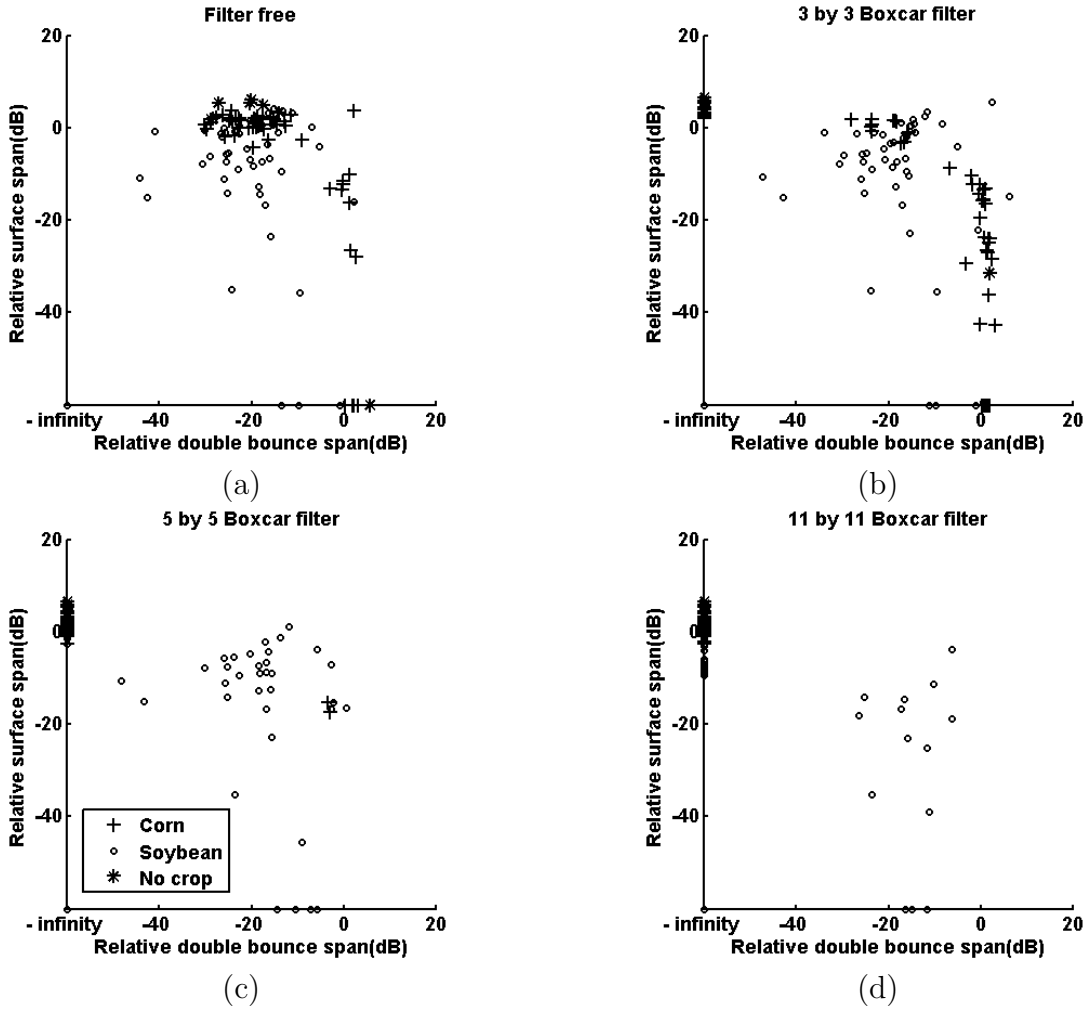

Figure 6.7: Relative surface versus relative double-bounce span for September 15^{th}(a) raw image (b) 3 by 3 window size boxcar filter (c) 5 by 5 window size boxcar filter (d) 11 by 11 window size boxcar filter. The in-situ data are gathered in the same day

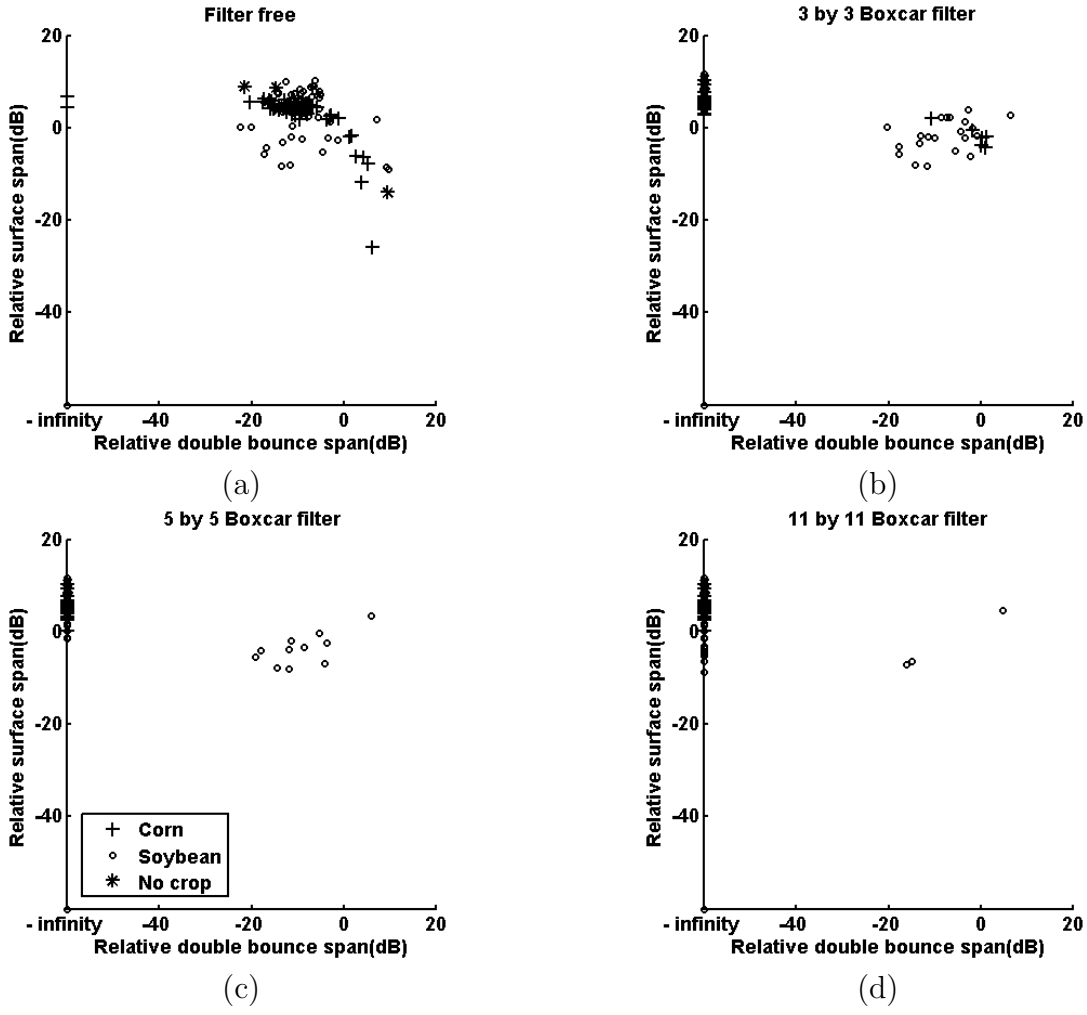

Figure 6.8: Relative surface versus relative double-bounce span for September 18^{th}(a) raw image (b) 3 by 3 window size boxcar filter (c) 5 by 5 window size boxcar filter (d) 11 by 11 window size boxcar filter. The in-situ data are gathered in the same day

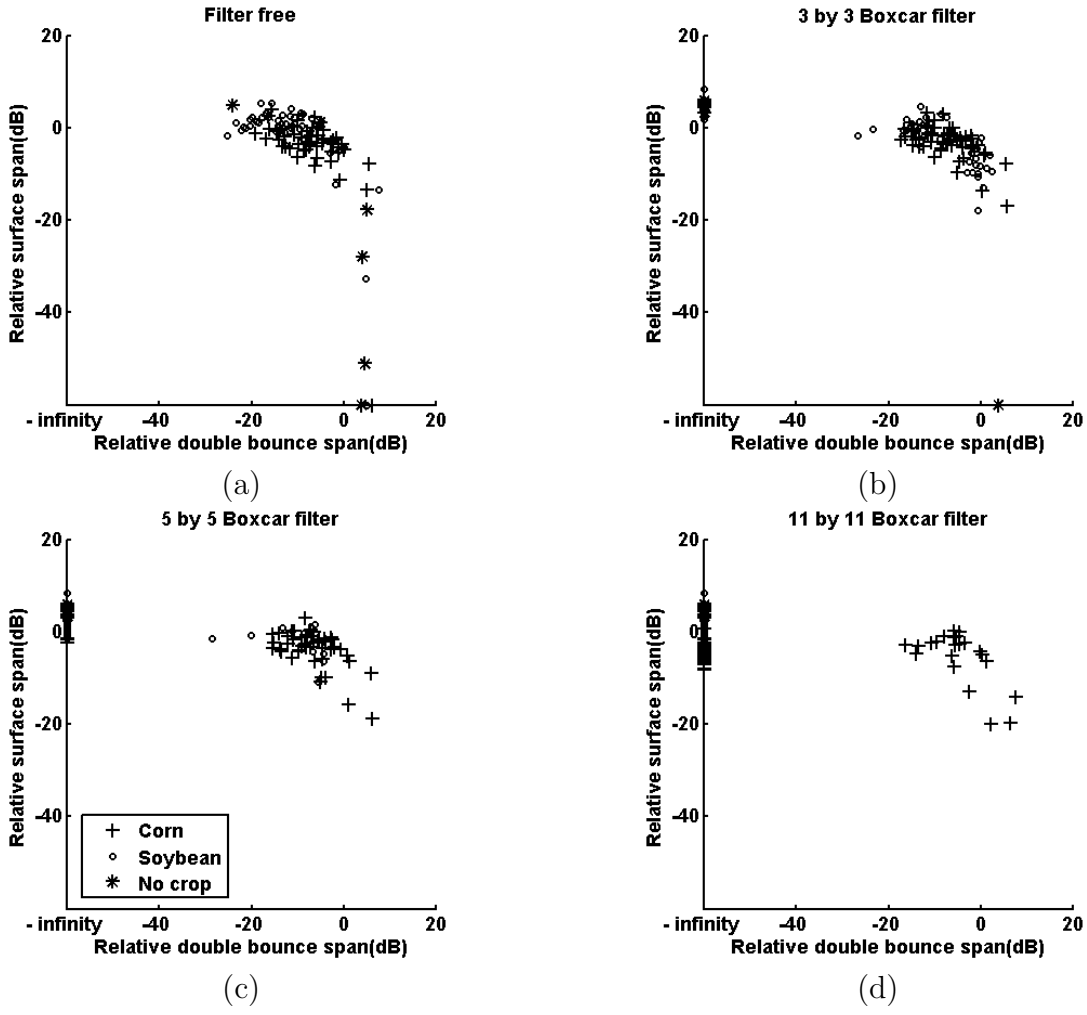

Figure 6.9: Relative surface versus relative double-bounce span for October 9^{th} (a) raw image (b) 3 by 3 window size boxcar filter (c) 5 by 5 window size boxcar filter (d) 11 by 11 window size boxcar filter. The in-situ data are gathered in the same day

The general location of the fields on the similar plots seems to be constant. This observation has been reported in previous chapter and it shows that fields behave somewhat consistently even in different dates until they will be harvested. But also the effect of incidence angle is undeniable. Similar incidence angles produced similar plots. For example figure 6.14 of November 8^{th} and figure 6.11 of October 15^{th} that has the same beam type and incidence angle produced similar plots.

In figure 6.9(a) we have soybeans double-bounce while they gradually move to the negative infinity (in 6.9(b),(6.9c), and 6.9(d)). This pattern is observable in different extents in all of the remaining dates. We also observed that most of the soybeans double-bounce signal disappears between 3 by 3 window size filtered and raw images (e.g. figures 6.11(a) and 6.11(b)). This proves that smallest amount of filtering hinders our ability to detect soybeans attenuation signal in our span values from the stems and the pods.

6.4 The Filtering Effect on H/α Sub-space

The effect of filtering on H/α sub-space for a nominal soybeans field is presented in figure 6.15. Figure 6.15(a), a representative for the raw image, due to the presence of speckle always has zero entropy therefore all the pixels are accumulated on the α angle axis. Smallest amount of filtering similar to 3 by 3 boxcar filter in figure 6.15(b) will reduce the effect of speckle and pixels migrate based on their entropy. Increasing the filtering window size to 5 by 5 will shrunk the cluster in figure 6.15(c) and eventually larger window size like 11 by 11 boxcar filter had the smallest cluster size. This pattern is observable in all of the fields no matter the contents. Our observation shows that the 5 by 5 boxcar filter is similar to an 11 by 11 refined Lee filter and because the latter produced superior results, it has been used in previous chapter. Since only the smoothing effect is the goal of observation in this section, one kind of filter with varying window size is observed. Thus we used boxcar filters for simplicity.

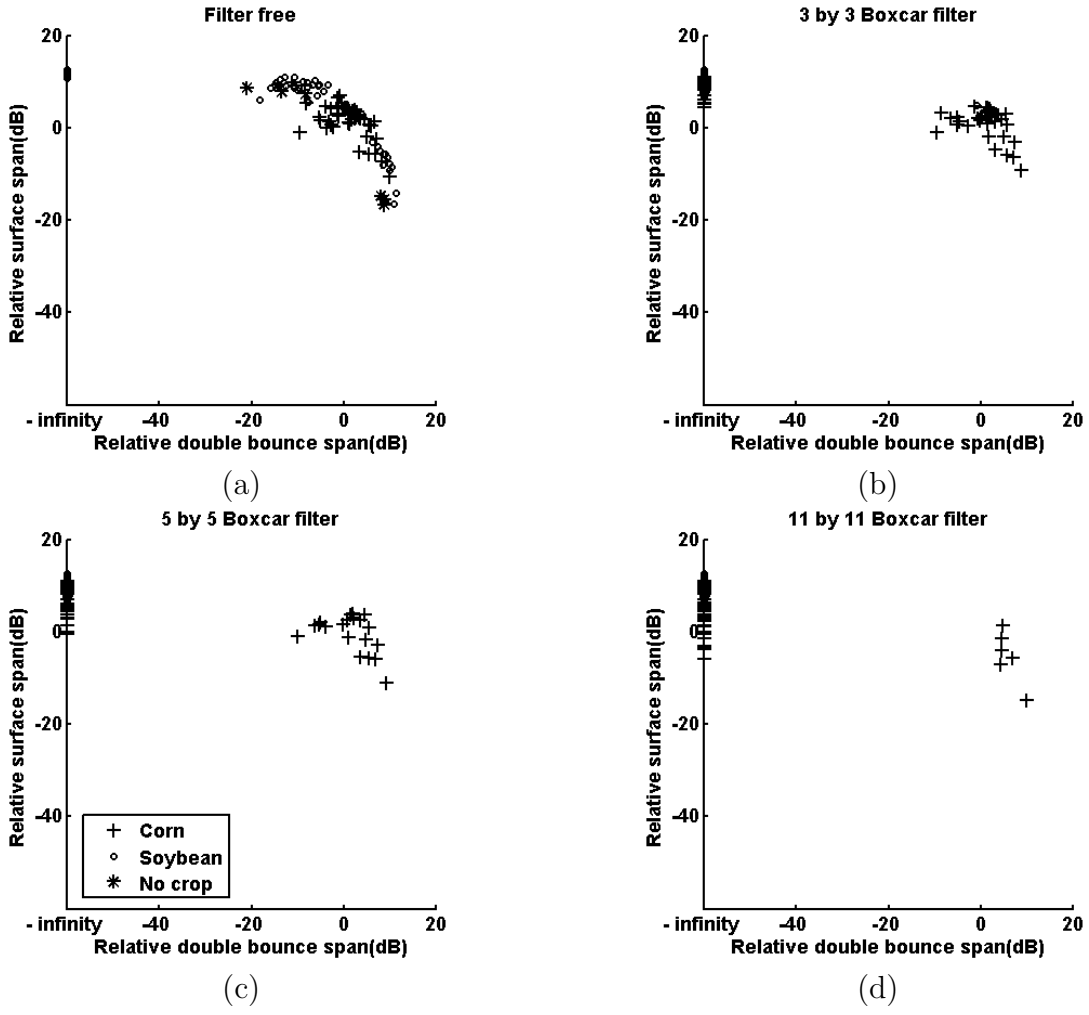

Figure 6.10: Relative surface versus relative double-bounce span for October 12^{th} (a) raw image (b) 3 by 3 window size boxcar filter (c) 5 by 5 window size boxcar filter (d) 11 by 11 window size boxcar filter. The in-situ data are gathered in the same day

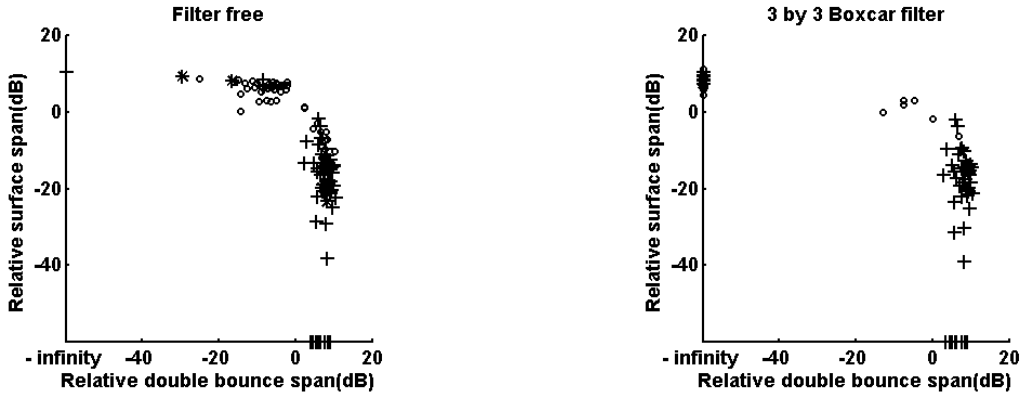

(a)

(b)

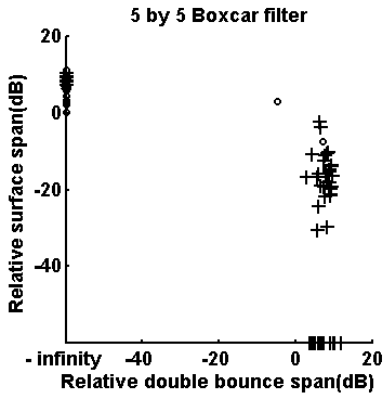

(c)

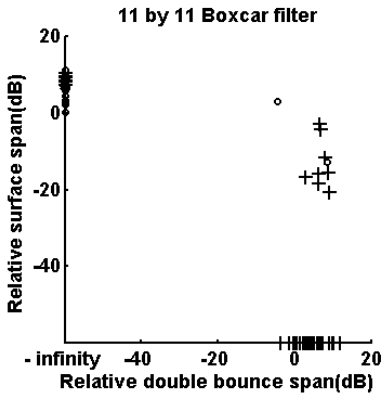

(d)

Figure 6.11: Relative surface versus relative double-bounce span for November 15^{th} (a) raw image (b) 3 by 3 window size boxcar filter (c) 5 by 5 window size boxcar filter (d) 11 by 11 window size boxcar filter. The in-situ data are gathered in the same day

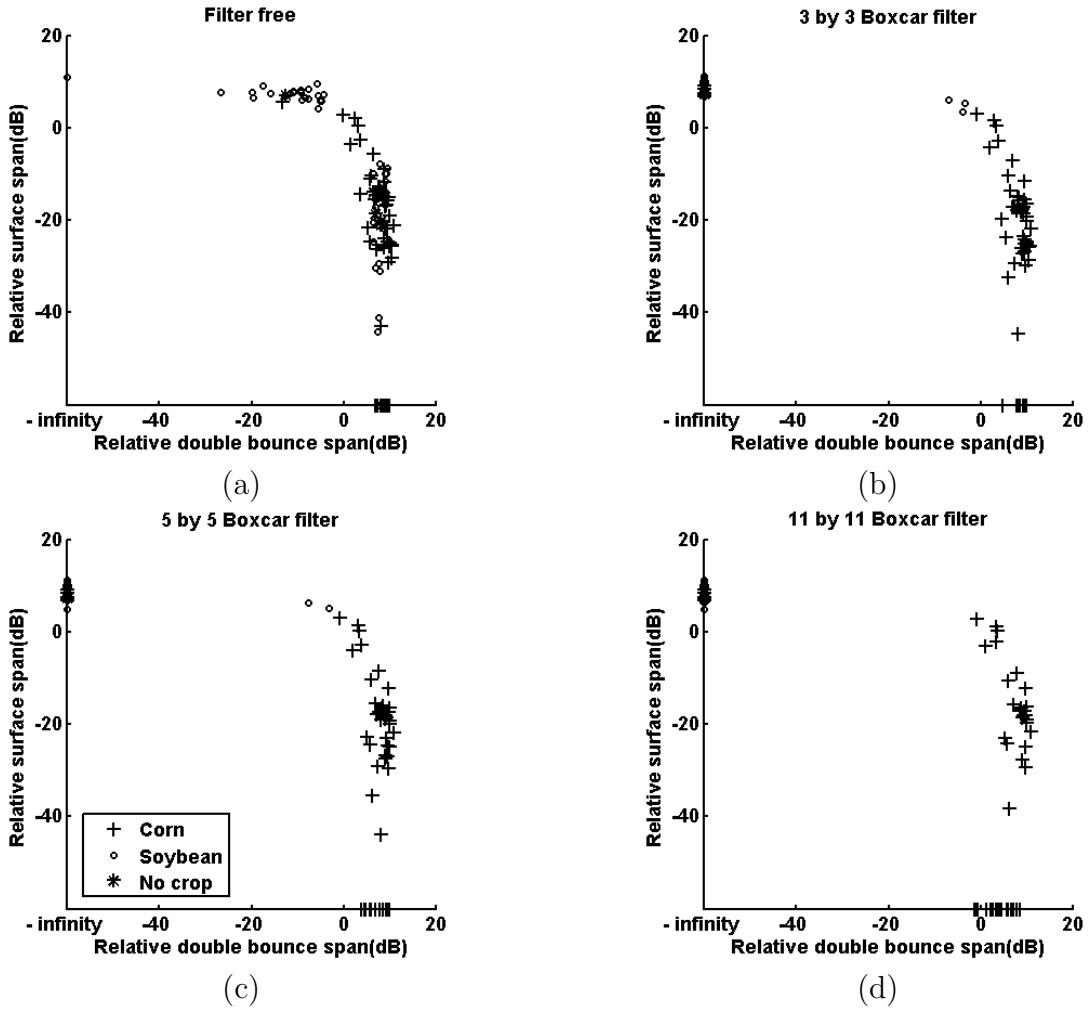

Figure 6.12: Relative surface versus relative double-bounce span for November 2^{nd} (a) raw image (b) 3 by 3 window size boxcar filter (c) 5 by 5 window size boxcar filter (d) 11 by 11 window size boxcar filter. The in-situ data are gathered in the same day

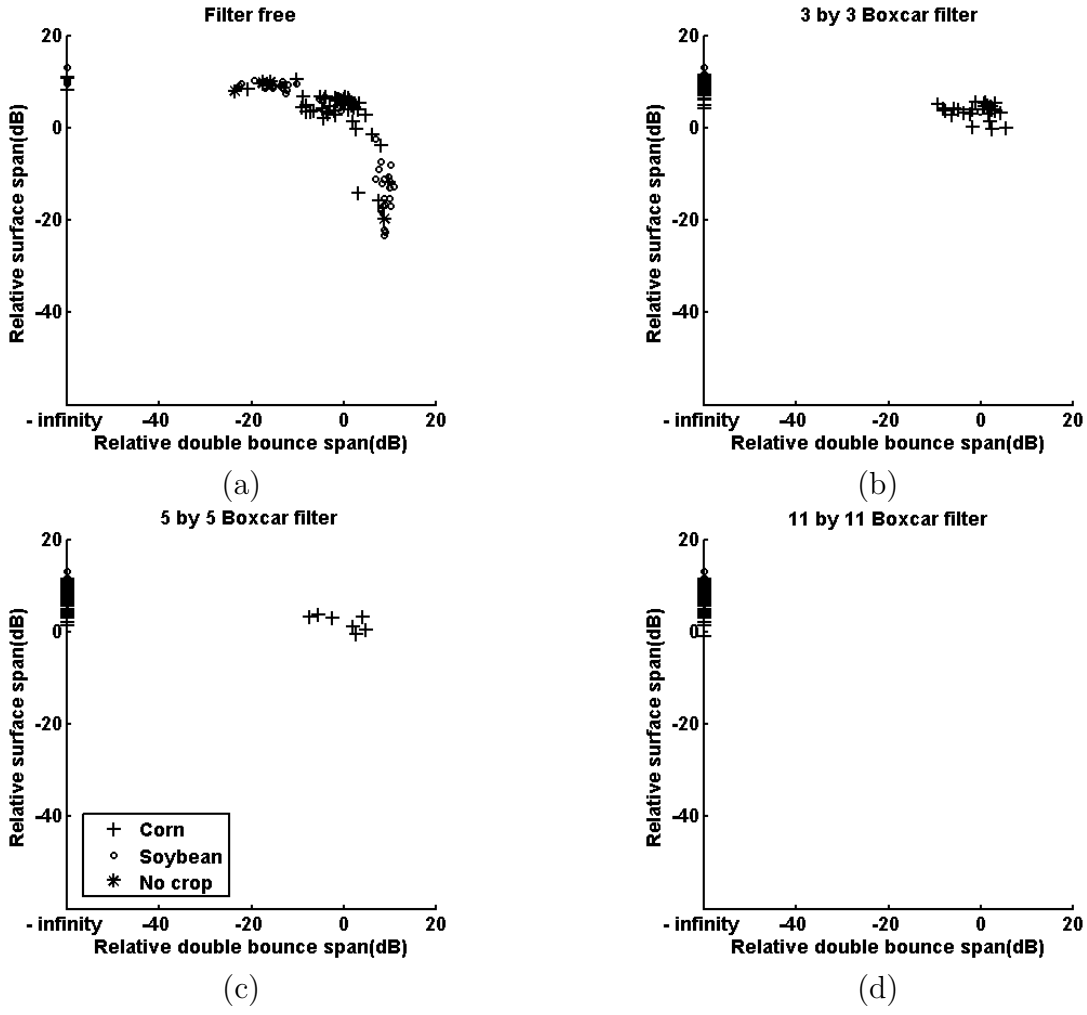

Figure 6.13: Relative surface versus relative double-bounce span for November 5^{th} (a) raw image (b) 3 by 3 window size boxcar filter (c) 5 by 5 window size boxcar filter (d) 11 by 11 window size boxcar filter. The in-situ data are gathered in the same day

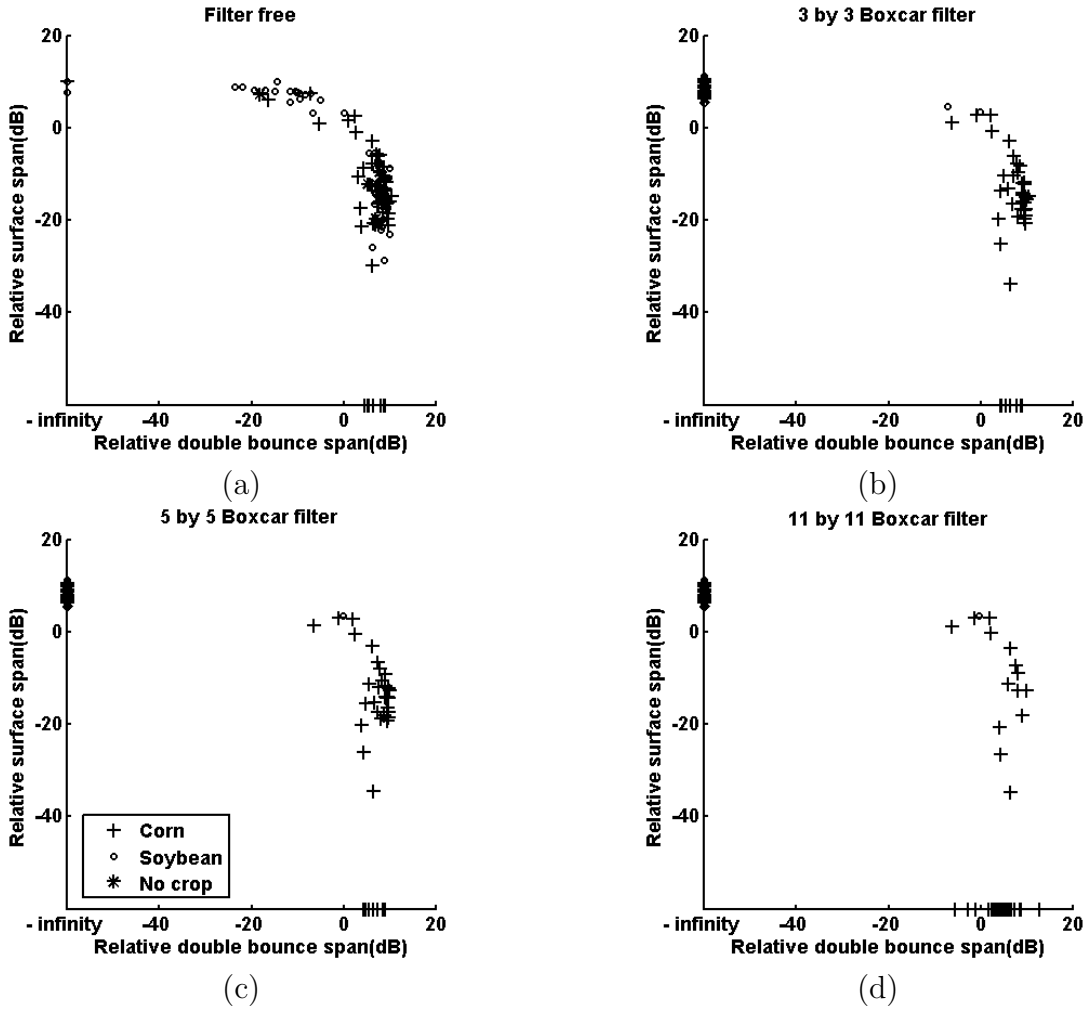

Figure 6.14: Relative surface versus relative double-bounce span for November 8^{th} (a) raw image (b) 3 by 3 window size boxcar filter (c) 5 by 5 window size boxcar filter (d) 11 by 11 window size boxcar filter. The in-situ data are gathered in the same day

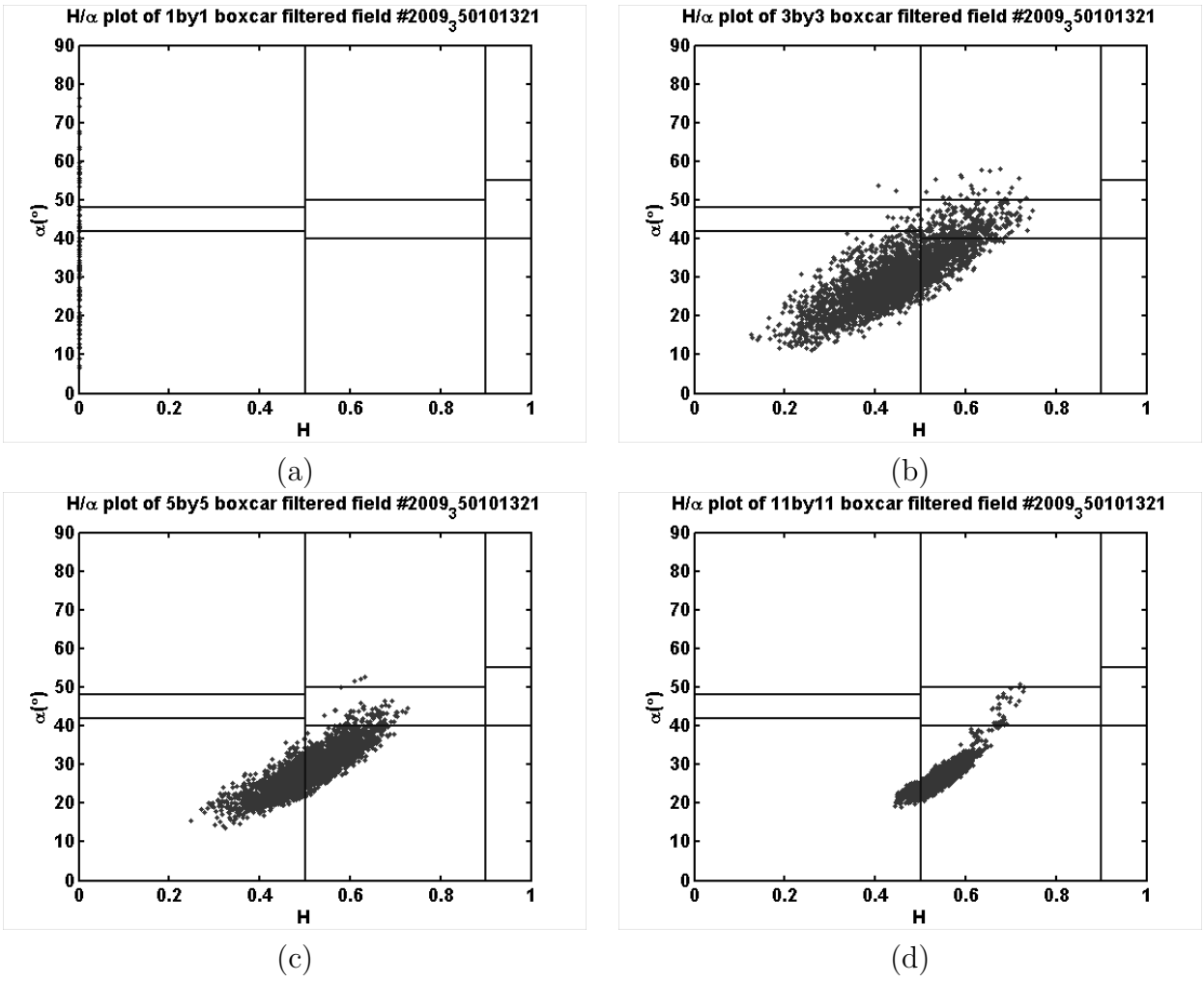

(a) (b)

(c) (d)

Figure 6.15: Filtering effect for typical harvested soybeans field on H/α sub-space (a) raw image (b) 3 by 3 window size boxcar filter (c) 5 by 5 window size boxcar filter (d) 11 by 11 window size boxcar filter. Although plot (a) seems to be empty but all the fields are gathered on the α axis due to the zero entropy of speckle.

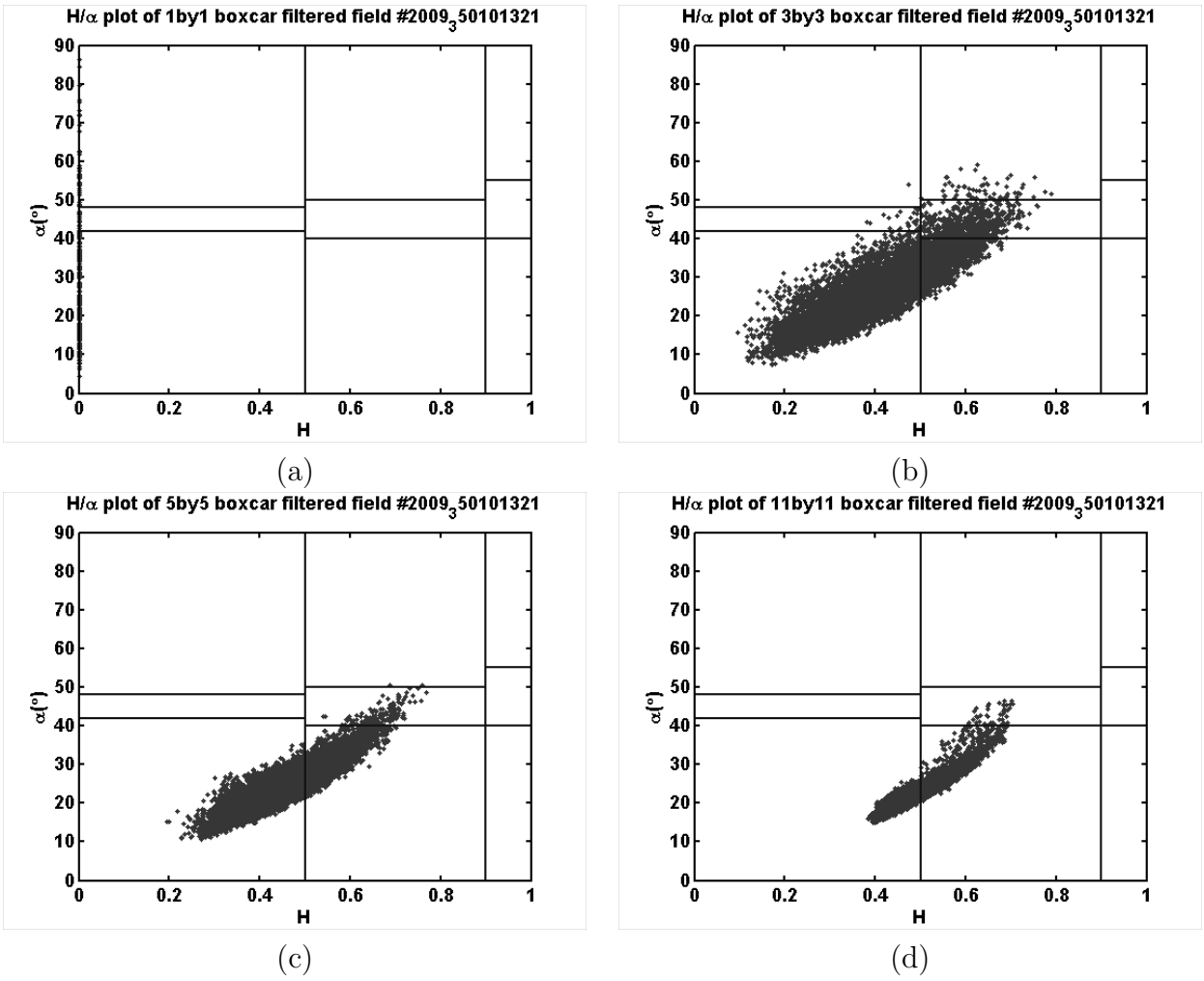

Figure 6.16: Filtering effect for typical harvested no cultivation field on S (a) raw image (b) 3 by 3 window size boxcar filter (c) 5 by 5 window size boxcar filter (d) 11 by 11 window size boxcar filter. Although plot (a) seems to be empty but all the fields are gathered on the α axis due to the zero entropy of speckle.

Most of the times cropped soybean, harvested soybean, and uncultivated land produced very similar H/α signatures. Figures 6.15, 6.16 and 6.17 present how similar these scatter plots could look like in terms of occupying different zones and in terms of their densities in each zone. Every sub figure in each of figures 6.15, 6.16, and 6.17 has a similar counterpart in another figure. This is the heart of the problem with soybeans fields. It appears that at least in terms of H/α sub-space no distinction between these three classes is possible for our C-Band RADARSAT-2 data. And the signal from the senesced soybeans stems and pods is not powerful enough to change this sub-space.

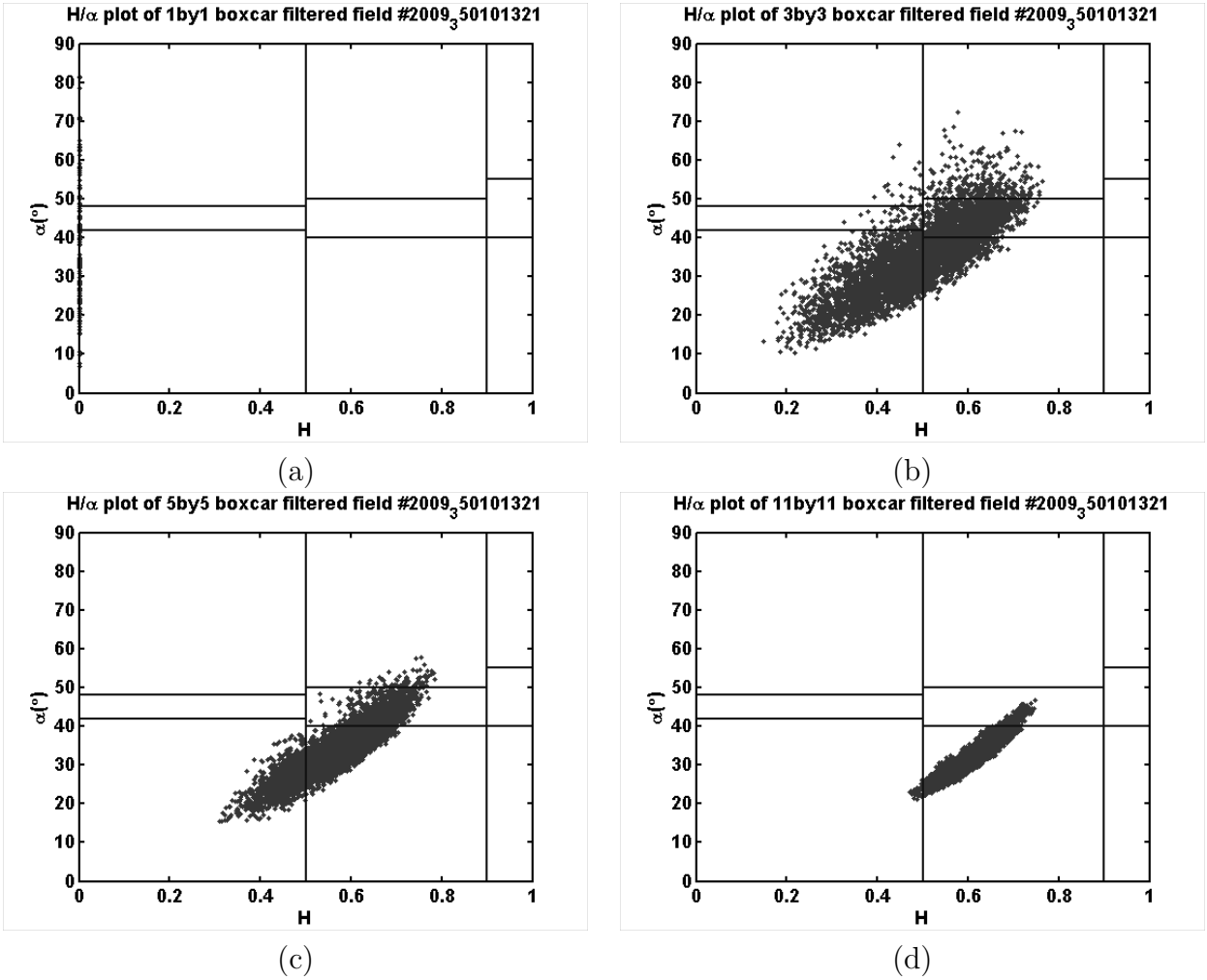

Figure 6.17: Filtering effect for typical cropped soybeans field on H/α sub-space (a) raw image (b) 3 by 3 window size boxcar filter (c) 5 by 5 window size boxcar filter (d) 11 by 11 window size boxcar filter. Although plot (a) seems to be empty but all the fields are gathered on the α axis due to the zero entropy of speckle.

6.4.1 Alternatives Speculations

We implemented Yamaguchi's[80] volume scattering modification to Freeman-Durden algorithm. In Yamaguchi's[80] approach volume scattering could be divided to three covariance matrices based on the $10 \log \frac{\langle |S_{VV}|^2 \rangle}{\langle |S_{HH}|^2 \rangle}$ value. This logarithmic ratio would discriminate between horizontal, vertical and random dipoles. There was a slight change in the outcome of our spans due to this modification. For example, the changes in the relative double-bounce span are varied in different dates from 0.12 dB in November 5^{th} up to 9.97 dB on October 15^{th}, but the general result of classification did not change. As we already mentioned ready-to-harvest soybeans crop has very little volume scattering in C band. We observed that directionality of the stems and branches (dipoles in volume scattering) of the soybeans crop is not enough to help distinguishing senesced soybeans from the harvested one and there are no leaves to provide us with volume scattering from disk like scatterers. Therefore we did not include Yamaguchi's modification in our mainstream algorithm but its code is provided in Appendix H. Yamaguchi's modification may become useful for other purposes such as forestry where volume scattering is more influential signal but not for soybeans in C-Band.

There are three main drawbacks for our data that makes it impossible to use texture analysis. First one is that, agricultural fields are assumed to be homogeneous. Therefore edge and object detections are irrelevant because there should be no room for an area or a target that would stand out. The second issue is that our resolution cell is very large in comparison to the scale of a single crop. Therefore in each resolution cell, more than one crop exists and a mixed signal is observed. The third problem is that speckle also acts as a homogeneous texture. On the other hand analysis based on texture are irrelevant in zero entropy, therefore performing texture analysis on raw images are also useless for agricultural fields.

In Freeman-Durden model, volume scattering is calculated straight forwardly from $\langle |S_{HV}|^2 \rangle$. If closely inspected, this actually comes from the assumptions made for Bragg scattering in

surface and double-bounce scattering. Bragg scattering is a 'zero entropy' based physical model used in physical optics (PO). In theory Bragg scattering covers only a narrow range of very low entropy surface scattering within the H/α sub-space. But this physical barrier has not stopped scientists from using this algorithm for cases where Bragg scattering would not be strictly applicable. For example, H/α scatter-plots of forests, where Freeman-Durden has been designed for, generally have much wider range of medium to low entropy surface scattering[45][13].

Senesced soybeans fields show considerably more surface scattering based on different methods. Analysis in section 6.2 based on multiple parameters described in table 2.1 shows that senesced soybeans is similar to bare soil and harvested soybeans fields. Also H/α plots presented in section 6.4 comes to the same conclusion. Based on the analysis in section 5.3, the defined H_{rough} parameter also cannot differentiate between senesced soybean, harvested soybeans and bare soil in harvesting season. H_{rough} also showed that soybeans fields are most of the time in smooth to mildly rough regions.

In the RFD algorithm, the r ratio is based on the H/α domain and therefore it covers almost all types of observable surface scattering. Therefore RFD is also modified to have better sensitivity to other types of surface scattering. But even RFD was not able to sense any difference in surface scattering span of senesced and harvested soybeans.

Yet more advanced surface scattering models may improve soybeans separation. Modified surface scattering formulations will introduce additional unknowns to our model. Solving such models are under-determined cases and they have optimization solutions. But whether or not it can drastically improve our ability to discern soybeans crop from the harvested field is not clear. Also using empirical models such as Oh[55] model for new equations adds additional assumptions for physical parameters such as RMS height and dielectric constant. One such model has already been developed by assuming cross polarized Fresnel reflection ratios only for the surface scattering. This assumption has resulted in under-determined

system of nine equations and eleven unknowns and could only be solved by optimization algorithms. Since one of the objectives of this study was to develop a standalone algorithm, these types of solutions were not investigated.

A great deal of C-Band SAR related literature for soybeans analysis, have used field observation of vegetation moisture and soil moisture. Chiu et al.[11] observed that the backscattering from the senesced soybeans is very sensitive to the soil moisture. Le Toan et al.[41], De Roo et al.[16], Wigneron et al.[76] in different researches used observed volumetric water content of canopy for soybeans observations on C-band. It appears that ground observations for vegetation and soil moisture would help to classify the harvested soybeans fields. But these extensive field-based measurements are the exact reason that remote sensing was introduced as an alternative in first place.

Another solution is the integration of optical imagery with SAR data. McNairn et al. [48] achieved higher accuracy by fusion of the optical imagery in comparison to using only C-band SAR for classification. Supervised classifications are familiar concept to any remote sensing project, but due to the fully automated constraint defined as our objectives it has been putted aside.

Maybe a better suggestion would be the use of multi channel SAR data, because no additional ground measurements are necessary. L band has greater sensitivity to the crops for medium to high biomass targets in comparison to C band ([33],[8]). But ready to harvest cropped soybeans is very low biomass vegetation. Therefore higher frequencies seem more promising. Wu et al.[78] showed that X-band SAR have backscattering from upper 30% of the soybeans crop while corn has backscattering from the leaves. Kwon et al.[40] used both X-band SAR and ground observation soil and vegetation moisture for their research on soybeans fields and reported a successful removal of vegetation by X-band SAR. Since we have successfully classified and removed the cropped corn fields, using high frequency channels such as X-band for the second step of our decision tree might be able to extract

the senesced soybeans fields.

6.5 Second Step of Decision Tree

Table 6.1: Final assessment results of both cropped corn and soybeans classification for 09/18/2009.

Class	Prod. Acc. (Percent)	User Acc. (Percent)	Prod. Acc. (Pixels)	User Acc. (Pixels)
CC	98.14815	58.24176	53/54	53/91
CS	27.08333	68.42105	13/48	13/19
H	9.090909	33.33333	1/11	1/3
Overall Accuracy =			(67/113) =	59.29%
Kappa Coefficient =				0.25

Table 6.2: Final assessment results of both cropped corn and soybeans classification for 10/09/2009.

Class	Prod. Acc. (Percent)	User Acc. (Percent)	Prod. Acc. (Pixels)	User Acc. (Pixels)
CC	93.47826	72.88136	43/46	43/59
CS	60.86957	35.89744	14/23	14/39
H	25	73.33333	11/44	11/15
Overall Accuracy =			(68/113) =	60.18%
Kappa Coefficient =				0.40

Section 6.3 implies that RFD algorithm on unfiltered raw RADARSAT-2 may provide some information about soybeans crop. Figure 6.18 presents the aftermath of corn classification on the remaining fields but the calculated spans in this figure are based on raw data RFD. The observable two clusters lead to an empirical second step decision tree for cropped soybeans discrimination.

The rule for this soybeans decision tree is:

I: if $R_{P_s} > R_{P_d}$ then it is cropped soybean.

The definition of this rule is solely based on experimental observation on similar graphs to figure 6.18. We observed that larger number of the senesced cropped soybeans have high surface scattering along with lower double-bounce scattering. This observation in no way is a

Table 6.3: Final assessment results of both cropped corn and soybeans classification for 10/12/2009.

Class	Prod. Acc. (Percent)	User Acc. (Percent)	Prod. Acc. (Pixels)	User Acc. (Pixels)
CC	100	93.87755	46/46	46/49
CS	86.95652	43.47826	20/23	20/46
H	38.63636	94.44444	17/44	17/18
Overall Accuracy =			(83/113) =	73.45%
Kappa Coefficient =				0.61

Table 6.4: Final assessment results of both cropped corn and soybeans classification for 10/15/2009.

Class	Prod. Acc. (Percent)	User Acc. (Percent)	Prod. Acc. (Pixels)	User Acc. (Pixels)
CC	98.03922	94.33962	50/51	50/53
CS	96	53.33333	24/25	24/45
H	40.54054	100	15/37	15/15
Overall Accuracy =			(89/113) =	78.76%
Kappa Coefficient =				0.68

Table 6.5: Final assessment results of both cropped corn and soybeans classification for 11/02/2009.

Class	Prod. Acc. (Percent)	User Acc. (Percent)	Prod. Acc. (Pixels)	User Acc. (Pixels)
CC	95.2381	80	40/42	40/50
CS	70	16.66667	7/10	7/42
NC	26.22951	76.19048	16/61	16/21
Overall Accuracy =			(63/113) =	55.75%
Kappa Coefficient =				0.37

Table 6.6: Final assessment results of both cropped corn and soybeans classification for 11/05/2009.

Class	Prod. Acc. (Percent)	User Acc. (Percent)	Prod. Acc. (Pixels)	User Acc. (Pixels)
CC	88.09524	86.04651	37/42	37/43
CS	70	17.07317	7/10	7/41
NC	40.98361	86.2069	25/61	25/29
Overall Accuracy =			(69/113) =	61.06%
Kappa Coefficient =				0.43

Table 6.7: Final assessment results of both cropped corn and soybeans classification for 11/08/2009.

Class	Prod. Acc. (Percent)	User Acc. (Percent)	Prod. Acc. (Pixels)	User Acc. (Pixels)
CC	96.66667	65.90909	29/30	29/44
CS	50	17.3913	4/8	4/23
H	54.66667	89.13043	41/75	41/46
Overall Accuracy =			(74/113) =	65.49%
Kappa Coefficient =				0.45

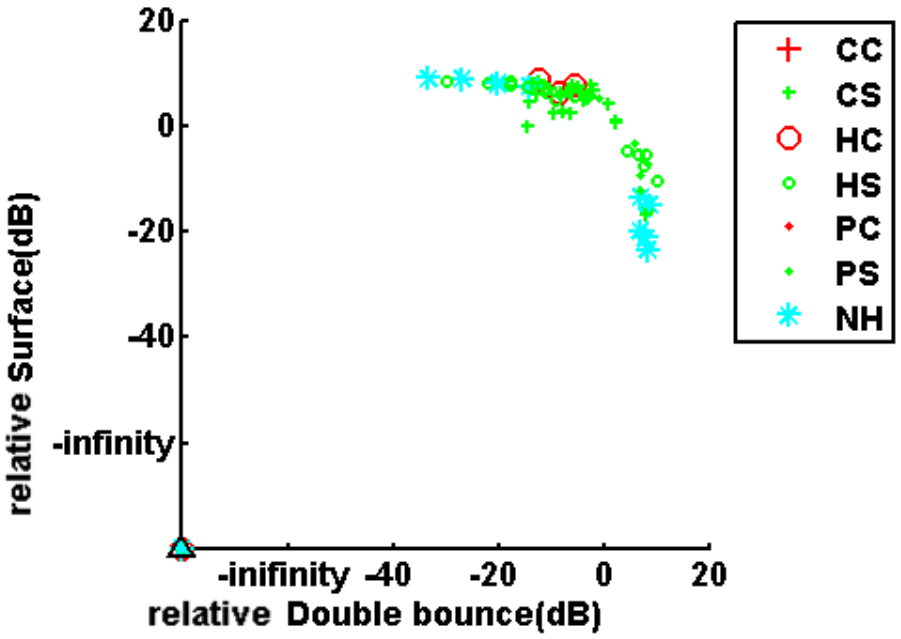

Figure 6.18: The raw data relative surface versus double-bounce span of the remaining fields after corn classification for October 15^{th}.

certain fact and as we mentioned before it was really hard to discriminate soybeans with high certainty in our observations. With this rule a two step classification is complete. Cropped corn and cropped soybeans is classified and the remaining fields are harvested fields (H). The harvested class also includes the no cultivation (NC or NH in our figures and tables), and partially corn (PC) and partially soybeans (PS) fields.

The confusion matrices for two step decision tree are included in Appendix I. Tables 6.1 to 6.7 are the accuracy assessment for our two step classification. The classification of

September 15^{th} is excluded because it had failed in our first step decision tree. Although these classifications produced better and more reliable results than unsupervised classifications but the weakness of the second step tremendously weakened the final assessment results. The maximum accuracy for harvest detection is 78.76% with $\kappa = 0.68$ in comparison to the 97.35% with $\kappa = 0.95$ for corn detection. These results will further improve if the PC class is fused with CC class as it is tabulated in table 6.8. The user's accuracy for harvested class are generally high, this means that classified harvested fields are most likely harvested fields in reality. But since the producer's accuracies are low, some of the harvested fields did not classified properly. Probably row direction, type of harvest, and the tillage effects had some

Table 6.8: The result of soybeans and corn two step decision tree with mixing CC and PC classes

Date	Accuracy	κ
09/18/2009	59.29%	0.24776
10/09/2009	62.83%	0.43270
10/12/2009	71.68%	0.57816
10/15/2009	78.76%	0.67660
11/02/2009	60.18%	0.42366
11/05/2009	65.49%	0.49426
11/08/2009	75.22%	0.59627

influence on the scattering behavior of soybean fields. No field observation regarding type of harvest and tillage effects were available, and in case of row directions where field data was available, due to the time constraints further observations has not been conducted. At least in the case of row directions they may have caused some soybean field to have higher roughness values. We decided to merge different row directions in one class due to our predefined objectives. If discrimination would have been applied for different row directions, classification results may have further improved.

We once again want to emphasize that other data sources such as field observation of vegetation moisture or SAR data with shorter wavelengths such as X-band is necessary to improve these results.

Chapter 7

Conclusion and future work

7.1 Conclusion

An algorithm based on both physical and statistical models have been formulated and implemented for harvest detection on PolSAR data. This algorithm uses the same physical models as Freeman-Durden decomposition. Freeman-Durden decomposition solves sets of under determined equations by assuming constant values for one of its unknowns each time. The proposed algorithm overcomes the under-determined system by adding an equation from another source to remove this degree of freedom. The statistical space of H/A/α was targeted since one is able to associate samples location in the feature space, with physical scattering characteristics. Therefore a physical and mathematical rationale was developed to connect the physically defined parameters to a ratio based on the statistical feature space. This ratio became the missing link for solving the same sets of equations as Freeman-Durden model. A novel solution have been mathematically developed leading to a forth degree polynomial with a single unknown. Since it is possible to produce an explicit answer to any fourth degree polynomial, the explicit roots based on the known parameters were formulated. The estimation of the remaining unknowns was then straightforward and the final power contributions of three physical based mechanisms of surface, double-bounce and volume scattering to the total power has been estimated.

Since the proposed algorithm is field-based rather than pixel based, each agricultural field must be extracted from the SAR image and fed separately to the proposed algorithm. Also a novel roughness measure were also introduced based on some statistical assumptions on the H/α sub-space. At first this new roughness measure has been coupled with surface scattering from each field to present the ability of the roughness measure in describing some

surface behaviors. Then the same roughness measure has been coupled with the double-bounce portion of total power and field observation of agricultural practice to describe the behavior of different crop type/stages in each SAR image. The latter observation postulated a decision tree classification scheme. The incidence angle played a great role; for very steep incidence angle the roughness measure was used as the rule, while for the remaining incidence angles the refined Freeman-Durden (RFD) algorithm's double-bounce has been used as the rule. This classification scheme failed on the image that was taken prior to harvest but performed extremely well for the images taken in the harvest season.

In chapter 6 soybeans fields have been analyzed with PolSAR parameters and it was concluded that our data and our methods are insufficient for discriminating senesced soybeans from the remaining fields. Some polarimetric parameters were analyzed without any acceptable outcome. The effect of filtering on soybeans signal was also analyzed and the final decision was made to perform the RFD algorithm on a unfiltered raw SAR data. Therefore another simple decision tree solely based on the inspection of the surface versus double-bounce scattering scatter-plots has been devised and implemented. As expected, the final result of the classification was not satisfactory. Therefore suggestions provided on the possible improvements for segregating senesced and harvested soybeans fields.

For evaluation and comparison, a series of unsupervised classification has also been performed and the classification assessment results did not show any superiority even over the proposed two step decision tree. Also the original Freeman-Durden (OFD) has been implemented and a comparison has been made between both RFD and OFD. Once again superiority of the RFD in case of corn fields was established. The maximum of 97.35% (99.08% if partial corn assumed as cropped corn) and the minimum of 83.19% overall accuracy for corn discrimination in harvest season has been achieved. As for the two step classification over corn and soybeans the maximum accuracy was only 78.76%.

7.2 Future Work

The proposed algorithm provided excellent results for separating senesced corn fields from the rest of the fields. But there is always room for improvements. Strictly speaking, the discrimination between senesced and harvested soybeans fields on the other hand was not a success. The reasons behind the problem and possible improvements have already been discussed in the soybeans chapter, but further improvements are a possible certainty. Therefore several future research directions are as follows

I: The RFD algorithm was compared to the OFD algorithm in terms of the processing routes. But the behavior of individual agricultural fields in terms of those processing routes has not been thoroughly investigated. The preliminary observations did not provide deep insights and more in-depth analysis could bring new lights to the matter. For example, multiple roots are not completely removed by the proposed algorithm. Both the existence reason and the removal would need further investigations.

II: H/α sub-space could also provide information about the different types of volume scattering. This concept could be used as another modification where three weighted volume scattering covariance matrices based on three volume scattering zones would be used in refined Freeman-Durden algorithm.

III: The filtering effect on the RFD algorithm's results are only briefly observed and discussed. Migration of the agricultural field due to the change in window size is another topic that could be well exploited.

IV: It seems that some fields have consistent span values even in different imaging situation while the others have not. The migration of the RFD spans in different RADARSAT-2 images and different dates are also an interesting topic to be exploited.

V: The proposed roughness measure and the spans resulted from RFD may contain some

information regarding the tillage practices inside agricultural fields. This line of research may include row direction, type of harvest and it needs a-priori knowledge gathered from field observations.

VI: The Bragg surface scattering used as the physical model for surface scattering is not an ideal model for agricultural fields. Using more general physical models that include wider range of surface scattering may enhance the results and therefore great deal of possibilities for improvement lie on this line.

VII: The performance of the proposed algorithm could be evaluated for other applications such as forestry although there are drawbacks. For example, for natural entities like forests where boundaries are not predefined this algorithm needs other methods to provide the boundaries. Sea ice on the other hand has natural boundaries that are not hard to extract, therefore RFD algorithm may provide interesting observations.

VIII: X-band SAR has the potential to observe soybean, this potential paired with a C-band image could also be exploited by RFD algorithm. The idea of multiple steps decision tree with multiple channels SAR could be very intriguing. Each frequency band could sense special crops and we believe that this is the best method for harvest detection with RFD algorithm.

Bibliography

[1] ALLPOSTERS.COM. Maize, or indian corn plant. Tech. rep.,

http://www.allposters.com/-sp/Maize-or-Indian-Corn-Plant-Posters_i2873260_.htm

[2] AN, W., CUI, Y., AND YANG, J. Three-component model-based decomposition for polarimetric SAR data. *IEEE Transactions on Geosciense and Remote Sensing 48*, 6 (2010), 2732–2739.

[3] BAGHDADI, N., BOYER, N., TODOROFF, P., EL HAJJ, M., AND BEGUE, A. Potential of SAR sensors TerraSAR-X, ASAR/ENVISAT and PALSAR/ALOS for monitoring sugarcane crops on reunion island. *Remote Sensing of Environment 113*, 8 (2009), 1724 – 1738.

[4] BAGHDADI, N., CRESSON, R., TODOROFF, P., AND MOINET, S. Multitemporal observations of sugarcane by TerraSAR-X images. *Sensors 10* (2010), 8899–8919.

[5] BARONTI, S., FRATE, F., FERRAZZOLI, P., PALOSCIA, S., PAMPALONI, P., AND SCHIAVON, G. SAR polarimetric features of agricultural areas. *International Journal of Remote Sensing 16*, 14 (1995), 2639–2656.

[6] BOERNER, W. B., MOTT, H., LÜNEBURG, E., LIVINGSTONE, C., BRISCO, B., J., B. R., S., P., CLOUDE, S., KROGAGER, E., LEE, J., SHULER, D., VAN ZYL, J., RANDALL, D., BUDKEWITSCH, P., AND POTTIER, E. *Principles and applications of imaging radar, Manual of Remote Sensing*, 3rd ed. John Wiley & Sons, Inc., Toronto, 1998.

[7] BOHNER, H. Re-thinking soybean row widths. Ministry of Agriculture Food & Rural Affairs, March 2005.

[8] Canisius, F. ., and R., F. ALOS PALSAR L-band polarimetric SAR data and in situ measurements for leaf area index assessment. *Remote Sensing Letters 3*, 3 (2012), 221–229.

[9] Chen, E. X., Li, Z. Y., Tan, B. X., Pang, Y., Tian, X., and Li, B. B. Supervised Wishart classifier for rice mapping using multi-temporal ENVISAT ASAR APS data. In *Envisat Symposium* (2007), vol. SP-636, pp. 23–27.

[10] Chen, J. S., Hui, L., and Pei, Z. Y. Application of ENVISAT ASAR data in mapping rice crop growth in southern china. *IEEE Transactions on Geoscience and Remote Sensing Letters 4(3)* (2007), 431–435.

[11] Chiu, T., Sarabandi, K., and Ulaby, F. T. Polarimetric backscattering measurements of herbaceous vegetation: a sensitivity study for soil moisture retrieval. In *International Geoscience and Remote Sensing Symposium (IGARSS)* (1996), vol. 2, pp. 1070–1072.

[12] Clabby, C. How science aims to feed seven billion people. *BBC In depth, online newspaper article* (2012).

[13] Cloude, S., and Pottier, E. An entropy based classification scheme for land applications of polarimetric SAR. *IEEE Transactions on Geoscience and Remote Sensing 35* (1997), 68–78.

[14] Crist, E. P., and Cicone, R. C. A physically-based transformation of thematic mapper data, the TM Tasseled Cap. *IEEE Transactions on Geosciences and Remote Sensing GE-22* (1984), 256–263.

[15] de Matthaeis, P., Ferrazzoli, P., Schiavon, G., and Solimini, D. Agriscatt and maestro: multifrequency radar experiments for vegetation remote sensing. In

MAESTRO-1/AGRISCATT: Radar Techniques for Forestry and Agricultural Applications, Final Workshop, The Netherlands (pp. 231-248). Paris, France: European Space Agency. (1992).

[16] De Roo, R., Du, Y., Ulaby, F., and Dobson, M. A semi-empirical backscattering model at L-band and C-band for a soybean canopy with soil moisture inversion. *IEEE Transactions on Geosciense and Remote Sensing 39*, 4 (2001), 864–872.

[17] De Roo, R. D., Ulaby, F. T., and Dobson, M. Using microwave radar for soil moisture inversion under soybean canopies. In *International Geoscience and Remote Sensing Symposium (IGARSS)* (1998), vol. 1, pp. 94–96.

[18] Dobson, M. C., and Ulaby, F. Priliminary evaluation of the SIR-B response to soil moisture, surface roughness, and crop canopy cover. *IEEE Transactions on Geosciense and Remote Sensing 24*, 4 (1986), 517–526.

[19] Dorff, E. The soybean, agriculture's jack-of-all-trades, is gaining ground across canada. *Component of Statistics Canada, Canadian Agriculture at a Glance 96-325-XIE* (2007), 1–14.

[20] Faucette, W. M. A geometric interpretation of the solution of the general quartic polynomial. *The American Mathematical Monthly 103*, 1 (1996), 51–57.

[21] Ferro Famil, L., Pottier, E., and Lee, J. Unsupervised classification of multifrequency and fully polarimetric SAR images based on the H/A/alpha-Wishart classifier. *IEEE Transactions on Geoscience and Remote Sensing 39*, 11 (2001), 2332–2342.

[22] Freeman, A. Fitting a two-component scattering model to polarimetric SAR data from forests. *IEEE Transactions on Geosciense and Remote Sensing 45*, 8 (2007), 2583–2592.

[23] Freeman, A., and Durden, S. A three component scatteriong model for plarimetric SAR data. *IEEE Transactions on Geoscience and Remote Sensing, 36*, 3 (1998), 963–973.

[24] Fung, A. K. *Microwave Scattering and Emission Models and their Applications.* Arctech House Norwood USA, 1994.

[25] Gallego, J., Craig, M., Michaelsen, J., Bossyns, B., and Fritz, S. Geoss community of practice ag 0703a. best practices for crop area estimation with remote sensing. Tech. rep., EUR - Scientific and Technical Research serie, 24104 EN - Joint Research Centre , Institute for the Protection and Security of the Citizen, 2008.

[26] Gupta, S. If we are what we eat, americans are corn and soy. Tech. rep.,

`http://articles.cnn.com/2007-09-22/health/kd.gupta.column_1_high-fructose-corn-syrup-corn-refiners-association-soybean-oil?_s=PM:HEALTH`

2007.

[27] Hajnsek, I. *INVERSION OF SURFACE PARAMETERS USING POLARIMETRIC SAR.* PhD thesis, Friedrich Schiller University Jena, 2001.

[28] Hajnsek, I., Pottier, E., and Cloude, S. Inversion of surface parameters from polarimetric SAR. *Geoscience and Remote Sensing, IEEE Transactions on 41*, 4 (april 2003), 727 – 744.

[29] Harris, T. Green team. Tech. rep., http://publications.mcgill.ca/headway/magazine/green-team/, 2012.

[30] "Harvest". In merriam-webster.com. Tech. rep., http://www.merriam-webster.com/dictionary/harvest, 2012.

[31] Hernandez, M. A., Robles, M., and Torero, M. Fires in russia, wheat production, and volatile markets: Reasons to panic? Tech. rep., International Food Policy Research Institute(ifpri.org), 2010.

[32] Hoekman, D. H., and Vissers, M. M. A new polarimetric classification approach evaluated for agricultural crops. *IEEE TRANSACTIONS ON GEOSCIENCE AND REMOTE SENSING 41*, 12 (2003), 2881–2889.

[33] Inoue, Y., Kurosu, T., Maeno, H., Uratsuka, S., Kozu, T., and Dabrowska-Zielinska, K. Season-long daily measurements of multifrequency (Ka, Ku, X, C and L) and full-polarization backscatter signatures over paddy rice and their relationship with biological variables. *Remote Sensing of Environment 81* (2002), 194–204.

[34] Jiao, X., McNairn, H., Shang, J., Pattey, E., Liu, J., and C., C. The sensitivity of RADARSAT-2 polarimetric SAR data to corn and soybean leaf area index. *Canadian Journal of Remote Sensing 37*, 1 (2011), 69–81.

[35] Kandel, H. Soybean nodulation(6/21/12). Tech. rep., http://www.ag.ndsu.edu/cpr/plant-science/soybean-nodulation-6-21-12/, 2012.

[36] Karlen, D., and Kasperbauer, M. J. Row orientation and configuration effects on canopy light spectra and corn growth. *Applied Agricultural Research 4*, 1 (1989), 51–56.

[37] Karlen, D. L., and Camp, C. R. Row spacing, plant population, and water management effects on corn in the atlantic coastal plain. *Agronomy Journal 77* (1985), 393–398.

[38] Kim, Y., Jackson, T., Bindlish, R., Lee, H., and Hong, S. Radar vegetation index for estimating the vegetation water content of rice and soybean. *IEEE Geoscience and Remote Sensing Letters* (2011).

[39] Kouskoulas, Y., Ulaby, F., and Pierce, L. The Bayesian hierarchical classifier (BHC) and its application to short vegetation using multifrequency polarimetric SAR. *IEEE Transactions on Geoscience and Remote Sensing 42*, 2 (feb. 2004), 469–477.

[40] Kwon, S., Hwang, J., and Oh, Y. Soil moisture inversion from X-band SAR and scatterometer data of vegetation fields. In *International Geoscience and Remote Sensing Symposium (IGARSS)* (jul. 2011), pp. 3140–3143.

[41] Le Toan, T., Nghiem, S., Kong, J., and Han, H. Application of random medium model to remote sensing of vegetation. In *Digest - International Geoscience and Remote Sensing Symposium (IGARSS)* (1991), vol. 4, pp. 1875–1878.

[42] Le Toan, T., Ribbes, F., Wang, L., Floury, N., Ding, K., Kong, J. A., Fujita, M., and Kurosu, T. Rice crop mapping and monitoring using ers-1 data based on experiment and modeling results. *IEEE Transactions of Geoscience and Remote Sensing 35* (1997), 41–56.

[43] Lee, J. Digital image enhancement and noise filtering by use of local statistics. *IEEE Transactions on Pattern Analysis and Machine Intelligence PAMI-2*, 2 (1980), 165–168.

[44] Lee, J., Grunes, M. R., Ainsworth, T. L., Du, L.-J., Schuler, D. L., and Cloude, S. R. Unsupervised classification using polarimetric decomposition and the complex wishart classifier. *IEEE Transactions on Geoscience and Remote Sensing 37*, 5 (1999), 2249–2258.

[45] Lee, J., and Pottier, E. *Polarimetric Radar Imaging: From Basics To Applications*. Taylor & Francis, Inc., 2009.

[46] Lopez-Sanchez, J. M., Ballester-Berman, J. D., and Hajnsek, I. First results of rice monitoring practices in spain by means of time series of TerraSAR-X dual-pol

images. *IEEE Journal Of Selected Topics In Applied Earth Observations And Remote Sensing 3(3)* (2010), 1–11.

[47] McNairn, H., and B., B. The application of C-band polarimetric SAR for agriculture: a review. *Canadian Journal of Remote Sensing 30*, 3 (2004), 525–542.

[48] McNairn, H., Champagne, C., Shang, J., Holmstrom, D., and G., R. Integration of optical and synthetic aperture radar (SAR) imagery for delivering operational annual crop inventories. *ISPRS Journal of Photogrammetry and Remote Sensing 64* (2009), 434–449.

[49] McNairn, H., Duguay, C., Brisco, B., and Pultz, T. The effect of soil and crop residue characteristics on polarimetric radar response. *Remote Sensing of Environment 80* (2002), 308–320.

[50] McNairn, H., van der Sanden, J., Brown, R., and Ellis, J. The potential of RADARSAT-2 for crop mapping and assessing crop condition. *Second International Conference on Geospatial Information in Agriculture and Forestry, Lake Buena Vista, Florida (USA), 10-12 January 2000 2* (2000), 81–88.

[51] MDA. RADARSAT-2 product description. Tech. rep., MacDonald, Dettwiler and Associates (MDA), 2009.

[52] Merzouki, A., McNairn, H., and Pacheco, A. Evaluation of the Dubois, Oh, and IEM radar backscatter models over agricultural fields using C-band RADARSAT-2 SAR image data. *Canadian Journal of Remote Sensing 36*, 2 (2010), S274–S286.

[53] Murthy, V. R. K. Crop growth modeling and its applications in agricultural meteorology. In *Satellite Remote Sensing and GIS Applications in Agricultural Meteorology AGM-8* (2003), pp. 235–261. Proceedings of a Training Workshop held 7-11 July 2003

in Dehra Dun, India Edited by M.V.K. Sivakumar, P.S. Roy, K. Harmsen, and S.K. Saha AGM-8, WMO/TD-No. 1182.

[54] Nag, P., and Kudrat, M. *Digital Remote Sensing.* Concept Publishing Company, 1998.

[55] Oh, Y., Sarabandi, K., and Ulaby, F. T. An empirical model and an inversion technique for radar scattering from bare soil surfaces. *IEEE Transactions on Geoscience and Remote Sensing 30* (1992), 370–381.

[56] Oliver, C. Review article information from SAR images. *J. Phys. D: Appl. Phys. 24* (2012), 1493–1514.

[57] Paris, J. Radar backscattering properties of corn and soybeans at frequencies of 1. 6, 4. 75, and 13. 3 GHz. *IEEE Transactions on Geosciense and Remote Sensing 21*, 3 (1982), 393–400.

[58] Peake, W. H., and Oliver, T. L. The response of terrestrial surfaces at microwave frequencies. Tech. Rep. AFAL-TR-70301, Columbus, Ohio: Ohio State University, Electroscience Laboratory, 2440-7, 1971.

[59] Pedersen, P. Row spacing in soybean. *Department of Agronomy, Iowa State University* (2007).

[60] Pedersen, P., and Lauer, J. G. Corn and soybean response to rotation sequence, row spacing, and tillage system. *Agronomy Journal 95* (2003), 965–971.

[61] Prasad, A. K., Chai, L., P., S. R., and Kafatos, M. Crop yield estimation model for iowa using remote sensing and surface parameters. *International Journal of Applied Earth Observation and Geoinformation 8* (2006), 26–33.

[62] Reigber, A., Jager, M., Neumann, M., and Ferro-Famil, L. Classifying polarimetric SAR data by combining expectation methods with spatial context. *International Journal of Remote Sensing 31*, 3 (2010), 727–744.

[63] Richards, J. A., Willsky, A. S., and Fisher, J. W. Expectation-maximization approach to target model generation from multiple synthetic aperture radar images. *Society of Photo-Optical Instrumentation Engineers 41*, 1 (2004), 150–166.

[64] Ritchie, S., Hanway, J., and Benson, G. How a corn plant develops. Tech. Rep. 48, Special Report, Iowa State Univ. of Sci. and Technol. Coop. Ext. Serv., Ames., http://www.extension.iastate.edu/hancock/info/corn.htm, 1993.

[65] Ritchie, S., Hanway, J., Thompson, H., and Benson, G. How a soybean plant develops. Tech. rep., Special Report, Iowa State Univ. of Sci. and Technol. Coop. Ext. Serv., Ames., http://weedsoft.unl.edu/documents/GrowthStagesModule/Soybean/Soybean.htm, 1997.

[66] Rouse, Jr., J., Haas, R., Schell, J., and Deering, D. W. Monitoring vegetation systems in the great plains with erts. *NASA Special Publication 351* (1974), 309.

[67] Ruck, G. T., Barrick, D. E., Stuart, W. D., and Krichbaum, C. K. *Radar Cross Section Handbook*. Plenum, 1970.

[68] Sancer, M. I. An analysis of the vector kirchhoff equations and the associated boundary line charge. *Radio Science 3* (1968), 141–144.

[69] Sato, A., Yamaguchi, Y., Singh, G., and Park, S. Four-component scattering power decomposition with extended volume scattering model. *IEEE Geoscience and Remote Sensing Letters 9*, 2 (2012), 166–170.

[70] Scurlock, J. M. ., Asner, G. P., and Gower, S. T. Worldwide historical estimates of leaf area index, 1932-2000. Tech. Rep. 0RNL/TM-2001/268, Oak Ridge National Laboratory for U.S. Department of Energy, 2001.

[71] Silver, S. *Microwave Antenna Theory and Design.* McGraw-Hill Book Company, New York, 1947.

[72] Solberg, R. Monitoring soil erosion in agricultural fields by ERS-1 SAR. In *Geoscience and Remote Sensing Symposium, IGARSS International* (1992), vol. 2, pp. 1356–1359.

[73] Tan, C. P., Koay, J. Y., Lim, K. S., Ewe, H. T., and T., C. H. Classification of multi-temporal SAR images for rice crops using combined entropy decomposition and support vector machine technique. *Progress In Electromagnetics Research, PIER 71* (2007), 19–39.

[74] van Zyl, J. J. Unsupervised classification of scattering behavior using radar polarimetry data. *IEEE Trans. Geosci. Remote Sensing 27* (1989), 36–45.

[75] Wegmuller, U., Santoro, M., Mattia, F., Balenzano, A., Satalino, G., Marzahn, P., Fischer, G., Ludwig, R., and Floury, N. Progress in the understanding of narrow directional microwave scattering of agricultural fields. *Remote Sensing of Environment 115*, 10 (2011), 2423–2433.

[76] Wigneron, J., Ferrazzoli, P., Olioso, A., Bertuzzi, P., and Chanzy, A. A simple approach to monitor crop biomass from C-band radar data. *Remote Sensing of Environment 69*, 2 (1999), 179–188.

[77] Wpclipart.com. corn on the cob. Tech. rep.,

`http://www.wpclipart.com/food/vegetables/corn/corn_on_the_cob.png.html`

2012.

[78] Wu, L., Moore, R. K., and Zoughi, R. Sources of scattering from vegetation canopies at 10 GHz. *IEEE Transactions on Geosciense and Remote Sensing GE-23*, 5 (1985), 737–745.

[79] Yajima, Y., Yamaguchi, Y., Sato, R., Yamada, H., and Boerner, W. M. PolSAR image analysis of wetlands using a modified four-component scattering power decomposition. *IEEE Transactions on Geoscience and Remote Sensing 46*, 6 (2008), 1667–1673.

[80] Yamaguchi, Y., Moriyama, T., Ishido, M., and Yamada, H. Four-component scattering model for polarimetric SAR image decomposition. *IEEE Transactions on Geoscience and Remote Sensing 43*, 8 (2005), 1699–1706.

[81] Yamaguchi, Y., Yajima, Y., and Yamada, H. A four-component decomposition of PolSAR images based on the coherency matrix. *IEEE Geoscience and Remote Sensing Letters 3*, 3 (2006), 292–296.

Appendix A

PolSAR-pro's Freeman-Durden Algorithm(OFD)

This Appendix describes the mathematical and physical reasoning behind the Pottier and Ferro-Famil's solution to Freeman-Durden algorithm. A short description of the OFD code and the Matlab code itself are provided in appendix D. As for the mathematical base of the formulas used in the code, it is provided in the following sections.

A.1 Extreme Volume Scattering

The OFD algorithm assumes both α and β to be complex values. Let us rewrite equations 3.27a,3.27b,3.27c, and 3.27d to reflect the complex β values,

$$\left\langle |S_{HH}|^2 \right\rangle_{new} = f_S \left(\Re(\beta)^2 + \Im(\beta)^2 \right) + f_D \left(\Re(\alpha)^2 + \Im(\alpha)^2 \right) \tag{A.1}$$

$$\left\langle |S_{VV}|^2 \right\rangle_{new} = f_S + f_D \tag{A.2}$$

$$\Re \left(\langle S_{HH} S_{VV}^* \rangle \right)_{new} = f_S \Re(\beta) + f_D \Re(\alpha) \tag{A.3}$$

$$\Im \left(\langle S_{HH} S_{VV}^* \rangle \right) = f_S \Im \left(\beta \right) + f_D \Im \left(\alpha \right) \tag{A.4}$$

Theoretically if there is no surface and double-bounce scattering exists therefore α and β would be zero, hence $\left\langle |S_{HH}|^2 \right\rangle_{new} = 0$. On the other hand the portion of surface and double-bounce scattering should also become zero, thus f_S and f_D should also be zero, and $\left\langle |S_{VV}|^2 \right\rangle_{new} = 0$. Hence when either of the $\left\langle |S_{HH}|^2 \right\rangle_{new}$ or $\left\langle |S_{VV}|^2 \right\rangle_{new}$ is close to zero then the original Freeman-Durden algorithm assumes that the extreme volume scattering is the undergoing process [1]. In this case

$$f_D = 0 \tag{A.5}$$

[1] Case 1: Volume Scatter > Total in the code in Appendix D

, and

$$f_S = 0 \tag{A.6}$$

In order to realize this case we define a new f_V to remove the effects of the remaining diagonal components of the scattering matrix. Therefore,

$$\begin{aligned}\frac{3}{8}\left(\left\langle|S_{HH}|^2\right\rangle_{new} + \left\langle|S_{VV}|^2\right\rangle_{new} + \left\langle|S_{HV}|^2\right\rangle + 2f_V\right) &= \frac{3}{8}\left(0 + 0 + 2\frac{f_V}{3} + 2f_V\right) \\ &= f_V\end{aligned}$$

hereto

$$f_{V_{new}} = \frac{3}{8}\left(\left\langle|S_{HH}|^2\right\rangle_{new} + \left\langle|S_{VV}|^2\right\rangle_{new} + \left\langle|S_{HV}|^2\right\rangle + 2f_V\right) \tag{A.7}$$

A.2 Surface Scattering (Odd Bounce)

Now let us assume that according to van Zyl's criteria [74], surface scattering (odd bounce)[2] occurs when $\Re\left(\langle S_{HH}S_{VV}^*\rangle\right)_{new} \geq 0$, in this case the real part of α is assumed to be -1 ($\Re(\alpha) = -1$) and the imaginary part of α is equal to zero($\Im(\alpha) = 0$). So,

$$\alpha = -1 \tag{A.8}$$

Now with using equation A.8, the system of four equations (A.1, A.2, A.3, and A.4), and six unknowns (f_S, f_D, $\Re(\alpha)$, $\Im(\alpha)$, $\Re(\beta)$, and $\Im(\beta)$) could be rewritten as:

$$\left\langle|S_{HH}|^2\right\rangle_{new} = f_S\,|\beta|^2 + f_D \tag{A.9}$$

$$\left\langle|S_{VV}|^2\right\rangle_{new} = f_S + f_D \tag{A.10}$$

$$\Re\left(\langle S_{HH}S_{VV}^*\rangle\right)_{new} = f_S\Re(\beta) - f_D \tag{A.11}$$

$$\Im\left(\langle S_{HH}S_{VV}^*\rangle\right) = f_S\Im(\beta) \tag{A.12}$$

[2]Odd Bounce segment of the code in Appendix D

In order to solve this system of four equations and four unknowns we can calculate the β from equations A.11 and A.12:

$$f_S^2\left(\Re\left(\beta\right)^2+\Im\left(\beta\right)^2\right)=\Im\left(\langle S_{HH}S_{VV}^*\rangle\right)^2+\left(\Re\left(\langle S_{HH}S_{VV}^*\rangle\right)_{new}+f_D\right)^2$$

thus,

$$|\beta|=\frac{\sqrt{\left(\Re\left(\langle S_{HH}S_{VV}^*\rangle\right)_{new}+f_D\right)^2+\Im\left(\langle S_{HH}S_{VV}^*\rangle\right)^2}}{f_s} \tag{A.13}$$

we substitute equation A.13 into equation A.9,

$$\left\langle|S_{HH}|^2\right\rangle_{new}=f_S\frac{\Im\left(\langle S_{HH}S_{VV}^*\rangle\right)^2+\left(\Re\left(\langle S_{HH}S_{VV}^*\rangle\right)_{new}+f_D\right)^2}{f_s^2}+f_D$$

then we have,

$$\left\langle|S_{HH}|^2\right\rangle_{new}f_S=\Im\left(\langle S_{HH}S_{VV}^*\rangle\right)^2+\left(\Re\left(\langle S_{HH}S_{VV}^*\rangle\right)_{new}+f_D\right)^2+f_Df_S$$

in order to substitute f_S in this equation, we can solve equation A.10 for f_S,

$$f_S=\left\langle|S_{VV}|^2\right\rangle_{new}-f_D \tag{A.14}$$

using equation A.14 now we have,

$$\begin{aligned}&\left\langle|S_{HH}|^2\right\rangle_{new}\left(\left\langle|S_{VV}|^2\right\rangle_{new}-f_D\right)=\\&\Im\left(\langle S_{HH}S_{VV}^*\rangle\right)^2+\left(\Re\left(\langle S_{HH}S_{VV}^*\rangle\right)_{new}+f_D\right)^2+f_D\left(\left\langle|S_{VV}|^2\right\rangle_{new}-f_D\right)\end{aligned}$$

therefore,

$$\begin{aligned}&\left\langle|S_{HH}|^2\right\rangle_{new}\left\langle|S_{VV}|^2\right\rangle_{new}-\left\langle|S_{HH}|^2\right\rangle_{new}f_D=\\&\Im\left(\langle S_{HH}S_{VV}^*\rangle\right)^2+\Re\left(\langle S_{HH}S_{VV}^*\rangle\right)_{new}^2+2\Re\left(\langle S_{HH}S_{VV}^*\rangle\right)_{new}f_D+f_D^2\\&+\left\langle|S_{VV}|^2\right\rangle_{new}f_D-f_D^2\end{aligned}$$

and the value for the f_D could be estimated from:

$$f_D=\frac{\left\langle|S_{HH}|^2\right\rangle_{new}\left\langle|S_{VV}|^2\right\rangle_{new}-\Im\left(\langle S_{HH}S_{VV}^*\rangle\right)^2-\Re\left(\langle S_{HH}S_{VV}^*\rangle\right)_{new}^2}{\left\langle|S_{HH}|^2\right\rangle_{new}+\left\langle|S_{VV}|^2\right\rangle_{new}+2\Re\left(\langle S_{HH}S_{VV}^*\rangle\right)_{new}} \tag{A.15}$$

The calculated β is its absolute value and as it was mentioned before in section 3.3.2, β is a complex number on the contrary to its underlying theory. Since α assumed to have no imaginary part, $\Im\left(\langle S_{HH}S_{VV}^*\rangle\right)$ in equation A.12 should be compensated. Although theoretically incorrect, one practical solution is to calculate β as a complex value.

A.3 Double-Bounce Scattering (Even Bounce)

Based on van Zyl's criteria [74], Double-bounce scattering (even bounce) occurs when $\Re\left(\langle S_{HH}S_{VV}^{*}\rangle\right)_{new}$ is negative. In this case the real part of β is assumed to be 1 ($\Re\left(\beta\right)=1$) and the imaginary part of β is equal to zero ($\Im\left(\beta\right)=0$).

$$\beta = 1 \tag{A.16}$$

It is notable that each time Freeman-Durden fixes an unknown like equation A.16, they actually meant fixing two unknowns being the real and imaginary part of either α or β. Accordingly in order to reformulate the even bounce segment of the OFD code[3], once again the four equations A.1, A.2, A.3, and A.4 could be rewritten as a new set of four equations and four unknowns,

$$\left\langle \left|S_{HH}\right|^{2}\right\rangle_{new} = f_S + f_D\left|\alpha\right|^{2} \tag{A.17}$$

$$\left\langle \left|S_{VV}\right|^{2}\right\rangle_{new} = f_S + f_D \tag{A.18}$$

$$\Re\left(\langle S_{HH}S_{VV}^{*}\rangle\right)_{new} = f_S - f_D\Re(\alpha) \tag{A.19}$$

$$\Im\left(\langle S_{HH}S_{VV}^{*}\rangle\right) = -f_D\Im\left(\alpha\right) \tag{A.20}$$

Note that in equations A.19 and A.20, there are negative signs in front of the double-bounce segments of equations. This is due to the ideal 180° phase angle between HH and VV for double-bounce scattering. In order to solve this system we can calculate the α from equations A.19 and A.20:

$$f_D^2\left(\Re\left(\alpha\right)^2+\Im\left(\alpha\right)^2\right) = \Im\left(\langle S_{HH}S_{VV}^{*}\rangle\right)^2 + \left(f_S - \Re\left(\langle S_{HH}S_{VV}^{*}\rangle\right)_{new}\right)^2$$

hence,

$$\left|\alpha\right| = \frac{\sqrt{\left(f_S - \Re\left(\langle S_{HH}S_{VV}^{*}\rangle\right)_{new}\right)^2 + \Im\left(\langle S_{HH}S_{VV}^{*}\rangle\right)^2}}{f_D} \tag{A.21}$$

we substitute equation A.21 in equation A.17,

$$\left\langle \left|S_{HH}\right|^{2}\right\rangle_{new} = f_D\frac{\Im\left(\langle S_{HH}S_{VV}^{*}\rangle\right)^2 + \left(f_S - \Re\left(\langle S_{HH}S_{VV}^{*}\rangle\right)_{new}\right)^2}{f_D^2} + f_S$$

[3]Even Bounce segment of the code in Appendix D

then we have,

$$\left\langle |S_{HH}|^2 \right\rangle_{new} f_D = \Im\left(\langle S_{HH} S_{VV}^* \rangle\right)^2 + \left(f_S - \Re\left(\langle S_{HH} S_{VV}^* \rangle\right)_{new}\right)^2 + f_S f_D$$

on the other hand from equation A.18 we have,

$$f_D = \left\langle |S_{VV}|^2 \right\rangle_{new} - f_S \tag{A.22}$$

by substituting f_D in the previous equation we have,

$$\left\langle |S_{HH}|^2 \right\rangle_{new} \left(\left\langle |S_{VV}|^2 \right\rangle_{new} - f_S\right) =$$
$$\Im\left(\langle S_{HH} S_{VV}^* \rangle\right)^2 + \left(f_S - \Re\left(\langle S_{HH} S_{VV}^* \rangle\right)_{new}\right)^2 + f_S \left(\left\langle |S_{VV}|^2 \right\rangle_{new} - f_S\right)$$

hence,

$$\left\langle |S_{HH}|^2 \right\rangle_{new} \left\langle |S_{VV}|^2 \right\rangle_{new} - \left\langle |S_{HH}|^2 \right\rangle_{new} f_S =$$
$$\Im\left(\langle S_{HH} S_{VV}^* \rangle\right)^2 + \Re\left(\langle S_{HH} S_{VV}^* \rangle\right)_{new}^2 - 2\Re\left(\langle S_{HH} S_{VV}^* \rangle\right)_{new} f_S + f_S^2 +$$
$$\left\langle |S_{VV}|^2 \right\rangle_{new} f_S - f_S^2$$

and the value for the f_S could be estimated from:

$$f_S = \frac{\left\langle |S_{HH}|^2 \right\rangle_{new} \left\langle |S_{VV}|^2 \right\rangle_{new} - \Im\left(\langle S_{HH} S_{VV}^* \rangle\right)^2 - \Re\left(\langle S_{HH} S_{VV}^* \rangle\right)_{new}^2}{\left\langle |S_{HH}|^2 \right\rangle_{new} + \left\langle |S_{VV}|^2 \right\rangle_{new} - 2\Re\left(\langle S_{HH} S_{VV}^* \rangle\right)_{new}} \tag{A.23}$$

A.4 Data Conditioning for Non-realizable $\langle S_{HH} S_{VV}^* \rangle_{new}$

In this case [4] if the absolute value of $\langle S_{HH} S_{VV}^* \rangle_{new}$ is bigger than the multiplication of the absolute values of the $\left\langle |S_{HH}|^2 \right\rangle_{new}$ and $\left\langle |S_{VV}|^2 \right\rangle_{new}$ then the following correction should be applied:

$$\Re\left(\langle S_{HH} S_{VV}^* \rangle\right)_{new} = \frac{\Re\left(\langle S_{HH} S_{VV}^* \rangle\right)_{new}}{|\langle S_{HH} S_{VV}^* \rangle|} \sqrt{\left\langle |S_{HH}|^2 \right\rangle_{new} \left\langle |S_{VV}|^2 \right\rangle_{new}} \tag{A.24}$$

and

$$\Im\left(\langle S_{HH} S_{VV}^* \rangle\right) = \frac{\Im\left(\langle S_{HH} S_{VV}^* \rangle\right)}{|\langle S_{HH} S_{VV}^* \rangle|} \sqrt{\left\langle |S_{HH}|^2 \right\rangle_{new} \left\langle |S_{VV}|^2 \right\rangle_{new}} \tag{A.25}$$

If this condition would be applied, the f_D for surface scattering (equation A.15) and f_S in double-bounce scattering (equation A.23) will become zero. This removes the possibility of having negative values for these two unknowns.

[4] Data conditioning for non realizable $\langle S_{HH} S_{VV}^* \rangle_{new}$ segment of the code in Appendix D

Appendix B

General Solution of the Quartic Polynomials

Suppose that we have the general polynomial equation of degree n:

$$a_n x^n + a_{n-1} x^{n-1} + \cdots + a_1 x + a_0 = 0 \tag{B.1}$$

where each of the a_i's is a rational number and the a_n is not equal to zero. Abel's theorem states that there exist an explicit solution for $n \leq 4$ and do not exist for $n \geq 5$[20]. Therefore one can express the roots of any forth degree polynomial in terms of coefficients a_4, a_3, a_2, a_1, and a_0 using only the operations of addition, subtraction, multiplication, division, and extraction of the roots. For a given $a_4x^4 + a_3x^3 + a_2x^2 + a_1x + a_0 = 0$, quartic polynomial roots are:

$$\begin{aligned} x_1 &= A + B + \tfrac{\sqrt{C+D}}{2} \\ x_2 &= A + B - \tfrac{\sqrt{C+D}}{2} \\ x_3 &= A - B + \tfrac{\sqrt{C-D}}{2} \\ x_4 &= A - B - \tfrac{\sqrt{C-D}}{2} \end{aligned} \tag{B.2}$$

where

$$\begin{aligned} A &= -\tfrac{a_3}{4\,a_4} \\ B &= \tfrac{1}{2}\sqrt{\tfrac{a_3^2}{4a_4^2} - 2\tfrac{a_2}{3a_4} + \tfrac{2^{1/3} I}{3a_4 (J+L)^{\frac{1}{3}}} + \tfrac{(J+L)^{1/3}}{(3\times 2^{\frac{1}{3}} a_4)}} \\ C &= \tfrac{a_3^2}{2a_4^2} - \tfrac{4a_2}{3a_4} - \tfrac{2^{\frac{1}{3}} I}{3a_4 (J+L)^{\frac{1}{3}}} - \tfrac{(J+L)^{\frac{1}{3}}}{3\times 2^{\frac{1}{3}} a_4} \\ D &= \frac{-\frac{a_3^3}{a_4^3} + \frac{4a_3 a_2}{a_4^2} - \frac{8a_1}{a_4}}{4\sqrt{\frac{a_3^2}{4a_4^2} - \frac{2a_2}{3a_4} + \frac{2^{\frac{1}{3}} I}{3a_4 (J+L)^{\frac{1}{3}}} + \frac{(J+L)^{\frac{1}{3}}}{3\times 2^{\frac{1}{3}} a_4}}} \end{aligned} \tag{B.3}$$

and

$$\begin{aligned} I &= {a_2}^2 + 12\, a_0\, a_4 - 3\, a_1\, a_3 \\ J &= 27\, a_4\, {a_1}^2 - 9\, a_1\, a_2\, a_3 + 2\, {a_2}^3 - 72\, a_0\, a_4\, a_2 + 27\, a_0\, {a_3}^2 \\ L &= \sqrt{-4I^3 + J^2} \end{aligned} \tag{B.4}$$

Appendix C

Registration

The second order polynomials of

$$\begin{cases} x = a_1 + a_2 \times X + a_3 \times Y + a_4 \times X \times Y \\ y = b_1 + b_2 \times X + b_3 \times Y + b_4 \times X \times Y \end{cases}$$

form have been used for registering UTM coordinate system to slant range-azimuth image coordinate systems. The polynomial coefficients a_1 trough b_4 are presented in table C.1 for different dates of RADARSAT-2 image acquisitions.

Table C.1: Second order polynomial coefficients for registration

	September		October			November		
	15	18	9	12	15	2	5	8
a_1	-5252.05	-1596.04	-5220	-1557.46	-2301.47	-5225.28	-1567.59	-2224.12
a_2	1239.28	898.69	1238.78	898.66	1346.23	1233.25	896.55	1326.81
a_3	239.63	-151.36	237.21	-156.48	-212.96	233.34	-157.48	-228.53
a_4	-1.95	-7.76	-2.01	-7.22	-5.55	-0.95	-7.03	-1.68
b_1	-7336.09	-11253.6	-7242.59	-11345.1	-11522.2	-7192.6	-11410.2	-11537.8
b_2	-335.26	436.67	-356.93	423.12	356.41	-345.81	420.27	366.32
b_3	1921.16	1978.98	1901.95	1969.99	2073.52	1909.74	1968.66	2081.08
b_4	-2.41	-3.28	0.7	-0.63	0.99	-0.72	-0.28	-0.59

The registration results for the aforementioned polynomials are as follows:

Table C.2: GCP coordinates in both UTM of SPOT image and slant range-azimuth of September 15^{th} RADARSAT-2 along with the estimated errors

UTM		slant range-azimuth		error		
X	Y	x	y	dx	dy	RMSE
4442000	6607000	1780.5	3796.25	1.65	-0.89	1.874727
3563000	4468000	202	13	-1.14	-1.8	2.130634
5898000	5959000	3414	2053	-2.65	2.86	3.898987
6035000	5012750	3368	194.25	-1.23	-3.84	4.032183
3730000	6595250	901	4025.33	-1.92	0.63	2.020718
4920500	4732000	1937	52	2.64	2.86	3.892197
5017000	5093250	2138	706	1.91	0.65	2.017573
4701500	5145750	1759.33	916.33	-1	1.07	1.464548
5215000	6737500	2757.67	3774	0.87	-0.77	1.161809
5215000	6737500	2757.67	3774	0.87	-0.77	1.161809

Table C.3: Test points coordinates in both UTM of SPOT image and slant range-azimuth of September 15^{th} RADARSAT-2 along with the estimated errors

UTM		slant range-azimuth		error		
X	Y	x	y	dx	dy	RMSE
3599250	5927250	583.67	2790.67	-3.51	-2.39	4.246434
4821750	5904250	2084.67	2320.67	1.89	-1.18	2.228116
4154250	5203250	1104	1219	3.07	3.66	4.777081
3514250	5055500	284.67	1155	4.78	-0.33	4.791378

Table C.4: GCP coordinates in both UTM of SPOT image and slant range-azimuth of September 18^{th} RADARSAT-2 along with the estimated errors

UTM		slant range-azimuth		error		
X	Y	x	y	dx	dy	RMSE
3931250	5489500	940.75	1257.75	2.26	1.92	2.965468
4776750	5162000	1725	968.5	0.99	1.68	1.95
3729250	6594750	567.5	3345.75	1.22	0.75	1.432096
4876750	6288500	1599.25	3222	2.54	1.92	3.184023
4463000	6092000	1279.75	2661	-1.88	-0.96	2.110924
5034000	5643000	1854	2018	0.72	-0.73	1.025329
4234000	5241000	1243.75	893.25	0.31	-1.01	1.056504
4667250	5793000	1508	2158	-3.62	-1.93	4.102353
3981500	5910750	903	2103	-1.73	-2.01	2.65198
4086000	5648750	1041	1634	-0.81	0.37	0.890505

Table C.5: Test points coordinates in both UTM of SPOT image and slant range-azimuth of September 18^{th} RADARSAT-2 along with the estimated errors

UTM		slant range-azimuth		error		
X	Y	x	y	dx	dy	RMSE
4371750	6349500	1154.75	3132	-1.59	2.09	2.626062
4721250	5622500	1588	1849	-1.89	1.22	2.249556
4923000	6196000	1655	3062	1.32	4.15	4.354871
3972000	6105250	858	2483	-3.29	-0.49	3.326289

Table C.6: GCP coordinates in both UTM of SPOT image and slant range-azimuth of October 9^{th} RADARSAT-2 along with the estimated errors

UTM		slant range-azimuth		error		
X	Y	x	y	dx	dy	RMSE
3730000	6595250	914.25	3987.25	0.09	-1.27	1.273185
5215000	6737500	2770.75	3735.25	0.19	3.12	3.12578
3931250	5489500	906.75	1809.75	-0.37	-1.86	1.896444
4777000	5162000	1873.25	890.25	2.73	0.83	2.853384
5144000	4807500	2245.5	78.5	-3.84	2.68	4.682734
4926500	5550250	2145	1576	1.52	0.69	1.669281
4555000	6734500	1959.86	3961.04	-0.76	1.55	1.726297
5838500	5133500	3170	460	1.84	0.07	1.841331
5631000	5910000	3087	2011	-0.41	-3.41	3.43456
5684000	5870000	3144	1915.5	-0.98	-2.4	2.592373

Table C.7: Test points coordinates in both UTM of SPOT image and slant range-azimuth of October 9^{th} RADARSAT-2 along with the estimated errors

UTM		slant range-azimuth		error		
X	Y	x	y	dx	dy	RMSE
4371750	6349500	1154.75	3132	1.79	-0.08	1.791787
4721250	5622500	1588	1849	-0.34	-4.94	4.951687
4923000	6196000	1655	3062	-0.16	-1.99	1.996422
3972000	6105250	858	2483	-1.35	-4.56	4.755639

Table C.8: GCP coordinates in both UTM of SPOT image and slant range-azimuth of October 12^{th} RADARSAT-2 along with the estimated errors

UTM		slant range-azimuth		error		
X	Y	x	y	dx	dy	RMSE
3729500	6595000	587.25	3210	2.63	0.51	2.678992
3932000	5488500	963	1117	1.49	-0.28	1.51608
4777750	5161500	1749	829	-1.5	0	1.5
4275000	6689000	1029.75	3622.5	-1.53	-0.45	1.594804
5219000	5654000	2039.5	1983.75	4.51	0.89	4.596977
5155750	4794000	2146	264.25	-1.3	-0.68	1.467106
4739750	6635000	1435.75	3709	-1.05	-2.41	2.628802
4587000	6188000	1389	2768.25	-2.58	0.12	2.582789
4401750	6266000	1216.75	2845.25	-1.94	1.33	2.352127
5161500	6509250	1821.25	3641.75	1.27	0.97	1.598061

Table C.9: Test points coordinates in both UTM of SPOT image and slant range-azimuth of October 12^{th} RADARSAT-2 along with the estimated errors

UTM		slant range-azimuth		error		
X	Y	x	y	dx	dy	RMSE
4323750	5333750	1327.5	977.25	0.51	-0.06	0.513517
5557000	6005250	2259.75	2815.5	4	0.02	4.00005
4241500	6403750	1055	3046	-1.04	-1.82	2.096187
5263750	6306250	1948.25	3282.5	1.85	-1.97	2.70248

Table C.10: GCP coordinates in both UTM of SPOT image and slant range-azimuth of November 2^{nd} RADARSAT-2 along with the estimated errors

UTM		slant range-azimuth		error		
X	Y	x	y	dx	dy	RMSE
4357750	6630250	1667.75	3941.25	-0.75	-0.48	0.890449
3540000	4704000	219.75	555	-2.44	0.32	2.460894
5692000	5932000	3144	2145.75	-2.41	2.41	3.408255
5779750	4944750	3026	231	-3.2	-0.34	3.218012
3729500	6595500	889.25	4096.5	-0.44	0.79	0.904268
4918500	4732000	1926	126	3.54	-0.69	3.606619
5106250	5050750	2227	668.5	1.01	-0.18	1.025914
4701500	5145750	1753	991	2.48	-0.22	2.489739
5215000	6737500	2746.5	3844	1.71	-1.61	2.348659
5212000	6702000	2733.5	3779	0.49	0	0.49

Table C.11: Test points coordinates in both UTM of SPOT image and slant range-azimuth of November 2^{nd} RADARSAT-2 along with the estimated errors

UTM		slant range-azimuth		error		
X	Y	x	y	dx	dy	RMSE
3578250	5992500	564	2997	-1.52	-1.68	2.265568
4692000	5853250	1903	2341.25	2.16	-2.02	2.957364
4152250	5203250	1090.75	1292.25	1.67	-0.56	1.761391
4284750	6161000	1475.25	3069.75	3.83	-2.84	4.768071

Table C.12: GCP coordinates in both UTM of SPOT image and slant range-azimuth of November 5^{th} RADARSAT-2 along with the estimated errors

UTM		slant range-azimuth		error		
X	Y	x	y	dx	dy	RMSE
3729500	6595000	567.5	3134.5	2.87	0.75	2.966378
3932000	5488500	943.5	1041	1.87	-0.37	1.906253
4777750	5161500	1727.75	753	-1.98	0.79	2.131783
4275000	6689000	1008.5	3546.5	-2.29	-0.46	2.335744
5155750	4794000	2126.5	188.25	0.4	0.68	0.788923
4600250	6182750	1381	2686.75	-2.19	-0.31	2.211832
5161500	6509250	1799.25	3567.25	0.53	2.97	3.016919
4454000	5336000	1417.87	959.61	-0.41	-0.31	0.514004
5555000	6005250	2235	2735	2.44	-2.52	3.507706
4241500	6403750	1034.5	2970.5	-1.25	-1.22	1.746683

Table C.13: Test points coordinates in both UTM of SPOT image and slant range-azimuth of November 5^{th} RADARSAT-2 along with the estimated errors

UTM		slant range-azimuth		error		
X	Y	x	y	dx	dy	RMSE
5263750	6306250	1927	3208	1.81	0.27	1.830027
4369750	5172750	1374.75	602	-1.87	-1.45	2.366305
5526000	5605000	2286	1939.75	-0.36	1.72	1.757271
3759500	5654750	767.5	1295.75	4.45	-0.5	4.478002

Table C.14: GCP coordinates in both UTM of SPOT image and slant range-azimuth of November 8^{th} RADARSAT-2 along with the estimated errors

UTM		slant range-azimuth		error		
X	Y	x	y	dx	dy	RMSE
3932000	5488750	1701	1314.25	-1.21	1.91	2.261017
4781000	5168500	2898	953	1.41	-2.03	2.471639
3729500	6595500	1177.25	3540.5	1.72	0.88	1.932046
5161000	6509250	3081.75	3880.75	2.33	1.55	2.798464
4915000	6595500	2733.25	3968.75	-2.05	-0.52	2.114923
4236250	6348250	1896.25	3208.75	-4.28	-0.6	4.321851
5350750	5846500	3488	2569.5	1.47	-1.33	1.982372
5077000	5282000	3259.25	1298.75	-0.59	0.33	0.676018
3518000	5944000	1052	2107	2	-1.49	2.494013
5160000	4793750	3484.25	315.25	-0.8	1.29	1.517926

Table C.15: Test points coordinates in both UTM of SPOT image and slant range-azimuth of November 8^{th} RADARSAT-2 along with the estimated errors

UTM		slant range-azimuth		error		
X	Y	x	y	dx	dy	RMSE
3348000	5142000	1011	378	-3	-1.37	3.298015
4805000	5890500	2756.5	2466.25	-0.89	2.01	2.198227
4203000	6185250	1893	2859	-2.17	0.52	2.231435
4266000	4961000	2263.75	340	-2.93	3.36	4.458083

Appendix D

OFD in Matlab

This appendix describes the code written for OFD algorithm by Pottier and Ferro-Famil. The segment of the code before the for loop is the initialization of some of the parameters. Then from the beginning of the for loop till $Freeman\ algorithm$ is basically the association of the variables written in table D.1 to their physical counterparts.

Table D.1: The covariance matrix equivalent values in the code

Parameter name	Mathematical description
C11	$\langle \lvert S_{HH} \rvert^2 \rangle$
C22	$\langle \lvert S_{HV} \rvert^2 \rangle$
C33	$\langle \lvert S_{VV} \rvert^2 \rangle$
C13_re	$\Re\left(\langle S_{HH} S_{VV}^* \rangle\right)$
C13_im	$\Im\left(\langle S_{HH} S_{VV}^* \rangle\right)$

The $Freeman\ algorithm$ section of the code is the subtraction of the multipliers of f_V from the equations 3.20, 3.21, and 3.22. Then the extreme volume scattering is the next process in segment $Case\ 1 : Volume\ Scatter > Total$. Segment

```
[Data conditionning for non realizable ShhSvv.* term]
```

is a correction part for especial cases of $f_D = 0$ in odd bounce and $f_S = 0$ in even bounce. The following two segments are for dominant *odd bounce* and dominant *even bounce* unknown estimations. Last but not the least is the *span corrections*, which is not applied in our data since it needs to sweep the whole dataset for the maximum and minimum span values.

```
function [Span_S,Span_D,Span_V,fs_r, fd_r, fv_r, alpha_r, ...
beta_r,Type_2 ]=FreemanDurdenPerPix(C4)



Span=C4(:,:,1)+2.*C4(:,:,6)+C4(:,:,16);
SpanMax=max(max(max(Span)));
SpanMin=min(min(min(Span)));
ALP=0;BET=0;
eps=1e-5;  % from  ../PolSARpro_v4.2.0./Soft./SVM./svm.cpp:
for i1=1:size(C4,1)
    for j1=1:size(C4,2)
        CC11 =C4(i1,j1,1);
    CC13_re = real(C4(i1,j1,13)) ;
    CC13_im = imag(C4(i1,j1,13));
    CC22 = 2.*C4(i1,j1,6);
    CC33 = C4(i1,j1,16);
%-----------------------------------------------------------------
%% Freeman algorithm
    FV = 3* CC22 / 2.;
    CC11 = CC11 - FV;
    CC33 = CC33 - FV;
    CC13_re = CC13_re - FV/ 3;
        Type_2=1;
%-----------------------------------------------------------------
%% Case 1: Volume Scatter > Total
    if ((CC11 <= eps) | (CC33(:,:) <= eps))
            FV = 3. .* (CC11 + CC22 + CC33 + 2 .* FV) ./ 8.;
```

```
            FD = 0.;
            FS = 0.;
            Type_2=2;
        else
%-------------------------------------------------------------
%% Data conditionning for non realizable ShhSvv.* term
            if ((CC13_re .* CC13_re + CC13_im .* CC13_im) > ...
CC11 .* CC33)
                rtemp = CC13_re .* CC13_re + CC13_im .* CC13_im;
                CC13_re = CC13_re .* sqrt(CC11 .* CC33 ./ rtemp);
                CC13_im = CC13_im .* sqrt(CC11 .* CC33 ./ rtemp);
                Type_2=3;
            end
%-------------------------------------------------------------
    %% Odd Bounce
            if (CC13_re >= 0.)
                ALP = -1.;
                FD = (CC11 .* CC33 - CC13_re .*...
                    CC13_re - CC13_im .* CC13_im) ./...
                    (CC11 + CC33 + 2 .* CC13_re);
                FS = CC33 - FD;
                BET = sqrt((FD + CC13_re) .* (FD + CC13_re) + ...
                    CC13_im .* CC13_im) ./ FS;
                Type_2=4;
            end
%-------------------------------------------------------------
    %% Even Bounce
            if (CC13_re < 0.)
```

```
                BET = 1.;
                FS = (CC11 .* CC33 - CC13_re .*...
                    CC13_re - CC13_im .* CC13_im) ./...
                    (CC11 + CC33 - 2 .* CC13_re);
                FD = CC33 - FS;
                ALP = sqrt((FS - CC13_re) .* (FS - CC13_re) +...
                    CC13_im .* CC13_im) ./ FD;
                Type_2=5;
            end
        end
         alpha_r(i1,j1)=ALP;beta_r(i1,j1)=BET;fs_r(i1,j1)=FS;
         fd_r(i1,j1)=FD;fv_r(i1,j1)=FV;

    Span_S(i1,j1) = FS .* (1 + BET .* BET);
    Span_D(i1,j1) = FD .* (1 + ALP .* ALP);
    Span_V(i1,j1) = 8. .* FV ./ 3.;
%-------------------------------------------------------------
%% Span corrections
%      if (Span_S(i1,j1) < SpanMin)
%  Span_S(i1,j1) = SpanMin;
%         end
%      if (Span_S(i1,j1) > SpanMax)
%  Span_S(i1,j1) = SpanMax;
%         end
%
%      if (Span_D(i1,j1) < SpanMin)
%  Span_D(i1,j1) = SpanMin;
%         end
```

```
%      if (Span_D(i1,j1) > SpanMax)
%  Span_D(i1,j1) = SpanMax;
%         end
%
%
%      if (Span_V(i1,j1) < SpanMin)
%  Span_V(i1,j1) = SpanMin;
%         end
%         if (Span_V(i1,j1) > SpanMax)
%  Span_V(i1,j1) = SpanMax;
%         end
    end
end
```

Appendix E

RFD in Matlab

This appendix provides the code written for RFD algorithm.

```
%   %   This is the code written to perform refined Freeman-Durden. Its
%   inputs are 4 by 4 covariance matrix and alpha over beta ratio.
function [Span_S,Span_D,Span_V,fs_r, fd_r, fv_r, alpha_rr, alpha_i,...
 alpha_r,beta_r,Type_1]=FreemanDurden(C4,aOverB)
            % The original formulation of the parameters
            % <|Shv|^2> = fv/3;
            %           removing fv/3 from real part of <ShhSvv*> and fv
            %           from <|Shh|^2> and  <|Svv|^2> leads to
            % <|Shh|^2>new = fs * beta^2 + fd * abs(alpha)^2;
            % <|Svv|^2>new = fs + fd;
            % R<ShhSvv*>new = fs * beta + fd * R(alpha);
            % I<ShhSvv*> =  fd * I(alpha);
            % abs(alpha)/beta= input
Type_1=1;                                       % Flag initialization(null)
eps=10^(-10);                                   % Calculation accuracy
global FieldID;                                 % Field Id number
%% Symbolic initialization for Freeman-Durden
% syms a b_r b_i d e c fv;                        % Knowns
syms fs fd alp_r alp_i bet ;                    % Unknowns


a=C4(:,:,1);                    % <|Shh|^2>
b_r=real(C4(:,:,13));           % R<ShhSvv*>
b_i=imag(C4(:,:,13));           % I<ShhSvv*>
```

```
            %   because the solution is based on C3(and not C4 therefore
            %   <|Shv|^2>= 2* C4(:,:,6)
c=2*C4(:,:,6);                  % 2 * <|Shv|^2>
d=C4(:,:,16);                   % <|Svv|^2>
            % e is alpha over beta ratio
e=ones(size(C4,1),size(C4,2))*aOverB;          % Resized for matrix
                                               %    manipulation purposes
const_mult=1;%min([min(min(a)),min(min(c)),min(min(d))]);
a=a/const_mult;b_r=b_r/const_mult;b_i=b_i/const_mult;
c=c/const_mult;d=d/const_mult;

if aOverB==0||aOverB<10^-1
%% No double-bounce
            % When H/A/alpha did not find even a single occurrance for
            % double-bounce scattering or very rare ocurrances
    fd_r=0;                                    % double scattering portion
    alpha_i=0;                                 % Imaginary part of alpha
    alpha_r=0;                                 % Absolute value of alpha
    alpha_rr=0;                                % Real part of alpha
    temp=nan;                                  % Dummy parameter represents
                                               %    beta
    fv_r=3*c/2*const_mult;                     % Volume scat. portion
    fs_r=d*const_mult-fv_r;                    % Surface scat. portion
    beta_r(1,1)=(b_r-fv_r/3)/fs_r;             % beta
            % The following root for beta_r_1 for some reason would not
            %   produce any real roots and therefore leads to a unique
            %   desired solution
    temp=sqrt((fv_r-a)/fs_r);
```

```
    if isreal(temp)
        beta_r(1,2)=temp;                   % Second beta
        alpha_r(1,2)=0;                     % Second beta
        alpha_i(1,2)=0;                     % Second beta
        alpha_rr(1,2)=0;                    % Second beta
    end
    Span_S =fs_r.* (1 + beta_r.^2);             % Span definitions
    Span_D =fd_r .* (1 + (alpha_i.^2+alpha_r.^2));
    Span_V = 8. .* fv_r ./ 3.;
    Type_1=2;                                   % flag of no double-bounce
elseif isinf(aOverB)||aOverB>10^2
%% No Surface scattering
            % When H/A/alpha did not find even a single occurrance for
            % surface scattering or very rare ocurrances
    fs_r=0;                                     % Surface scat. portion
    beta_r=0;                                   % beta
    alpha_i=0;                                  % Imaginary part of alpha
    temp=nan;                                   % Dummy for beta
    fv_r=3*c/2*const_mult;                      % Volume scat. portion
    fd_r=d*const_mult-fv_r;                     % Double bounce scat. portion
    alpha_r=(b_r*const_mult-fv_r/3)/fd_r;       % Real part of alpha
            % The following root for alpha, for some reason would not
            %   produce any real roots and therefore leads to a unique
            %   desired solution
    alpha_r2=sqrt((fv_r-a)/fd_r);
    if isreal(alpha_r2)
        alpha_r(1,2)=alpha_r2;                  % Second alpha
        beta_r(1,2)=0;                          % Second alpha
```

```
        alpha_i(1,2)=0;                         % Second alpha
    end
    alpha_rr=alpha_r;                           % Real part of alpha
    Span_S =fs_r.* (1 + beta_r.^2);             % Span definitions
    Span_D =fd_r .* (1 + (alpha_i.^2+alpha_r.^2));
    Span_V = 8. .* fv_r ./ 3.;
    Type_1=7;                                   % Flag for no Surface Scat.
elseif aOverB==-100
%% No Surface scattering
            % When H/A/alpha did not find even a single occurrance for
            % surface scattering or very rare ocurrances
    fs_r=0;                                     % Surface scat. portion
    beta_r=0;                                   % beta
    alpha_i=0;                                  % Imaginary part of alpha
    fv_r=3*c/2*const_mult;                      % Volume scat. portion
    fd_r=0;                     % Double bounce scat. portion
    alpha_r=0;      % Real part of alpha
            % The following root for alpha, for some reason would not
            %   produce any real roots and therefore leads to a unique
            %   desired solution
    alpha_rr=alpha_r;                           % Real part of alpha
    Span_S =fs_r.* (1 + beta_r.^2);             % Span definitions
    Span_D =fd_r .* (1 + (alpha_i.^2+alpha_r.^2));
    Span_V = 8. .* fv_r ./ 3.;
    Type_1=10;                                   % Flag for Only volume.
else
%% The remaining cases of scatterings
    Type_1=3;                                   % Flag for general case
```

```
    fv=3*c/2;                                   % volume scattering portion
    b_r=b_r-fv/3;                               % R<ShhSvv*>_new
    a=a-fv;                                     % <|Shh|^2>_new
    d=d-fv;                                     % <|Svv|^2>_new
    %% Solving by matlab solver (very slow and mostly just for checking)
    temp01=solve('(b_r-bet*d+(bet^2*d-a)/bet/(1-e^2))^2+b_i^2-e^2*...
((bet^2*d-a)^2/bet^2/(1-e^2)^2)',bet);
    temp=vpa(subs(temp01(1)));
    be=nan;
    %% Explicit solution
            %   not accurate due to rounding errors in 15th or 16th digit
% %     [x1,x2,x3,x4]=PolyRoots4thDeg(d^2*e^2   ,   -2*b_r*d*e^2   ,...
% %         -b_r^2 - b_i^2 + b_r^2*e^2 + b_i^2*e^2   ,   2*a*b_r,-a^2);
% %     temp=[x1,x2,x3,x4];
    %% removing complex roots
            %   since the answer is forth digree polynomial
    for i=1:4
        if isreal(temp(i))%||double(abs(imag(temp(i))))<eps
            be(i)=real(temp(i));
        end
            %   very small imaginary parts(looking for hidden multiple
            %   roots). This case is not used in order to single out unique
            %   roots.
% % %         if double(abs(imag(temp(i))))<eps
% % %             be(i)=real(temp(i));
% % %         end
    end
            %   If there is not even a single unique root this part will
```

```
          %   look for it. Notice that even a single negative unique root
          %   is an answer in this case
  if isnan(be)==1
      for i=1:4
          if double(abs(imag(temp(i))))<eps
               be(i)=real(temp(i));
          end
      end
%      if isnan(be)==1
          %   Absolutly No root has been detected for beta
          Type_1=4;                          % Flag for no root
%      end
  end
  %% Estimation of unknows for general case
  fd=d./(1-e^2)-a./(be.^2)/(1-e^2);          % Double bounce portion
  %% The remaining of the estimation
  alp_i=b_i./fd;                             % Imaginary part of alpha
  fs=d-fd;                                   % Surface scattering portion
  alp_r=(b_r-be.*fs)./fd;                    % Real part of alpha
  %% Equation 5 test
  test01=find(double(be)>0);                 % Positiveness of beta
                                             % Positiveness of surface,
                                             % double-bounce and beta.
  test02=find(double(be)>=0&double(fd)>=0&double(fs)>=0);
  if isempty(test02)==0
      if size(test02,2)>1
          Type_1=5;                          % Flag for no acceptable root
      end
```

```
    end
            % updated for the multiplier
    fv_r=fv*const_mult;                         % Volume scattering portion
    fd_r=double(fd(test01))*const_mult;         % Double bounce portion
    fs_r=double(fs(test01))*const_mult;         % Surface scat. portion
    alpha_i=double(alp_i(test01));              % Imaginary part of alpha
    alpha_rr=double(alp_r(test01));             % Real part of alpha
            %   which one is the correct one no one knows but I guess using
            %   beta for comparison is a better idea although it is not
            %   fully coorrect since this two are somehow independant.
%     alpha_r=double(alp_r(test01));
                                                % Absolute value of alpha
    alpha_r=sqrt(double(alp_i(test01)).^2+double(alp_r(test01)).^2);
    beta_r=double(be(test01));                  % beta
    Span_S =fs_r.* (1 + beta_r.^2);             % Span definitions
    Span_D =fd_r .* (1 + (alpha_i.^2+alpha_r.^2));
    Span_V = 8. .* fv_r ./ 3.;
    beta_r=temp;
end
```

Appendix F

Unsupervised Classifications Results

In the following section an example describing the interpretation of the classification results and its necessary steps has been presented. These steps are designed to calculate the confusion matrix and compare different unsupervised classifications. In a supervised classification training sites are the parameters used for labeling the classes but in the case of unsupervised classifications naming the resulted classes are not trivial. Thus this section presents an example of how to assign such a class names to an unsupervised classification.

F.1 Example of Classification Results: November 8^{th}

An EM-PLR classification was performed on the 8^{th} of November RADARSAT-2 image. Then for every class mentioned in table 4.5(e.g. CC) the percentage of classified pixels from different class numbers were calculated (rows in table F.1). The final result of this process has been presented in table F.1.

	Classification results							
	Unclassified	Class#1	Class#2	Class#3	Class#4	Class#5	Class#6	Class#7
CC	0.0695	**35.6399**	0.8892	5.5839	**10.2849**	0	47.3239	**0.2086**
CS	0.7868	0	**96.3743**	0	0	0.1276	2.7113	0
HC	3.2581	3.771	8.0196	0.7392	3.0857	0.7766	**80.3497**	0
HS	8.1071	0.1642	61.5367	0	0.0035	3.2954	26.8931	0
NC	4.9288	0	78.0106	0	0	0	17.0607	0
PC	**20.7266**	1.9546	2.9424	**7.7725**	0	**66.1435**	0.4604	0
Σ	37.8769	41.5297	247.7728	14.0956	13.3741	70.3431	174.7991	0.2086
Lbl.	PC_n	CC_n	CS_n	PC_n	CC_n	PC_n	HC_n	CC_n

Each value inside the table F.1 is the percent of the pixels belonging to the left hand side class name inside the pixels classified as the upper side class number. Table F.1 was used to

extract the most probable ground truth class name for each class number; these values are the bold values in each row and the corresponding 'New Class' row at the end of the table F.1. In the next step, we merge the classes with the same name.

It is observable that classes such as NC (no crop) and HS (harvested soybeans) are not classified properly with this classification. Also note that there is no partially harvested corn field existing in the scene as there is no rows representing this class in table F.1. The merge process leads to the final sets of classes which will be used to calculate the unsupervised classification accuracy.

We used the November 12 and 13^{th} ground truth data to calculate the accuracies. The confusion matrices are the following four tables

Table F.1: Ground Truth (Pixels)

Class	CC	CS	HC	PC	Total
PC_n	2683	86	2299	703	5771
CC_n	21894	0	3302	6919	32115
CS_n	422	9064	3862	467	13815
HC_n	22459	255	38694	15803	77211
PC_n	2683	86	2299	703	5771
Total	50141	9491	50456	24595	134683

Table F.2: Ground Truth(Percent)

Class	CC	CS	HC	PC	Total
PC_n	5.35	0.91	4.56	2.86	4.28
CC_n	43.66	0	6.54	28.13	23.84
CS_n	0.84	95.5	7.65	1.9	10.26
HC_n	44.79	2.69	76.69	64.25	57.33
PC_n	5.35	0.91	4.56	2.86	4.28
Total	100	100	100	100	100

The overall accuracy was equal to 52.2375% (70355/134683) while the κ coefficient was 0.2991. As it can easily be observed, the table F.1 is based on number of pixels. The table F.2 is the estimated percentages. As for tables F.3 and F.4, respectively commission/omission

Table F.3: Commission and omission errors

Class	Commission (Percent)	Omission (Percent)	Commission (Pixels)	Omission (Pixels)
CC_n	31.83	56.34	10221/32115	28247/50141
CS_n	34.39	4.5	4751/13815	427/9491
HC_n	49.89	23.31	38517/77211	11762/50456
PC_n	87.82	97.14	5068/5771	23892/24595

Table F.4: Producer's and User's accuracies

Class	Prod. Acc. (Percent)	User Acc. (Percent)	Prod. Acc. (Pixels)	User Acc. (Pixels)
CC_n	43.66	68.17	21894/50141	21894/32115
CS_n	95.5	65.61	9064/9491	9064/13815
HC_n	76.69	50.11	38694/50456	38694/77211
PC_n	2.86	12.18	703/24595	703/5771

and producer/user accuracies are tabulated.

F.2 Field-Based Labeling

Since the accuracy of the previous labeling schemes were not satisfactory, a new labeling procedure were defined. In this approach the total number of each class number existing in each polygon was calculated. Then the class number with the maximum occurrence was assigned as temporary class label to that polygon. As an example the result of such a process has been shown in table F.5.

Then a new classification image were produced to have a single value filling each of those polygons and a new sets of statistics were calculated and again the same idea used for labeling in the previous section(i.e., using the maximum probable class) were used to rename this new labels. Table F.6 is representing these results.

And the classification accuracy assessments are provided in tables F.7, F.8, F.9, and F.10. The overall accuracy was 67.9114% (61324/90300) and κ coefficient was 0.5304. The classification results using the field based labeling rather than pixel based labeling improved the results.

Table F.5: Field-based temporal labeling for the unsupervised EM-PLR with 10 times more probable, K=20 of 11/08/2009 with the field data of the 11/12/2009.

Field_ID		Unclassified	Class#1	Class#2	Class#3	Class#4	Class#5
2009_350100349	CC		60	276	0	0	0
2009_350100147	CC		2764	0	1564	776	0
2009_350100758	CC	33	2035	0	743	1214	0
2009_350101196	CC		1038	0	41	1057	0
2009_350101375	CC		990	37	50	105	0
2009_350101476	CC		5726	60	0	31	0
2009_350101552	CC		1333	49	78	572	0
2009_350101074	CC		1980	0	149	851	0
2009_350101987	CC		530	0	25	119	0
2009_350102045	CC		458	0	0	156	0
2009_350101256	CS	74	0	1308	0	0	12
2009_350101234	CS			7756			
2009_350100144	HC	90	906	251	296	1037	0
2009_350101253	HC			290	0	0	85
2009_350100243	HC		43	0	0	0	0
2009_350101229	HC	224	0	78	0	449	0
2009_350101226	HC		434	0	0	0	0
2009_350101220	HC	298	0	172	0	0	289
2009_350100416	HC		258	1	60	0	0
2009_350100244	HC		175	25	0	0	0
2009_350102026	HC	957	0	3043	0	0	0
2009_350102031	HC			2	0	0	0
2009_350101197	HS	994	0	116	0	0	560
2009_350101198	HS	278	0	86	0	0	333
2009_350100820	HS			1906	0	0	0
2009_350101321	HS			2961			
2009_350100145	HS	1086	0	375			
2009_350101076	HS		93	5789	0	2	0
2009_350101251	HS	42	0	97	0	0	1
2009_350101191	HS	793	0	9418	0	0	0
2009_350100350	HS			5178			
2009_350101988	HS			1141	0	0	0
2009_350100143	HS	875	0	3157	0	0	973
2009_350101999	HS	522	0	160	0	0	0
2009_350102054	HS	3	0	4479	0	0	0
2009_350100142	NC	320	0	6945	0	0	0
2009_350101190	NC	614	0	7838	0	0	0
2009_350100153	PC		1431	23	110	33	0
2009_350101103	PC						
2009_350101127	PC		1239	444	0	0	0
2009_350101252	PC		651	0	30	567	0
2009_350101490	PC		695	0	194	227	0
2009_350102007	PC		936	0	369	1030	0

Class#6	Class#7	TOTAL	NewC
6456		6792	Class#6
104	64	5272	Class#1
622	35	4682	Class#1
1739		3875	Class#6
808		1990	Class#1
5291		11108	Class#1
2711		4743	Class#6
2643		5623	Class#6
1423		2097	Class#6
662		1276	Class#6
255		1649	Class#2
		7756	Class#2
3330		5910	Class#6
3459		3834	Class#6
5022		5065	Class#6
6143		6894	Class#6
3951		4385	Class#6
3092		3851	Class#6
2180		2499	Class#6
4788		4988	Class#6
2394		6394	Class#2
4335		4337	Class#6
4469		6139	Class#6
3835		4532	Class#6
13		1919	Class#2
		2961	Class#2
		1461	Class#0
151		6035	Class#2
2396		2536	Class#6
421		10632	Class#2
		5178	Class#2
107		1248	Class#2
2807		7812	Class#2
1023		1705	Class#6
14		4496	Class#2
2135		9400	Class#2
1098		9550	Class#2
1094		2691	Class#1
5691		5691	Class#6
2909		4592	Class#6
3844		5092	Class#6
1082		2198	Class#6
1183	110	3628	Class#6

Table F.6: Field-based labeling confusion matrix for the unsupervised EM-PLR with 10 times more probable, K=20 of 11/08/2009 with the field data of the 11/12/2009.

	Unclassified	Class#1	Class#2	Class#3	Class#4	Class#5	Class#6	total
CC	3.4873	**47.0627**	0	0	0	0	49.45	100
CS	3.0409	0	96.9591					100
HC	3.1688	0	12.8226	0	0	0	84.0086	100
HS	5.9466	0	68.8848	0	0	0	25.1686	100
NC	2.3325	0	**97.6675**					100
PC	3.6079	10.6688	0	0	0	0	**85.7233**	100
Sum	21.584	57.7315	276.334	0	0	0	244.3505	
Lbl		CC_n	NC_n				PC_n	

Table F.7: Ground Truth (Pixels)

Class	CC	NC	PC	Total
Unclassified	1655	442	862	2959
CC_n	22335	0 2549	24	884
NC_n	0	18508	0	18508
PC_n	23468	0 20481	4	3949
Total	47458	18950	23892	90300

Table F.8: Ground Truth(Percent)

Class	CC	NC	PC	Total
Unclassified	3.49	2.33	3.61	3.28
CC_n	47.06	0	10.67	27.56
NC_n	0	97.67	0	20.5
PC_n	49.45	0	85.72	48.67
Total	100	100	100	100

Table F.9: Commission and omission errors

Class	Commission (Percent)	Omission (Percent)	Commission (Pixels)	Omission (Pixels)
CC_n	10.24	52.94	2549/24884	25123/47458
NC_n	0	2.33	0/18508	442/18950
PC_n	53.4	14.28	23468/43949	3411/23892

Table F.10: Producer's and User's accuracies

Class	Prod. Acc. (Percent)	User Acc. (Percent)	Prod. Acc. (Pixels)	User Acc. (Pixels)
CC_n	47.06	89.76	22335/47458	22335/24884
NC_n	97.67	100	18508/18950	18508/18508
PC_n	85.72	46.6	20481/23892	20481/43949

Appendix G

Confusion Matrices for CC

Confusion matrices for the first step cropped corn decision tree classifications are as follows:

Table G.1: Corn classification results for September 15^{th}

	CC	NCC	Total
CC	0	23	23
NCC	54	36	90
Total	54	59	113

Table G.2: Corn classification results for September 18^{th}

	CC	NCC	Total
CC	53	38	91
NCC	1	21	22
Total	54	59	113

Table G.3: Corn classification results for October 9^{th}

	CC	NCC	Total
CC	43	16	59
NCC	3	51	54
Total	46	67	113

Table G.4: Corn classification results for October 12^{th}

	CC	NCC	Total
CC	46	3	49
NCC	0	64	64
Total	46	67	113

Table G.5: Corn classification results for October 15^{th}

	CC	NCC	Total
CC	50	3	53
NCC	1	59	60
Total	51	62	113

Table G.6: Corn classification results for November 2^{nd}

	CC	NCC	Total
CC	41	10	51
NCC	1	61	62
Total	42	71	113

Table G.7: Corn classification results for November 5^{th}

	CC	NCC	Total
CC	37	6	43
NCC	5	65	70
Total	42	71	113

Table G.8: Corn classification results for November 9^{th}

	CC	NCC	Total
CC	29	15	44
NCC	1	68	69
Total	30	83	113

Appendix H

RFD with Yamaguchi's Volume in Matlab

This appendix provides the code written for RFD algorithm using the Yamaguchi's[80] correction for volume scattering.

```
%   %   This is the code written to perform refined Freeman-Durden with
% Yamaguchi's volume scattering corrections.
%   Its inputs are 4 by 4 covariance matrix and alpha over beta ratio.
% notes:
function [Span_S,Span_D,Span_V,fs_r, fd_r, fv_r, alpha_rr, alpha_i, alpha_r, beta_r,Type_1]=..
    FreemanDurden(C4,aOverB)
            % The original formulation of the parameters
            % <|Shv|^2> = fv/3;
            %           removing fv/3 from real part of <ShhSvv*> and fv
            %           from <|Shh|^2> and  <|Svv|^2> leads to
            % <|Shh|^2>new = fs * beta^2 + fd * abs(alpha)^2;
            % <|Svv|^2>new = fs + fd;
            % R<ShhSvv*>new = fs * beta + fd * R(alpha);
            % I<ShhSvv*> =  fd * I(alpha);
            % abs(alpha)/beta= input
Type_1=1;                                   % Flag initialization(null)
eps=10^(-10);                               % Calculation accuracy
global FieldID;                             % Field Id number
%% Symbolic initialization for Freeman-Durden
% syms a b_r b_i d e c fv;                    % Knowns
syms fs fd alp_r alp_i bet ;                % Unknowns
```

```
a=C4(:,:,1);                    % <|Shh|^2>
b_r=real(C4(:,:,13));           % R<ShhSvv*>
b_i=imag(C4(:,:,13));           % I<ShhSvv*>
            %   because the solution is based on C3(and not C4 therefore
            %   <|Shv|^2>= 2* C4(:,:,6)
c=2*C4(:,:,6);                  % 2 * <|Shv|^2>
d=C4(:,:,16);                   % <|Svv|^2>
            % e is alpha over beta ratio
e=ones(size(C4,1),size(C4,2))*aOverB;          % Resized for matrix
                                                %    manipulation purposes
const_mult=1;%min([min(min(a)),min(min(c)),min(min(d))]);
a=a/const_mult;b_r=b_r/const_mult;b_i=b_i/const_mult;
c=c/const_mult;d=d/const_mult;

if aOverB==0||aOverB<10^-1
%% No double-bounce
            % When H/A/alpha did not find even a single occurrance for
            % double-bounce scattering or very rare ocurrances
    fd_r=0;                                     % double scattering portion
    alpha_i=0;                                  % Imaginary part of alpha
    alpha_r=0;                                  % Absolute value of alpha
    alpha_rr=0;                                 % Real part of alpha
    temp=nan;                                   % Dummy parameter represents
                                                %    beta

    if 10*log(d/a)<-2
        fv=2*c;                                % volume scattering portion
        b_r=b_r-fv/4;                           % R<ShhSvv*>_new
```

```
    a=a-fv;                                 % <|Shh|^2>_new
    d=d-3*fv/8;                                 % <|Svv|^2>_new
   Span_V = 15. .* fv ./ 8.;
elseif 10*log(d/a)>2
    fv=2*c;                                % volume scattering portion
    b_r=b_r-fv/4;                           % R<ShhSvv*>_new
    a=a-3*fv/8;                                 % <|Shh|^2>_new
    d=d-fv;                                 % <|Svv|^2>_new
    Span_V = 15. .* fv ./ 8.;
else
    fv=3*c/2;                               % volume scattering portion
    b_r=b_r-fv/3;                           % R<ShhSvv*>_new
    a=a-fv;                                 % <|Shh|^2>_new
    d=d-fv;                                 % <|Svv|^2>_new
    Span_V = 8. .* fv ./ 3.;
end
fs_r=d;                                     % Surface scat. portion
beta_r(1,1)=b_r/fs_r;                       % beta
        % The following root for beta_r_1 for some reason would not
        %   produce any real roots and therefore leads to a unique
        %   desired solution
temp=sqrt(a/fs_r);
if isreal(temp)
    beta_r(1,2)=temp;                  % Second beta
    alpha_r(1,2)=0;                    % Second beta
    alpha_i(1,2)=0;                    % Second beta
    alpha_rr(1,2)=0;                   % Second beta
end
```

```
    fv_r=fv;
    Span_S =fs_r.* (1 + beta_r.^2);            % Span definitions
    Span_D =fd_r .* (1 + (alpha_i.^2+alpha_r.^2));
    Type_1=2;                                  % flag of no double-bounce
elseif isinf(aOverB)||aOverB>10^2
%% No Surface scattering
            % When H/A/alpha did not find even a single occurrance for
            % surface scattering or very rare ocurrances
    fs_r=0;                                    % Surface scat. portion
    beta_r=0;                                  % beta
    alpha_i=0;                                 % Imaginary part of alpha
    temp=nan;                                  % Dummy for beta
%% Yamaguchi's fv
     if 10*log(d/a)<-2
        fv=2*c;                               % volume scattering portion
        b_r=b_r-fv/4;                           % R<ShhSvv*>_new
        a=a-fv;                                 % <|Shh|^2>_new
        d=d-3*fv/8;                                 % <|Svv|^2>_new
        Span_V = 15. .* fv ./ 8.;
    elseif 10*log(d/a)>2
        fv=2*c;                               % volume scattering portion
        b_r=b_r-fv/4;                           % R<ShhSvv*>_new
        a=a-3*fv/8;                                 % <|Shh|^2>_new
        d=d-fv;                                 % <|Svv|^2>_new
        Span_V = 15. .* fv ./ 8.;
    else
        fv=3*c/2;                               % volume scattering portion
        b_r=b_r-fv/3;                           % R<ShhSvv*>_new
```

```
        a=a-fv;                                 % <|Shh|^2>_new
        d=d-fv;                                 % <|Svv|^2>_new
        Span_V = 8. .* fv ./ 3.;
     end
%     fv_r=3*c*const_mult;                      % Volume scat. portion
    fd_r=d;                    % double-bounce scat. portion
    alpha_r=(b_r)/fd_r;      % Real part of alpha
            % The following root for alpha, for some reason would not
            %   produce any real roots and therefore leads to a unique
            %   desired solution
    fv_r=fv;
    alpha_r2=sqrt((fv)/fd_r);
    if isreal(alpha_r2)
        alpha_r(1,2)=alpha_r2;                  % Second alpha
        beta_r(1,2)=0;                          % Second alpha
        alpha_i(1,2)=0;                         % Second alpha
    end
    alpha_rr=alpha_r;                           % Real part of alpha
    Span_S =fs_r.* (1 + beta_r.^2);             % Span definitions
    Span_D =fd_r .* (1 + (alpha_i.^2+alpha_r.^2));
    Type_1=7;                                   % Flag for no Surface Scat.
elseif aOverB==-100
%% No Surface scattering
            % When H/A/alpha did not find even a single occurrance for
            % surface scattering or very rare ocurrances
    fs_r=0;                                     % Surface scat. portion
    beta_r=0;                                   % beta
    alpha_i=0;                                  % Imaginary part of alpha
```

```
%% Yamaguchi's fv
     if 10*log(d/a)<-2
        fv=2*c;                                 % volume scattering portion
        b_r=b_r-fv/4;                             % R<ShhSvv*>_new
        a=a-fv;                                   % <|Shh|^2>_new
        d=d-3*fv/8;                                   % <|Svv|^2>_new
        Span_V = 15. .* fv ./ 8.;
    elseif 10*log(d/a)>2
        fv=2*c;                                 % volume scattering portion
        b_r=b_r-fv/4;                             % R<ShhSvv*>_new
        a=a-3*fv/8;                                   % <|Shh|^2>_new
        d=d-fv;                                   % <|Svv|^2>_new
        Span_V = 15. .* fv ./ 8.;
    else
        fv=3*c/2;                                 % volume scattering portion
        b_r=b_r-fv/3;                             % R<ShhSvv*>_new
        a=a-fv;                                   % <|Shh|^2>_new
        d=d-fv;                                   % <|Svv|^2>_new
        Span_V = 8. .* fv ./ 3.;
     end
    fv_r=fv;                                    % Volume scat. portion
    fd_r=0;                     % double-bounce scat. portion
    alpha_r=0;      % Real part of alpha
            % The following root for alpha, for some reason would not
            %   produce any real roots and therefore leads to a unique
            %   desired solution
    alpha_rr=alpha_r;                           % Real part of alpha
    Span_S =fs_r.* (1 + beta_r.^2);             % Span definitions
```

```
    Span_D =fd_r .* (1 + (alpha_i.^2+alpha_r.^2));
    Type_1=10;                                  % Flag for Only volume.
else
%% The remaining cases of scatterings
    Type_1=3;                                  % Flag for general case
            % over 2 is according to their codes. I am not sure about the
            %   validity
%% Yamaguchi's fv
     if 10*log(d/a)<-2
        fv=2*c;                                % volume scattering portion
        b_r=b_r-fv/4;                            % R<ShhSvv*>_new
        a=a-fv;                                  % <|Shh|^2>_new
        d=d-3*fv/8;                                  % <|Svv|^2>_new
        Span_V = 15. .* fv ./ 8.;
    elseif 10*log(d/a)>2
        fv=2*c;                                % volume scattering portion
        b_r=b_r-fv/4;                            % R<ShhSvv*>_new
        a=a-3*fv/8;                                  % <|Shh|^2>_new
        d=d-fv;                                  % <|Svv|^2>_new
        Span_V = 15. .* fv ./ 8.;
    else
        fv=3*c/2;                                % volume scattering portion
        b_r=b_r-fv/3;                            % R<ShhSvv*>_new
        a=a-fv;                                  % <|Shh|^2>_new
        d=d-fv;                                  % <|Svv|^2>_new
        Span_V = 8. .* fv ./ 3.;
    end
    %% Solving by matlab solver (very slow and mostly just for checking)
```

```
% %     temp01=solve('(b_r-bet*d+(bet^2*d-a)/bet/(1-e^2))^2+b_i^2-e^2*((bet^2*d-a)^2/bet^2/(1-e
% %     temp=vpa(subs(temp01(1)));
% %     be=nan;
    %% Explicit solution
            %   not accurate due to rounding errors in 15th or 16th digit
    [x1,x2,x3,x4]=PolyRoots4thDeg(d^2*e^2   ,   -2*b_r*d*e^2   ,...
        -b_r^2 - b_i^2 + b_r^2*e^2 + b_i^2*e^2   ,   2*a*b_r,-a^2);
    temp=[x1,x2,x3,x4];
    be=nan;
    %% removing complex roots
            %   since the answer is forth digree polynomial
    for i=1:4
        if isreal(temp(i))%||double(abs(imag(temp(i))))<eps
            be(i)=real(temp(i));
        end
            %   very small imaginary parts(looking for hidden multiple
            %   roots). This case is not used in order to single out unique
            %   roots.
% % %         if double(abs(imag(temp(i))))<eps
% % %             be(i)=real(temp(i));
% % %         end
    end
            %   If there is not even a single unique root this part will
            %   look for it. Notice that even a single negative unique root
            %   is an answer in this case
    if isnan(be)==1
        for i=1:4
            if double(abs(imag(temp(i))))<eps
```

```
                be(i)=real(temp(i));
            end
        end
%       if isnan(be)==1
            %   Absolutly No root has been detected for beta
            Type_1=4;                           % Flag for no root
%       end
    end
    %% Estimation of unknows for general case
    fd=d./(1-e^2)-a./(be.^2)/(1-e^2);           % double-bounce portion
    %% The remaining of the estimation
    alp_i=b_i./fd;                              % Imaginary part of alpha
    fs=d-fd;                                    % Surface scattering portion
    alp_r=(b_r-be.*fs)./fd;                     % Real part of alpha
    %% Equation 5 test
    test01=find(double(be)>0);                  % Positiveness of beta
                                                % Positiveness of surface,
                                                % double-bounce and beta.
    test02=find(double(be)>=0&double(fd)>=0&double(fs)>=0);
    if isempty(test02)==0
        if size(test02,2)>1
            Type_1=5;                           % Flag for no acceptable root
        end
    end
            % updated for the multiplier
    fv_r=fv*const_mult;                         % Volume scattering portion
    fd_r=double(fd(test01))*const_mult;         % double-bounce portion
    fs_r=double(fs(test01))*const_mult;         % Surface scat. portion
```

```
    alpha_i=double(alp_i(test01));              % Imaginary part of alpha
    alpha_rr=double(alp_r(test01));             % Real part of alpha
            %   which one is the correct one no one knows but I guess using
            %   beta for comparison is a better idea although it is not
            %   fully coorrect since this two are somehow independant.
%     alpha_r=double(alp_r(test01));
                                                % Absolute value of alpha
    alpha_r=sqrt(double(alp_i(test01)).^2+double(alp_r(test01)).^2);
    beta_r=double(be(test01));                  % beta
    Span_S =fs_r.* (1 + beta_r.^2);             % Span definitions
    Span_D =fd_r .* (1 + (alpha_i.^2+alpha_r.^2));
    beta_r=temp;
end
```

Appendix I

Confusion Matrices for CC,CS

Confusion matrices for the second decision tree classifications are as follows:

Table I.1: Confusion matrix for 09/18/2009

	CC	CS	H	Total
CC	53	33	5	91
CS	1	13	5	19
H	0	2	1	3
Total	54	48	11	113

Table I.2: Confusion matrix for 10/09/2009

	CC	CS	H	Total
CC	43	6	10	59
CS	2	14	23	39
H	1	3	11	15
Total	46	23	44	113

Table I.3: Confusion matrix for 10/12/2009

	CC	CS	H	Total
CC	46	2	1	49
CS	0	20	26	46
H	0	1	17	18
Total	46	23	44	113

Table I.4: Confusion matrix for 10/15/2009

	CC	CS	H	Total
CC	50	1	2	53
CS	1	24	20	45
H	0	0	15	15
Total	51	25	37	113

Table I.5: Confusion matrix for 11/02/2009

	CC	CS	H	Total
CC	40	0	10	50
CS	0	7	35	42
NC	2	3	16	21
Total	42	10	61	113

Table I.6: Confusion matrix for 11/05/2009

	CC	CS	H	Total
CC	37	0	6	43
CS	4	7	30	41
NC	1	3	25	29
Total	42	10	61	113

Table I.7: Confusion matrix for 11/08/2009

	CC	CS	H	Total
CC	29	0	15	44
CS	0	4	19	23
H	1	4	41	46
Total	30	8	75	113